

AD/A-003 304

**THE SHOCK AND VIBRATION BULLETIN. PART 3.
SHOCK TESTING, SHOCK ANALYSIS**

**Naval Research Laboratory
Washington, D. C.**

August 1974

DISTRIBUTED BY:

NTIS

**National Technical Information Service
U. S. DEPARTMENT OF COMMERCE**

Best Available Copy

023110

Bulletin 44
(Part 3 of 5 Parts)

AD A003304

THE SHOCK AND VIBRATION BULLETIN

Part 3
Shock Testing, Shock Analysis

AUGUST 1974

Reproduced by
NATIONAL TECHNICAL
INFORMATION SERVICE
U. S. Department of Commerce
Springfield, VA 22161

A Publication of
THE SHOCK AND VIBRATION
INFORMATION CENTER
Naval Research Laboratory, Washington, D.C.

FOR INFORMATION ONLY

NOT FOR SALE
DISTRIBUTION

Office of the Information Center
Naval Research Laboratory, Code 6020
Washington, D.C. 20390



D D C
RECEIVED
JAN 21 1975
D

Office of
The Director of Defense
Research and Engineering

Approved for public release: distribution unlimited.

72-AZ-1-333

215

Best Available Copy

REPRODUCTION QUALITY NOTICE

This document is the best quality available. The copy furnished to DTIC contained pages that may have the following quality problems:

- **Pages smaller or larger than normal.**
- **Pages with background color or light colored printing.**
- **Pages with small type or poor printing; and or**
- **Pages with continuous tone material or color photographs.**

Due to various output media available these conditions may or may not cause poor legibility in the microfiche or hardcopy output you receive.

☐

If this block is checked, the copy furnished to DTIC contained pages with color printing, that when reproduced in Black and White, may change detail of the original copy.

ACCESSION NO.	
NTIS	Write Section <input checked="" type="checkbox"/>
DOC	Bull. Section <input type="checkbox"/>
UNANNOUNCED	<input type="checkbox"/>
JUSTIFICATION	
BY	
DISTRIBUTION/AVAILABILITY CODES	
DISC.	AVAIL. REC. BY SPECIAL
A 21	

SYMPOSIUM MANAGEMENT

THE SHOCK AND VIBRATION INFORMATION CENTER

Henry C. Pusey, Director
 Edward H. Schell
 Rudolph H. Volin
 J. Gordon Showalter

Bulletin Production

Graphic Arts Branch, Technical Information Division,
 Naval Research Laboratory

Best Available Copy

Bulletin 44

(Part 3 of 5 Parts)

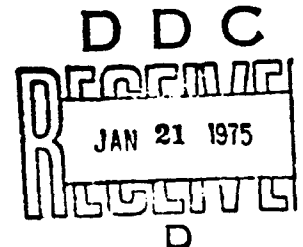
THE SHOCK AND VIBRATION BULLETIN

AUGUST 1974

**A Publication of
THE SHOCK AND VIBRATION
INFORMATION CENTER
Naval Research Laboratory, Washington, D.C.**

The 44th Symposium on Shock and Vibration was held at the Rice Hotel and Lyndon B. Johnson Space Center, Houston, Texas on 4-7 December 1973. The National Aeronautics and Space Administration was the host.

**Office of
The Director of Defense
Research and Engineering**



CONTENTS

PAPERS APPEARING IN PART 3

Shock Testing

DIGITALLY CONTROLLED TRANSIENT WAVEFORM TESTING — ALTERNATE METHOD TO SLOW SINE SWEEP	1
B.K. Kim, Jet Propulsion Laboratory, Pasadena, California	
COMPARISON OF SHOCK SPECTRUM TECHNIQUES AND THE METHOD OF LEAST FAVORABLE RESPONSE	7
A.F. Witte and R.J. Wolf, Kaman Sciences Corporation, Colorado Springs, Colorado	
APPLICATION OF LEAST FAVORABLE RESPONSE TECHNIQUES INCORPO- RATING FIELD DATA FOURIER TRANSFORM PHASE ANGLE	25
R.J. Wolf and A.F. Witte, Kaman Sciences Corporation, Colorado Springs, Colorado	
MATCHING SHOCK SPECTRA WITH SUMS OF DECAYING SINUSOIDS COMPEN- SATED FOR SHAKER VELOCITY AND DISPLACEMENT LIMITATIONS	43
D.O. Smallwood and A.R. Nord, Sandia Laboratories, Albuquerque, New Mexico	
A CASE FOR DAMPED OSCILLATORY EXCITATION AS A NATURAL PYROTECHNIC SHOCK SIMULATION	57
D.B. Nelson and P.H. Prasthofer, Sandia Laboratories, Livermore, California	
DEVELOPMENT OF A PYROTECHNIC SHOCK TEST FACILITY	73
D.R. Powers, McDonnell Douglas Astronautics Company, Santa Monica, California	
STUDY OF AN EXPERIMENTAL TECHNIQUE FOR APPLICATION TO STRUCTURAL DYNAMIC PROBLEMS	83
R.F. Snell, McDonnell Douglas Astronautics Company, Huntington Beach, California	
TIMEWISE OUTPUT OF PYROTECHNIC BOLTS	101
V.H. Neubert, The Pennsylvania State University, University Park, Pennsylvania and R.P. Parker, Uniroyal Research Center, Middlebury, Connecticut	
PYROTECHNIC SHOCK REDUCTION	111
S.N. Prescott, Jet Propulsion Laboratory, Pasadena, California	

IMPACT TESTING WITH THE 35-FOOT CENTRIFUGE	125
J.V. Otts, Sandia Laboratories, Albuquerque, New Mexico	
FRAGMENT VELOCITIES FROM EXPLODING LIQUID PROPELLANT TANKS ..	133
R.L. Bessey, Southwest Research Institute, San Antonio, Texas	

Shock Analysis

PIPING DESIGN FOR HYDRAULIC TRANSIENT PRESSURE	141
C.C. Huang, R.J. Bradshaw, Jr., U.S. Army Engineer Division, Huntsville, Alabama and H.H. Yen, Sperry-Rand Corporation, Huntsville, Alabama	
POPPING MOTOR DOME SHOCK DURING FIRST STAGE SEPARATION ON POSEIDON MISSILE FLIGHTS	157
L.R. Pendleton and R.L. Henrikson, Lockheed Missiles and Space Company, Sunnyvale, California	
SCALING OF WATER IMPACT DATA FOR SPACE SHUTTLE SOLID ROCKET BOOSTER	165
R. Madden, H A. Wright, Bolt Beranek and Newman, Inc., Cambridge, Mass- achusetts and D.A. Kross, NASA Marshall Space Flight Center, Huntsville, Alabama	
IDENTIFICATION OF AN OPTIMUM SET OF TRANSIENT SWEEP PARAMETERS FOR GENERATING SPECIFIED RESPONSE SPECTRA	177
R.C. Rountree, The Aerospace Corporation, El Segundo, California and C.R. Freberg, University of Southern California, Los Angeles, California	
ANALYSIS OF OPEN CELL POLYURETHANE FOAM UNDER IMPACT LOADING	193
V. Sepecenko, Boeing Aerospace Company, Seattle, Washington	
MEASUREMENT OF PEAK PRESSURES PRODUCED AT THE GROUND SURFACE BY SHALLOW BURIED EXPLOSIVES	203
B.L. Morris, U.S. Army Mobility Equipment Research and Development Center, Fort Belvoir, Virginia	

PAPERS APPEARING IN PART 1

Summaries of Papers Presented at 44th Symposium

PAPERS APPEARING IN PART 2

Invited Papers

SPACE SHUTTLE DYNAMICS

Mr. Robert F. Thompson, Manager, Space Shuttle Program, Lyndon B.
Johnson, Space Center, Houston, Texas

VIKING DYNAMICS — AN OVERVIEW

Dr. Richard E. Snyder, NASA Langley Research Center, Hampton, Virginia

VIKING ORBITER — DYNAMICS OVERVIEW

Mr. Ben K. Wada, Jet Propulsion Laboratory, Pasadena, California

VIKING LANDER DYNAMICS

Mr. Joseph C. Pohlen, Martin Marietta Aerospace, Denver, Colorado

Structural Dynamics

PERFORMANCE OF STATISTICAL ENERGY ANALYSIS

R.F. Davis and D.E. Hines, McDonnell Douglas Astronautics Company,
Huntington Beach, California

**PREDICTION OF SHOCK ENVIRONMENTS BY TRANSFER FUNCTION
MEASUREMENT TECHNIQUES**

G.C. Kao, J.M. Cantril, G.D. Shipway, Wyle Laboratories, Huntsville,
Alabama, and M.A. Boyd, U.S. Army Corps of Engineers, Huntsville, Alabama

**DETERMINATION OF GUIDEWAY ROUGHNESS FROM CONSTRUCTION
TOLERANCES**

B.J. Brock, Vought Systems Division LTV Aerospace Corporation,
Dallas, Texas

**SELECTED SYSTEM MODES USING THE DYNAMIC TRANSFORMATION WITH
—MODAL SYNTHESIS**

E.J. Kuhar, General Electric Company, Philadelphia, Pennsylvania

**STRUCTURAL DYNAMICS COMPUTATIONS USING AN APPROXIMATE
TRANSFORMATION**

C.S. O'Hearne and J.W. Shipley, Martin Marietta Aerospace, Orlando, Florida

**LINEAR LUMPED-MASS MODELING TECHNIQUES FOR BLAST
LOADED STRUCTURES**

W.J. Liss, Jr. and N.J. DeCapua, Bell Laboratories, Whippany, New Jersey

**DEVELOPMENT AND CORRELATION: VIKING ORBITER ANALYTICAL
DYNAMIC MODEL WITH MODAL TEST**

B.K. Wada, J.A. Garba and J.C. Chen, Jet Propulsion Laboratory, Pasadena,
California

MODAL TEST RESULTS OF THE VIKING ORBITER

E.L. Leppert, B.K. Wada, Jet Propulsion Laboratory, Pasadena, California,
and R. Miyakawa, Martin-Marietta Aerospace, Denver, Colorado (assigned
to the Jet Propulsion Laboratory)

**IMPLEMENTATION OF INTERACTIVE GRAPHICS TO A TRANSIENT
RESPONSE RING CODE**

R.W. Buchanan, T.N. Vogel and P.G. Underwood, Lockheed Missiles and
Space Company, Sunnyvale, California

COMPUTER GENERATED DISPLAYS OF STRUCTURES IN VIBRATION
H.N. Christiansen, Brigham Young University, Provo, Utah

**VIBRATION REDUCTION BY USING BOTH THE FINITE ELEMENT STRAIN
ENERGY DISTRIBUTION AND MOBILITY TECHNIQUES**
J. J. Sciarra, Boeing Vertol Company, Philadelphia, Pennsylvania

**INFLUENCE OF ELASTIC SUPPORTS ON NATURAL FREQUENCIES OF
CANTILEVER BEAMS**
R.F. Solberg, Jr., Southwest Research Institute, San Antonio, Texas

PAPERS APPEARING IN PART 4

Underwater Problems

**APPLICATION OF MECHANICAL IMPEDANCE CONCEPTS TO THE COUPLING
PROBLEM OF STRUCTURES IN SHOCK ENVIRONMENT**
R. Aquilina and L. Gaudriot, Center D-Etudes et de Recherches Techniques
Sous-Marines, Direction Des Constructions Et Armes Navales, Toulon, France

**THE NAVY LARGE FLOATING SHOCK PLATFORM-PART I: PHYSICAL
DESCRIPTION AND CAPABILITIES**
C.G. Schrader, West Coast Shock Facility, San Francisco, California

**THE NAVY LARGE FLOATING SHOCK PLATFORM-PART II: SHOCK
CHARACTERISTICS**
E.W. Clements, Naval Research Laboratory, Washington, D.C.

**THE EFFECT OF UNIFORM EXTERNAL PRESSURIZATION ON THE DYNAMIC
RESPONSE OF ISOTROPIC CYLINDRICAL SHELLS**
F.J. Dzialo, University of Massachusetts, Amherst, Massachusetts

**ON DEFINING TIME DOMAINS FOR RADIATION DAMPING AND ADDED MASS
EFFECTS IN FLUID-STRUCTURAL INTERACTION**
A.V. Clark Jr., Naval Research Laboratory, Washington, D.C.

Environments and Measurements

HARPOON MISSILE FLIGHT ENVIRONMENTAL MEASUREMENT PROGRAM
V.S. Noonan, J.L. Gubser and R.D. Harmening, McDonnell Douglas Astro-
nautics Company, St. Louis, Missouri

**NARROW BAND TIME HISTORY ANALYSIS OF TRANSPORT AIRCRAFT
VIBRATION DATA**
R.E. Thaller and J. Pearson, Air Force Flight Dynamics Laboratory, Wright-
Patterson AFB, Ohio

PRELIMINARY MEASUREMENT AND ANALYSIS OF THE VIBRATION ENVIRONMENT OF COMMON MOTOR CARRIERS
W.N. Sharpe, T.J. Kusza, F.W. Sherman and J.W. Goff, School of Packaging, Michigan State University, East Lansing, Michigan

THE DYNAMIC ENVIRONMENT OF LANDING CRAFT
M.B. Gens, Sandia Laboratories, Albuquerque, New Mexico

A RESONANCE-TYPE BACK-TO-BACK CALIBRATOR FOR ACCELEROMETERS
J.A. Macinante, N.H. Clark, B.H. Cresswell, CSIRO, Division of Applied Physics, National Standards Laboratory, Sydney, Australia

A NEW TRANSVERSE CALIBRATOR FOR ACCELEROMETERS
J.A. Macinante, N.H. Clark, and B.H. Cresswell, CSIRO, Division of Applied Physics, National Standards Laboratory, Sydney, Australia

PAPERS APPEARING IN PART 5

Isolation and Damping

DESIGN OF CONSTRAINED LAYER TREATMENTS FOR BROAD TEMPERATURE DAMPING
D.I.G. Jones, Air Force Materials Laboratory, Wright-Patterson AFB, Ohio

REDUCTION OF INTERIOR CABIN NOISE LEVELS IN A HELICOPTER THROUGH ADDITIVE DAMPING
J.P. Henderson, Air Force Materials Laboratory, Wright-Patterson AFB, Ohio and A.D. Nashif, University of Dayton, Dayton, Ohio

VIBRATION DAMPING AND ISOLATION WITH ENERGY ABSORBING COMPOSITES
J. Nunes, Brunswick Corporation, Skokie, Illinois

SUPPRESSION OF TORSIONAL VIBRATION WITH ZERO TORSIONAL STIFFNESS COUPLINGS
J.M. Vance, University of Florida, Gainesville, Florida and R.A. Brown, E.I. du Pont de Nemours and Company, Inc., Wilmington, Delaware

Vibration Testing and Analysis

DEVELOPMENT OF SAM-D MISSILE RANDOM VIBRATION RESPONSE LOADS
P.G. Hahn, Martin Marietta Aerospace, Orlando, Florida

EVALUATION OF BLOCKED ACOUSTIC PRESSURE ON STIFFENED CYLINDRICAL SHELLS
V.M. Conticelli, Aeritalia S.p.A., Naples, Italy, and G.C. Kao, Wyle Laboratories, Huntsville, Alabama

**REDUCTION OF HULL NOISE AND VIBRATION BY CENTER OF PERCUSSION
ROADARM DESIGN**

D.D. Ustick, U.S. Army Tank-Automotive Command, Warren, Michigan

SYNCHRONIZATION AND PHASE ANGLE OF TWO UNBALANCED ROTORS

M. Paz, University of Louisville, Louisville, Kentucky, P.H. Schrader and

R. Blackmon, Vibrating Equipment Division, Rexnord, Inc., Louisville, Kentucky

**EXPERIMENTAL INVESTIGATION OF THE DYNAMIC RESPONSE OF
CANTILEVER ANTISOTROPIC PLATES**

R.L. Sierakowski, University of Florida, Gainesville, Florida and C.T. Sun,

Iowa State University, Ames, Iowa

SPACECRAFT VIBRATION TEST LEVEL COST OPTIMIZATION STUDY

J.P. Young, NASA Goddard Space Flight Center, Greenbelt, Maryland

FLIGHT QUALIFICATION OF SPECIAL EQUIPMENT

J. Pearson and R.E. Thaller, Air Force Flight Dynamics Laboratory, Wright-

Patterson AFB, Ohio

THE USE OF LISSAJOUS FIGURES IN VIBRATION TESTING

J.D. Ray, Memphis State University, Memphis, Tennessee and C.W. Bert,

University of Oklahoma, Norman, Oklahoma

STRUCTURAL DYNAMIC RESPONSE ANALYSIS OF ROCKET TEST SLEDS

T.N. Gardner, Mechanics Research Incorporated, Los Angeles, California

CONSIDERATION OF THE RESPONSE OF A SLED BORNE MISSILE

A.R. Glaser, Rockwell International, Columbus, Ohio and L.C. Mixon,

6585th Test Group, Holloman AFB, New Mexico

**FLOW-INDUCED VIBRATIONS OF A GLASS-REINFORCED PLASTIC
SONAR DOME**

D.A. King, Rockwell International Corporation, Anaheim, California

**AERO-ACOUSTIC ENVIRONMENT OF A RECTANGULAR CAVITY WITH A
LENGTH TO DEPTH RATIO OF FOUR**

L.L. Shaw and D.L. Smith, Air Force Flight Dynamics Laboratory, Wright-

Patterson AFB, Ohio

**RESPONSE OF LINEAR DYNAMICAL SYSTEMS UNDER NONSTATIONARY
RANDOM EXCITATIONS**

T.S. Sankar and D. Doan, Sir George Williams University, Montreal, Canada

**MEANS OF CONTROLLING THE DYNAMIC MOTION OF BOTTOM MOORED
MINE CASES EXPOSED TO HIGH CURRENT**

J.J. O'Neill, J. Berezow and J.E. Goeller, Naval Ordnance Laboratory, Silver

Spring, Maryland

SHOCK TESTING

DIGITALLY CONTROLLED TRANSIENT WAVEFORM TESTING - ALTERNATE METHOD TO SLOW SINE SWEEP

B. K. Kim
Jet Propulsion Laboratory
Pasadena, California

Development of a transient waveform testing methodology in lieu of the conventional slow sine-sweep forced vibration testing is reported. Various advantages of the digitally controlled transient testing are presented, and procedures for generating the exact time-history pulse shape are discussed.

INTRODUCTION

In the recent years the environmental testing methodology has experienced a rapid change since the introduction of digitally controlled vibration and acoustic systems [1]. Successful marriage of a digital minicomputer with a hardware-fast Fourier processor and the existing vibration exciter-amplifier systems has received industry acceptance in random and sine-sweep testing.

In 1969, Favour, LeBrun, and Young [2] suggested a way of testing to a specified transient time history using the fast Fourier transform technique and a digital control system. This transient waveform control concept not only offers a new method of testing, but more importantly, it offers a new concept in test philosophy that governs random and sine-type testing.

In a spacecraft design, the primary loading on the spacecraft structure may be caused by launch and separation transients. The finite number of telemetered flight transient data constitutes the load basis for the next similar type of spacecraft structure design. The static and sine-sweep vibration specifications are derived from the enveloped shock spectra computed from the transient data. Thus the spacecraft test philosophy is formulated from three mutually complementing investigations: namely, (1) what are the maximum flight loads that lead to the environmental specification, (2) how to design the spacecraft such that it will survive the flight loads with some margin

of confidence, and (3) how to verify the design by testing in a controlled manner. This triangular relationship is depicted in Fig. 1.

The purpose of this paper is to present transient waveform testing methods as an alternate approach to the conventional slow sine-sweep test for a system level qualification test. It is presented from the viewpoint of the test concept and implementation. The digital test control system is assumed throughout. The term "transient" shall be defined as a time-history, pulse-like oscillatory waveform of short duration, typically in the order of a second.

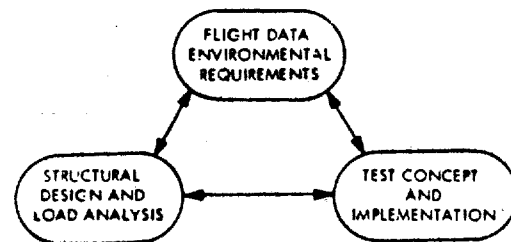


Fig. 1 - Mutual relationship between specification, design, and testing

TRANSIENT TESTING CONCEPTS

Although the conventional slow sine-sweep test is well understood and routinely implemented, it does present severe problems in

testing a complex structure such as a Viking-type spacecraft system, namely:

- (1) Since each mode is excited separately from the base, a peak select response control scheme is necessary to prevent overtesting.
- (2) The control capability of a closed-loop servo is highly sensitive to the modal Q, sweep rate, and switching slopes. This fact will result in severe overshoot-undershoot control errors for high-Q resonances, particularly in low-frequency primary structural modes.
- (3) Fatigue cycle buildup may increase the damage potential beyond recovery during the qualification vibration testing.

Thus, a large complex structure with low damping is susceptible to overtest and or undertest by a sweeping sine-type environmental test.

The proposed transient testing is intended to alleviate the above problem areas. The basic idea that is common in all forms of transient testing is that of open-loop control, which eliminates the servo control problems associated with high-Q resonances as well as the need for the peak select switching circuitry. However, the open-loop test requires an accurate estimate of the instantaneous transfer functions between the input command signal and the response points on the structure. The transfer function typically includes the cascaded product of power amplifier, shaker, fixture, specimen, and all the control electronic circuitry. It is not practical to generate a mathematical model for each cascaded transfer function. The total end-to-end transfer function is measured experimentally by applying a known function through the test system. There are three ways of generating the system transfer function $H(\omega)$:

- (1) Input a delta function-like single pulse $u(t)$ and obtain the response $v(t)$ in the calibration process as proposed in Ref. [3]. Then

$$H(\omega) = \frac{V(\omega)}{U(\omega)} \quad (1)$$

where $U(\omega)$, $V(\omega)$ represent the Fourier transform of $v(t)$ and $u(t)$, respectively in complex form. However, to obtain a well-conditioned

$H(\omega)$, it is necessary to give a substantial input pulse level, and this may have a damaging effect on a sensitive structure such as a spacecraft.

- (2) Input a constant low-level sine with slow sweep rate. This does not require the Fourier processing capability to produce the gain $|H(\omega)|$.
- (3) Input a band-passed, low-level random noise and calculate $H(\omega)$ from the cross-spectrum normalized to the input spectrum.

$$U^*(\omega) \cdot V(\omega) = H(\omega) \cdot |U(\omega)|^2 + U^*(\omega) \cdot N(\omega) \quad (2)$$

where $N(\omega)$ represents the Fourier transform of $n(t)$, the system noise. Since the input random signal $u(t)$ and the electronic system noise $n(t)$ are uncorrelated, the last term in Eq. (2) vanishes. Furthermore, with statistical averaging,

$$H(\omega) = \frac{\sum_{i=1}^M U_i^*(\omega) \cdot V_i(\omega)}{\sum_{i=1}^M |U_i(\omega)|^2} \quad (3)$$

It is important to minimize the system noise error in a low-level calibration test for the fatigue considerations. For a large structure that is sensitive to fatigue, the third method is preferred over the first two since a better signal-to-noise ratio and higher statistical confidence are achieved by frequency domain averaging as shown in Eq. (3).

TRANSIENT TESTING IMPLEMENTATION

Once the accurate system transfer function $H(\omega)$ is calculated and stored in the computer core, the necessary input waveform $y(t)$ can be synthesized to achieve the desired specification as the response.

Ideally, if a transient phenomenon can be represented by a "typical" time-history waveform $x(t)$, then $y(t)$ is readily synthesized by

$$y(t) = \mathcal{F}^{-1} \left\{ \frac{X(\omega)}{H(\omega)} \right\} \quad (4)$$

and the precise phase relationship is carried through. Details of implementing this method are presented in Ref. [3]. This is known as Transient Waveform Control. The hardware

implementation is shown in Fig. 2, and the software requirement is illustrated in Fig. 3. However, the phase spectra cannot be averaged and enveloped like the amplitude spectra. This fact presents the problem of how one could define a "typical" phase.

The severity of transient events are most commonly enveloped as max-max shock spectra, assuming the modal excitation causing the most damage. Given a shock spectrum as the test specification, there are several methods of deriving specific time histories that then can be implemented by the Transient Waveform Control method as follows:

- (1) Recently Yang and Saffell [4] suggested a scheme to generate a time function $f(t)$ such that

$$f(t) = \sum_{m=1}^M a_m f_m(t) \quad (5)$$

$$\left. \begin{aligned} f_m(t) &= \sin 2\pi b_m t \\ &\cdot \sin 2\pi N_m b_m t \text{ for } 0 \leq t \leq T_m \\ &= 0 \text{ for } t > T_m \end{aligned} \right\} \quad (6)$$

An iterative scheme is proposed to compute a_m 's such that $f(t)$ satisfies the desired shock spectrum. To generate a unique $f(t)$, this method requires the additional information of phase distributions and amplitude ratios.

- (2) Assuming the phase distribution is in general random in nature, the phase can be randomized by a pseudorandom sequence as it is done for digital vibration control systems [5]. That is, given a desired amplitude spectrum $A(\omega)$, equivalent complex spectrum $X(\omega)$ is found as

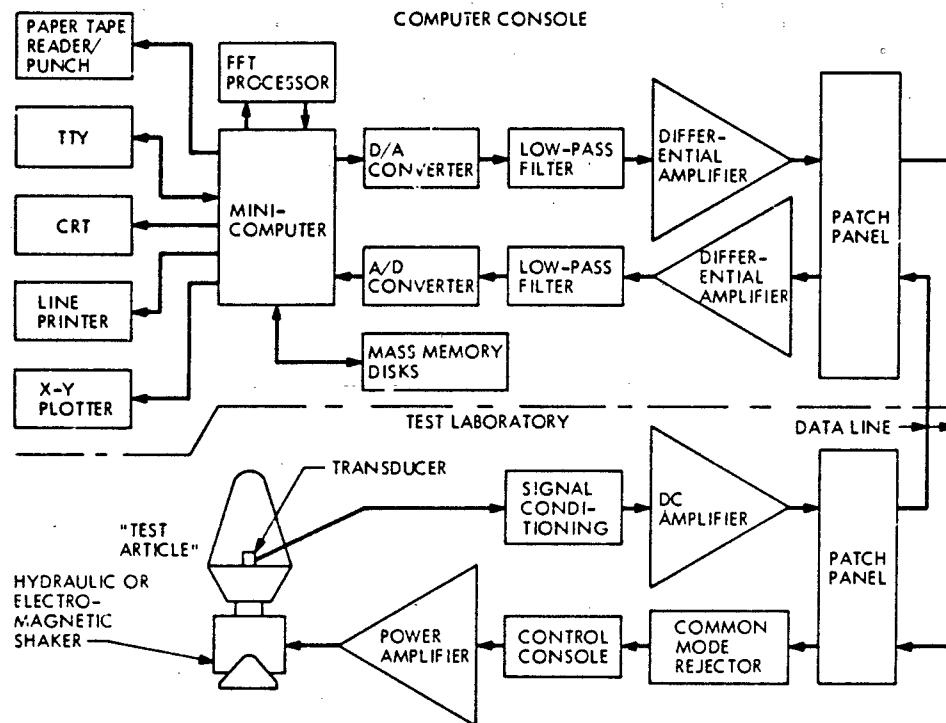


Fig. 2 - Transient waveform control, functional hardware block diagram

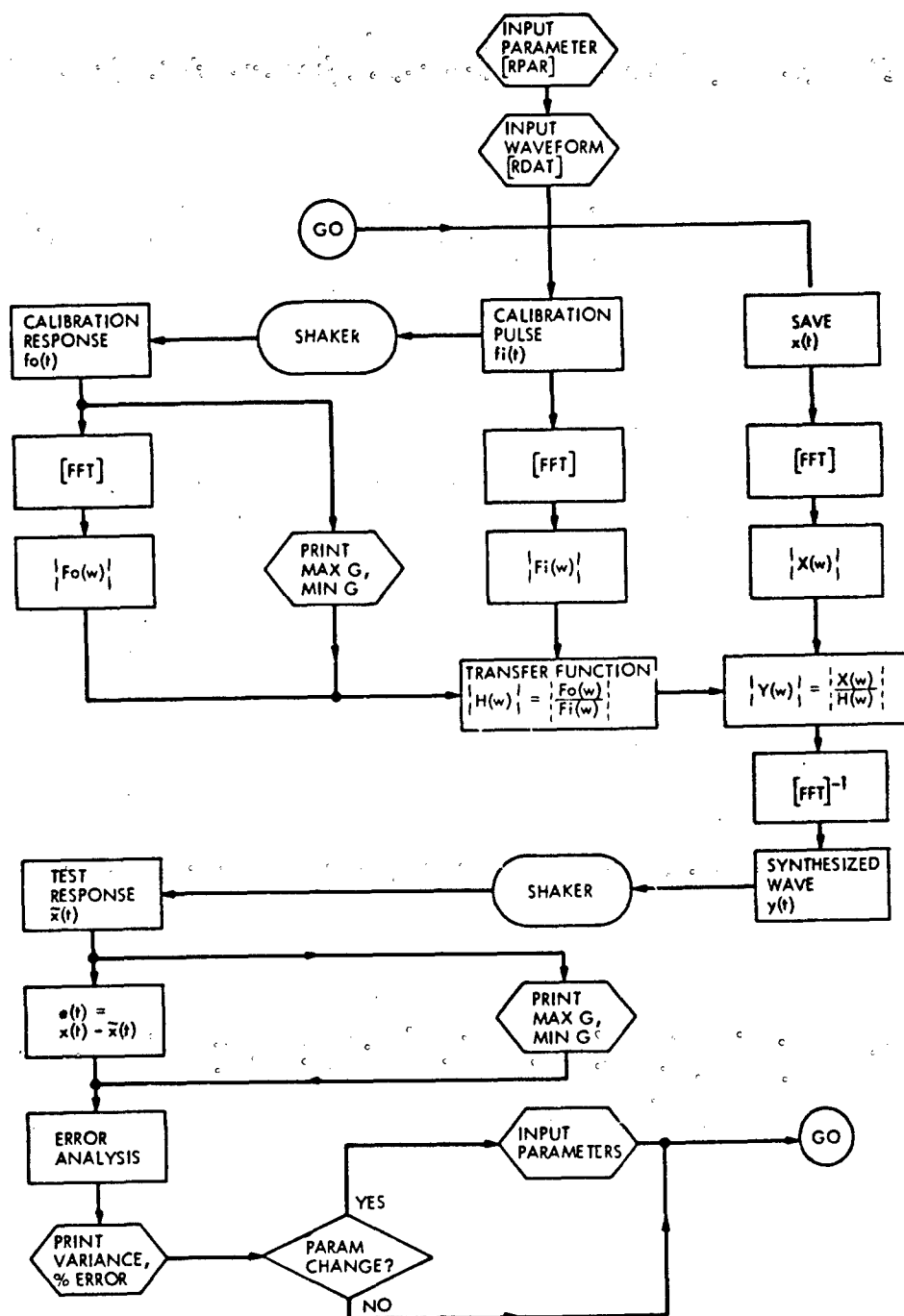


Fig. 3 - Transient waveform control, software flow chart

$$X(\omega) = \frac{1}{\sqrt{2}} \{p(\omega) + jq(\omega)\} \cdot A(\omega) \quad (7)$$

where $p(\omega)$, $q(\omega) = \pm 1$, the pseudo-random sequence. Then the complex $X(\omega)$ constitutes a one-to-one relationship with the desired waveform $x(t)$.

- (3) The fast-swept sine approach fixes the phase distribution, and thus the resulting waveform is identically repeatable. With the transfer function obtained in the calibration process, the input requirement is

$$|Y(\omega)| = \frac{A(\omega)}{|H(\omega)|} \quad (8)$$

and this is transmitted via a digitally controlled swept oscillator. The logarithmic sweep rate N octaves/minute is derived from the frequency resolution required,

$$\Delta f = \frac{1}{T} \quad (9)$$

where

T = total pulse duration in seconds

Δf = frequency resolution in Hertz

and

$$f_2 = f_1 \cdot \exp\left(\frac{Nt}{60} \cdot \ln 2\right) \quad (10)$$

where

f_1 = initial frequency in Hertz

f_2 = final frequency in Hertz

Then the desired sweep rate is

$$N = \frac{60}{\ln 2} \cdot \Delta f \cdot \ln\left(\frac{f_2}{f_1}\right) \quad (11)$$

- (4) A rapid burst of random noise excitation can also be implemented to deliver the desired amplitude spectrum $A(\omega)$. Once the input requirement amplitude is computed as in Eq. (8), the pseudo-random sequences $p(\omega)$, $q(\omega)$ are used to compute the time history.

$$y(t) = \frac{1}{\sqrt{2}} \cdot^{-1} \left[\{p(\omega) + jq(\omega)\} |Y(\omega)| \right] \quad (12)$$

However, for the short-duration time required, the statistical averaging process may not ensure convergence.

SUMMARY

The concept of transient testing is analyzed in light of the shortcomings involved in a conventional slow sine-sweep test. Several different modes of computing the system transfer function and how one could implement the various methods in an environmental testing laboratory are explained. Definite advantages in open-loop control, fatigue considerations and overall simplicity in implementation are stressed. Coupled with the inherent advantages of a digital test system, the transient testing concept presents an alternate scheme over the conventional slow sine-sweep testing for large complex structures.

REFERENCES

1. Chapman, C.P., "Computer-Controlled Environmental Test Systems: Criteria for Selection, Installation and Maintenance," Society of Automotive Engineers, Paper 720819, New York, 1972.
2. Favour, J.D., LeBrun, J.M., and Young, J.P., "Transient Waveform Control of Electromagnetic Test Equipment," 40th Shock and Vibration Bulletin, Part 2, December 1969.
3. Kim, B.K., "Induced Shock Pulse Testing by Transient Waveform Control," JPL Quarterly Technical Review, Vol. III, No. 2, Jet Propulsion Laboratory, Pasadena, Calif., July 1973.
4. Yang, R.C., and Saffell, H.R., "Development of a Waveform Synthesis Technique - A supplement to Response Spectrum as a Definition of Shock Environment," 42nd Shock and Vibration Bulletin, Part 2, January 1972.
5. Heizman, C.L., "A Digitally Controlled Vibration or Acoustic Testing: Part III. Hardware Requirements and Implementation," Proceedings, Mt. Prospect, Illinois: Institute of Environmental Sciences, 1969, pp. 387-409.

This work was supported by the National Aeronautics and Space Administration under Contract NAS 7-100

COMPARISON OF SHOCK SPECTRUM TECHNIQUES AND THE METHOD OF LEAST FAVORABLE RESPONSE**

A. F. Witte and R. J. Wolf
Kaman Sciences Corporation
Colorado Springs, Colorado

A study has been performed to compare critical component shock response when laboratory test inputs are defined by shock response spectrum methods and by a method which utilizes the Fourier spectrum of the field environment and the frequency response function of the critical component. The technique which utilizes the Fourier spectrum is known as the method of Least Favorable Response and results in conservative laboratory response in the time domain and an excellent match of the field response in the frequency domain. This paper describes methods and criteria used to perform the study and presents the significant results in abbreviated form along with general conclusions derived from the study.

NOMENCLATURE

$F[x(t)]$	Fourier transform of $x(t)$
$F^{-1}[X(\omega)]$	inverse Fourier transform of $X(\omega)$
$H(\omega)$	frequency response function
$H^*(\omega)$	the conjugate of the complex quantity of $H(\omega)$
t	time
$\ddot{x}(t)$	input acceleration
$X(\omega)$	Fourier spectrum of $\ddot{x}(t)$
$X_e(\omega)$	Fourier spectrum modulus envelope
$\ddot{y}(t)$	response acceleration
$Y(\omega)$	Fourier spectrum of $\ddot{y}(t)$
ω	frequency
ϕ	frequency dependent phase angle

** This work was performed under contract to the U. S. Army SAFEGUARD System Command, Contract Number DAHC60-68-C-0020.

INTRODUCTION

The use of shock response spectra for defining dynamic loads and laboratory environmental test criteria to qualify hardware for field shock environments has within the past few years become very controversial. This controversy has been augmented by certain technological advances in digital calculation of the Fourier transform and in digital control of vibration exciters. Both advances make it possible to generate in the laboratory complex acceleration time histories which can be analytically expressed or represented as a series of time samples.[1]

Methods of synthesizing field shock response spectra in the laboratory have been devised which utilize digitally controlled exciters and oscillatory transients. These often better describe field environments than the normally used classical shock pulse which can be easily reproduced on conventional shock machines.[2] However, the controversy over the applicability of shock response spectra still exists since calculational advances also make it possible to utilize the Fourier spectrum to specify laboratory test inputs.

Critics of shock spectrum cite the fact that its use in its most popular

form necessarily requires the assumption that the system in question be accurately represented by a linear single degree-of-freedom system whose damping is independent of its resonance frequency. Shock spectrum techniques are often applied to situations where the system in question is clearly not single degree-of-freedom in nature and damping is not independent of resonance frequencies. The conservatism of shock response spectrum techniques for defining test criteria often depends on the method of laboratory synthesis, the biases applied to the field shock spectra to insure adequate conservatism in the laboratory, and the actual dynamic characteristics of the system to be tested.

Smallwood has suggested that a method proposed by Shinozuka for evaluating the effects of seismic motions on structures has applicability in specifying worst case criteria for laboratory environmental tests.[3,4] The technique which is known as the method of "Least Favorable Response" (LFR) utilizes the envelope of the Fourier spectra moduli for the ensemble of all known field environments. It also uses the actual dynamic characteristics of the system in the form of the frequency response function. The input obtained using the Least Favorable Response theory will result in a critical component response whose absolute value is maximum for all possible inputs having Fourier spectra less than the field envelope. Thus, provided the field data adequately represents realistic situations, it insures that the laboratory test will result in a conservative and a worst case situation in the time domain. The method of LFR also insures that adequate "simulation" in the frequency domain will be accomplished.

An analytical study, which is presented in this paper, has been performed to compare shock spectrum and LFR techniques. The study utilized both single degree-of-freedom and multiple degree-of-freedom systems. Classical pulses and decaying periodics were used to encompass or synthesize ensembled field shock spectra and conservatively biased envelopes. The results were compared with those obtained using the method of LFR. Comparisons of time histories, Fourier spectra, and shock response spectra were made.

The results of the study indicate that the method of LFR produces a conservative response (approximate factors

of 2 were observed for the situations examined) and an adequate match of the field mean plus 3 standard deviation shock spectrum. The method of Least Favorable Response also insures that the system response will be adequately "simulated" in the frequency domain. The use of shock response spectrum methods resulted in an undertest or overttest depending on enveloping, biasing, and synthesizing criteria as well as system dynamic characteristics. The use of shock spectrum may not insure adequate laboratory "simulation" in the frequency domain.

LABORATORY SIMULATION OF FIELD ENVIRONMENTS USING SHOCK SPECTRUM METHODS

The primary objective of laboratory environmental qualification tests is to "simulate" field environments for the purpose of evaluating the structural and operational reliability and integrity of hardware which must survive operational field environments. The problem becomes one of adequately measuring and defining the field environment and establishing laboratory test criteria which result in a suitable and conservative "simulation" of this environment. Both simulation and conservatism must be such that survivability in the laboratory guarantees survivability in the field. On the other hand, the criteria must not be unrealistically conservative as to impose severe design, manufacturing, and cost penalties on the hardware.

Shock spectrum techniques are presently the primary methods for determining system design criteria to insure hardware survivability for specified shock environments and for specifying laboratory shock test criteria. The primary advantage of shock spectrum is that it is relatively simple to understand and apply. However, its simplicity also results in several problems and caveats which one must consider in its application.

To apply the most often utilized shock spectrum concepts, the physical system whose response is of interest must be represented by a linear single degree-of-freedom system. Application of these shock spectrum techniques also implies that only the maximum response of the system is of interest and that damping is independent of resonance frequencies. Shock spectrum methods have been applied to many systems for which the above requirements are not applicable.

The ability of a shock spectrum to uniquely describe a time history is questionable; several time histories may produce the same shock spectrum within specified tolerance bands. This fact is the cause of considerable disagreement over the validity of shock spectrum as an indication of damage potential. Many advocate matching shock spectra with transients simulating the field time histories. That is, if the field time history is oscillatory in nature, the laboratory time history used to match field shock spectra must also be oscillatory.

The use of single degree-of-freedom shock spectrum techniques in specifying test criteria for complex multiple degree-of-freedom structures to simulate transient vibration and shock is extremely controversial. For shock spectrum to have real meaning in terms of loads generated in a multiple degree-of-freedom system, the systems response must be limited primarily to one mode. This can happen only if the excitation has the frequency content which corresponds to only one of the systems modal frequencies. However, many realistic field transients have wideband frequency content which generally causes modal coupling and simultaneous excitation of several system modes.

In many situations field data is very limited in the number of events for which shock data has been obtained. Thus, there is a very good possibility that data for a worst case situation may not be available.

The normal procedure for using the available field data is to overlay all shock spectra and encompass the overlay with shock spectra for classical pulses or synthesize the shock spectrum envelope using combined decaying periodics. However, this may not account for possible worst case situations which can statistically arise in the field.

In order to account for possible statistical variation in data obtained from various field events, the shock spectrum data from the same nominal environment is sometimes treated as a random process. This is done by ensemble averaging and calculating the frequency dependent mean shock spectrum and the variance. The laboratory test specification is then based on the frequency dependent mean value increased by a factor which is some multiple of the standard deviation of the ensembled shock spectra. The method has merit in that it applies statistical logic in an

attempt to account for the worst case field situations.

THE METHOD OF LEAST FAVORABLE RESPONSE

There is another approach for establishing shock and vibration tests criteria which has been recently suggested, it is termed the method of "Least Favorable Response". The theory of "Least Favorable Response" is a relatively new concept, being originated primarily by M. Shinozuka [3] and R. F. Drenich [5] in 1968. Like shock spectrum, "Least Favorable Response" (LFR) was devised primarily for estimating effects of seismic shock on structures. The first suggestion for its application to shock excited vehicle structures was made by D. O. Smallwood in 1971-72 [4]. As a result the technique is not very well known.

The method of "Least Favorable Response" in terms of field and laboratory environments is briefly summarized as follows: The Fourier transform of field input time histories is computed for all available field data. An envelope $X_e(\omega)$, of the composite spectrum moduli is generated. The frequency response function, $H(\omega)$, for the critical component is then computed from a realistic model, or measured in the laboratory. Using this information, it can be shown [3,4,5] that an input shock whose Fourier transform defined by the expression

$$X(\omega)_{\text{lab input}} = \frac{X_e(\omega) H^*(\omega)}{|H(\omega)|} \quad (1)$$

(where * denotes the complex conjugate) will result in the maximum critical component response, $\ddot{y}(t)$, which can be generated by any possible input whose Fourier transform is contained within the field shock envelope $X_e(\omega)$. The time history of the laboratory shock input is then obtained by computing the inverse Fourier transform of $X(\omega)_{\text{lab input}}$ that is,

$$\begin{aligned} \ddot{x}(t)_{\text{lab input}} &= F^{-1} [X(\omega)] \\ &= F^{-1} \left[\frac{X_e(\omega) H^*(\omega)}{|H(\omega)|} \right] \end{aligned} \quad (2)$$

The above expression is a unique, analytically determined test input obtained from an envelope of field data in the frequency domain and the dynamic

characteristics of test specimen involved. For a rigorous development of the Least Favorable Response theory, the reader is referred to previous work by Shinozuka, Smallwood, and Drenich, [3,4,5].

Least Favorable Response offers advantages over shock spectrum in the following areas: (1) it accommodates an arbitrary multiple degree-of-freedom system, (2) it puts an envelope on the Fourier transform of the actual field data, and (3) it accounts for the worst case situation. However, several caveats must be considered in its application: (1) as with shock spectrum methods, phase information for field environments is not utilized, (2) the critical component within the system must be identified and its frequency response function must be known, (3) a Least Favorable Input (LFI) must be determined for each critical component, i.e., an individual test must be specified for each critical component to obtain its Least Favorable Response, and (4) Least Favorable Response theory is rigorously applicable to only linear systems.

STUDY DESCRIPTION

The analytical study outlined in this paper was performed on both single degree-of-freedom systems and multiple degree-of-freedom systems, each representing critical components within a complete hardware system. The single degree-of-freedom systems provided a relatively simple means of checking theory and computational techniques. They also provided a logical basis for comparing shock spectrum and Least Favorable Response techniques.

The multiple degree-of-freedom systems were also used to obtain results which could be utilized to compare shock spectrum and Least Favorable Response methods. Of primary concern for both types of systems was the simulation of the environment in both the time and frequency domains. Conservatism of results when compared to field data was also of concern.

Four systems were used in the study, two single degree-of-freedom systems and two multiple degree-of-freedom systems. Each system whose input and response defined by $\ddot{x}(t)$ and $\ddot{y}(t)$ respectively, were identified with a case number. See Fig. 1.

Case 1 was a single degree-of-freedom system having its resonance frequency of 650 Hz correspond to a

notch in the ensembled field Fourier spectra envelope, thus requiring the systems driving point impedance to be relatively large compared to the source impedance.

Case 2 was a single degree-of-freedom system having its resonance frequency of 800 Hz correspond to a peak in the ensembled field Fourier spectra envelope, thus requiring the driving point impedance of the component to be small compared to the source impedance.

Case 3 was a two degree-of-freedom system having a different damping ratio for each spring/mass element and having closely coupled resonance frequencies. The resonance frequencies of 650 and 800 Hz corresponded to a notch and a peak in the ensembled Fourier spectra. The top mass was considered the critical component.

Case 4 was a two degree-of-freedom system also having a different damping ratio for each spring/mass element with little coupling between resonance frequencies of 800 and 1200 Hz. Again the top mass was considered the critical component.

Thus, the four cases corresponded to some of the limiting situations which one can encounter in the critical component/environmental source relationship.

The objective of the study on each of the four cases was to compare the critical component response due to inputs defined by shock spectrum techniques, the method of Least Favorable Response, and field environments. Comparison of input and response data was accomplished by spectral decomposition using both Fourier and shock response spectra. Data were also compared in the time domain.

Field input data, from which laboratory shock specifications for this study were determined, consisted of five different analytically derived events, each representing an environment to which the critical components would be subjected during their useable life. These events were synthesized by summing analytically generated decaying sinusoids. The frequency content and the amplitude of the frequency components varied from one event to the next. Figs. 2, 3, and 4 show the input time history, Fourier spectrum modulus, and shock spectrum for one of the five events.

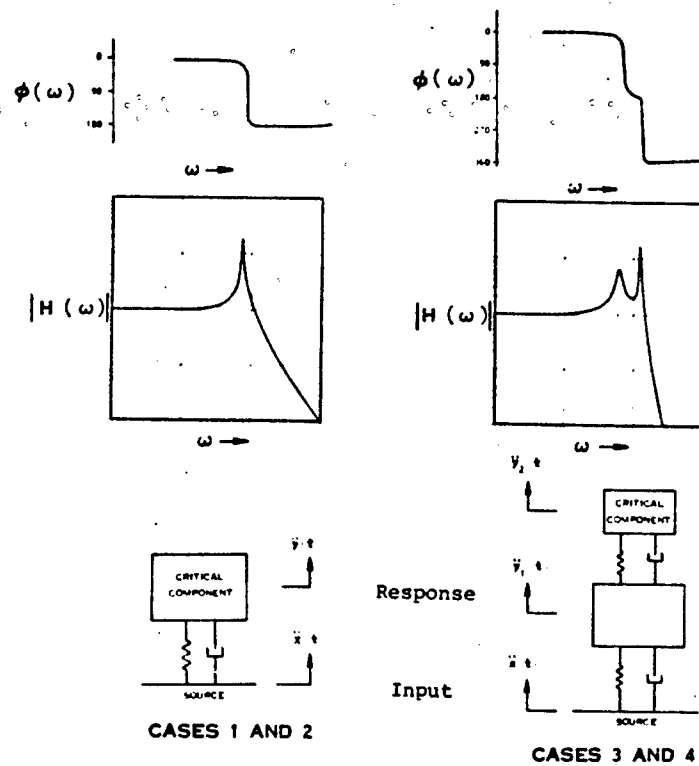


Fig. 1 - Study cases.

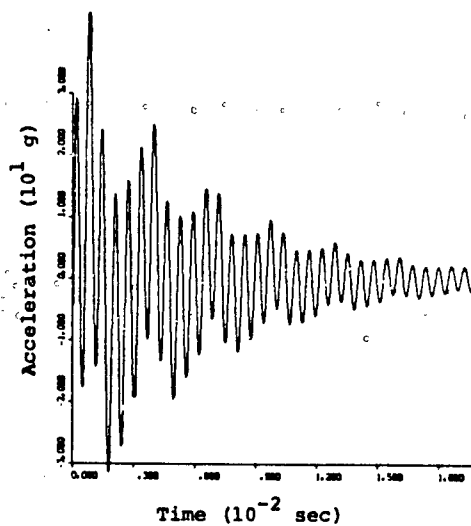


Fig. 2 - Input time history for Field Event 2-B.

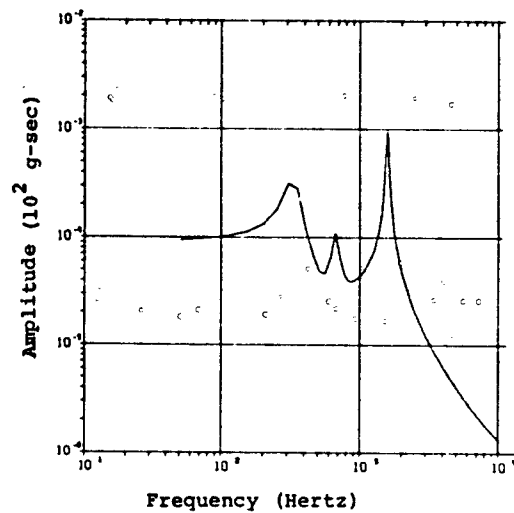


Fig. 3 - Input Fourier spectrum modulus for Field Event 2-B.

Each critical component case was examined in terms of an analytical "laboratory test" situation which is identified by a test number. Only a few plots are included with the following discussion since to include all data would result in a paper of unreasonable size. The data included are typical and are utilized to illustrate the techniques used, and results obtained.

"Laboratory Test" 1. (Half-sine envelope). Input parameters were obtained by calculating the maximax shock response spectrum for each of the five field events. These shock spectra were overlaid as shown in Fig. 5 and an envelope was drawn around the ensemble. The unshaded area represents the frequency range of particular interest. The shock spectrum for a 140 g, $.66 \times 10^{-3}$ second half-sine pulse was used to encompass the ensemble envelope and the Fourier spectrum of the half-sine was calculated. This half-sine was used to define a laboratory input. The response for each critical component case was obtained in both the time and frequency domains. Figs. 6, 7, 8, 9, and 10 illustrate input and response data for Laboratory Test 1, Case 1 only.

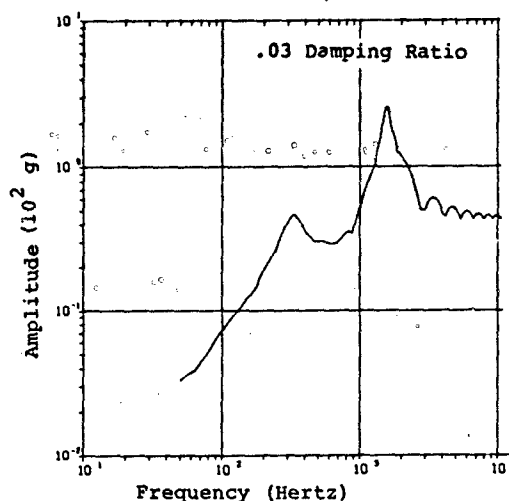


Fig. 4 - Maximax shock response spectrum for Field Event 2-B.

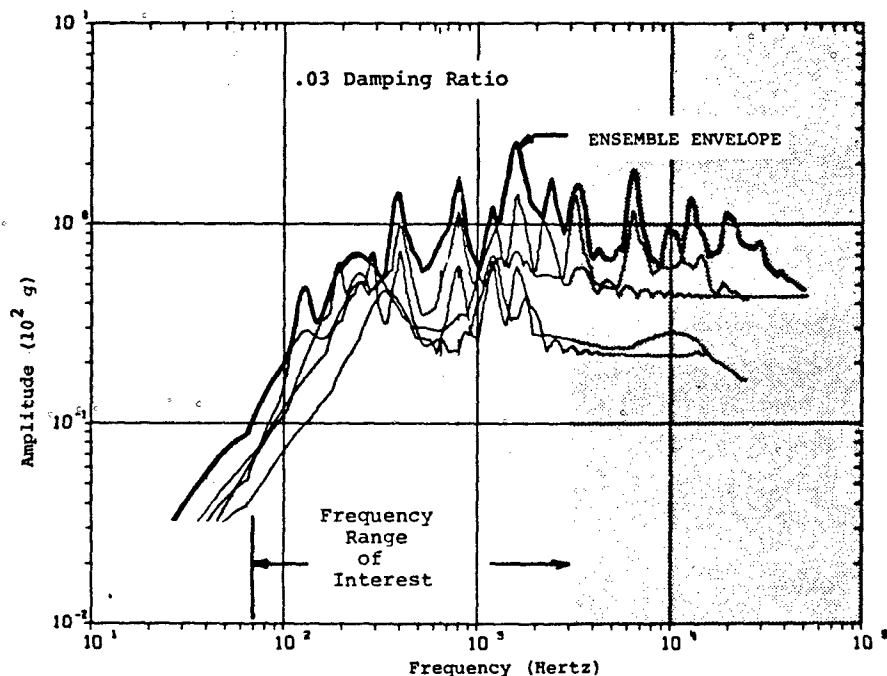


Fig. 5 - Envelope of maximax shock response spectra ensemble for all field events.

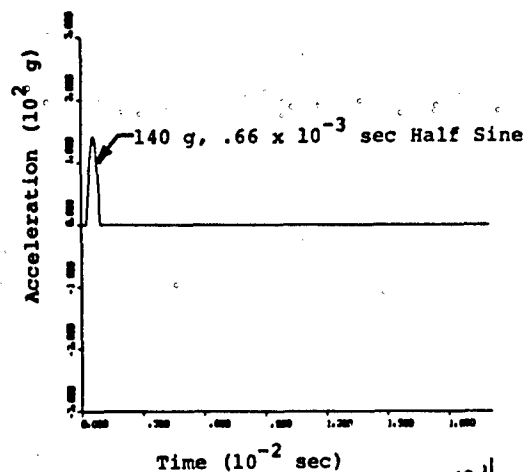


Fig. 6 - Input time history for Laboratory Test 1.

Fig. 7 - Maximax shock response spectrum for Laboratory Test 1.

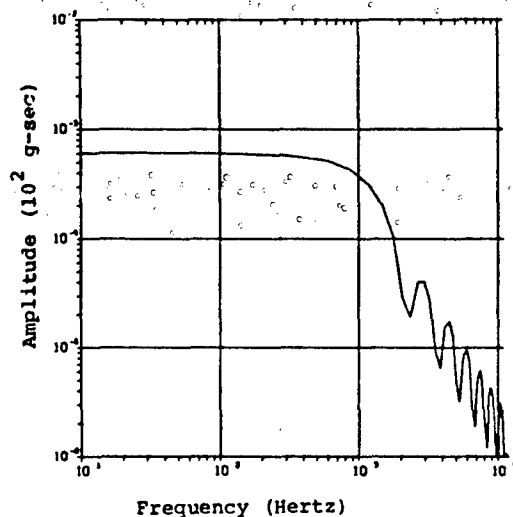
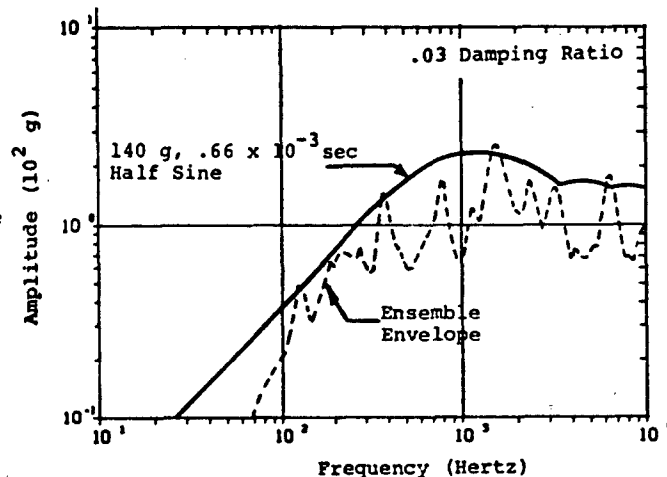


Fig. 8 - Input Fourier spectrum modulus for Laboratory Test 1.

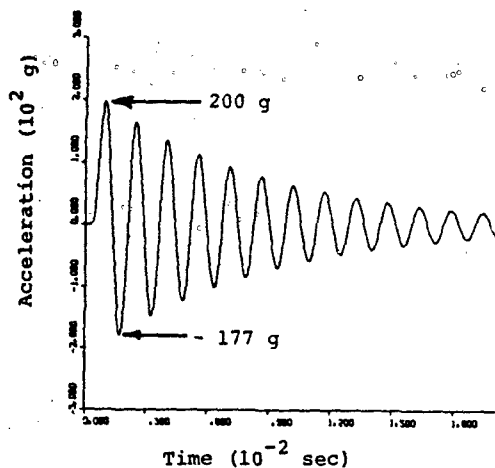


Fig. 9 - Response time history for Laboratory Test 1; Case 1.

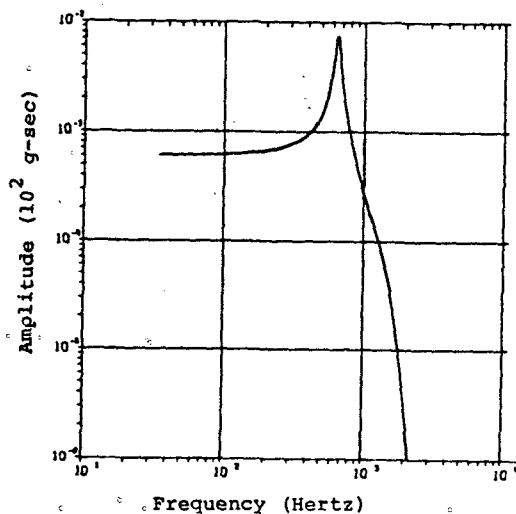


Fig. 10 - Response Fourier spectrum modulus for Laboratory Test 1; Case 1.

"Laboratory Test" 2. (Half-sine mean + 3σ .) Input parameters were obtained by calculating the frequency dependent mean value of the field shock response spectrum ensemble, calculating the frequency dependent standard deviation and then enveloping the mean plus three standard deviation as shown in Fig. 11. Again, the unshaded area indicates the frequency range of interest. The shock spectrum for a 205 g, $.616 \times 10^{-3}$ second

half-sine was used to encompass the mean plus three standard deviation shock spectrum and the Fourier spectrum of the half-sine was calculated. The response of each critical component case was determined in both the time and frequency domains. Input and response data were similar to that illustrated for Test 1.

"Laboratory Test" 3. ("SHOC" envelope.) Shaker optimized periodic transients (SHOC) [2], were used to match the envelope of the field shock spectrum ensemble. Note that the criteria for matching the field shock spectrum was for the spectrum of the shaker optimized transient to fall within $\pm 20\%$ tolerances over 90% of the frequency range of interest. The Fourier spectrum of the input transient was obtained as well as the time history and Fourier spectrum of the critical component response for all cases. Figs. 12, 13, 14, 15, and 16 illustrate input and response data for Laboratory Test 3, Case 1 only.

"Laboratory Test" 4. ("SHOC" mean + 3σ .) Shaker optimized periodic transients were used to match the envelope of the field mean plus three standard deviation shock spectrum using the same criteria as those used in Laboratory Test 3. The input and response data were similar to that illustrated for Test 3.

"Laboratory Test" 5. (Least Favorable Response.) The Fourier spectra of field inputs were calculated and ensembled and an envelope of the ensemble was formed. See Fig. 17. The envelope of the ensemble $X_e(\omega)$ was used with each of the critical component frequency response functions to obtain a Least Favorable Input via Eq. (1). The Least Favorable Input for Case 1 is shown in both the time and frequency domains in Figs. 18 and 19. Shown in Figs. 20, 21 and 22 are the shock response spectrum for the input and the critical component response in the time and frequency domains.

Response to Field Events. The response to all field events were obtained in the form of time histories and Fourier spectra for all critical component cases. Peak response amplitudes were determined and an envelope of response Fourier spectra for all field events were obtained. Figs. 23 and 24 show the response time history and Fourier spectrum for Case 1 to one of the field events.

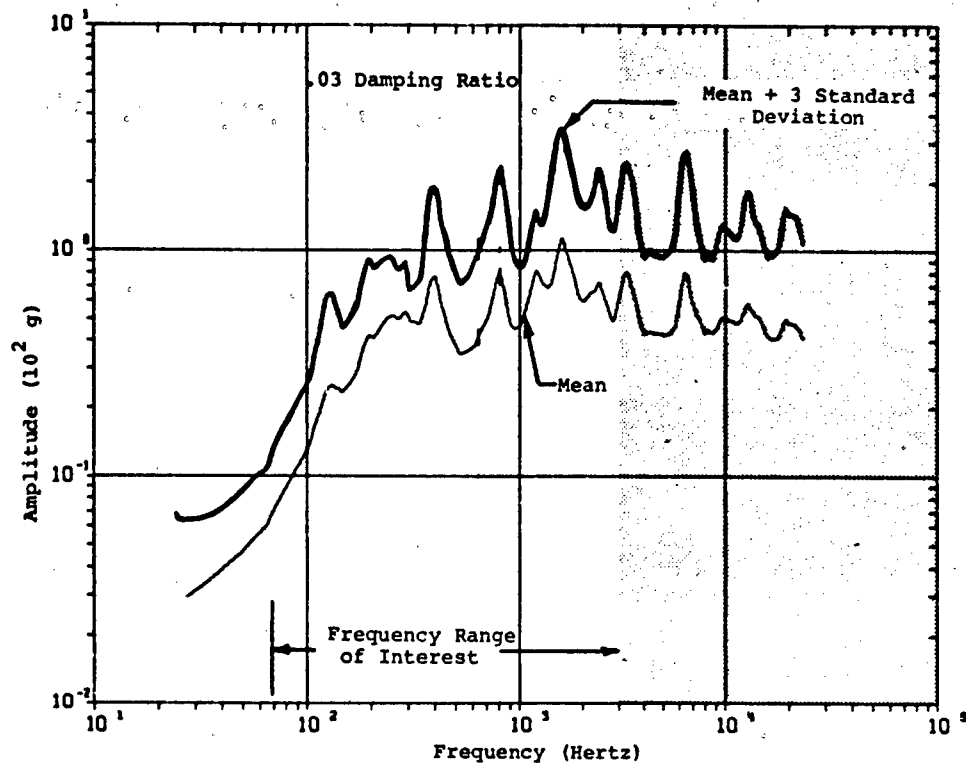


Fig. 11 - Mean and mean plus 3σ shock response spectra for all field events.

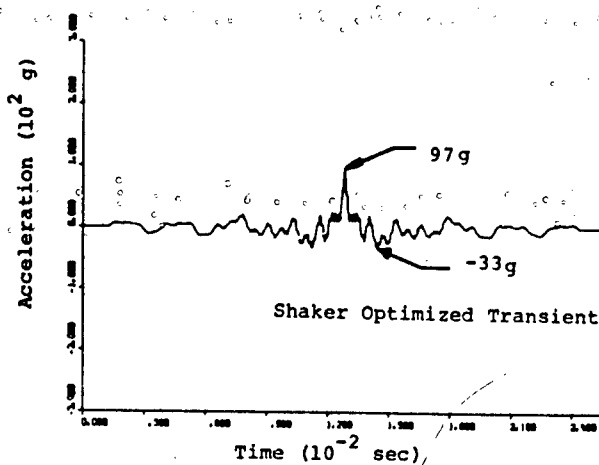


Fig. 12 - Input time history for Laboratory Test 3.

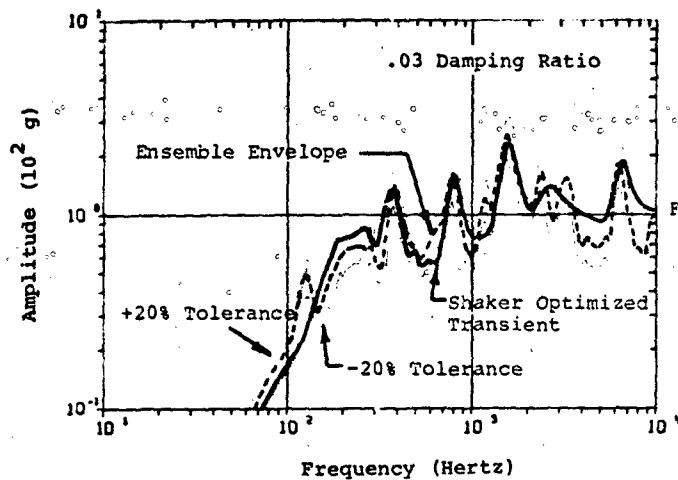
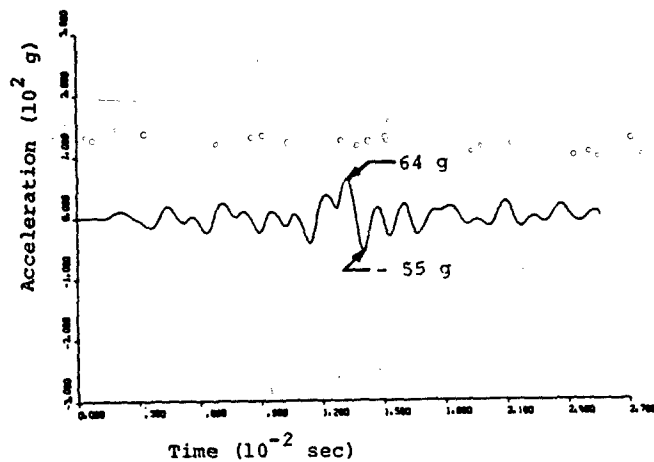
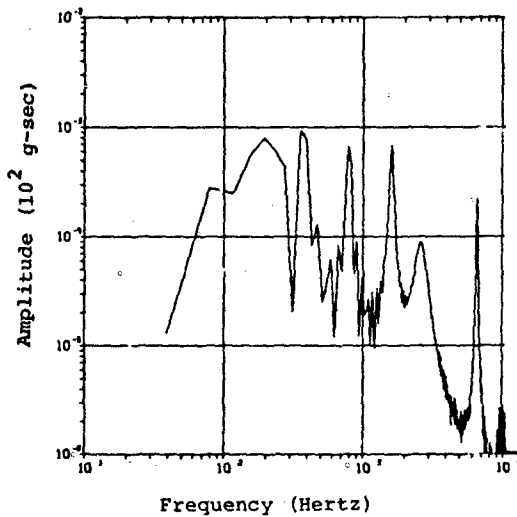


Fig. 14 - Fourier spectrum modulus for Laboratory Test 3 input.



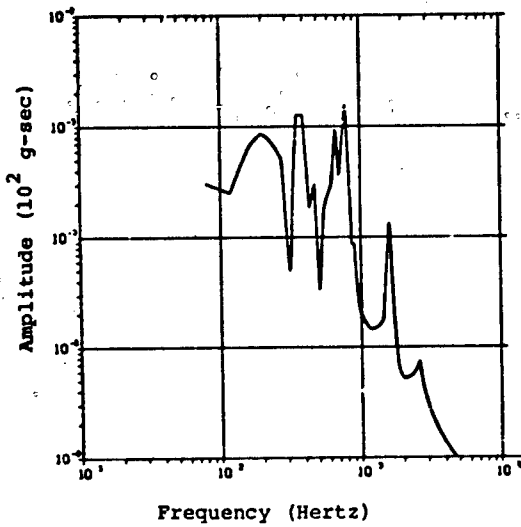


Fig. 16 - Response Fourier spectrum modulus for Laboratory Test 3; critical component Case 1.

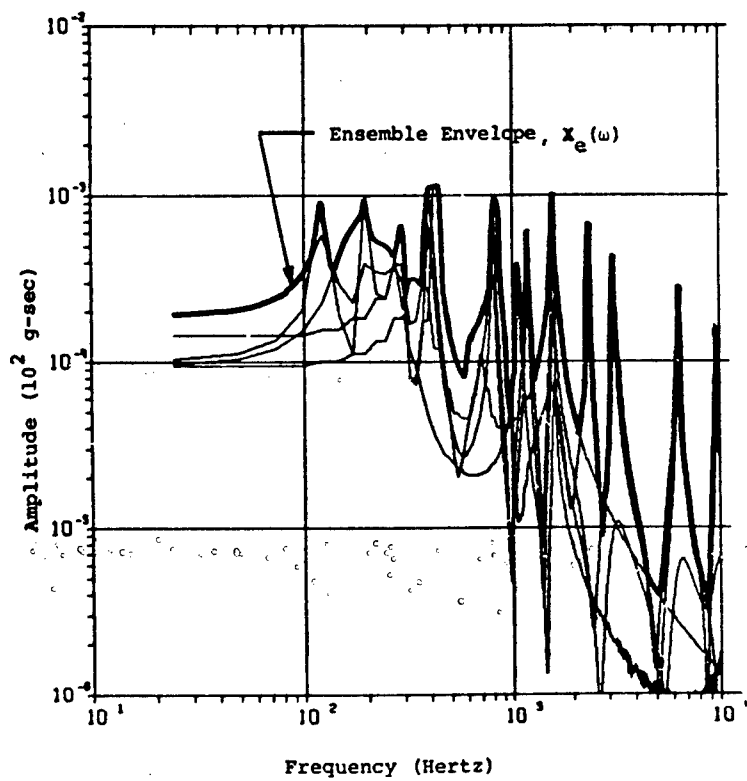


Fig. 17 - Ensemble of field input Fourier spectra.

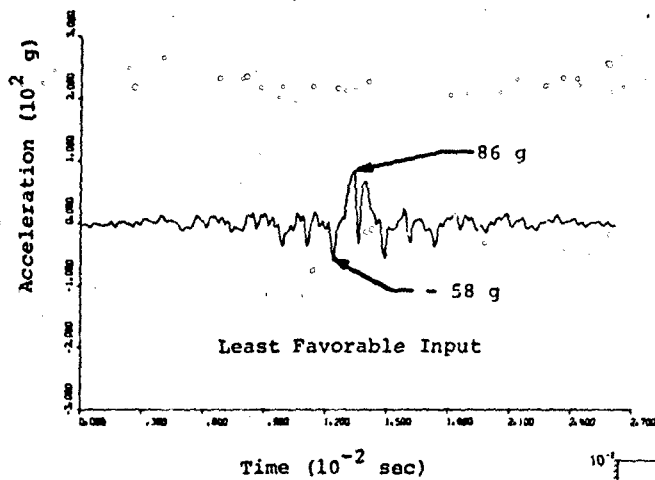


Fig. 18 - Input time history for Laboratory Test 5; Case 1.

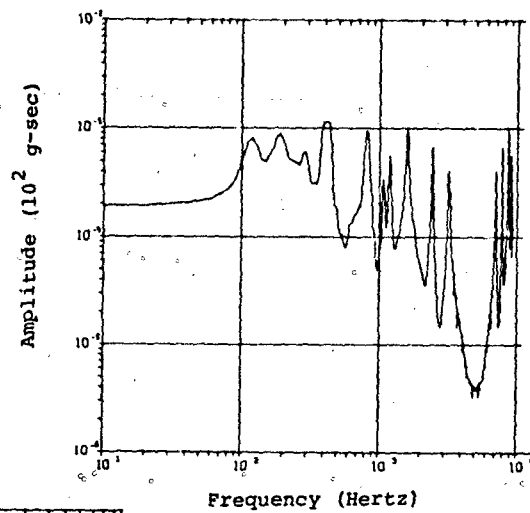


Fig. 19 - Fourier spectrum modulus for Laboratory Test 5; Case 1.

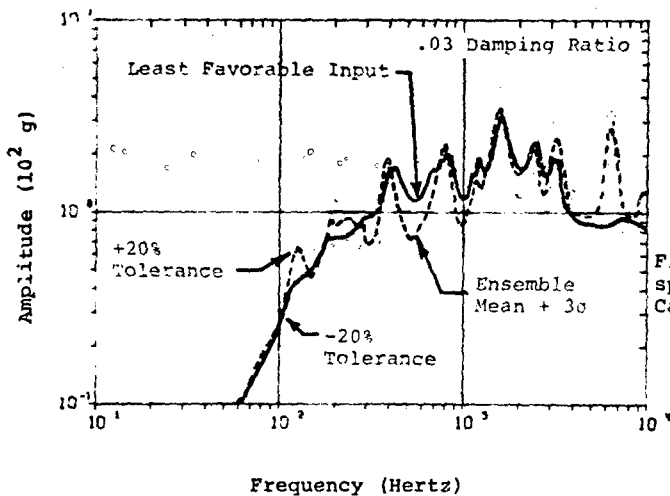


Fig. 20 - Input maximax shock spectrum for Laboratory Test 5; Case 1.

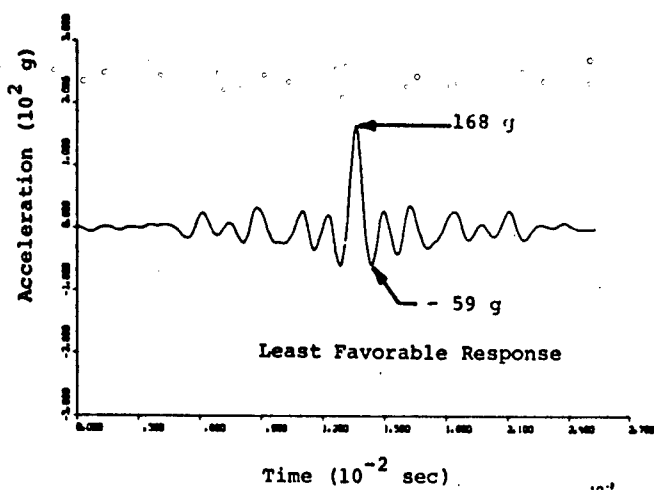


Fig. 21 - Response time history for Laboratory Test 5; Case 1.

Fig. 22 - Response Fourier spectrum modulus for Laboratory Test 5; Case 1.

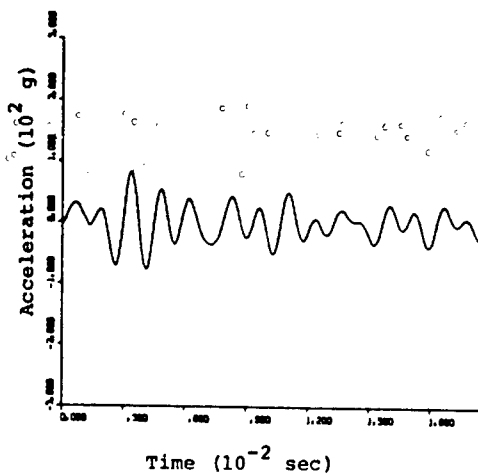
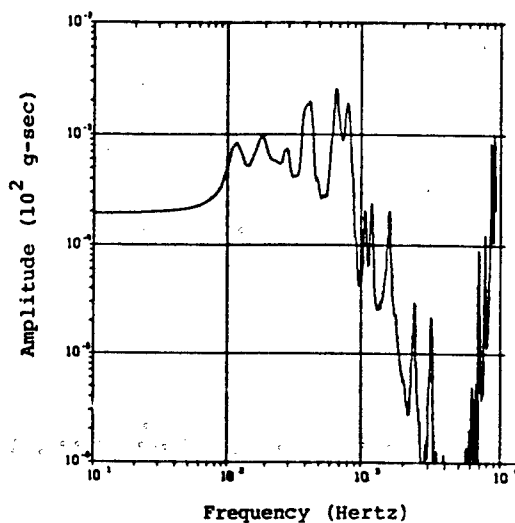


Fig. 23 - Response time history for Field Event 5-D; Case 1.

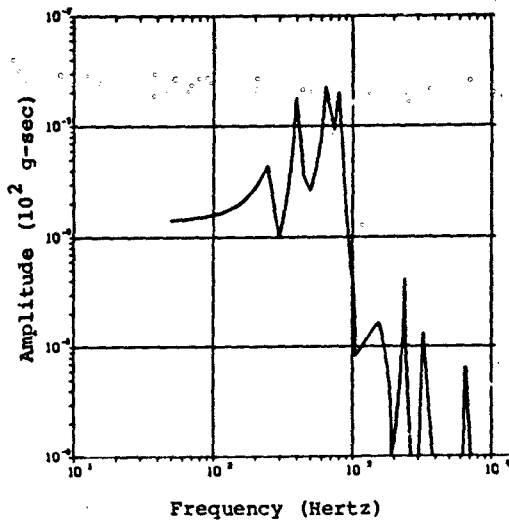


Fig. 24 - Response Fourier spectrum modulus for Field Event 5-D; Case 1.

The envelope of the response Fourier spectra for all field events is shown in Fig. 25.

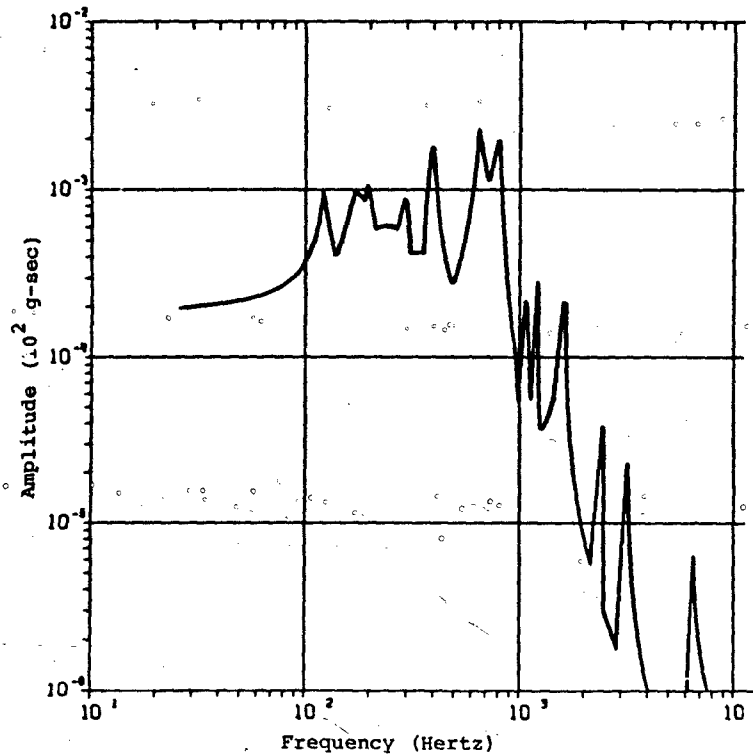


Fig. 25 - Envelope of response Fourier spectrum ensemble for all field events; critical component Case 1.

STUDY RESULTS

In order to compare the various test methods and draw conclusions field and test input data were compared using time histories, Fourier spectra, and shock response spectra. Critical component response data were also compared in the time and frequency domains as schematically indicated in Fig. 26. Table 1 and Fig. 27 summarize and compare the test results in terms of peak input and response amplitudes. Results for all four critical component cases are shown. Peak input and response amplitudes are plotted in Fig. 27 using a logarithmic ordinate since equal percentage differences are represented by equal distances on a log scale. Comparisons of shock response spectra and Fourier spectra are not presented because of the considerable amount of data required for comparison. This data is verbally compared in the following paragraphs.

As one would initially suspect, peak input acceleration amplitudes do

not give an indication of the severity of the environment in terms of component response since component response is also dependent on the frequency content of the input.

Matching or enveloping the field input maximax shock spectrum ensemble did not guarantee matching or enveloping the ensembled field input Fourier spectra and in turn did not guarantee matching or enveloping the ensembled field response Fourier spectra.

The results in terms of peak response accelerations using shock response spectrum methods were highly dependent on biasing criteria used to insure response conservatism, on the type of pulse used to "simulate" the environment, and on the dynamic characteristics of the critical component. The use of shock response spectrum in the situations described in this paper resulted in both an undertest and an overtest in terms of peak critical component response accelerations. Using shock response spectrum techniques

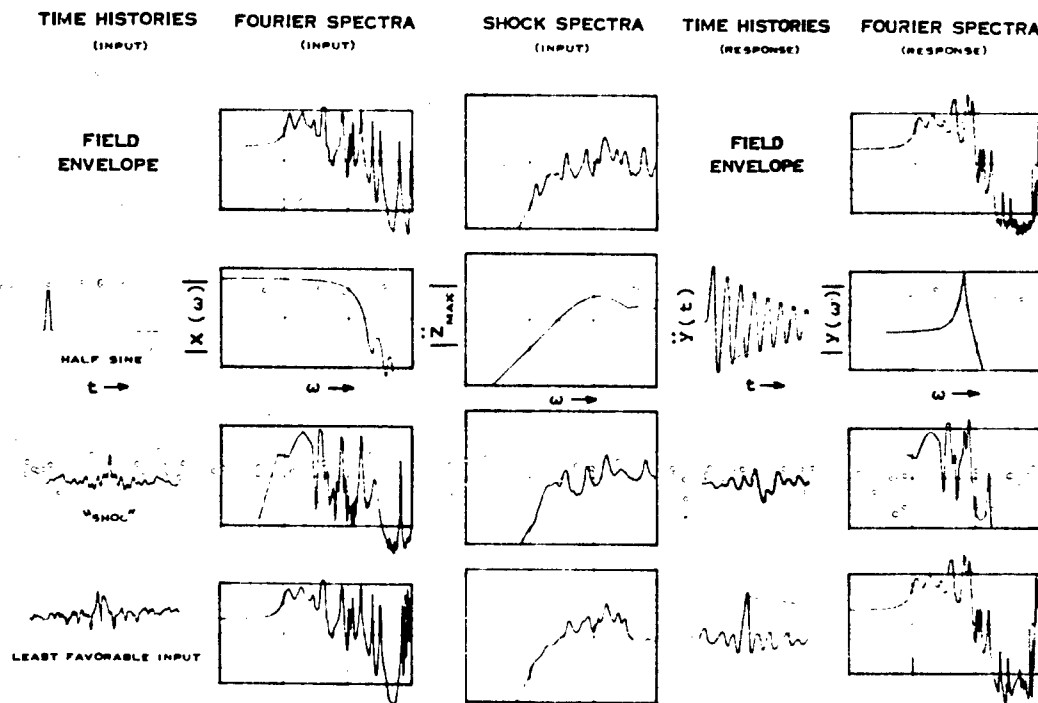


Fig. 26 - Schematic of data comparison.

TABLE 1
SUMMARY OF INPUT AND RESPONSE DATA

TEST NUMBFR	INPUT	PEAK INPUT AMPLITUDE	CRITICAL COMPONENT PEAK RESPONSE AMPLITUDE			
			CASE 1	CASE 2	CASE 3	CASE 4
	Field (All Events)	44g	84g	158g	350g	101g
1	Half-Sine Envelope	140g	202g	222g	510g	277g
2	Half-Sine Mean + 3 σ	205g	275g	309g	720g	391g
3	"SHOC" Envelope	97g	64g	157g	281g	86g
4	"SHOC" Mean + 3 σ	137g	85g	233g	450g	127g
5	Least Favorable Input/Response					
	Case 1	87g	168g			
	Case 2	97g		297g		
	Case 3	100g			540g	
	Case 4	110g				264g

L1 LFI FOR CASE 1
 L2 LFI FOR CASE 2
 L3 LFI FOR CASE 3
 L4 LFI FOR CASE 4
 LFR LEAST FAVORABLE RESPONSE
 FM FIELD MAXIMUM
 SE SHOC, ENVELOPE
 SM SHOC, MEAN + 3 σ
 HE HALF-SINE ENVELOPE
 HM HALF-SINE, MEAN + 3 σ

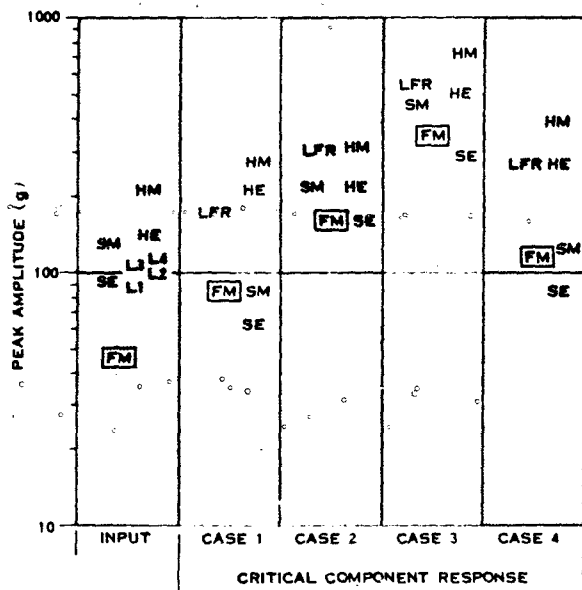


Fig. 27 - Summary of input and response peak amplitudes.

did not insure enveloping or matching either the input or response Fourier spectrum.

The method of Least Favorable Input/Response in all cases resulted in a match of field input and response Fourier spectra and conservative critical component peak response accelerations. The amount of conservatism varied from 1.5 to 2.6. Smallwood also has observed approximate factors of 2 conservatism in his results [4]. In all cases examined, the maximax shock spectrum of the Least Favorable Input did an excellent job of matching the field ensemble mean plus three standard deviation shock response spectrum envelope within the $\pm 20\%$ tolerances over 90% of the frequency range of interest (see Fig. 20). The only frequencies at which an adequate match did not occur were at the critical component resonance frequencies, which in terms of shock response spectra are the most important.

SUMMARY AND CONCLUSIONS

A study has been performed which compares results from field events and laboratory tests whose input criteria were derived using shock spectrum and Least Favorable Input/Response methods. Four critical component cases were examined, two single degree-of-freedom and two multiple degree-of-freedom systems.

The results of the study are summarized as follows:

(1) Shock spectrum methods resulted in both overtests and undertests of critical components.

(2) The use of shock spectrum methods did not necessarily insure that the frequency content of inputs were properly reproduced in the laboratory.

(3) The use of shock spectrum methods did not necessarily insure that the frequency content of responses were properly reproduced in the laboratory.

(4) Results using shock spectrum were dependent on enveloping and biasing methods and value judgement.

(5) The use of Least Favorable Input/Response always resulted in conservative responses in terms of peak amplitudes; approximate factors between 1.5 and 2.6 were observed.

(6) Both field input and response Fourier spectrum moduli were matched in the laboratory when Least Favorable Input/Response was used.

The conclusions from the study are that the use of Least Favorable Input/Response results in an excellent means of providing both the conservatism and the similitude for laboratory qualification testing. However, methods of deriving input specifications and performing tests are more complicated than those used with shock spectrum methods.

To date, electro-dynamic or electro-hydraulic exciters are the only devices which can accurately reproduce a Least Favorable Input and these are in some situations limited in both force and frequency capabilities. A new method of producing Least Favorable Inputs may be required to meet some of the high amplitude, high frequency criteria necessary to simulate many of the normally encountered field shock environments.

REFERENCES

- [1] LeBrun, J. M., Favour, J., "Feasibility and Conceptual Design Study-Vibration Generator Transient Waveform Control System", Final Report prepared for NASA June 1969, Contract NAS 5-15171, Goddard Space Flight Center, Greenbelt, Maryland, by Aerospace Group, The Boeing Company, Kent, Wash. This report also released as Boeing Document D2-114438-1.
- [2] Smallwood, D. O., Witte, A. F., "The Use of Shaker Optimized Periodic Transients in Matching Field Shock Spectra", The Shock and Vibration Bulletin 43, (Part 1 of 4 Parts), June 1973.
- [3] Shinozuka, M. "Maximum Structural Response to Seismic Excitations", Journal of the Engineering Mechanics Division, Proceedings of the American Society of Civil Engineers, October 1970, pp. 729-738.
- [4] Smallwood, D. O., "A Transient Vibration Test Technique Using Least Favorable Responses", The Shock and Vibration Bulletin 43, (Part 1 of 4 Parts), June 1973.
- [5] Drenich, R. F., "Model-Free Design of Aseismic Structures", Journal of the Engineering Mechanics Division, Proceedings of the American Society of Civil Engineers, August 1970, pp. 483-493.

DISCUSSION

Mr. Kalbfleisch (McDonnell Douglass Astronautics Company): You alluded to the overttest or conservatism in the use of the shock spectrum on your models, relative to the two forms of input, the halfsine pulse and the ensemble of decaying sinusoids. Was the overttest factor dependent on the form of input?

Mr. Witte: It was highly dependent on the dynamic characteristics of the system. When the resonances fell within a notch of either the field Fourier spectrum or the field input shock spectrum we found that there was a considerable overttest. When the dynamic characteristics corresponded to a peak in the input shock response spectrum we did a pretty good job in terms of peak amplitudes.

Mr. Enochson (Agabian Associates): One standard problem that you always encounter is the presence of small values or zeros when you divide by frequency response functions like gain in defining the least favorable responses. How do you handle that kind of a problem in the computational procedure?

Mr. Witte: We have experienced that problem and the frequency response function becomes very ragged at these low levels, and in the analytical study we just let it go. We were interested up to 3000 Hz and we really didn't have the problem with frequency response functions up to that point.

Mr. Chapman (Jet Propulsion Laboratory): How do you implement this test once you have decided what the parameters are? It wasn't clear to me when you found H (ω) whether you were talking about the subsystem under investigation or whether you were talking about the subsystem mounted on a fixture, which in turn, was mounted on a shaker.

Mr. Witte: The frequency response function is the transfer function between the point at which you define the input and the point at which you define the response of the critical component.

Mr. Chapman: Where was this response, was it on the package itself? You took field data and you know what the response was in the field, now what do you do with it? Would you use an electrodynamic shaker to test it?

Mr. Witte: Yes.

Mr. Chapman: You put the package on a fixture, which in turn is mounted to a shaker; you know what you would like the response of this package to be, but in some manner you have to take the transfer function of the fixture and the shaker into consideration.

Mr. Witte: This is a phase independent method.

Mr. Chapman: That was not made clear, but then you run into the problem of how to specify phase.

Mr. Witte: What we have done is to have insured ourselves that we will test to the worst case situation in terms of peak amplitudes of the critical component. We also have insured ourselves that we have matched the field input Fourier spectrum modulus, and if it is a linear system, then one necessarily matches the field response Fourier response modulus.

APPLICATION OF LEAST FAVORABLE RESPONSE TECHNIQUES INCORPORATING FIELD DATA FOURIER TRANSFORM PHASE ANGLE*

R. J. Wolf and A. F. Witte
Kaman Sciences Corporation
Colorado Springs, Colorado

A comparison of critical component shock responses resulting from laboratory test inputs defined by conventional shock spectrum techniques and by a method utilizing the Fourier spectrum of the field environments and frequency response function of the critical component, which is called the "Method of Least Favorable Response", has been done by Witte and Wolf [1]. This paper extends that comparison by modifying Least Favorable Response theory to include field data time history Fourier transform phase angle information, and obtaining solutions for four cases of interest. The results are then compared with Least Favorable Response analyses. It is found that inclusion of field data Fourier transform phase angle (for the case of decaying periodic time histories) represents an upper bound on system response which is significantly lower than the worst case analysis of Least Favorable Response (LFR).

NOMENCLATURE

t time
 ω frequency
 i $\sqrt{-1}$
 $x(t)$ input acceleration in time domain
 $X(\omega)$ input acceleration in frequency domain. $X(\omega)$ is the Fourier transform of $x(t)$
 $y(t)$ response acceleration in time domain
 $Y(\omega)$ response acceleration in the frequency domain. $Y(\omega)$ is the Fourier transform of $y(t)$
 $H(\omega)$ the frequency response function of the system

$X_e(\omega)$ the envelope of the moduli of the Fourier transforms of the input acceleration time histories which defines field environment
 $\theta(\omega)$ the phase angle of the Fourier transform of an input acceleration time history
 $\phi(\omega)$ the phase angle of the frequency response function
 $|A|$ magnitude of any complex quantity A

Note: "Field data" refers to the acceleration time histories that define the environment which a system is subjected to, and are typically measured in the field.

INTRODUCTION

The method of Least Favorable Response (LFR) is a technique for computing the absolute maximum response of a system having a known frequency response function and subjected to a number of given input time histories.

* This work was performed under contract to the U. S. Army SAFEGUARD System Command, Contract Number DAHC60-68-C-0020.

It also provides a means for computing the input time history which results in this maximum response. Smallwood [2] has proposed this technique to establish laboratory test criteria.

Witte and Wolf [1] have made a study comparing the method of Least Favorable Response to classical shock spectrum techniques. The results of this study indicate that for a class of input field time histories which are decaying periodics, the Least Favorable Response is approximately twice the field response experienced for a single degree-of-freedom system. In some cases, this may be considered as overly conservative and would result in unrealistic cost/weight/performance penalties. It has been suggested by Smallwood [3] that utilizing field data Fourier transform phase angle information as well as the envelope of the modulus will result in lower response amplitudes than those obtained using Least Favorable Response analysis, while still being upper bounds on the system response.

If the established bounds on the field data Fourier transform phase angle are carried through the Least Favorable Response analysis, the problem reduces to that of determining the absolute maximum response for any input time history whose Fourier transform moduli is less than or equal to the envelope of the field moduli and whose Fourier transform phase angle is within the bounds established.

A formulation of the Least Favorable Response analysis including phase angle has been done analytically by Smallwood [3] in terms of delay functions. A slightly different formulation suited to digital techniques is presented in this paper. A phase function $U(\omega)$ is defined

$$U(\omega) = \cos\{\theta(\omega)\}$$

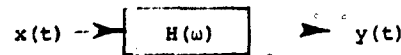
where $\theta(\omega)$ is the phase angle of the Fourier transform of the field data. The Least Favorable Response for a given Fourier transform moduli envelope, $X_e(\omega)$, and allowable band of phase functions $U(\omega)_{\max}$ and $U(\omega)_{\min}$ is formulated.

Least Favorable Input and Response calculations including bounds of allowable phase angle have been performed numerically and compared with the usual Least Favorable Inputs and Responses, and with shock spectrum results of Witte and Wolf [1].

THE LEAST FAVORABLE RESPONSE THEORY INCLUDING FIELD DATA FOURIER TRANSFORM PHASE ANGLE

Let us assume that an arbitrary configuration can be represented by a linear system as shown below, where $H(\omega)$ is the system frequency response function, and

Input Linear System Response



Single Input/Single Output
Linear System

$x(t)$ and $y(t)$ are the system input and response, respectively. Note that it is not required that $x(t)$ and $y(t)$ have the same physical units. For example, $x(t)$ could be an acceleration and $y(t)$ the relative strain between two points. Let $X(\omega)$ and $Y(\omega)$ be the Fourier spectra of $x(t)$ and $y(t)$. Then

$$X(\omega) = \int_{-\infty}^{\infty} x(t)e^{-i\omega t} dt, \quad (1)$$

$$x(t) = \frac{1}{2\pi} \int_{-\infty}^{\infty} X(\omega)e^{i\omega t} d\omega, \quad (2)$$

$$Y(\omega) = \int_{-\infty}^{\infty} y(t)e^{-i\omega t} dt, \quad (3)$$

$$y(t) = \frac{1}{2\pi} \int_{-\infty}^{\infty} Y(\omega)e^{i\omega t} d\omega. \quad (4)$$

With the aid of the frequency response function, $H(\omega)$,

$$y(t) = \frac{1}{2\pi} \int_{-\infty}^{\infty} H(\omega)X(\omega)e^{i\omega t} d\omega, \quad (5)$$

where i is the imaginary unit.

The Least Favorable Input, $x_{LFI}(t)$, for the general case is defined as the input that produces the absolute maximum response equal to

$$|y|_{\max} < \frac{1}{2\pi} \int_{-\infty}^{\infty} |X(\omega)| |H(\omega)| d\omega. \quad (6)$$

Let us express an input $X(\omega)$, and the frequency response function, $H(\omega)$, in their polar form

Let us express an input $X(\omega)$, and the frequency response function, $H(\omega)$, in their polar form

$$X(\omega) = |X(\omega)| e^{i\theta(\omega)}, \quad (7)$$

$$H(\omega) = |H(\omega)| e^{i\phi(\omega)}, \quad (8)$$

the response $y(t)$ is then given by

$$\begin{aligned} y(t) &= \frac{1}{2\pi} \int_{-\infty}^{\infty} X(\omega) H(\omega) e^{i\omega t} d\omega \\ &= \frac{1}{2\pi} \int_{-\infty}^{\infty} |X(\omega)| |H(\omega)| e^{i\theta(\omega)} e^{i\phi(\omega)} e^{i\omega t} d\omega \end{aligned} \quad (9)$$

or

$$\begin{aligned} y(t) &= \frac{1}{2\pi} \int_{-\infty}^{\infty} |X(\omega)| |H(\omega)| e^{i\{\theta(\omega) + \phi(\omega) + \omega t\}} d\omega. \end{aligned}$$

Now if one defines the moduli of the input as

$$|X(\omega)| = X_e(\omega)$$

where $X_e(\omega)$, is defined such that $X_e(\omega) \geq |X_i(\omega)|$, $i = 1, n$, for all ω , then, $X_e(\omega)$ will, by definition, represent an upper bound on the moduli of the Fourier transforms of the individual input time histories, $x_1(t)$, $x_2(t)$, ..., $x_n(t)$. Maximizing Eq. (9) through [4]

$$e^{i\{\theta(\omega) + \phi(\omega) + \omega t\}} = e^0 = 1 \quad (10)$$

by selecting

$$(1) \quad t = 0$$

$$(2) \quad \theta(\omega) = -\phi(\omega)$$

$$(3) \quad |X(\omega)| = X_e(\omega)$$

we obtain what is commonly referred to as the "Least Favorable Response". Substituting these expressions into Eq. (7), we obtain an expression for the "Least Favorable Input", $x(t)_{LFI}$, as follows

$$X(\omega)_{LFI} = X_e(\omega) e^{-i\phi(\omega)} \quad (11)$$

or

$$x(t)_{LFI} = \frac{1}{2\pi} \int_{-\infty}^{\infty} X_e(\omega) e^{-i\phi(\omega)} e^{i\omega t} d\omega. \quad (12)$$

This can also be written as

$$x(t)_{LFI} = \frac{1}{2\pi} \int_{-\infty}^{\infty} \frac{X_e(\omega)}{|H(\omega)|} H^*(\omega) e^{-i\omega t} d\omega. \quad (13)$$

(where * denotes the complex conjugate). This states that an input acceleration given by Eq. (12) will result in a maximum system response $y(t)_{\max}$ which could result from any possible input, $X(\omega)$, which is contained within the envelope $X_e(\omega)$.

As shown, Shinozuka [4] obtained the Least Favorable Response through maximizing Eq. (9) by choosing

$$(1) \quad t = 0$$

$$(2) \quad \theta(\omega) = -\phi(\omega)$$

These assumptions do indeed maximize the response $y(t)$. However, they in general, lead to system responses which are extreme upper limits and are not least upper bounds. It is not required to arbitrarily choose $\theta(\omega) = -\phi(\omega)$, which is the absolute worst possible case, when in fact the phase angle $\theta_1(\omega)$ for all time histories $x_i(t)$ is a known function obtained from the Fourier transform of the input time histories; and bounds of experienced and allowable phase angles can be established. The extreme generality of the "Least Favorable Response" can further be reduced by noting that system responses can have only a real component; since all original time histories are real, the resulting responses must also be real. Then the response, $y(t)$, is given by

$$\begin{aligned} y(t) &= \frac{1}{2\pi} \int_{-\infty}^{\infty} |X_e(\omega)| |H(\omega)| \\ &\quad \{\cos[\theta(\omega) + \phi(\omega) + \omega t]\} d\omega, \end{aligned} \quad (14)$$

and the maximum response is given by

$$\begin{aligned} y(t)_{\max} &= \frac{1}{2\pi} \int_{-\infty}^{\infty} |X_e(\omega)| |H(\omega)| \\ &\quad \{\cos[\theta(\omega) + \phi(\omega) + \omega t]\} d\omega. \end{aligned} \quad (15)$$

Smallwood [3] has considered Eq. (14), introduced the delay function defined by

$$\delta(\omega) = \frac{-\theta(\omega)}{\omega},$$

and proceeded with an analysis on that basis. However, since $\cos(\delta(\omega)\omega)$, i.e., $\cos \theta(\omega)$, is a better behaved function, having a much smaller dynamic range, 0(1), and is easier to work with and envelope, than $\delta(\omega)$, let us proceed as follows. Expanding

$$|\cos\{\theta(\omega) + \phi(\omega) + \omega t\}|$$

in terms of the cosine of the sum of the two angles $\theta(\omega)$ and $\{\phi(\omega) + \omega t\}$ we obtain

$$|\cos \theta(\omega) + \{\phi(\omega) + \omega t\}|$$

$$= |\cos \theta(\omega) \cos \{\phi(\omega) + \omega t\}$$

$$- \sin \theta(\omega) \sin \{\phi(\omega) + \omega t\}|$$

or

$$= |\cos \theta(\omega) \cos \{\phi(\omega) + \omega t\}$$

$$- (\pm) \sqrt{1 - \cos^2 \theta(\omega)} \sin \{\phi(\omega) + \omega t\}| \quad (16)$$

where (\pm) must be determined by what quadrant $\cos \theta$ is in. Let us further introduce a dependent variable, $U(\omega)$, which we will simply call the "Phase Function".

$$U(\omega) = \cos\{\theta(\omega)\}. \quad (17)$$

Now, the frequency response function phase angle, $\phi(\omega)$, is considered to be known, ωt is also known, hence for any general situation

$$\cos\{\phi(\omega) + \omega t\} = C_1(\omega, t) \text{ is Known} \quad (18)$$

$$\sin\{\phi(\omega) + \omega t\} = C_2(\omega, t) \text{ is Known} \quad (19)$$

Substitution of Eqs. (17), (18), (19), into Eq. (16) yields

$$|\cos\{\theta(\omega) + \phi(\omega) + \omega t\}|$$

$$= |U(\omega) C_1(\omega, t)$$

$$- (\pm) \sqrt{1 - U(\omega)^2} C_2(\omega, t)|$$

and since C_1 and C_2 are exact known functions, the value of $U(\omega)$ is the only quantity which cannot be exactly defined. Therefore, if the bounds on the phase function $U(\omega)$ can be determined by

$$U(\omega)_{\max} \geq U_i(\omega) \text{ for } i = 1 \rightarrow n$$

and

$$U(\omega)_{\min} \leq U_i(\omega) \text{ for } i = 1 \rightarrow n$$

then the upper bound on $|\cos\{\theta(\omega) + \phi(\omega) + \omega t\}|$ is determined by:

$$|\cos\{\theta(\omega) + \phi(\omega) + \omega t\}|$$

$$= U(\omega)_{M_1} C_1(\omega, t)$$

$$- (\pm) \sqrt{1 - U(\omega)_{M_2}^2} C_2(\omega, t)$$

where $U(\omega)_{M_1} = U(\omega)_{\max}$ or $U(\omega)_{\min}$ and

$U(\omega)_{M_2} = U(\omega)_{\max}$ or $U(\omega)_{\min}$ depending

upon the sign and magnitude of $C_1(\omega, t)$ and $C_2(\omega, t)$ and the sign of $\{(\pm)\}$ such that the combination yields the maximum value. For example, if $C_1(\omega, t)$, $C_2(\omega, t)$, and $-(\pm)$ are all positive then the above expression becomes

$$|\cos\{\theta(\omega) + \phi(\omega) + \omega t\}|$$

$$= U(\omega)_{\max} C_1(\omega, t)$$

$$+ \sqrt{1 - U(\omega)_{\min}^2} C_2(\omega, t)$$

where $U(\omega)_{\max}$ and $U(\omega)_{\min}$ are the upper and lower envelopes of the contributing phase functions $U_i(\omega) = \cos\{\theta_i(\omega)\}$.

The Least Favorable Response for a given Fourier transform moduli envelope $X_e(\omega)$ and allowable band of phase functions $U(\omega)_{\max}$ and $U(\omega)_{\min}$ is then given by:

$$y(t)_{\max} = \frac{1}{2\pi} \int_{-\infty}^{\infty} X_e(\omega) |H(\omega)| \quad (20)$$

$$\{U(\omega)_{M_1} C_1(\omega, t)$$

$$- (\pm) \sqrt{1 - U(\omega)_{M_2}^2} C_2(\omega, t)\} d\omega,$$

the corresponding Least Favorable Input is given by:

$$x(t)_{LFI} = \left[F^{-1} \frac{F^1 [y(t)_{\max}]}{H(\omega)} \right] \quad (21)$$

where F^1 and F^{-1} are the Fourier transform and inverse transform, respectively.

THE ANALYTICAL STUDY

The analytical study consisted of numerically evaluating Eq. (20) to determine the Least Favorable Response for an envelope of five time histories for four frequency response functions of interest. The corresponding Least Favorable Inputs determined by Eq. (21) were evaluated via fast Fourier transform techniques. The time histories and frequency response functions were identical to those used in the study by Witte and Wolf [1], which compared in detail to the mechanical shock test criteria which were generated from an ensemble of hypothetical field measured time histories by conventional shock spectrum techniques and by the method of Least Favorable Response (LFR). This was done so that the results obtained could be compared to those obtained by shock spectrum and Least Favorable Response techniques, and a more meaningful insight into the effect of including field data Fourier transform phase angle information could be reached.

The hypothetical field measured time histories were generated by a summation of decaying sinusoids of the form:

$$x_i(t) = \sum_{i=1}^n A_i e^{-\xi_i \omega_i t} \sin(\omega_i t + \phi_i).$$

Table 1 gives the frequency and amplitude content of the first time history and Fig. 1 shows a computer plot of the corresponding time history which is labeled #5-A. Similarly, Table 2 and Fig. 2 identify the second time history labeled #5-D; Table 3 and Fig. 3 identify time history #5-G; Table 4 and Fig. 4 identify time history #2-B; while Table 5 and Fig. 5 correspond to hypothetical field time history #7-G.

TABLE 1

COMPOSITE DECAYING SINE TIME HISTORY
CONTENT, #5-A $\Delta t = .400E-04$

i	A_i (g)	ξ_i (dimensionless)	$\frac{\omega_i}{2\pi}$ (hertz)	ϕ_i radians
1	.100E+00	.100E+00	.127E+03	0.0
2	.800E-01	.100E+00	.191E+03	2.50
3	.600E-01	.100E+00	.286E+03	0.0
4	.400E-01	.100E-01	.398E+03	0.0
5	.200E-01	.100E-01	.796E+03	0.0
6	.100E-01	.100E-01	.119E+04	0.0
7	.500E-02	.500E-02	.159E+04	0.0
8	.250E-02	.500E-02	.318E+04	0.0
9	.100E-02	.500E-02	.637E+04	0.0
10	.500E-01	.500E-02	.955E+04	0.0

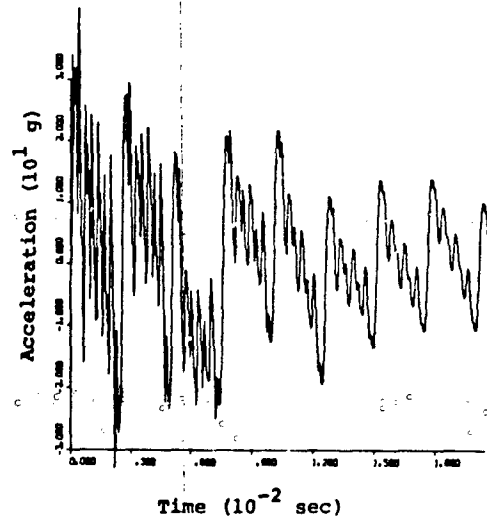


Fig. 1 - Computer plot of time history #5-A.

TABLE 2
COMPOSITE DECAYING SINE TIME HISTORY
CONTENT, #5-D $\Delta t = .200E-04$

1	A_1	t_1	$\frac{u_1}{2\pi}$	ϕ_1
	(g)	(dimensionless)	(hertz)	radians
1	.130E+00	.100E+00	.255E+03	0.0
2	.104E+00	.100E+00	.573E+03	2.50
3	.780E-01	.100E+00	.159E+04	0.0
4	.520E-01	.100E-01	.318E+04	0.0
5	.260E-01	.100E-01	.127E+05	0.0
6	.130E-01	.100E-01	.191E+05	0.0
7	.650E-02	.500E-02	.637E+04	0.0
8	.325E-02	.500E-02	.239E+04	0.0
9	.130E-02	.500E-02	.796E+03	0.0
10	.650E-01	.500E-02	.382E+03	0.0

TABLE 3
COMPOSITE DECAYING SINE TIME HISTORY
CONTENT, #5-G $\Delta t = .400E-04$

1	A_1	t_1	$\frac{u_1}{2\pi}$	ϕ_1
	(g)	(dimensionless)	(hertz)	radians
1	.500E-01	.500E-02	.127E+03	0.0
2	.40E-01	.500E-02	.191E+03	2.50
3	.300E-01	.500E-02	.286E+03	0.0
4	.200E-01	.500E-02	.398E+03	0.0
5	.100E-01	.100E-01	.796E+03	0.0
6	.500E-02	.100E-01	.119E+04	0.0
7	.250E-02	.100E-01	.159E+04	0.0
8	.125E-02	.100E+00	.318E+04	0.0
9	.500E-03	.100E+00	.637E+04	0.0
10	.250E-01	.100E+00	.955E+04	0.0

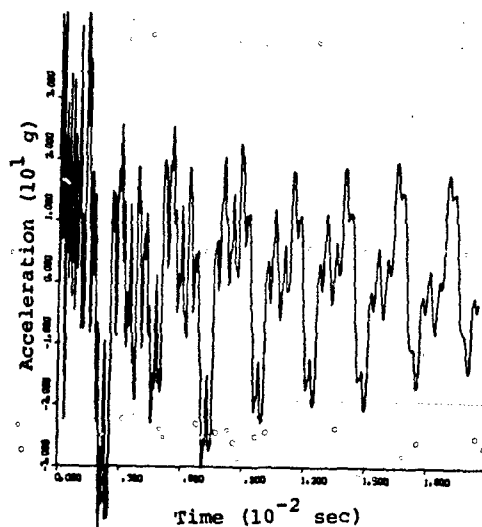


Fig. 2 - Computer plot of time history
#5-D.

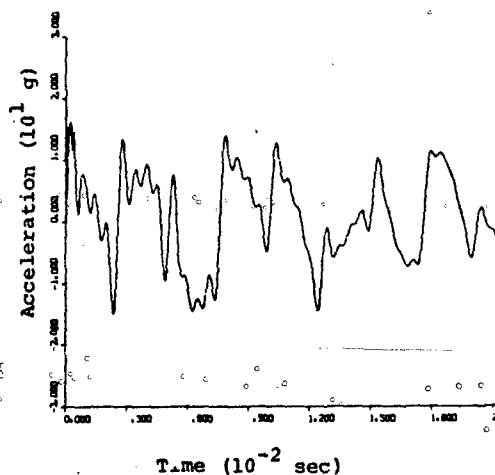


Fig. 3 - Computer plot of time history
#5-G.

TABLE 4
COMPOSITE DECAYING SINE TIME HISTORY
CONTENT, #2-B $\Delta t = .1925E-04$

1	A_i (g)	C_i (dimensionless)	$\frac{\omega_i}{2\pi}$ (hertz)	θ_i radians
1	.300E+00	.145E-01	.157E+04	0.0
2	.500E-01	.500E-01	.662E+03	2.50
3	.150E+00	.100E+00	.331E+03	0.9

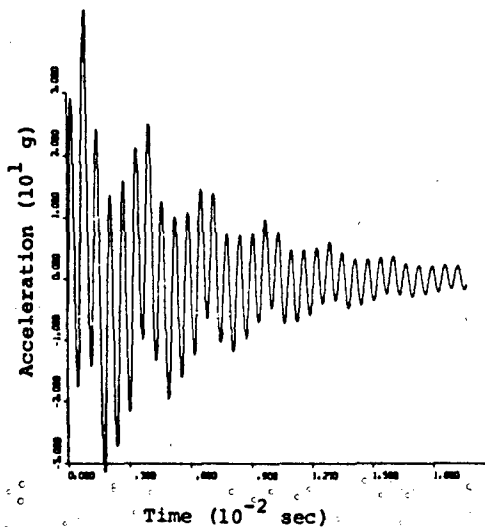


Fig. 4 - Computer plot of time history #2-B.

TABLE 5
COMPOSITE DECAYING SINE TIME HISTORY
CONTENT, #7-G $\Delta t = .740E-04$

1	A_i (g)	C_i (dimensionless)	$\frac{\omega_i}{2\pi}$ (hertz)	θ_i radians
1	.400E-01	.100E-01	.107E+04	0.0
2	.200E-01	.100E-01	.161E+04	0.0
3	.200E-01	.100E-01	.107E+04	0.0
4	.200E-00	.100E+00	.172E+03	0.0
5	.160E+00	.100E+00	.258E+03	2.50

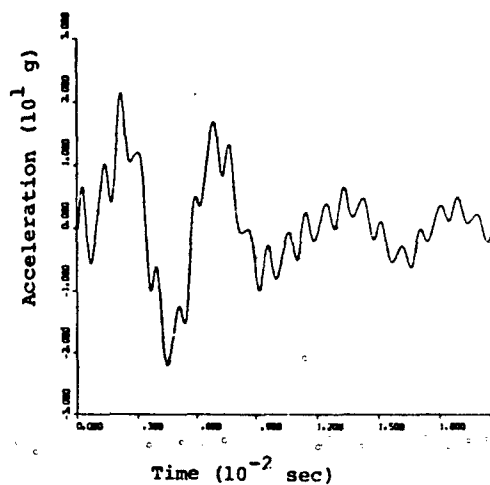


Fig. 5 - Computer plot of time history #7-G.

The moduli of the Fourier transform of these time histories and the corresponding Fourier transform phase functions, $U(\omega)$, (defined in the previous section by $U(\omega) = \cos(\theta)$, where θ is the Fourier transform phase angle) are shown in Figs. 6, 7, 8, 9, and 10.

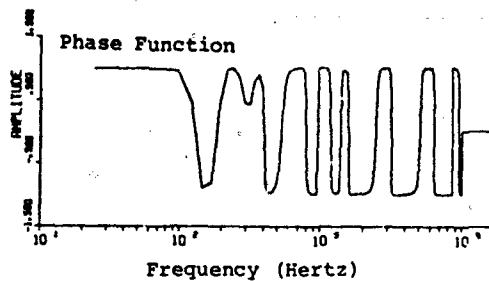
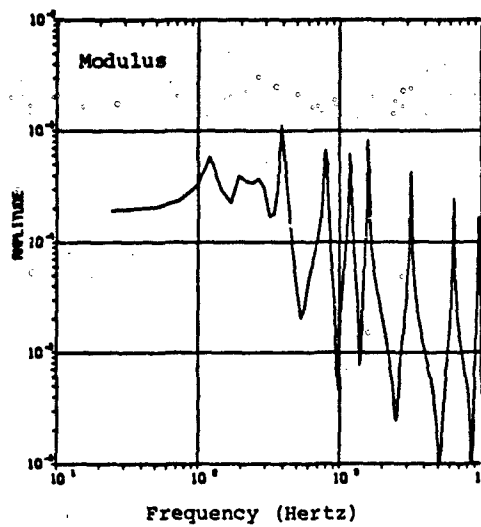


Fig. 6 - Modulus of Fourier transform and corresponding phase function for Event 5-A time history.

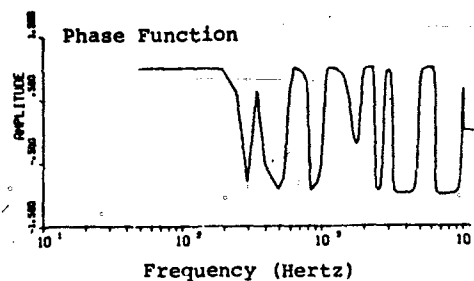
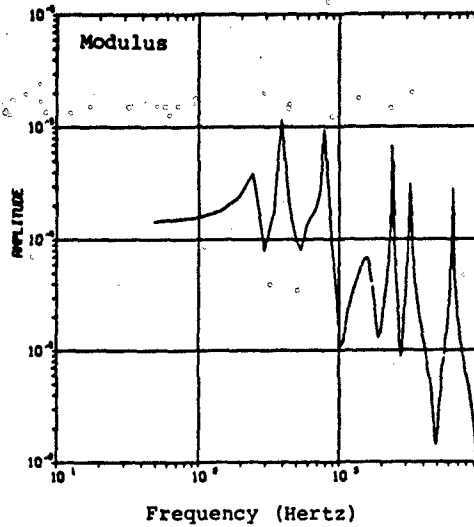


Fig. 7 - Modulus of Fourier transform and corresponding phase function for Event 5-D time history.

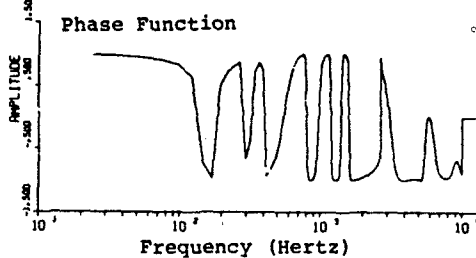
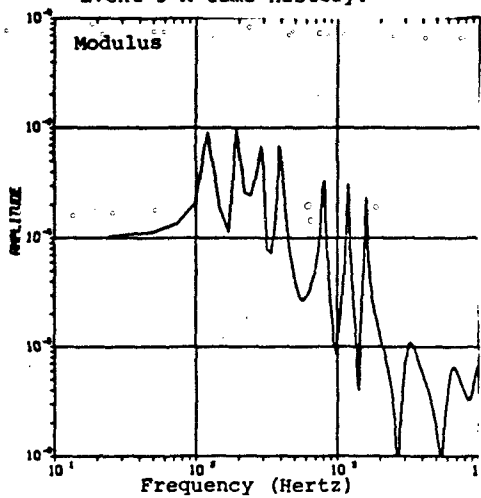


Fig. 8 - Modulus of Fourier transform and corresponding phase function for Event 5-G time history.

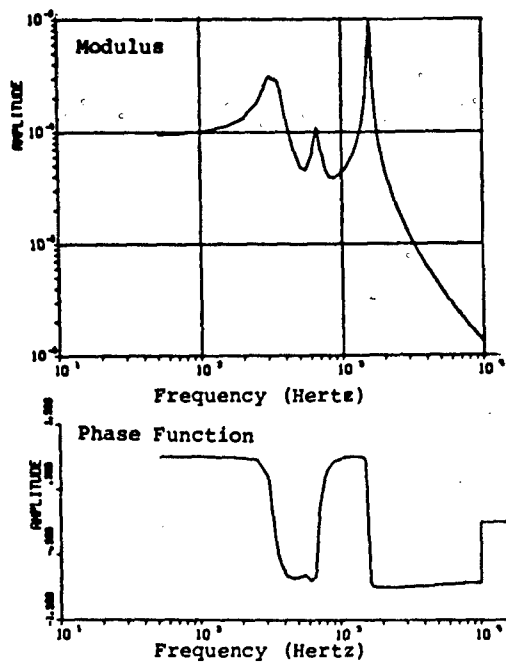


Fig. 9 - Modulus of Fourier transform and corresponding phase function for Event 3-B time history.

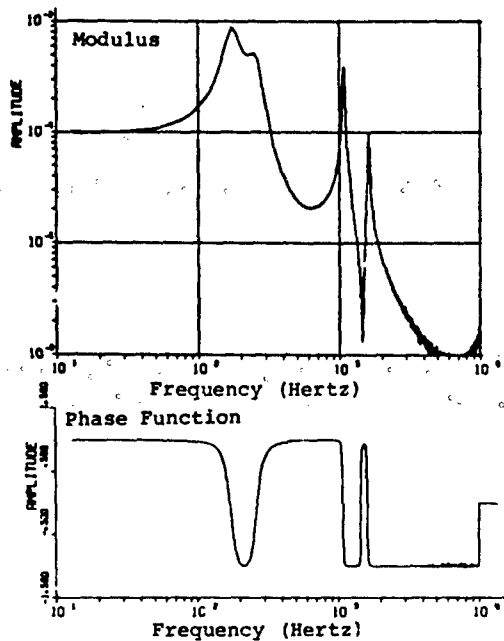


Fig. 10 - Modulus of Fourier transform and corresponding phase function for Event 7-G time history.

Figure 11 shows the overlay of the five Fourier transform moduli and an overlay of their corresponding phase functions.

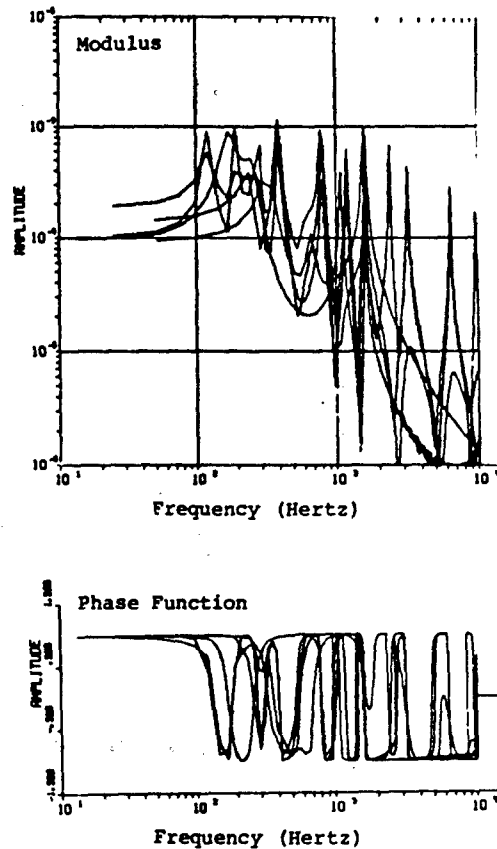


Fig. 11 - Ensemble overlay of moduli of Fourier transforms and corresponding phase functions of five time histories.

Fig. 12 gives the resulting envelope of the Fourier transform moduli, X_e , along with the maximum $U_{\max}(\omega)$ and the minimum $U_{\min}(\omega)$ of the corresponding functions. The curves of Fig. 12 along with the systems frequency response function, $H(\omega)$, provide the input required to compute the systems maximum response amplitude for any input time history whose Fourier transform moduli is less than or equal to the envelope, X_e , and whose corresponding Fourier transform phase function (phase angle) is bounded by $U_{\max}(\omega)$ and $U_{\min}(\omega)$. That is, these are the required field data determined functions which are used to evaluate the integral of Eq. (20). In evaluation of this integral, time and frequency increments were selected so that fast Fourier transform techniques could be used to compute the Least Favorable Inputs given by Eq. (21). That is

$$t = \frac{1}{NAf} = \frac{2\pi}{NA\omega}.$$

Frequency response functions were generated for both single degree-of-freedom systems and multiple degree-of-freedom systems, each representing critical components within a complete hardware system. The single degree-of-freedom systems provided a relatively simple means of checking theory and computational techniques. They also provided a logical basis for comparing shock spectrum and Least Favorable Response techniques, since shock spectrum is only rigorously applicable to single degree-of-freedom systems.

The multiple degree-of-freedom systems were also used to obtain results which could be utilized to compare shock spectrum and Least Favorable Response methods.

Four systems were used in the study, two single degree-of-freedom systems and two multiple degree-of-freedom systems. Each system whose input and response are defined by $\dot{X}(t)$ and $\dot{Y}_i(t)$, respectively, were identified with a case number.

Case 1 was a single degree-of-freedom system (critical component) having a resonance frequency of 650 Hertz and a critical damping ratio of .03 (see Fig. 13). The resonance frequency was such that it corresponded to a notch in the ensembled field Fourier spectra and thus requiring its driving point impedance to be relatively large compared to the source impedance.

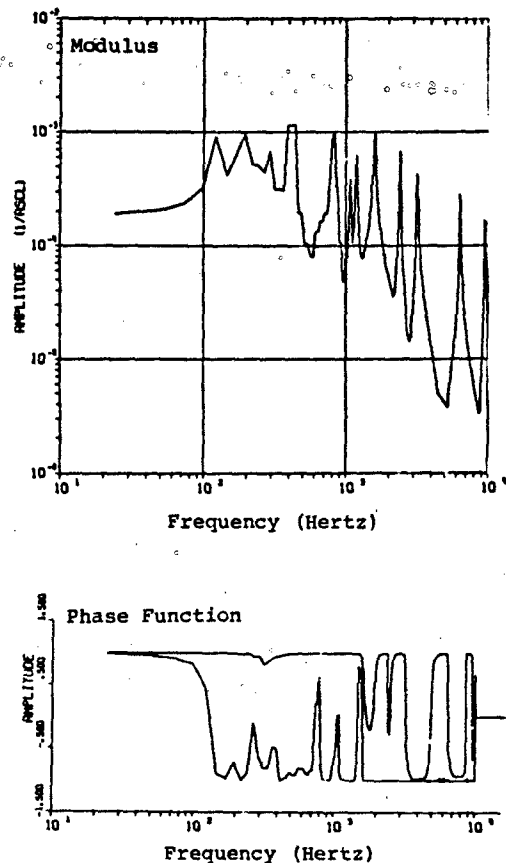


Fig. 12 - Envelope of moduli of Fourier transforms and corresponding maximum $(U(\omega)_{\max})$ and minimum $(U(\omega)_{\min})$ phase functions.

Case 2 was a single degree-of-freedom system having a resonance of 800 Hertz and a critical damping ratio of .03 (see Fig. 14). The resonance frequency was such that it corresponded to a peak in the ensembled field Fourier spectra requiring the driving point impedance of the component to be small compared to the source impedance.

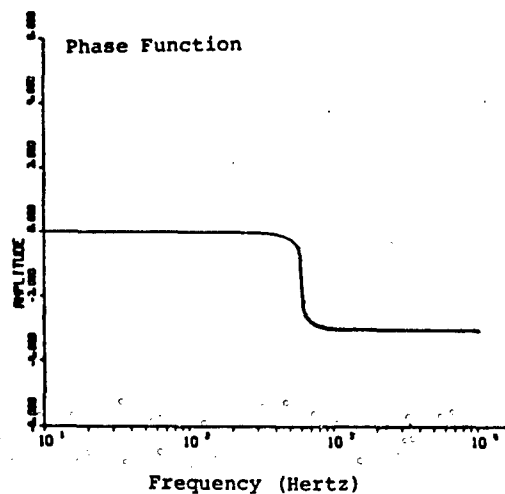
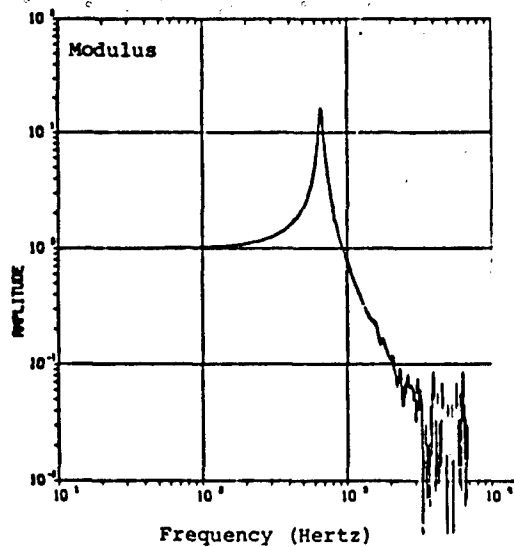


Fig. 13 - Single degree-of-freedom frequency response function with resonance at 650 Hertz. (Case 1).

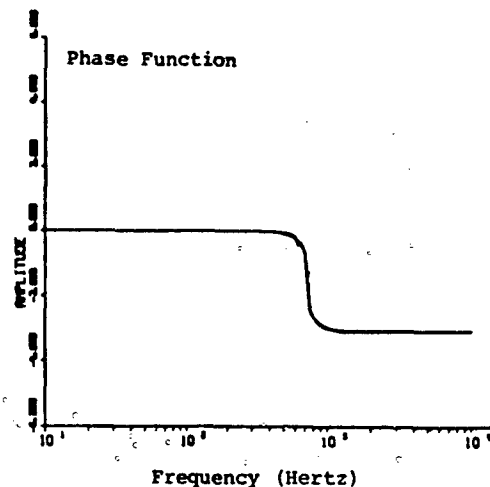
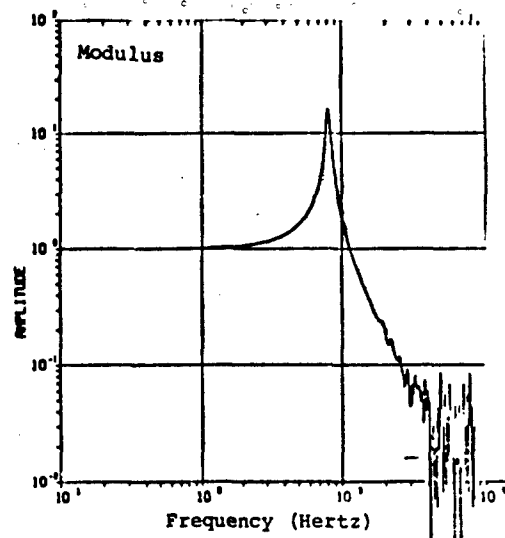


Fig. 14 - Single degree-of-freedom frequency response function with resonance at 800 Hertz. (Case 2).

Case 3 was a two degree-of-freedom system having non-uniform damping characteristics and closely coupled resonance frequencies as shown in Fig. 15. These frequencies corresponded to a notch and a peak in the ensembled Fourier spectra. The first resonance corresponding to a high-driving point impedance compared to the source impedance and the second resonance corresponding to a low-driving point impedance compared to the source. The frequency response function utilized is that between the input and the second mass.

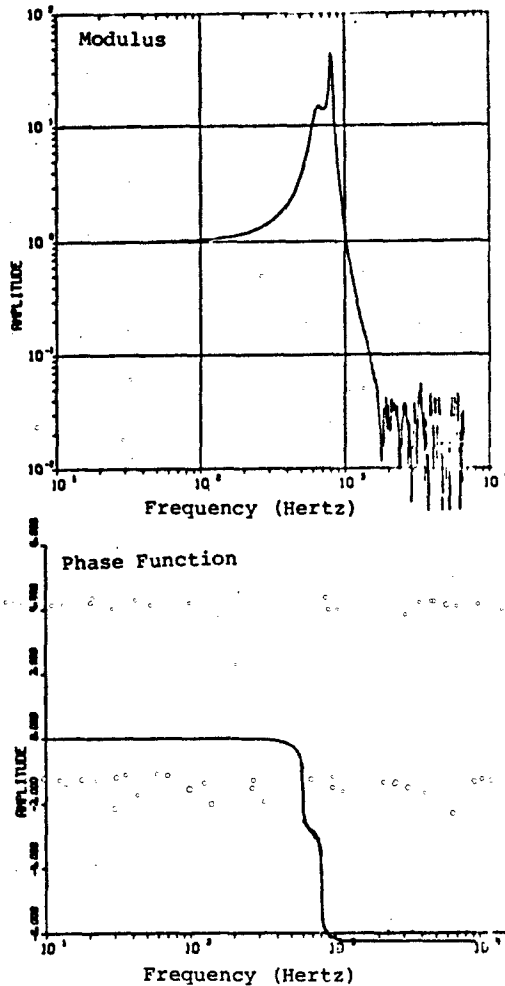


Fig. 15 - Two degree-of-freedom frequency response function with closely coupled modes. (Case 3)

Case 4 was a two degree-of-freedom system having non-uniform damping characteristics and little coupling between resonance frequencies as shown in Fig. 16. The first resonance corresponding to a high-driving point impedance as compared to the impedance of the source and the second resonance corresponding to the impedance when compared to the source impedance. Again the frequency response function is that between the input and the second mass.

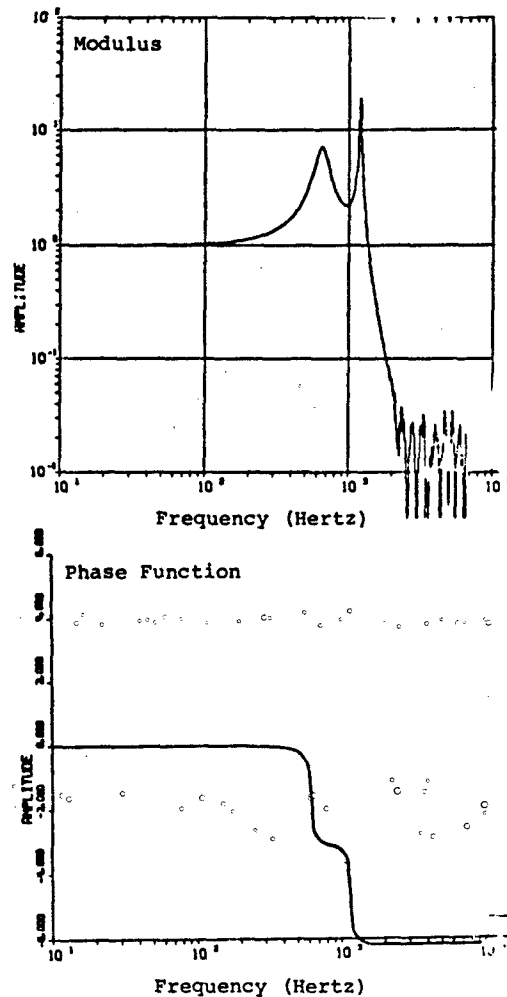


Fig. 16 - Two degree-of-freedom frequency response function with remotely coupled modes. (Case 4)

These four cases corresponded to some of the limiting situations which one can encounter in the critical component/environmental source relationship [1].

STUDY RESULTS

Critical component maximum response amplitudes including field data Fourier transform phase angle information computed via Eq. (20) for the four frequency response functions of interest are shown in Figs. 17 through 20, where they are compared to Least Favorable Responses computed with the same field data time histories and frequency response functions. It is seen that, for the decaying periodic time histories considered, including field data Fourier transform phase angle information reduced peak response amplitudes approximately 30 percent while still representing an upper bound on the field response amplitudes. A detailed summary of the results and comparison with the results obtained by conventional shock spectrum techniques is given in Fig. 21.

It should be pointed out that if the bounds of allowable phase functions are small and $U_{min}(\omega) \rightarrow U_{max}(\omega)$, and if the envelope of the moduli is light, i.e., $|X_i(\omega)| \rightarrow X_e$ for all i , the resulting Least Favorable Input with Fourier transform phase angle reduces to duplication of the original input time histories, and corresponding response becomes exactly the critical component response.

SUMMARY AND CONCLUSIONS

Least Favorable Input and Response calculations including bounds of allowable phase angle have been performed numerically and compared with the usual Least Favorable Inputs and Responses.

It is seen that for the class of input time histories considered, decaying periodics, the typical conservatism factor of 2 can be reduced to typically 1.3 by including field data established bounds on allowable phase angles. Also, as established bounds on allowable phase angles approach each other and as the moduli of the field data Fourier transform approach that of the envelope, X_e , the analysis reduces to reproduction of the original time histories.

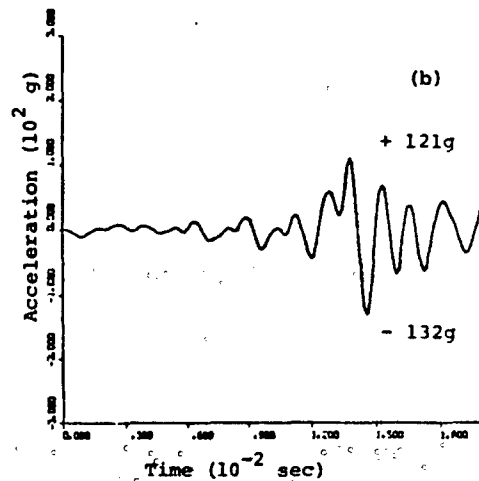
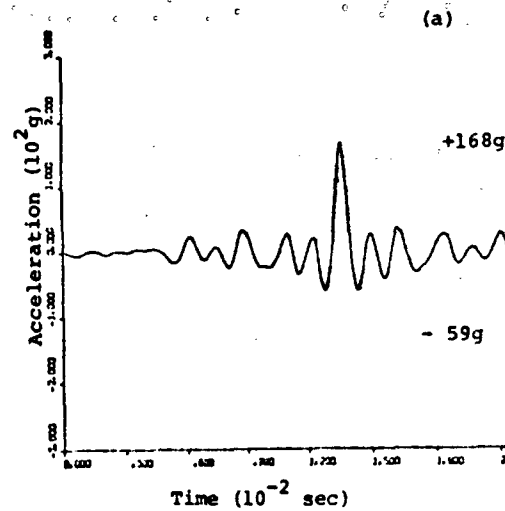


Fig. 17 - (a) Least Favorable Response for the frequency response function of Case 1 and the five ensembled time histories, and (b) is a response obtained when including Fourier transform phase angle enveloping.

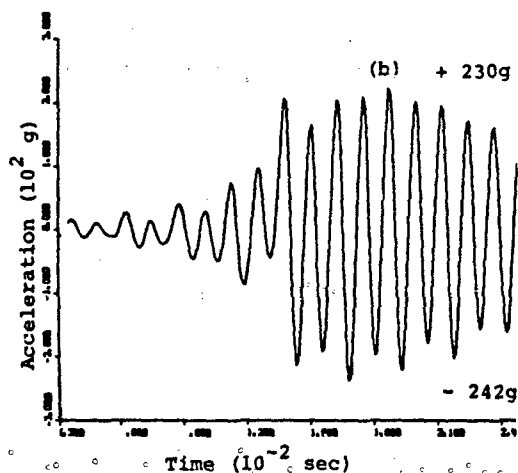
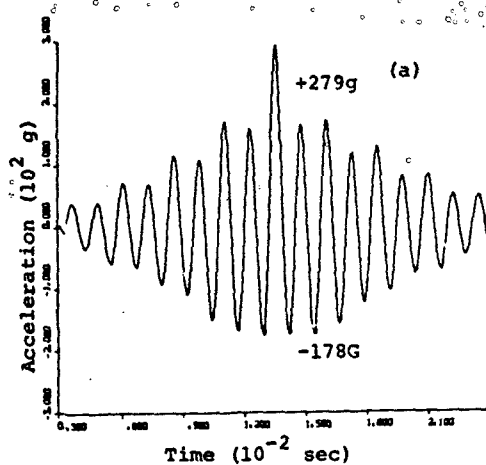


Fig. 18 - (a) Least Favorable Response for the frequency response function of Case 2 and the five ensemble time histories, and (b) is the response obtained when including Fourier transform phase angle enveloping.

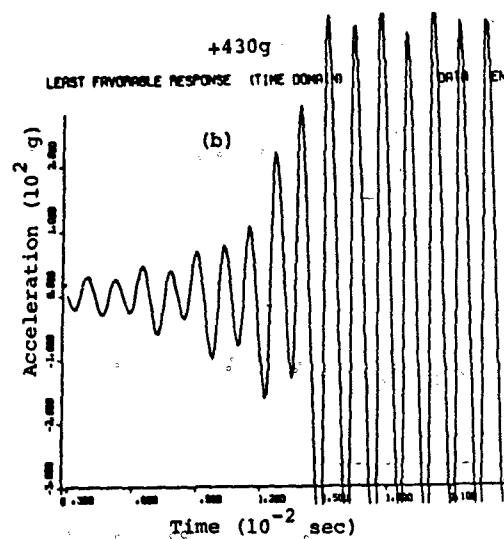
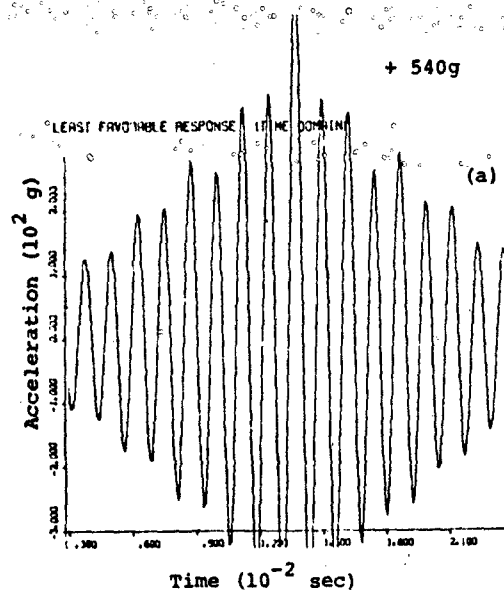


Fig. 19 - (a) Least Favorable Response for the frequency response function of Case 3 and the five ensemble time histories, and (b) is the response obtained when including Fourier transform phase angle enveloping.

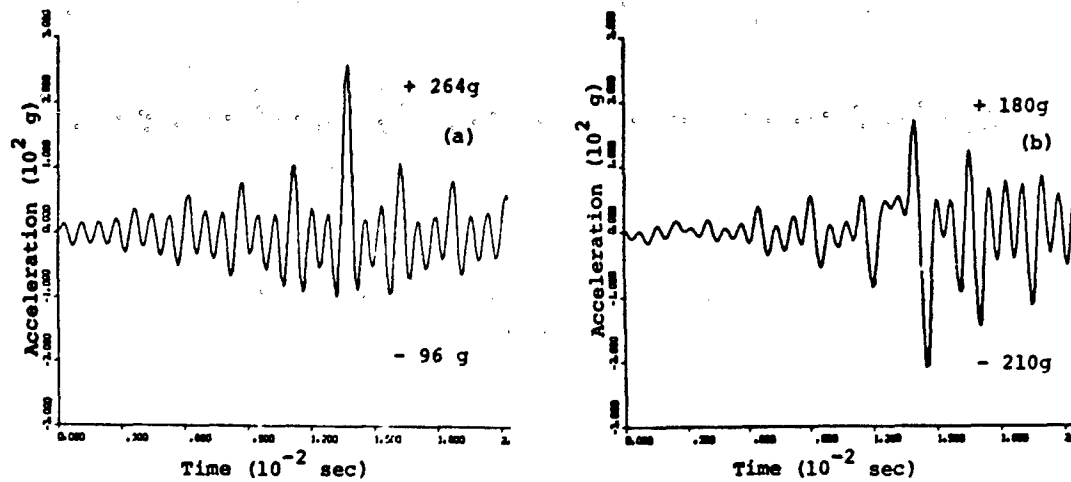


Fig. 20 - (a) Least Favorable Response for the frequency response function of Case 4 and the five ensembled time histories, and (b) is the response obtained when including Fourier transform phase angle enveloping.

L1 LFI FOR CASE 1
 L2 LFI FOR CASE 2
 L3 LFI FOR CASE 3
 L4 LFI FOR CASE 4
 LFR LEAST FAVORABLE RESPONSE
 FM FIELD MAXIMUM
 L01 LFR FOR CASE 1
 L02 LFR FOR CASE 2
 L03 LFR FOR CASE 3
 L04 LFR FOR CASE 4
 LFR0 LEAST FAVORABLE RESPONSE

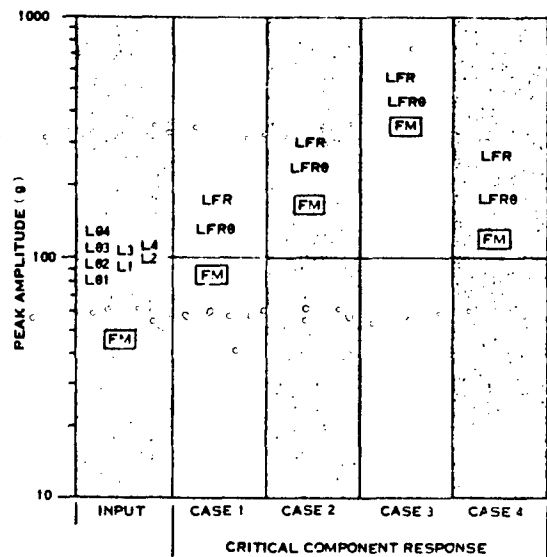


Fig. 21 - Summary of input and response peak amplitudes.

REFERENCES

- (1) A.F. Witte and R.J. Wolf, "Comparison of Shock Spectrum Techniques and the Method of Least Favorable Responses," K-74-20U (R), Kaman Sciences Corporation, Colorado Springs, Colorado, 7 March 1974.
- (2) D.O. Smallwood, "A Transient Vibration Test Technique Using Least Favorable Responses," SC-DR-71-0897, Sandia Laboratories, Albuquerque, New Mexico, February 1972.
- (3) D.O. Smallwood, "An Extension of a Transient Vibration Technique Using Least Favorable Responses," SC-RR-73-0735, Sandia Laboratories, Albuquerque, New Mexico, November 1972.
- (4) M. Shinozuka, "Maximum Structural Response to Seismic Excitation," Journal of the Engineering Mechanics Division, Proceedings of the American Society of Civil Engineers, pp. 729-738, October 1970.

DISCUSSION

Mr. Koen (Bell Laboratories): You overlapped the phase angle you have a minimum and a maximum. Did you choose a value of phase in between the two, or what value phase did you choose to give you the worst condition?

Mr. Wolf: You have to go back and look at that integral and choose whichever produces the maximum response.

Mr. Koen: Do you mean somewhere between those?

Mr. Wolf: No.

Mr. Koen: Is it either the minimum or the maximum?

Mr. Wolf: It is either the minimum or the maximum that bounds it. But you pick the one that results in the maximum response in that integral.

Mr. Gertel (Kinetic Systems): Is it necessary to know the system in order to get this least favorable response and thereby determine the input that produces that?

Mr. Wolf: Yes.

Mr. Gertel: So the limitation of the system is that you must know the characteristics of the system that you propose to test?

Mr. Wolf: Right but being good designers we all claim to know that?

Mr. Gertel: I wouldn't dispute that. I am just projecting the possibilities of a generalized type of requirement. Could we extend your method by just continuing to hypothesize numerous systems and then come up with some new composite environment that might be used for a generalized

case, or perhaps the system is not really applicable to that?

Mr. Wolf: It is flexible to the degree that you know what the response function is. There is a lot of work being done in trying to define that; especially in the areas where you take ratios of very small numbers; there is statistical theory being applied and there is also a lot being done in smoothing of the measurements in terms of measuring the frequency response function. So yes, the limitation, in terms of how well you know the response function is really a limitation of the analysis, but it does encompass a pretty generalized sort of response function.

Mr. Forkois (Naval Research Laboratory): Could you correlate this with the damage of the system? If you have the data from a field system can you determine whether it is in a damaged or an undamaged condition? I think the criterion should be the duplication of the damage in the laboratory that you had out in the field, and this is associated with fragility levels and sensitivities of the equipment. We may have a 10 cent correction and we are spending a million dollars to test the equipment. You test something and you don't want it to be damaged this is the essential point. What constitutes damage to this particular critical item?

Mr. Wolf: With this sort of approach you end up subjecting the hardware to a minimum of oscillations, that is the problem of fatigue is minimized. In addition you have guaranteed yourself that to within the limits that the field data is known, and the limits that the response function is known that the test item will survive. There is another point; yesterday there was a discussion the cost effectiveness of setting the environment levels there was one factor that should have been included, namely the mental anguish factor associated with a failure. I'm not sure the cost of that can be put in dollars and cents.

Mr. Bogdanoff (Purdue University): I am familiar with the work of Drenick in connection with least favorable inputs and this arose in the area of earthquakes. He hypothesized an input at a given location where, data is far removed from that particular spot and he also got worst responses which were roughly a factor of two bigger than others that will meet similar criteria. You got the same thing. Now the question still boils down to this; when you start tempering the response for a suitable design value you have not indicated, at least as far as I can see, any way in which one can cut this worst case down with some notion of the probability that the design value will not be exceeded.

Mr. Wolf: There are a number of papers extending this philosophy but using probability theory.

Mr. Bogdanoff: This is still not a solved question, it is ad-hoc at best.

Mr. Wolf: You still have the question of what is the probability of something occurring to a certain level, that is not considered here and that is probably next on our agenda.

Mr. Sanders (Rockwell International): I think your paper is a pretty valuable contribution, but you addressed yourself to that undertest or overtest subject and my experience has been that most of those are associated with failures. Secondly you limited yourself to linear systems and any system that I know of that approaches a failure mode becomes nonlinear. And if you look at a structural failure of any type when it starts yielding it is no longer linear and many of them are not linear otherwise. Are you projecting this system into the area of failure conditions because this is the one that really grabs management? They don't care whether you vibration test or shock test so long as you are not associated with that problem, and I think that is a direction where we need answers.

Mr. Wolf: We have tossed around how we include a nonlinear response function and I am not sure where it is going to go from there, but I'd like to point out that there is another case where it is important, and that is not when you are concerned about the survivability of a little electronics black box in the structure. I know what the response function of the black box and I have to make sure that the black box is going to work and that it will see the right environment in the laboratory; there we can do a pretty good job still having a linear response function and still talking about a failure mode.

Mr. Fritz (General Electric Company): How would you consider the interaction effects? Many cases of shock problems have interactions leading to a spectral dip effect which is quite serious.

Mr. Wolf: We haven't considered that at all. Perhaps Art has a comment.

Mr. Witte: Are you talking about the reactive portion of the specimen, the mechanical impedance problem?

Mr. Fritz: I'm talking about the case when the equipment can interact with the shock, which is a typical situation in many cases of shock, such as shipboard shock. They have called it the spectral dip effect.

Mr. Witte: We tried to consider this when we had chosen our critical component cases. In the first case, where the peak corresponded to a notch in the Fourier spectrum, we assumed that the impedance of the test specimen was high compared to the impedance of source and you would get this dip effect. There is a great deal of data when you start comparing all of these things, and we have compared this data in tabular form in our paper. I think that when you look at it you will see some interesting comparisons.

Mr. Fritz: My second question concerns the phase problem. When you started out saying you would minimize the phase error I expected you somehow to get into the physics of the problem. That is if you had a spectrum you could always develop a system that would give you the worst possible additions of the phase response to that spectrum.

Mr. Wolf: Yes and that condition is the least favorable response. The effort is then to back off from that to the extent that we know what the phase is.

Mr. Gertel: Interestingly there was a paper presented in a similar vein in that they used these various Army earthquake techniques for reconstituting a time history from an earthquake or a ground motion shock spectrum. Are you familiar with that concept, and if so, have compared your least favorable response shock motions to the earthquake type motions?

Mr. Wolf: Although this least favorable analysis evolved from the earthquake people, and we have branched off from it, we are not in very good communication with what they are doing at this time.

MATCHING SHOCK SPECTRA WITH SUMS OF DECAYING SINUSOIDS COMPENSATED FOR SHAKER VELOCITY AND DISPLACEMENT LIMITATIONS

D. O. Smallwood and A. R. Nord
Sandia Laboratories
Albuquerque, New Mexico

The use of sums of exponentially decaying sinusoids to match acceleration shock response spectra offers several advantages. The principal disadvantage is that the resulting transients do not have zero velocity and displacement changes, and hence cannot be accurately reproduced on existing shaker systems. A method is described in which the decaying sinusoids are modified to reduce the velocity and displacement changes to zero. Basically, the method used is to add a negative amplitude, time shifted rapidly decaying sinusoid to the transient. It is shown that the values of the amplitude and delay can be used to control the change in velocity and displacement, respectively. The frequency can be used to control the low-frequency content of the waveform. The value chosen for the decay rate is apparently not critical. Examples are shown to illustrate that the displacement waveforms can now be predicted. A method is also described for picking the decaying sinusoid components to match a given shock spectrum. First, values are picked assuming each component acts independently from the others. A family of normalized acceleration shock response spectra curves can be used for this purpose. These values are used as the initial values in a computer routine which will then modify the magnitude of the components to match the spectrum. The resulting synthesized pulse can then be reproduced on a shaker using digital techniques.

NOMENCLATURE

A	Amplitude scale factor for a decaying sinusoid (see Eq. 1)	S_1	The desired value for the acceleration shock response spectrum at the frequency ω_1
B_i	The calculated acceleration shock response at the frequency ω_i	t	Time
f	Frequency, $\omega/2\pi$	U	Unit step function
i	$\sqrt{-1}$ or an integer subscript	$x(t)$	Displacement at any time
m	The subscript "m" refers to values for the velocity and displacement compensating pulse.	$\dot{x}(t)$	Velocity at any time
n	The number of summed decaying sinusoids	$\ddot{x}(t)$	Acceleration at any time
		ζ	Decay rate (see Eq. 1)
		η	Damping coefficient, fraction of critical damping

— This work supported by the U. S. Atomic Energy Commission

τ Delay (sec)

ω Circular frequency (rad/sec)

INTRODUCTION

It has been recognized for many years that electrodynamic or electrohydraulic shakers could be used to simulate many transient field events. As the shock spectrum of the environment was the most common tool for characterizing these events, efforts centered around the development of techniques to reproduce a time history on a shaker system which would match a specified shock spectrum.

Many different time histories can be generated which will match the same shock spectrum. These waveforms can be quite different in appearance and it is not clear that they will all produce equivalent test item damage in the laboratory. However, since field environments can also produce time histories which are quite different in appearance, it has not been shown that a single method for generating time histories will be superior for simulating all environments. Many methods should be available, and the particular method chosen should depend on the general characteristics of the field time histories.

Several analog techniques [1, 2, 3] were developed which would produce time histories whose shock spectra would match a wide variety of specified shock spectra. These techniques are generally difficult to set up and usually require the application of many low-level pulses for system equalization. After LeBrun and Favour [4] published a method for reproducing very complex time histories on a shaker system using digital techniques, it was only natural that the versatility of digital methods would be exploited to produce methods for generating time histories whose shock spectra would match specified spectra. It was also recognized by the developers of the various methods [5, 6] that for accurate reproduction on a shaker system a time history should have zero velocity and displacement changes.

There are physical reasons to believe that many acceleration-time field environments can be represented by sums of decaying sinusoids [7] and the examination of field records supports this conclusion. For this reason pulses of this type were considered as one of the available methods for simulating transient

events in the laboratory. Several of the early analog methods [2, 3] used pulses of this type.

A disadvantage of decaying sinusoids is that nonzero velocity and displacement changes are characteristic of these transients. The velocity and displacement changes result from the fact that each half-cycle of the acceleration-time waveform is smaller than the preceding one; hence, there is an accumulation of area (i.e., velocity) as the acceleration is integrated. Techniques using these pulses were moderately successful because the shaker system will act as a high-pass filter removing the low frequency energy from the waveform. This, combined with the flexure restoring force, will force the velocity and displacement to return to zero. The manner in which the acceleration-time waveform will be distorted to remove the velocity and displacement change will be characteristic of the individual shaker system used. This makes it difficult to predict the velocity and displacement waveforms until after the test is run. The velocity and displacement waveforms are important as the shaker system places limits on the magnitudes which can be reproduced. The magnitudes of the velocity and displacement requirements for a given acceleration waveform are useful for test planning as will be illustrated in a later example.

The purpose of this paper is to show that if the pulses are modified to remove the velocity and displacement changes, more accurate control of the acceleration, velocity, and displacement requirements will result. Procedures for synthesizing a pulse, using digital methods, to match a specified shock spectrum are also discussed.

MODIFICATIONS OF ACCELERATION-TIME DECAYING SINUSOIDS TO OBTAIN ZERO VELOCITY AND DISPLACEMENT CHANGES

The basic waveform will be a sum of several decaying sinusoids as given by Eq. (1).

$$\ddot{x}(t) = \sum_{i=1}^n A_i e^{-\zeta_i \omega_i t} \sin \omega_i t \quad (1)$$

The acceleration, velocity, and displacement time histories for a single component are shown as Fig. 1.

As mentioned earlier, the velocity and displacement changes are not zero. A sum of several decaying sinusoids will exhibit a

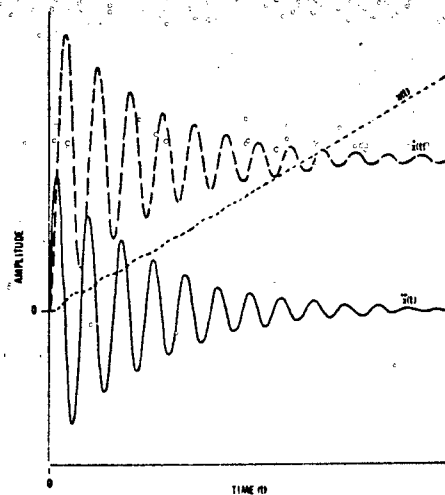


Fig. 1 - Decaying sinusoid acceleration, velocity, and displacement characteristics

similar characteristic. If a pulse could be added having velocity change opposite to the velocity change of the basic waveform, the net velocity change would be reduced to zero. A similar argument can be used to reduce the displacement change.

Let

$$\begin{aligned} \ddot{x}(t) = U(t) \sum_{i=1}^n A_i e^{-\zeta_i \omega_i t} \sin \omega_i t \\ + U(t + \tau) A_m e^{-\zeta_m \omega_m (t + \tau)} \sin \omega_m (t + \tau) \end{aligned} \quad (2)$$

where

$U(t)$ is a unit step function, i.e.,

$$\begin{aligned} U(t) &= 0 \text{ for } t < 0 \\ &= 1 \text{ for } t \geq 0 \end{aligned}$$

The time shifted term has been added for velocity and displacement compensation.

Integrating the velocity becomes

$$\begin{aligned} \dot{x}(t) = U(t) \sum_{i=1}^n \frac{A_i}{\omega_i (\zeta_i^2 + 1)} \\ \left[-e^{-\zeta_i \omega_i t} (\zeta_i \sin \omega_i t + \cos \omega_i t) + 1 \right] \\ + U(t + \tau) \frac{A_m}{\omega_m (\zeta_m^2 + 1)} \\ \left\{ -e^{-\zeta_m \omega_m (t + \tau)} \left[\zeta_m \sin \omega_m (t + \tau) + \cos \omega_m (t + \tau) \right] + 1 \right\} \end{aligned} \quad (3)$$

Integrating again the displacement becomes

$$\begin{aligned} x(t) = U(t) \sum_{i=1}^n \left\{ \frac{A_i e^{-\zeta_i \omega_i t}}{\omega_i^2 (\zeta_i^2 + 1)^2} \left[(\zeta_i^2 - 1) \sin \omega_i t + 2\zeta_i \cos \omega_i t \right] \right. \\ \left. + \frac{A_i t}{\omega_i (\zeta_i^2 + 1)} - \frac{2\zeta_i A_i}{\omega_i^2 (\zeta_i^2 + 1)^2} \right\} \\ + U(t + \tau) \left\{ \frac{A_m e^{-\zeta_m \omega_m (t + \tau)}}{\omega_m^2 (\zeta_m^2 + 1)^2} \left[(\zeta_m^2 - 1) \sin \omega_m (t + \tau) + 2\zeta_m \cos \omega_m (t + \tau) \right] \right. \\ \left. + \frac{A_m (t + \tau)}{\omega_m (\zeta_m^2 + 1)} - \frac{2\zeta_m A_m}{\omega_m^2 (\zeta_m^2 + 1)^2} \right\} \end{aligned} \quad (4)$$

Let

$$\frac{A_m}{\omega_m(\zeta_m^2 + 1)} = - \sum_{i=1}^n \frac{A_i}{\omega_i(\zeta_i^2 + 1)} \quad (5)$$

and

$$\frac{A_m \tau}{\omega_m(\zeta_m^2 + 1)} = \frac{2\zeta_m A_m}{\omega_m^2(\zeta_m^2 + 1)^2} + \sum_{i=1}^n \frac{2\zeta_i A_i}{\omega_i^2(\zeta_i^2 + 1)^2} \quad (6)$$

By substituting Eq. (5) into Eq. (3) and letting $t \rightarrow \infty$ it can be seen that the residual velocity will be zero. Therefore, once ω_m and ζ_m have been picked, A_m can be used to control the residual velocity. Similarly, τ can be used to control the residual displacement. In fact, by substituting Eqs. (5) and (6) into Eqs. (2), (3), and (4), it can be shown that

for $t \leq -\tau$

$$x(t) = \dot{x}(t) = \ddot{x}(t) = 0,$$

and for $t \rightarrow \infty$

$$x(\infty) = \dot{x}(\infty) = \ddot{x}(\infty) = 0,$$

which are the desired boundary conditions. The value chosen for the decay rate, ζ_m is not critical. $\zeta_m = 1$ is a typical value. It will be shown that ω_m can be chosen to control the low frequency roll-off of the modified acceleration-time history's shock spectrum. Procedures for picking the A_i 's, ω_i 's, and ζ_i 's are given in the next section.

Once the parameters ω_m , ζ_m , A_i 's, and ω_i 's have been picked, Eq. (5) can be used to solve for A_m . Then, Eq. (6) can be used to solve for τ .

Letting t be greater than τ in Eqs. (2), (3), and (4) gives

$$x(t) = \sum_{i=1}^n A_i e^{-\zeta_i \omega_i t} \sin \omega_i t + A_m e^{-\zeta_m \omega_m (t+\tau)} \sin \omega_m (t+\tau) \quad (7)$$

$$\dot{x}(t) = \sum_{i=1}^n \frac{-A_i e^{-\zeta_i \omega_i t}}{\omega_i(\zeta_i^2 + 1)} (\zeta_i \sin \omega_i t + \cos \omega_i t) - \frac{A_m e^{-\zeta_m \omega_m (t+\tau)}}{\omega_m(\zeta_m^2 + 1)} [\zeta_m \sin \omega_m (t+\tau) + \cos \omega_m (t+\tau)] \quad (8)$$

$$x(t) = \sum_{i=1}^n \frac{A_i e^{-\zeta_i \omega_i t}}{\omega_i^2(\zeta_i^2 + 1)^2} \left[(\zeta_i^2 - 1) \sin \omega_i t + 2\zeta_i \cos \omega_i t \right] + \frac{A_m e^{-\zeta_m \omega_m (t+\tau)}}{\omega_m^2(\zeta_m^2 + 1)^2} \left[(\zeta_m^2 - 1) \sin \omega_m (t+\tau) + 2\zeta_m \cos \omega_m (t+\tau) \right] \quad (9)$$

Note that for $t > \tau$ the acceleration, velocity, and displacement functions are sums of decaying sines and cosines. Therefore, it is reasonable to expect that for many cases the wave forms of all three to be similar. Because the velocity terms and the displacement

terms are divided by ω and ω^2 respectively, the velocity and displacement time histories tend to be dominated by the low frequency terms. This sometimes gives the waveforms an appearance different from the acceleration waveform. It is also reasonable to expect that the magnitude of the maximum positive and negative peaks will be nearly the same.

It is permissible for all the sinusoids to start at a different time. For example, if $\ddot{x}(t)$ is defined by

$$\ddot{x}(t) = \sum_{i=1}^n U(t - \tau_i) A_i e^{-\zeta_i \omega_i (t - \tau_i)} \sin \omega_i (t - \tau_i) + U(t + \tau) A_m e^{-\zeta_m \omega_m (t + \tau)} \sin \omega_m (t + \tau) \quad (10)$$

The required magnitude for A_m is the same as before (Eq. 5) and the required τ is given by

$$\tau = \frac{\omega_m (\zeta_m^2 + 1)}{A_m} \left\{ \frac{2 \zeta_m A_m}{\omega_m^2 (\zeta_m^2 + 1)^2} + \sum_{i=1}^n \left[\frac{A_i \tau_i}{\omega_i (\zeta_i^2 + 1)} + \frac{2 \zeta_i A_i}{\omega_i^2 (\zeta_i^2 + 1)^2} \right] \right\} \quad (11)$$

In summary, the required velocity and displacement compensation can be accomplished by adding a time shifted, rapidly decaying sinusoid. The low frequency roll-off of

the shock spectrum can be controlled with ω_m , the velocity change with A_m , and the displacement change with the time shift τ . Examples in a later section will illustrate the waveforms which can be expected and the advantages over noncompensated waveforms.

PROCEDURES FOR MATCHING ACCELERATION SHOCK SPECTRA WITH DECAYING SINUSOIDS

The normalized acceleration shock spectra of a 3% critically damped system for a single frequency decaying sinusoid is shown as Fig. 2. The actual peak response ratios as a function of the decaying sinusoid decay rate, ζ , for different values of critical damping, η , are included as Fig. 3. Appendix A gives the value of the peak input as a function of the magnitudes, A_i , of the components.

To match a specified shock spectrum, first sinusoid components are picked for each peak in the shock spectrum.

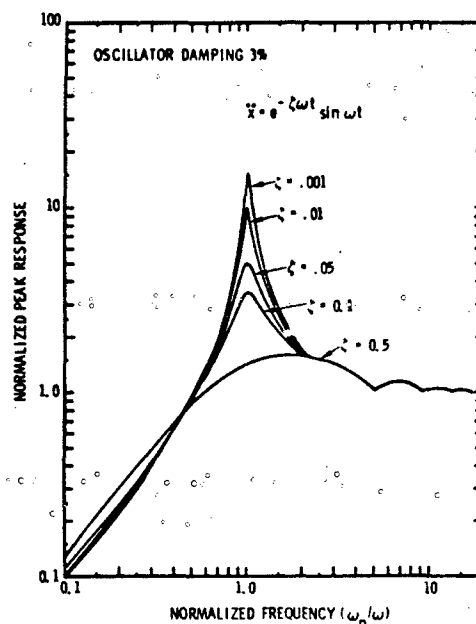


Fig. 2 - Normalized shock spectra for a single frequency decaying sinusoid

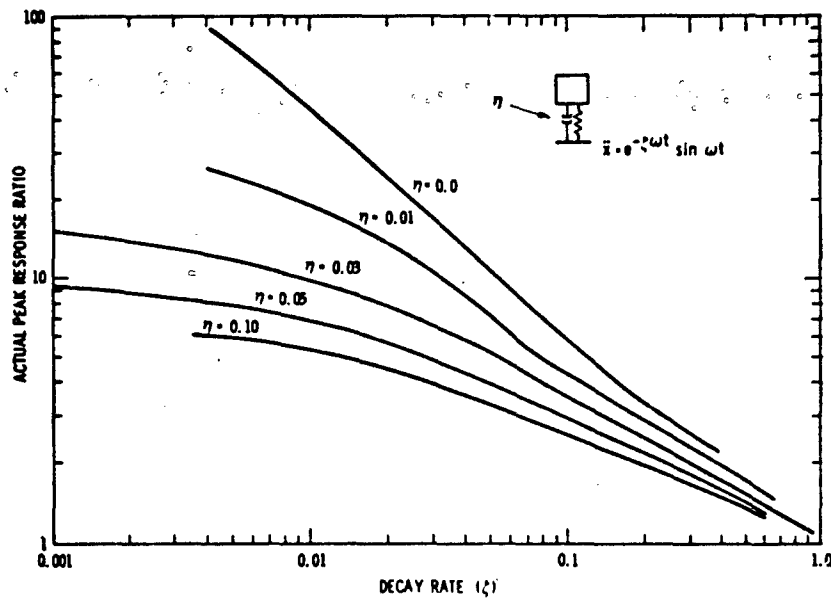


Fig. 3 - Peak response ratio for a decaying sinusoid

If sufficient information is known about the decay rate of the original field data, this information can be used to aid in picking the decay rates, ζ_i . Nelson and Prasthofer [7] also offer suggestions for picking the decay rates. Frequently, the shape of the shock spectra curves as shown in Fig. 2 can aid in picking the decay rates, ζ_i . The amplitudes are then chosen, using Fig. 3, for each sinusoid, assuming each component will act independently. The amplitudes, A_i , can be either positive or negative. Nelson and Prasthofer [7] show that the values for the shock spectrum at frequencies between the ω_i 's can be changed by changing the signs of the A_i 's.

The frequency of the compensating pulse is then chosen by noting the lowest frequency for which the shock spectrum is to be matched. Later examples will show that the frequency, ω_m , should be one-half to one-third of this lowest frequency. The decay rate for the compensating pulse is then chosen (any value between 0.5 and 1.0 will usually work). A manual or computer aided iteration is then performed to refine the values for the amplitudes, A_i . A program has been written to aid in this step. A block diagram of the computer

code is given as Fig. 4. S_i is the desired value of the shock spectrum at the frequency f_i .

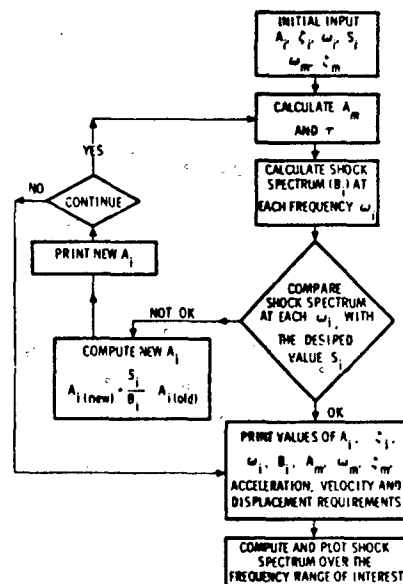


Fig. 4 - Flow diagram for picking decaying sinusoids to match a given shock spectrum

The iteration method shown in Fig. 4 will not guarantee convergence; therefore, operator interaction is provided to stop the iteration if convergence does not occur. This presents no real difficulty as the program is run on a time-shared interactive computer.

The plotted shock spectrum is then compared with the desired spectrum. If convergence did occur, the spectrum will match the desired spectrum at the frequencies ω_i . However, the values of the spectrum at intermediate values may not be at the desired levels. If the intermediate values are too high, the decay rates ζ_i can be made smaller. If the intermediate values are too low, the decay rates can be increased or components can be added at the intermediate frequencies. Care should be taken to match the notches in the spectrum as well as the peaks, as evidence exists [8] to indicate that they may be more important than the peaks. The velocity and displacement requirements can be adjusted by changing ω_m . In general, raising ω_m will reduce the velocity and displacement requirements. The procedures are then repeated until a satisfactory fit is obtained.

The transient can then be reproduced on a shaker system using digital or analog techniques.

EXAMPLES USING MODIFIED DECAYING SINUSOIDS

Several examples will now be given to illustrate the waveforms which can be expected, and to show the advantages of the modified waveforms over non-compensated forms.

Example 1

Consider a single 100 Hz, 10% decay rate, 1g decaying sinusoid. For compensation, a 100 Hz, 50% decay rate decaying sinusoid will be added. For this case Eqs. (5) and (6) reduce to

$$A_m = -A_i \frac{\zeta_m^2 + 1}{\zeta_i^2 + 1}$$

$$\tau = \frac{1}{\omega_m} \left[\frac{2\zeta_m}{\zeta_m^2 + 1} - \frac{2\zeta_i}{\zeta_i^2 + 1} \right]$$

Solving these equations gives

$$A_m = -1.24 g$$

and

$$\tau = 0.958 \text{ msec}$$

The acceleration, velocity, displacement and shock spectrum for this waveform are plotted as Fig. 5.

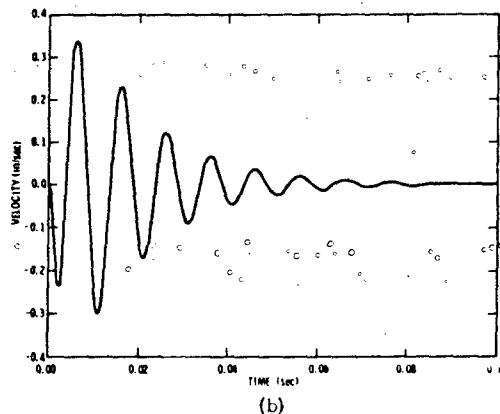
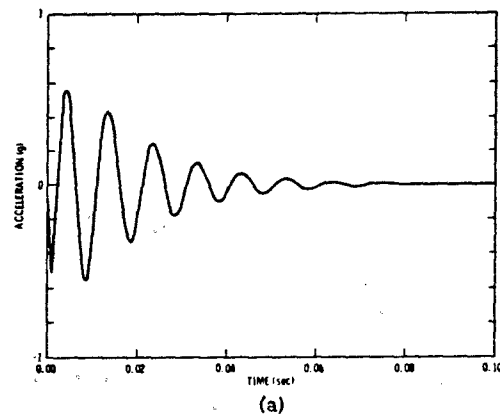
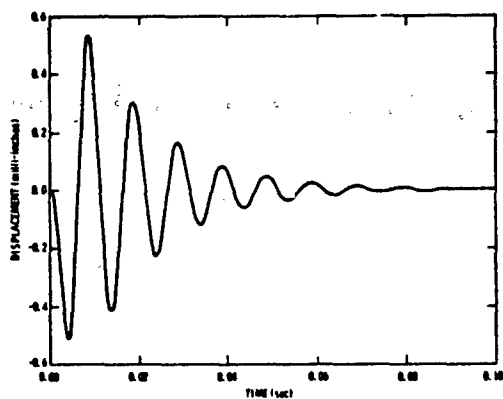
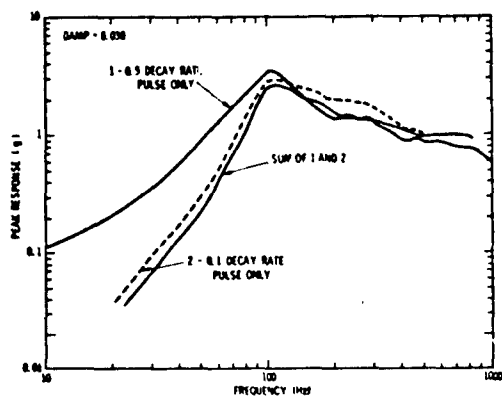


Fig. 5 - (Example 1) 100 Hz, 10% decay rate decaying sinusoid with a 100 Hz velocity compensating pulse



(c)



(d)

Fig. 5 - (Example 1) 100 Hz, 10% decay rate decaying sinusoid with a 100 Hz velocity compensating pulse

While a compensating pulse with the same frequency as the primary pulse can be used, the shock spectrum will be significantly distorted from that of the primary pulse alone. The velocity and displacement waveforms are quite symmetrical (i.e., the positive and negative peaks are approximately equal in amplitude and number) making efficient use of the shaker capabilities.

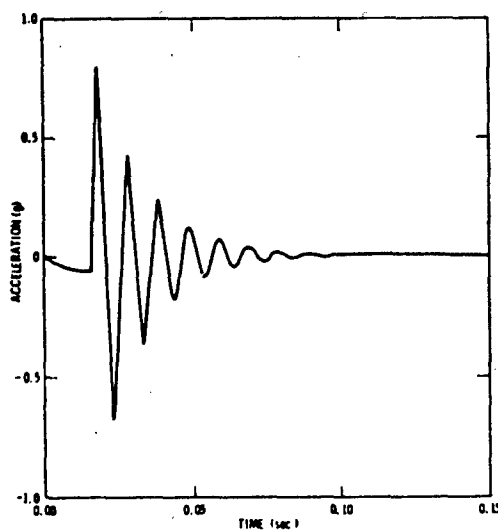
Example 2

Again, consider a 100 Hz, 10% decay rate, 1g decaying sinusoid. For compensation, a 10 Hz (one-tenth of the primary frequency), 100% decay rate pulse will be used. Solving Eqs. (5) and (6) gives

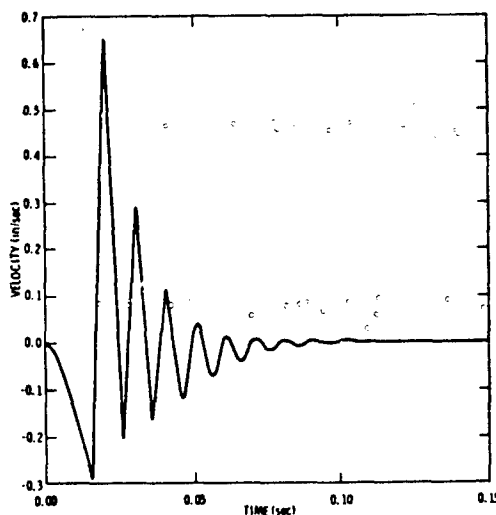
$$A_m = -0.198 \text{ g}$$

$$\tau = 0.0156 \text{ sec}$$

The acceleration, velocity, displacement, and shock spectrum are shown as Fig. 6. The



(a)



(b)

Fig. 6 - (Example 2) 100 Hz, 10% decay rate decaying sinusoid with a 10 Hz velocity compensating pulse

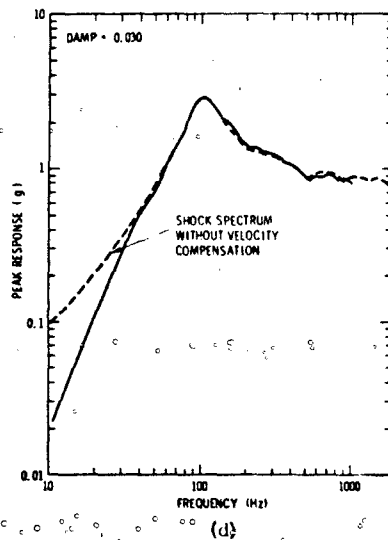
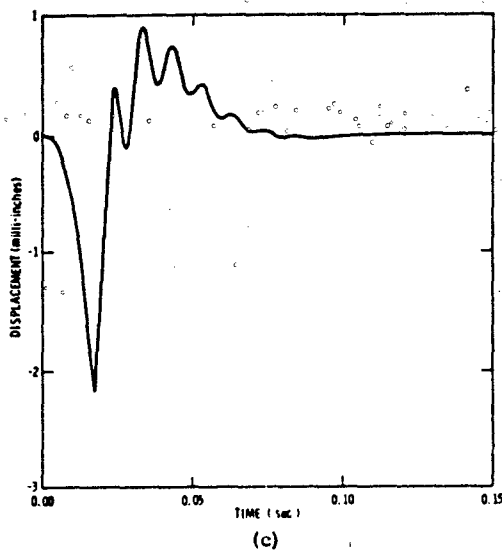


Fig. 6 - (Example 2) 100 Hz, 10% decay rate decaying sinusoid with a 10 Hz velocity compensating pulse

shock spectrum now shows little distortion above 30 Hz. This is a general result. The shock spectrum can usually be matched to a frequency extending down to about two to three times the compensating frequency. As the compensating frequency is lowered, the velocity and displacement requirements become

larger. In this example, the displacement requirements are six times the displacement required for Example 1. It is seen that a compromise can be reached, trading low-frequency performance for lower displacement and velocity requirements. This can be very useful when attempting to match a shock spectrum to as low a frequency as possible while remaining within the capability of a particular shaker system.

Example 3

In this case, a complex shock spectrum [6] will be matched by adding five decaying sinusoids and a compensating pulse. This example is included to illustrate the complexity of spectra which can be matched, and to show how the pulse can be tailored to give the maximum low-frequency performance while remaining within the capabilities of a shaker system. The assumed limits of the shaker system were 8 inches, peak-to-peak displacement and ± 100 in/sec. velocity. Three iterations were required to arrive at the waveform shown. The acceleration, velocity, displacement, and shock spectrum are shown as Fig. 7. The sinusoid components are given

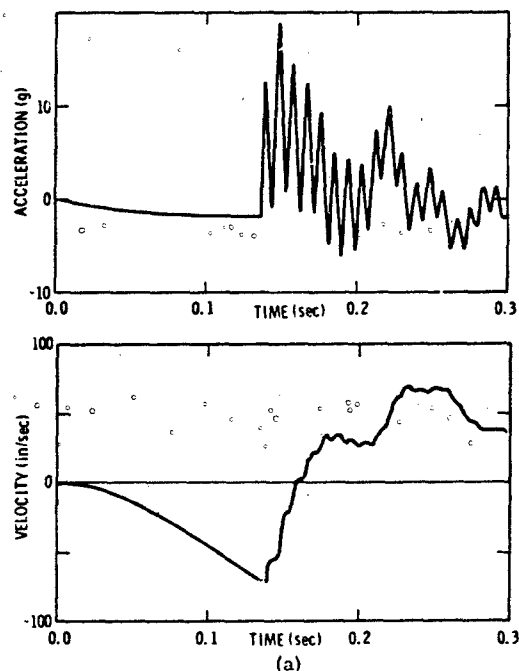


Fig. 7 - A complex shock spectrum matched with velocity compensated decaying sinusoids

in Table I. The acceleration and velocity waveforms will return to zero for times exceeding one second. An acceptable match of the shock spectrum is achieved down to 3 Hz.

Example 4

This example is included to illustrate how a shaker system will typically distort a waveform if compensation is not used. For this example, a single 40 Hz, 5% decay rate, 15 g decaying sinusoid will be shown as actually reproduced, using the techniques of LeBrun and Favour [4] on a slip table driven by an MB C220 shaker.

The pulse was reproduced in two forms - first, without compensation and, second, with a 10 Hz, 100% decay rate compensating pulse added. For the compensated pulse

$$A_m = -7.48 \text{ g}$$

$$\tau = 0.0155 \text{ sec.}$$

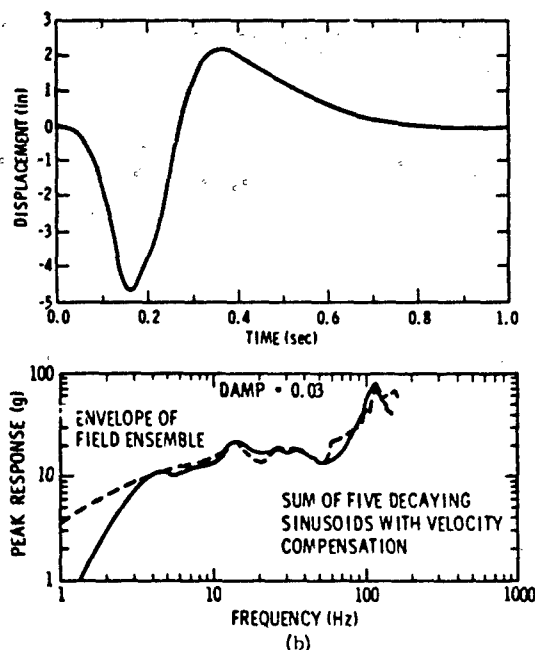


Fig. 7 - A complex shock spectrum matched with velocity compensated decaying sinusoids

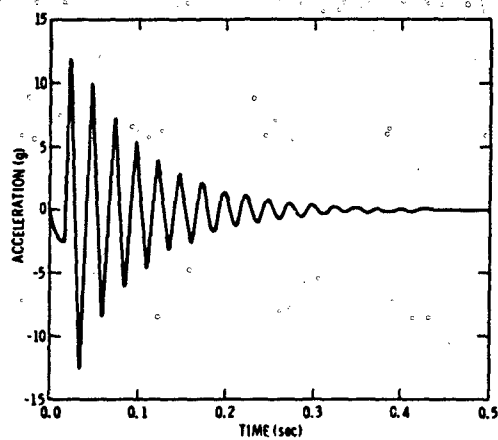
TABLE I
Components for Example 3

Freq. (Hz)	Decay Rate (ζ)	Amplitudes (g)	Delay (Sec)
1	1.0	-5.82	0
4	0.5	10	0.136
14	0.17	10	0.136
28	0.007	2	0.136
38	0.035	2	0.136
110	0.018	10	0.136

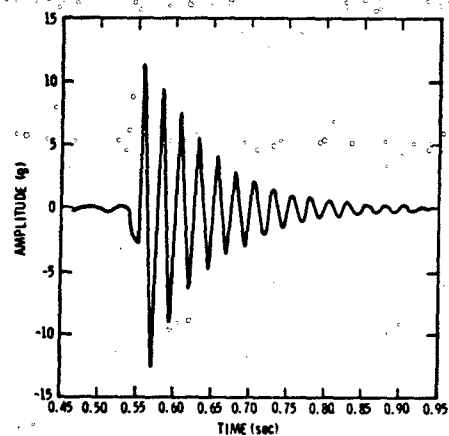
The results are shown as Figs. 8 and 9. The ideal or desired acceleration for each of two waveforms is shown on the left side of Fig. 8. The waveforms, as they were actually reproduced, are shown on the right. The ideal or desired displacements for each waveform were computed from Eq. (4) and are plotted on

the left of Fig. 9. These are the expected displacements if the acceleration time history is accurately reproduced.

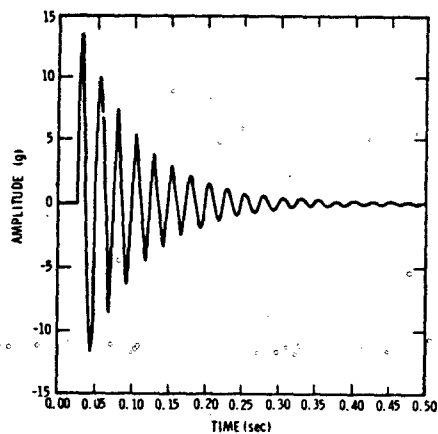
The actual table displacements, as measured with a displacement transducer, are on the right.



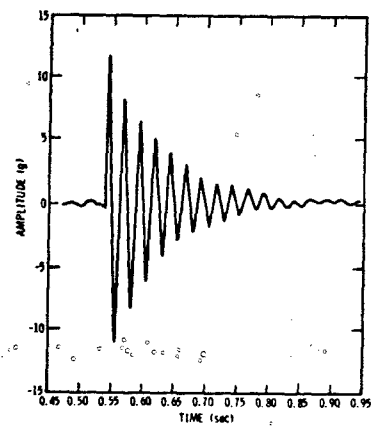
(a)
Desired Compensated
Acceleration



(b)
Actual Compensated
Acceleration

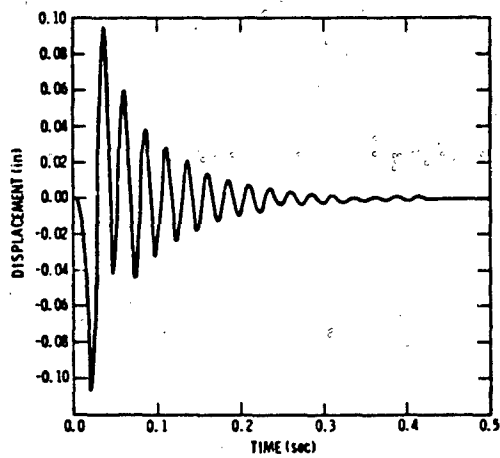


(c)
Desired Noncompensated
Acceleration

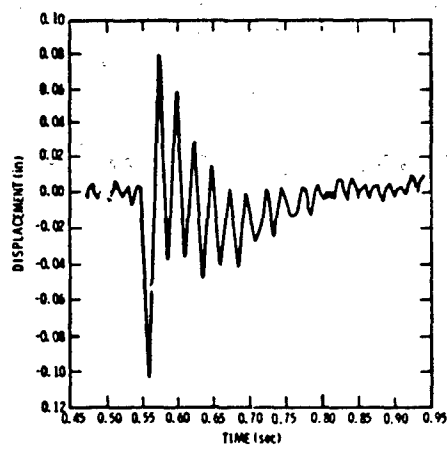


(d)
Actual Noncompensated
Acceleration

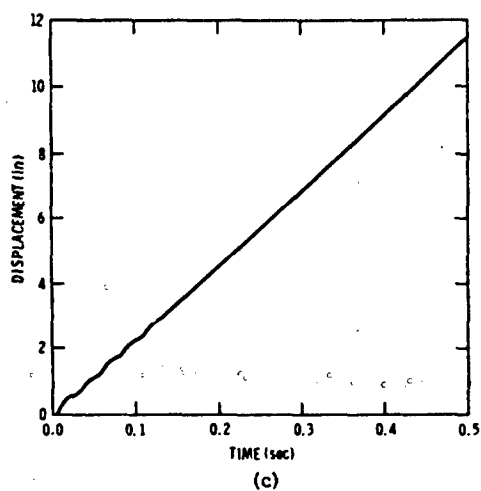
Fig. 8 - Desired and actual acceleration time histories
for Example 4



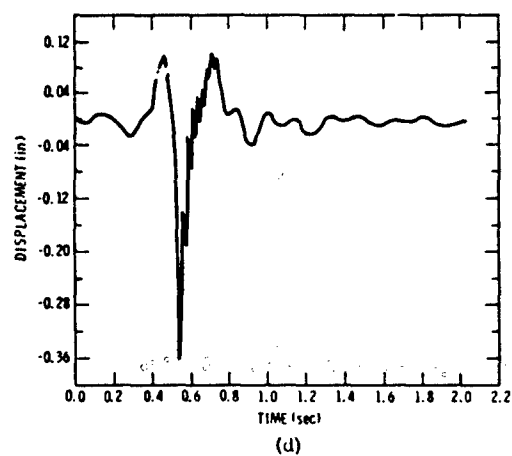
Desired Compensated
Displacement



Actual Compensated
Displacement



Desired Noncompensated
Displacement



Actual Noncompensated
Displacement

Fig. 9 - Desired and actual displacement time histories
for Example 4

The actual compensated acceleration waveform was quite close to the desired waveform. The actual noncompensated acceleration waveform was also quite close to the desired waveform except that the first few positive peaks were smaller than they should have been. This is the effect of the shaker acting as a high-pass filter and the flexure restoring force, removing the velocity and displacement changes. This observation is confirmed when the actual noncompensated displacement is examined. The theoretical noncompensated displacement becomes very large for large times, where the actual displacement returns to zero. The actual compensated displacement, while somewhat distorted, is very near the theoretical value. Thus, the objective of being able to predict the displacement requirements has been accomplished. The importance of this is reinforced by examining the results of a hypothetical 30 g experiment instead of the 15 g experiment. The noncompensated pulse would have required a displacement of 0.72 inch, exceeding the 0.5 inch limit of the shaker. The shaker armature would have driven into the mechanical stops, seriously distorting the pulse and abruptly ending the test. The compensated pulse would have required a displacement of 0.2 inch, well within the shaker capabilities. More importantly, the operator could have predicted the displacement requirements for the compensated pulse before the test and proceeded knowing that the displacement limits of the shaker would not be exceeded.

CONCLUSIONS

Several different methods for reproducing a shock spectrum on a shaker system are useful for different applications. One method which is useful for a large number of applications is the sum of several decaying sinusoids. A disadvantage of the decaying sinusoid method is a characteristic nonzero velocity and displacement change which makes the prediction of the velocity and displacement requirements difficult. A method has been demonstrated which will permit the determination of these requirements by modifying the basic waveform.

The modification can be easily implemented using digital methods.

REFERENCES

1. J. D. Crum and R. L. Grant, "Transient Pulse Development," Shock and Vibration Bulletin No. 41, Part 5, pp. 167-176, Dec. 1970.
2. G. W. Painter and H. J. Perry, "Simulating Flight Environment Shock on an Electrodynamic Shaker," Shock and Vibration Bulletin, No. 33, Part 3, pp. 85-96, Mar. 1964.
3. R. T. Fandrich, Jr., "Shock Pulse Time History Generator," Proceedings of the Institute of Environmental Sciences, pp. 31-36, 1969.
4. J. D. Favour, J. D. LeBrun, and J. P. Young, "Transient Waveform Control of Electromagnetic Test Equipment," Shock and Vibration Bulletin, No. 40, Part 2, pp. 157-172, 1969.
5. R. C. Yang and H. R. Saffell "Development of a Waveform Synthesis Technique - A Supplement to Response Spectrum as a Definition of Shock Environment," Shock and Vibration Bulletin, No. 42, Part 2, pp. 45-53, Jan. 1972.
6. D. O. Smallwood and A. F. Witte "The Use of Shaker-Optimized Periodic Transients in Matching Field Shock Spectra," Shock and Vibration Bulletin No. 43, Part 1, pp. 139-150, 1973.
7. D. B. Nelson and P. H. Prasthofer "A Case for Damped Oscillatory Excitation as a Natural Pyrotechnic Shock Simulation," Presented at the 44th Shock and Vibration Symposium Dec. 1973.
8. George J. O'Hara "Effect Upon Shock Spectra of the Dynamic Reaction of Structures," Proceeding of the Society for Experimental Stress Analysis Vol. 18, No. 1, pp. 145-151, May 1961.

APPENDIX A

Magnitude of the First Peak of a Decaying Sinusoid

Let a time history be defined by

$$a(t) = e^{-\zeta \omega t} \sin \omega t \quad t \geq 0 \quad (A-1)$$

To find the magnitude of the first peak differentiate Eq. (A-1) and set equal to zero.

$$\frac{da}{dt} = \omega e^{-\zeta \omega t} (\cos \omega t - \zeta \sin \omega t) .$$

$\frac{da}{dt}$ will be equal to zero whenever $\cos \omega t$

$$= \zeta \sin \omega t \text{ or } \omega t = \tan^{-1} \frac{1}{\zeta} . \quad (A-2)$$

The first peak will be for $0 \leq \omega t \leq \frac{\pi}{2}$.

Substituting ωt from Eq. (A-2) into (A-1) gives the magnitude of the first peak. The results are presented as Fig. A-1.

For small ζ , $A_{\max} \approx 1-1.57 \zeta$.

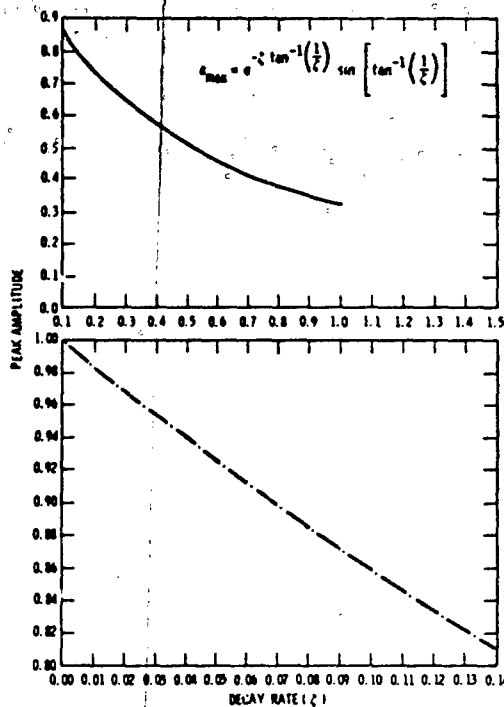


Fig. A-1 - Peak amplitude of a decaying sinusoid as a function of the decay rate

DISCUSSION

Mr. Forkoia (Naval Research Laboratory):

Wouldn't it be simpler to do portions of the spectrum in sequence, for example, in frequency bands of from 5 to 100 and 100 up to 500 etc., rather than trying to simulate the whole spectrum at once? It seems to me that you have an incomprehensible problem here.

Mr. Smallwood: I will admit that you can do this, but if you do it you have to justify it and that is perhaps the more difficult problem. It is not that difficult to match the shock spectrum over a quite wide frequency band, from 10 to 20 Hz up to 2000 Hz, on a electrodynamic shaker as long as you are within the limitations of the shaker system.

A CASE FOR DAMPED OSCILLATORY EXCITATION AS A NATURAL PYROTECHNIC SHOCK SIMULATION*

D. B. Nelson, P. H. Prasthofer
Sandia Laboratories
Livermore, California 94550

A rationale is established for using decaying oscillatory excitation to simulate a pyrotechnic environment. A methodology for specification suitable for use on electrodynamic exciters is developed. The advantages of this technique in relation to the various descriptors of shock severity are described and bounds are developed for the response. These concepts are illustrated with a numerical example.

NOMENCLATURE

$\{a\}$	Vector representation of system accelerations	$[\beta]$	$N \times 1$ matrix
a_i	Acceleration of the i^{th} system mass	$\delta(t)$	Dirac delta function defined as the unit strength impulse $\int \delta(t) dt = 1$
C_j	Modal damping coefficient	ξ	The fraction of critical damping of a single-degree-of-freedom oscillator
E	The infinite integral of the square of a function	$\{n\}$	Vector representation of generalized system modal motion variables
$G(f)$	The Fourier transform of $g(t)$	ω_n	Undamped natural radian frequency of a single-degree-of-freedom oscillator
$g(t)$	A real function of time		
$h(t)$	General system impulse response		
$[K]$	Diagonal stiffness matrix		
$[k]$	General stiffness matrix		
$[M]$	Diagonal mass matrix		
$[m]$	General mass matrix		
$[U]$	Matrix of system eigenvectors		
u_{ij}	The element occupying the position corresponding to the intersection of the j^{th} row and the i^{th} column of the matrix $[U]$		
$\{x\}$	Vector representation of system displacements		
$x(t)$	A general response		
$y(t)$	A general excitation		
$[\alpha]$	$N \times 1$ matrix		

INTRODUCTION

Pyrotechnic shocks occur in the operational environment of virtually all aerospace systems. Missile stage separations and detonations of explosive components, for instance, all impart shocks to the adjoining structures. Such a shock, which can generate very high-intensity local stress waves near its origin, is transmitted into the rest of the structure, inducing vibrational motion. Laboratory testing of components and substructures which are expected to encounter such excitation has been the subject of considerable research over the past several years. This research is motivated, at least in part, by the development of more sophisticated, and often more delicate, componentry. The test levels imposed on such systems by some test methods, e.g., unidirectional pulses, in order to provide a sufficient safety factor over the entire frequency range may result in unnecessary and sometimes

*This work was supported by the United States Atomic Energy Commission. Contract Number AT-(29-1)-789.

unattainable design requirements for the components as well as for the supporting structure.

Pyrotechnically induced environments experienced by substructures and components are often of such a nature that simulation and/or qualification testing using electrodynamic exciters is feasible. The induced shock is usually a transient oscillation lasting less than a second, with structurally damaging energy concentrated in the working frequency range of most vibration exciters. Much attention has been focused upon characterizing this type of shock so that a meaningful test specification may be derived. There is much controversy related to the traditional use of the shock response spectrum (SRS) versus the energy spectral density (ESD) as an indicator of the shock severity and as an environmental descriptor for shock test specifications. Exclusive use of these descriptors for shock test specifications has resulted in the development of test techniques which employ excitation which neither resembles the actual environment nor, in many cases, adequately excites the test specimen. Some of these techniques, in fact, often result in severe overtesting. The attendant frustration has led to the development of very sophisticated methods whereby a shock signature may be specified and achieved on electrodynamic exciters. [1,2] Other methods combine oscillatory functions of one form or another with the SRS or ESD of the resultant acceleration as the test criterion. The particular waveforms specified by various test laboratories include reproduction of actual field data, [1,2] waveforms derived from the inverse Fourier transform of an ESD envelope, [3] and superpositions of modulated oscillatory functions. [4-7]

In this paper a case is developed for specifying a superposition of exponentially decaying oscillatory waveforms as excitation of the exciter-specimen system with either the SRS or ESD of the resultant acceleration as the accompanying spectral descriptor. Significant features of the technique, which has been routinely used at Sandia Laboratories for the past two years, are as follows:

1. If the ESD or the undamped SRS of the recommended excitation envelops the corresponding description of the environment, it is guaranteed that the "energy" of the response of all system parts will be at least as great as that experienced in the field.
2. If the excitation of the exciter-specimen system is judiciously

chosen, a reasonable bound exists on the maximum system response.

3. The excitation may be specified in a straightforward manner using existing spectral descriptors.
4. Sophisticated generation and equalization equipment is useful but not required.

SPECTRAL DESCRIPTORS

An indication of the severity of shock excitation has been classically expressed by the SRS. The SRS has great appeal because of the intuition it imparts to the analyst about the physical effect of the shock. Much of the controversy regarding its use has focused on the proper range of its applicability. The SRS in a rigorous sense applies only to structures that can be modeled as single-degree-of-freedom (SDF) systems. If the natural frequency of the structure is not known, as is generally the case, then by choosing a test waveform whose SRS envelops that of the field data over the frequency range of interest one is guaranteed that the peak response of this SDF system model to the laboratory test will be higher than that due to the field environment, no matter what its natural frequency may be. These conclusions are not valid, however, if the structure is multi-degree-of-freedom; this is easily demonstrated by modal analysis techniques.

Consider the undamped description of a multi-degree-of-freedom structure excited at its base given by

$$[m]\{\ddot{x}\} + [k]\{x\} = [\alpha] y(t) \quad (1)$$

where $y(t)$ is the base displacement. Differentiating twice and letting $\{a\} = \{\ddot{x}\}$ one obtains Equation (2)

$$[m]\{\ddot{a}\} + [k]\{a\} = [\alpha] \ddot{y}(t) \quad (2)$$

where $\ddot{y}(t)$ is the base acceleration. Equation (2) may be subjected to a transformation to modal coordinates [8]; i.e., let

$$\{a\} = [U]\{\eta\} \quad (3)$$

where the columns of $[U]$ are the system eigenvectors. Premultiplication by $[U]^T$ yields the uncoupled (diagonalized) description of the system given by Equation (4).

$$[M] \{\ddot{\eta}\} + [K] \{\eta\} = [\beta] \ddot{y}(t) \quad (4)$$

If it can be assumed that $[\beta]$ is the same for the laboratory test as for the expected field environment, then by enveloping the SRS of the environment with that of the test input motion one is guaranteed that the peak response of each modal variable η_j to the laboratory excitation will be at least as great as to the measured field excitation. Let the modal responses due to the environment be called η_j and those from the test v_j . If the test SRS envelops the environment SRS, it is clear that

$$\max |v_j| \geq \max |\eta_j| \quad \text{for all } j \quad (5)$$

The acceleration response of the j^{th} mass in the N-degree-of-freedom system may be expressed in terms of the modal coordinates as

$$a_{je} = \sum_{j=1}^N u_j \eta_j \quad \text{for the environment}$$

and

$$a_{jt} = \sum_{j=1}^N u_j v_j \quad \text{for the test}$$

To assure that the peak response of each mass in the test be at least as great as the response to the field environment, it is required that

$$\max |a_{jt}| \geq \max |a_{je}| \quad (6)$$

or

$$\max \left| \sum_{j=1}^N u_j v_j \right| \geq \max \left| \sum_{j=1}^N u_j \eta_j \right| \quad (7)$$

This, however, is not guaranteed by merely satisfying the inequality shown in Equation (5); i.e., the condition that the maxima of all the individual v_j exceed the maxima of the individual η_j does not imply that their sum does the same, since, in general, the maxima of the η_j , as well as of the v_j , do not occur at the same time. Therefore, an arbitrary test method enveloping a specified SRS does not guarantee that the system will be adequately tested.

A more definite statement concerning the response of a system to a test may be made if the ESD or the residual undamped SRS of the excitation closely envelops the corresponding spectral descriptor of the expected or measured environment. The ESD of a function $g(t)$ is defined in terms of the corresponding Fourier

transform $G(f)$. If the Fourier transform pair is defined as

$$\begin{aligned} G(f) &= \int_{-\infty}^{\infty} g(t) e^{-i2\pi ft} dt \\ g(t) &= \int_{-\infty}^{\infty} G(f) e^{+i2\pi ft} df \end{aligned} \quad (8)$$

the "energy" is

$$E = \int_{-\infty}^{\infty} g^2(t) dt \quad (9)$$

and, by Rayleigh's Theorem [9], may be expressed in terms of $G(f)$ as

$$E = \int_{-\infty}^{\infty} |G(f)|^2 df \quad (10)$$

The squared magnitude of $G(f)$ is called the two-sided energy spectral density and since the Fourier transform of a real function exhibits Hermitian symmetry, i.e., $G(f) = G^*(-f)$, $|G(-f)| = |G(f)|$, it is symmetric about $f = 0$. Thus only the values for positive frequency need be considered, which results in the alternate representation for the energy.

$$E = \int_0^{\infty} 2|G(f)|^2 df \quad (11)$$

where $2|G(f)|^2$ is commonly called the one-sided energy spectral density.

The response $x(t)$ of any particular variable of a linear, multi-degree-of-freedom structure to an excitation $y(t)$ is given by the convolution

$$x(t) = h(t) * y(t) \equiv \int_0^t h(\tau) y(t - \tau) d\tau \quad (12)$$

The Fourier transform of Equation (12) is

$$X(f) = H(f) Y(f) \quad (13)$$

and the response "energy" is

$$E = \int_{-\infty}^{\infty} x^2(t) dt = \int_{-\infty}^{\infty} |X(f)|^2 df \quad (14)$$

Substitution for $X(f)$ yields

$$E = \int_{-\infty}^{\infty} |H(f)|^2 |Y(f)|^2 df \quad (15)$$

If another excitation $u(t)$ is chosen so that the corresponding ESD envelopes $|Y(f)|^2$ for all f , i. e.,

$$|U(f)|^2 = |Y(f)|^2 \quad (16)$$

and if $H(f)$ can be considered constant, the "energy" of the response to the excitation $u(t)$ will be at least as great as the response to $x(t)$. This guarantee applies to any motion variable, thus assuring adequate testing of the system in terms of response "energy." Note that no restriction has been made on the order of the system. The only necessary assumptions are that the system is linear and that $H(f)$ is the same for the test as for the environment. The latter is hardly ever completely true but is usually presumed to be so.

The Fourier transform from which the ESD is determined is intimately related to the zero-damped residual SRS. The impulse response of a zero-damped, SDF oscillator is $\omega_n \sin \omega_n t$ for $t > 0$. Consider, once again, an excitation $y(t)$ which causes a response $x(t)$; i. e.,

$$x(t) = y(t) * \omega_n \sin \omega_n t \quad (17)$$

Now, as far as $x(t)$ is concerned, the right-hand side of Equation (17) could represent a system described by the impulse response function $y(t)$, excited by a sine function of frequency $\omega_n = 2\pi f_n$. The steady state solution of such an equation is

$$y_{ss}(t) = \omega_n |X(f_n)| \sin(\omega_n t + \phi) \quad (18)$$

where $X(f_n)$ is the Fourier transform of the function $x(t)$ evaluated at the excitation frequency. The steady state peak, and also the peak of the residual SRS, is then

$$\max |y_{ss}(t)| = \omega_n |X(f_n)| \quad (19)$$

Therefore, it is entirely equivalent to specify a test excitation so that either the ESD or the residual undamped SRS is enveloped. In fact, since the maxi-max SRS is always at least as great or greater than the residual SRS, enveloping the maxi-max undamped SRS guarantees enveloping of the residual undamped SRS. This, in turn, assures the energy bound on the response (albeit more conservative) developed for the ESD envelope. The use of the undamped

SRS in all cases is significant, in that enveloping a damped SRS does not guarantee that the corresponding undamped spectrum will also be enveloped.

The envelope criteria outlined above are not completely adequate as environmental descriptors or as specifications for laboratory testing. Neither the SRS nor the ESD embodies the element of time to the extent that a completely satisfactory restriction is imposed on the duration of the excitation. Some measure of this duration, however, can be ascertained from the local ratio of the undamped to damped SRS. The response of a damped oscillator to a bounded input always has a finite bound. For example, the peak response of a damped oscillator to a unit amplitude sine function whose frequency corresponds to the resonant frequency of the oscillator is $1/2 \zeta$. This response level, once it has been reached, is then independent of any additional time duration of the forcing function. On the other hand, the peak response of an undamped oscillator to a sympathetic input always increases with the duration of the input. Thus, the longer the input, the greater the response of the oscillator. If one then notes the ratio of damped to undamped SRS levels, an estimate of the time duration of the input may be obtained. Hence, a dual specification of some sort is required.

If the test method can be restricted so that the excitation is a superposition of decaying oscillations, control of the test duration as well as the spectrum can be maintained. Furthermore, the resulting response acceleration signatures are reminiscent of those commonly observed when the environment is pyrotechnically induced. This is not coincidental, however, since most structures respond naturally in this manner to impulsive excitation.

STRUCTURAL RESPONSE

Pyrotechnic shocks are commonly modeled as impulsive forcing functions, since the duration of excitation is usually much less than the response times of structural components. When multi-degree-of-freedom structures are impulsively loaded, all vibrational modes are excited with an intensity which depends on the energy transmission properties of the structure. The higher-frequency energy (that above a few kHz) is usually found to affect only those components near the pyrotechnic event, thus eliminating

it from consideration in many system vibration models. Hence, a finite, linear, lumped-element model of relatively low order is often a very good approximation of mechanical system behavior.

The system of differential equations written in matrix form for an N-degree-of-freedom model with no damping and impulsive loading is given by Equation (20) in terms of the vector variable $\{x\}$ which represents the displacements of the model masses.

$$[m]\ddot{x} + [k]x = [o] \delta(t) \quad (20)$$

where $[m]$ and $[k]$ are $N \times N$, $[o]$ is $N \times 1$, and $\delta(t)$ is the Dirac "delta function" representing an impulsive force.

A transformation to modal coordinates, i.e., $\{x\} = [U]\{\eta\}$, yields

$$[M]\ddot{\eta} + [K]\eta = [\beta] \delta(t) \quad (21)$$

where $[M]$ and $[K]$ are now diagonal $N \times N$ matrices. The matrix $[\beta]$ is $N \times 1$ and $\{\eta\}$ is the transformed displacement vector. Introducing damping into the system via the modal equations yields N equations of the form,

$$M_j \ddot{\eta}_j + C_j \dot{\eta}_j + K_j \eta_j = \beta_j \delta(t) \quad (22)$$

The solution of Equation (22), with zero initial conditions, is given by Equation (23)

$$\eta_j = A_j e^{-\gamma_j t} \sin(\omega_j t)$$

where $\gamma_j = \frac{C_j}{2M_j}$ and $\omega_j^2 = \frac{K_j}{M_j} - \gamma_j^2$ (23)

Thus, the displacement of the j^{th} mass in the system model is a linear combination of the modal displacements; i.e., from $\{x\} = [U]\{\eta\}$, one obtains

$$x_j = \sum_{j=1}^N u_{j,j} \eta_j \quad (24)$$

Substitution of Equation (23) yields

$$x_j = \sum_{j=1}^N u_{j,j} A_j e^{-\gamma_j t} \sin \omega_j t \quad (25)$$

which is a superposition of N exponentially decaying sinusoids. The corresponding acceleration \ddot{x}_j is, by two differentiations of Equation (25),

$$\ddot{x}_j = \sum_{j=1}^N u_{j,j} A_j \left[(\gamma_j^2 - \omega_j^2) \sin \omega_j t - 2\gamma_j \omega_j \cos \omega_j t \right] e^{-\gamma_j t} \quad (26)$$

which, for the case of light damping where $\gamma \ll \omega$, is also approximately a superposition of decaying sinusoids.

It is interesting to note that for this idealized case of light damping and uncoupled modes, the response is made up of decaying sinusoids that are either in phase or exactly out of phase, depending on whether the $u_{j,j}$ coefficient is positive or negative. Thus excitation consisting of a superposition of decaying oscillatory functions as a transient vibration test of substructures or components which are expected to experience pyrotechnically (impulsively) induced environments appears to be a natural choice. Furthermore the ESD and the SRS of functions in this class are such that reasonably detailed spectral shaping may be achieved.

RESPONSE BOUND

Specification of oscillatory excitation with a decay rate approximating that of the expected or measured environment provides some assurance that no part of the system will be severely overtested. The response $x(t)$ of any particular linear system variable to an excitation $y(t)$ may again be written as the convolution

$$x(t) = h(t) * y(t) \quad (27)$$

where $h(t)$ is the impulse response corresponding to the variable of interest. If the impulse response and the excitation are of exponential order, i.e.,

$$|h(t)| \leq M_1 e^{-\alpha t} \quad (28)$$

and

$$|y(t)| \leq M_2 e^{-\beta t} \quad (29)$$

then the magnitude of $x(t)$ is bounded; i. e.,

$$|x(t)| = \left| \int_0^t h(\tau) y(t-\tau) d\tau \right| \leq \int_0^t |h(\tau)| |y(t-\tau)| d\tau = B(t) \quad (30)$$

where

$$B(t) = \int_0^t M_1 e^{-\alpha\tau} M_2 e^{-\beta(t-\tau)} d\tau \quad (31)$$

Carrying out the indicated integration yields

$$B(t) = \frac{M_1 M_2}{(\beta - \alpha)} (e^{-\alpha t} - e^{-\beta t}) \quad (32)$$

Hence if the environment is known to be of exponential order and if the test excitation is specified to be of approximately the same order, the system response to the test will be bounded by the same value as the response to the environment. The maximum value of this bound B_M is found to be

$$B_M = \frac{M_1 M_2}{\beta} \exp \left(-\frac{\alpha \beta}{1 - \frac{\alpha}{\beta}} \right) \quad (33)$$

and is plotted versus the ratio $\frac{\alpha}{\beta}$ in Figure 1.

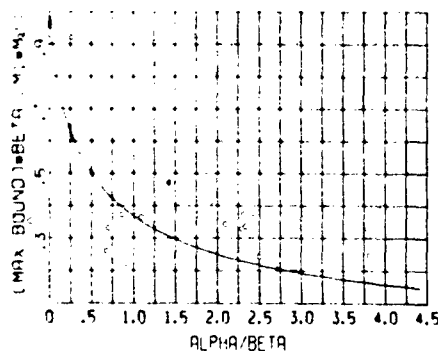


Figure 1. Normalized Bound on the Response of a System of Exponential Order α When the Excitation is of Exponential Order β

As an example of the utility of this bound, assume a 5 percent damped SRS oscillator is excited at its base by a damped sine acceleration with a 2 percent decay rate, unit amplitude, and a frequency equal to the undamped natural frequency of the oscillator. The impulse response of the oscillator is approximately

$$h(t) = \omega_1 e^{-0.05\omega_n t} \sin \omega_1 t \quad (34)$$

and the excitation may be formulated as

$$y(t) = e^{-0.02\omega_n t} \sin \omega_2 t \quad (35)$$

where $\omega_1 \approx \omega_2 \approx \omega_n$. With $\alpha = 0.05\omega_n$ and $\beta = 0.02\omega_n$, Equation (33) yields a value of B_M of 10.8 g's, whereas the actual peak response is about 5.5 g's. For this very simple example, a better bound is $\frac{\omega_n}{2\alpha} = 10$, which is the peak response to an undamped excitation. However, the bound of 10.8 g's is valid for any excitation satisfying the inequality

$$|y(t)| \leq e^{-0.02\omega_n t} \quad (36)$$

irrespective of the waveform complexity.

WAVEFORM CHARACTERISTICS

It is recognized that a damped sinusoid of strict mathematical form is neither a realizable acceleration specification for limited displacement equipment nor a good candidate for excitation of a vibration exciter. However, with a few minor modifications it becomes quite acceptable for either. The classical form of the damped sinusoid is given by the Laplace transform pair

$$F(s) = \frac{A\omega}{(s+c)^2 + \omega^2} \quad (37)$$

$$f(t) = A e^{-\zeta\omega_n t} \sin \omega t$$

where

$$0 \leq \zeta < 1$$

$$\omega = \omega_n \sqrt{1 - \zeta^2}$$

$$c = \zeta\omega_n$$

The infinite integral of $f(t)$ is clearly nonzero; therefore, as an acceleration specification it results in a residual velocity. Furthermore, there is significant energy in the low-frequency region of the corresponding spectrum which results in sometimes unwanted stimulation of low-frequency exciter-specimen resonances if $f(t)$ is used as excitation of the exciter amplifier.

A natural set of conditions when electrodynamic exciters are used is that initial and final values of table acceleration, velocity, and displacement be zero; i.e.,

$$\begin{aligned} \lim_{t \rightarrow 0} a(t) &= 0 \\ \lim_{t \rightarrow \infty} a(t) &= 0 \\ \lim_{t \rightarrow 0} v(t) &= \lim_{t \rightarrow \infty} \int_0^t a(\tau) d\tau = 0 \\ \lim_{t \rightarrow 0} d(t) &= \lim_{t \rightarrow \infty} \int_0^t v(\tau) d\tau = 0 \end{aligned} \quad (38)$$

If the Laplace transform of $a(t)$ is $A(s)$, the initial and final conditions may be interpreted in terms of the initial and final value theorems; i.e., if

$$A(s) = \int_0^\infty e^{-st} a(t) dt \quad (39)$$

then

$$\begin{aligned} \lim_{s \rightarrow \infty} sA(s) &= 0 \\ \lim_{s \rightarrow 0} sA(s) &= 0 \\ \lim_{s \rightarrow \infty} sV(s) &= \lim_{s \rightarrow 0} s \frac{A(s)}{s} = 0 \\ \lim_{s \rightarrow 0} sD(s) &= \lim_{s \rightarrow 0} s \frac{A(s)}{s^2} = 0 \end{aligned} \quad (40)$$

Satisfaction of these equalities demands that $A(s)$ contain a numerator factor s^2 and a denominator polynomial of at least fourth order

with no poles at the origin. A Laplace transform representation [10] satisfying the above conditions is

$$A(s) = \frac{s^2}{(s+a)(s+b)} \cdot \frac{A\omega}{(s+c)^2 + \omega^2} \quad (41)$$

which may be inverted to yield

$$\begin{aligned} a(t) &= A\omega \left\{ \frac{a^2 e^{-at}}{(a-b)[(c-a)^2 + \omega^2]} \right. \\ &\quad \left. - \frac{b^2 e^{-bt}}{(a-b)[(c-b)^2 + \omega^2]} \right\} \\ &\quad + A \sqrt{\frac{(c^2 - \omega^2)^2 + 4c^2 \omega^2}{[(b-c)^2 + \omega^2][(a-c)^2 + \omega^2]}} \\ &\quad \cdot e^{-ct} \sin(\omega t + \phi) \end{aligned} \quad (42)$$

where

$$\phi = \tan^{-1}\left(\frac{-2c\omega}{c^2 - \omega^2}\right) - \tan^{-1}\left(\frac{\omega}{a-c}\right) - \tan^{-1}\left(\frac{\omega}{b-c}\right)$$

The function $a(t)$ in Equation (42) is the sum of a damped sinusoid and an overdamped type of function with parameters which automatically guarantee that the initial and final conditions of the motion variables are zero. Hence, the selection of the parameters (a , b , c , and ω) is somewhat arbitrary. However, the idea is to create a damped oscillation approximating a damped sinusoid, which is realized if $c = \xi\omega_n$ and $\omega = \omega_n \sqrt{1 - \xi^2}$, where ω_n and ξ are the so-called undamped natural frequency and damping factors, respectively, of the classical damped sine function. Then convenient choices of "a" and "b" are

$a = \frac{\omega_n}{2\pi}$ and $b = 2\xi\omega_n$ which cause the overdamped function to last about half as long as the oscillation and to have most of its effect on the velocity and displacement variables in the first cycle or two of the oscillation. A plot of the waveform with frequency normalized to 1 Hz and $\xi = 0.05$ is shown in Figure 2. Note that the first negative peak is greater in magnitude than the first positive peak but that the waveform, in most respects, closely resembles a classical damped sinusoid.

A superposition of the functions described in Equation (42) is thus a reasonable

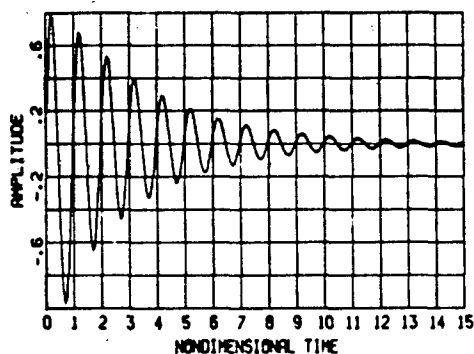


Figure 2. Unit Amplitude Proposed Oscillatory Waveform With $\zeta = 0.05$ Decay

choice for a transient acceleration specification. If automatic control equipment is available, such a waveform could be caused to exist at the exciter table. Systems including this capability of equalization, representing the "ultimate" in transient vibration testing, have been developed [1, 2] and are commercially available. In the absence of such equipment, however, one is faced with having to deal with the transfer function of the exciter-specimen combination and must somehow tailor the input waveform to achieve the required acceleration.

If, rather than an acceleration signature, the SRS or ESD of the acceleration is specified, a superposition of functions of the form given by Equation (42) may be used as the input voltage to the exciter amplifier. For reasonably linear systems, the amplitude of each component waveform may be adjusted independently at a low test level to achieve a desired peak acceleration. The subsequent superposition may then be fine-tuned so that a properly tailored spectral descriptor is obtained. As will be shown, this may require adjustment of the relative signs of the component waveforms. Since five or fewer components are usually adequate for a given specification, this is not an inordinate requirement.

Other decaying oscillatory functions could be used as excitation voltage, e.g., a pure damped sine function or variations of it, but that given by Equation (42) is particularly well-suited to electrodynamic exciters. As will be illustrated, the energy in the low-frequency region is extremely low, thus minimizing the excitation of the resonance due to the combination of the total mass and the exciter flexures. This feature allows higher peak g levels to be achieved at mid- and upper-range frequencies on a given exciter system.

RELATION OF OSCILLATORY WAVEFORMS TO SPECTRAL DESCRIPTORS

The 5 percent damped SRS of the decaying oscillatory waveform given by Equation (42) is shown in Figure 3. Normalized amplification versus normalized frequency is displayed for decay rates of $\zeta = 0.02, 0.05$ and 0.10 . Several features of the SRS are worth noting. In contrast to the shock response spectra of unidirectional pulses which exhibit a significant response over a wide frequency band, the response spectra of Figure 3 are prominent in the vicinity of the frequency of the oscillation and are significantly lower in the structurally damaging, low-frequency region. The response amplification, as one might expect, increases with decreasing decay rate and also becomes more "peaked." The SRS is almost identical to that of a pure decaying sinusoid, which demonstrates the relative insensitivity of the SRS to nonfundamental differences in the formulation of exponentially decaying oscillatory driving functions.

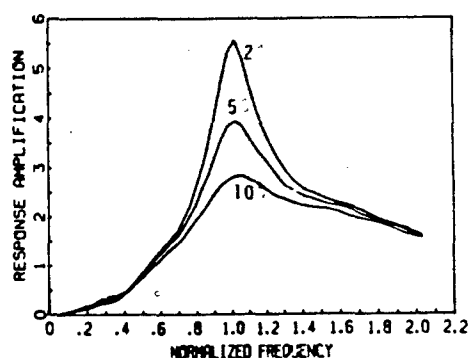


Figure 3. Shock Response Spectrum (5% Damping) of Oscillatory Waveform Shown in Figure 1 With $\zeta = 0.02, 0.05$, and 0.10 Decay

The ESD's of the function of Equation (42) for $\zeta = 0.02, 0.05$, and 0.10 and $\omega = 2\pi \cdot 1$ are shown in Figure 4 and illustrate the manner in which the energy is concentrated in the frequency domain. The ratio of the $\zeta = 0.02$ peak to the $\zeta = 0.10$ peak is 25, as for a damped sine function, but there is a conspicuous absence of energy in the low-frequency region. This is due to the high-pass filtering effect of the factor $\frac{s^2}{(s+a)(s+b)}$ in the Laplace transform representation of Equation (41).

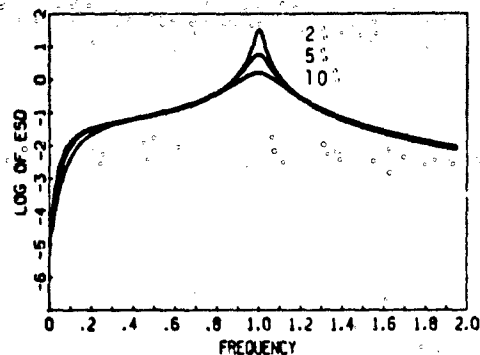


Figure 4. Energy Spectral Density of Oscillatory Waveform Shown in Figure 1 With $\xi = 0.02, 0.05$, and 0.10 Decay

Since most specifications involve a superposition of functions, it is necessary to consider the effect of interaction of the component waveforms on the spectral descriptors. Waveforms consisting of two unit amplitude components of normalized frequencies $f_1 = 1$ and $f_2 = 1.5$ with decay rates of $\xi = 0.05$ are shown added in Figure 5 and subtracted in Figure 6. The shock response spectra of the added and subtracted composite excitations are shown in Figure 7. The in-phase composite exhibits two distinct peaks at the component frequencies. In contrast, the out-of-phase composite exhibits a higher level in the frequency range between the two component frequencies, while displaying a lower response for frequencies less than f_1 and greater than f_2 .

These properties of the SRS are most easily explained in terms of the ESD of a damped sine function. The Fourier transform of a damped sine function

$$g(t) = A e^{-\xi \omega_n t} \sin(\sqrt{1 - \xi^2} 2\pi f_n t) \quad (43)$$

in terms of the normalized frequency $f_r = \frac{f}{f_n}$ is

$$G(f_r) = \frac{A \sqrt{1 - \xi^2}}{2\pi f_n} \frac{(1 - f_r^2) - i 2\xi f_r}{(1 - f_r^2)^2 + 4\xi^2 f_r^2} \quad (44)$$

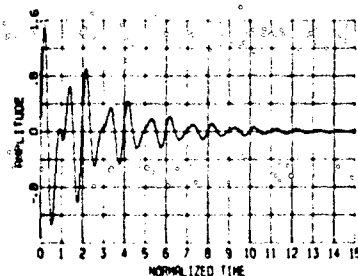


Figure 5. Superposition of Two Unit Amplitude Waveforms of Frequencies f_1 and $1.5 f_1$ When Added

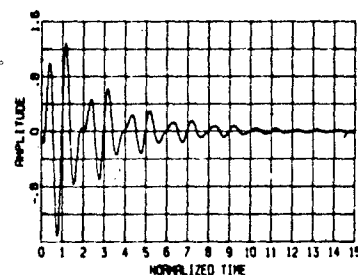


Figure 6. Superposition of Two Unit Amplitude, $\xi = 0.05$ Oscillatory Waveforms of Frequencies f_1 and $1.5 f_1$ When Subtracted

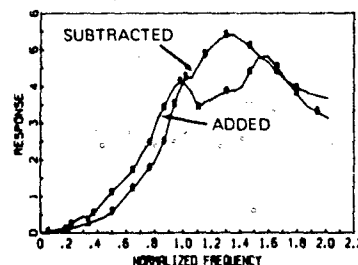


Figure 7. Five Percent Damped Shock Response Spectrum of the Superposition of Two Unit Amplitude Waveforms of Frequencies f_1 and $1.5 f_1$, When the Components Are Either Added (A) or Subtracted (S)

The real and imaginary parts of $G(f_r)$ are shown in Figure 8 for positive values of f_r . Note that the imaginary part is much more localized on the frequency axis than is the real part and also that the real part experiences a

sign change at $f_n = 1$, while the imaginary part is always negative.

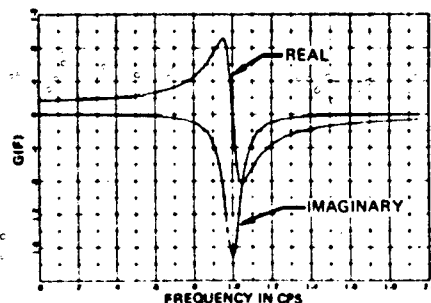


Figure 8. Real and Imaginary Parts of the Fourier Spectrum of a Decaying Sinusoid

The ESD of the sum of two damped sine functions with natural frequencies f_1 and f_2 is

$$|G(f)|^2 = [\text{Re}\{G_1(f)\} + \text{Re}\{G_2(f)\}]^2 + [\text{Im}\{G_1(f)\} + \text{Im}\{G_2(f)\}]^2 \quad (45)$$

where $G_1(f)$ and $G_2(f)$ are each of the form shown in Equation (44). Therefore, the superposition of two damped sine functions sufficiently separated in frequency so that the imaginary parts do not interact, but within the range where the real parts are significant, has quite different effects in the region $f_1 < f < f_2$, depending on the respective signs.

The ESD of the superposition is shown in Figure 9. Except in the region of the peaks, the difference in the curves is much more drastic than for the corresponding shock response spectra shown in Figure 6. In fact, for the 5 percent damped SRS representation the shape of the two spectra is distinctly different, yet both fall within the ± 3 dB (+41%, -29%) commonly allowed for in test specifications. This is not true, however, in the case of the ESD, which exhibits a 15 dB difference in the region between the peaks for the two cases. Thus if the ESD or the equivalent residual undamped SRS is to be used as a test criterion, more attention must be directed toward attaining the proper phase (sign) relationship between component waveform, or more relaxed tolerances must be allowed.

If the spectrum to be enveloped is very peaked in nature, it is natural to select a superposition of in-phase waveforms, as these tend

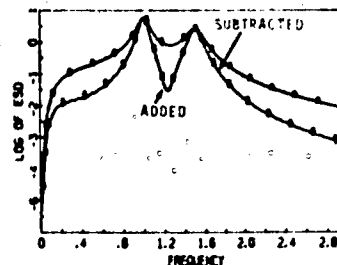


Figure 9. Energy Spectral Density of the Superposition of Two Unit Amplitude Oscillatory Waveforms of Frequencies f_1 and $1.5 f_1$ When the Components Are Either Added (A) or Subtracted (S)

to accentuate the peaks and valleys of the frequency spectrum. If, on the other hand, the spectrum is broad, a synthesis of component waveforms combined alternately in and out of phase becomes the natural choice, as this method of combination tends to smear out the local character of the spectrum. It is particularly significant, however, that, unlike the single-sided pulses, either the inphase or the alternating in- and out-of-phase combination results in very little energy in the low frequency region.

MECHANICS OF SPECIFICATION

A test excitation specification of a composite of decaying oscillatory functions may be approximated from the properties of the damped sine function and its Fourier transform. The maximum of the one-sided ESD of a damped sine function is

$$\max [|G(f)|^2] = \frac{1}{2} \left(\frac{A}{\zeta 2\pi f_n} \right)^2 \quad (46)$$

and occurs at the frequency

$$f_m = f_n \sqrt{1 - 2\zeta^2} \quad (47)$$

The so-called half-power bandwidth where the ESD is one half its maximum is approximately

$$B_{1/2} \approx 2\zeta f_m \quad (48)$$

Thus measurements from the ESD are sufficient to determine A , ζ , and f_n . The procedure is as follows:

1. Determine f_m from the ESD as the frequency at which a dominant peak occurs.
2. Determine ζ from Equation (48) by measuring the bandwidth between points where the ESD is half its peak value.
3. Determine f_n from Equation (47) (f_m is usually a very good approximation).
4. Determine A from Equation (46) being sure that the ESD is the "one-sided" version.

EXAMPLE

The system chosen to demonstrate the shock specification technique is shown in Figure 10. It consists of a three-degree-of-freedom substructure contained within a conically shaped parent structure. The parent was chosen to be a 30-inch truncated aluminum cone with a wall thickness of 0.25 inch and end diameters of 20 and 6 inches. The parameters of an approximate lumped element model for axial loading may be derived by dividing the cone into six segments and calculating the equivalent mass and axial spring rate for each section from Equations (49) and (50).

$$K_i = \frac{EA_i}{L_i} \quad (49)$$

$$M_i = \rho D_i t L_i \quad (50)$$

where

L_i = length of i^{th} section

D_i = average diameter of i^{th} section

A_i = average cross-sectional area of the i^{th} section

t = wall thickness

ρ = material density

E = Young's modulus

The parameters describing the lumped element substructure model were determined so that the undamped driving point admittance, i.e., the complex frequency domain representation of the velocity-to-force ratio, would be of the normalized form

$$\frac{V(s)}{F(s)} = \frac{(s^2 + 1)(s^2 + b^2)(s^2 + d^2)}{s(s^2 + a^2)(s^2 + c^2)} \quad (51)$$

where

$$1 < a < b < c < d < \infty$$

Frequency scaling was applied to Equation (51) to locate the zeros at 333, 500, and 800 Hz, and the poles at 0, 400, and 666 Hz. [11]

The lumped model of the composite structure with corresponding parameter values is shown schematically in Figure 11.

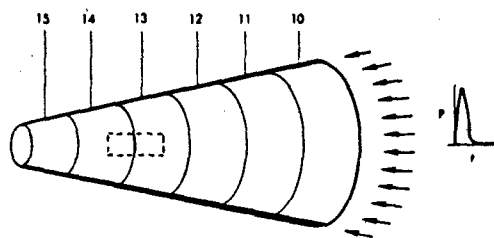


Figure 10. Conical Parent Structure Showing Substructure (Shaded) Attachment at Mass Station 14 and Applied Impulsive Loading

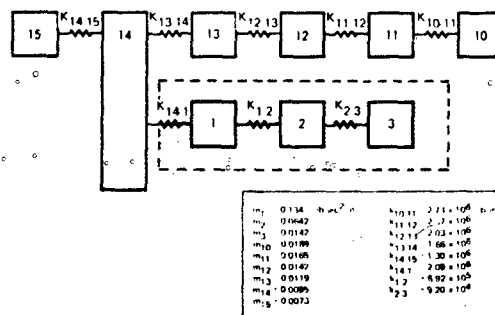


Figure 11. Lumped Model Schematic of Parent Structure and Substructure

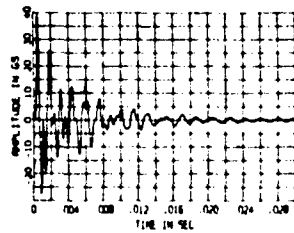
Viscous damping elements, while not shown, are automatically inserted in parallel with the spring elements by the computer code [12] used for the dynamic solution. The damping coefficient for the i^{th} element is calculated according to the equation

$$C_i = 2\zeta_i \left(K_i \frac{M_{i1} M_{i2}}{M_{i1} + M_{i2}} \right)^{1/2} \quad (52)$$

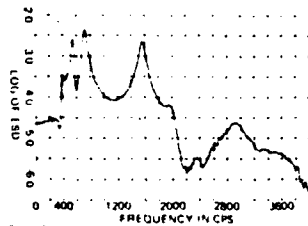
where ξ_i is the damping factor associated with the classical single-degree-of-freedom system consisting of the i^{th} spring and the masses which it connects. The damping factor is specified by the user prior to calculation and was assigned a value of 0.05 throughout this example.

The composite spring-mass model was excited by an impulsive axial force applied at the base of the parent structure. This was accomplished by specifying the initial velocity of mass 10 to be 20 in/s in the solution of the system equations. The specification procedure suggested above was then used to define an acceleration input to Mass 1 of the substructure.

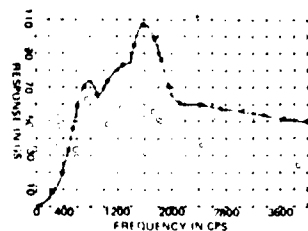
The response of Mass 1 to the "field" excitation and the corresponding ESD and SRS are shown in Figure 12. Three significant peaks in the ESD suggest that three oscillatory components are required; viz., at 550 Hz, 700 Hz, and 1550 Hz. The amplitudes and decay rates were estimated from the ESD and Equations (46), (47), and (48) to be 8 g's and 0.034; 18 g's and 0.048; and 20 g's and 0.034, respectively. It is clear from the ESD that the 550 and 700 Hz components should be combined additively and the character of the ESD between 700 and 1550 Hz suggests that the 1550 Hz component should be of opposite sign. Figure 13 shows the resulting shock signature and corresponding spectral descriptors.



a. Acceleration Response in g's of Mass 1 of Figure 2

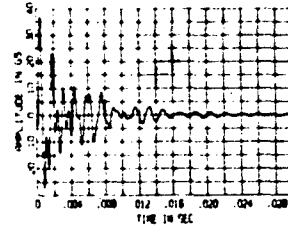


b. Base 10 Log of the Energy Spectral Density of the Waveform (Figure 12a)

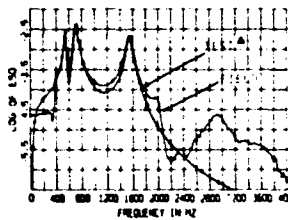


c. Base Excited Shock Spectrum Analysis (5% Damped) of the Waveform (Figure 12a)

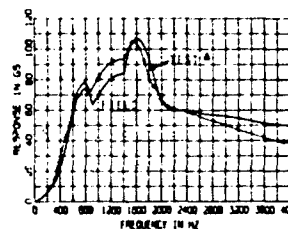
Figure 12. Acceleration Response and Spectral Descriptors of Mass 1 of the Substructure Due to Impulsive Excitation Applied at the Base of the Parent Structure



a. Acceleration Specification



b. Base 10 Log of the ESD's of the Acceleration Specification and the Field Response

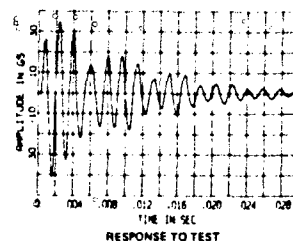
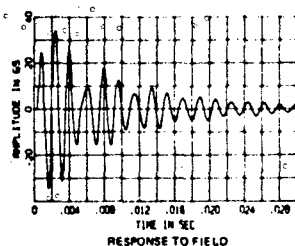


c. Base Excited SRS Analysis (5% Damped) of the Acceleration Specification and the Field Response

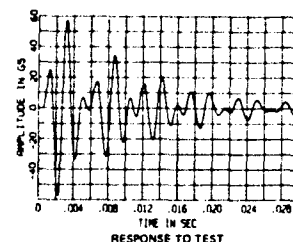
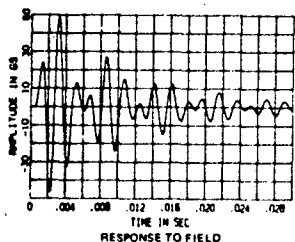
Figure 13. Acceleration Specification and Corresponding Spectral Descriptors for the Laboratory Test of a Section of the Substructure

The responses of the substructure components to the specified test excitation are compared to the response to the field test simulation in Figures 14 and 15. The signatures are different in detail but similar in

character; i.e., the initial peaks, frequency, and decay rate are nearly the same. Thus when some conservatism is added to the specification, adequate, but not severe, overtesting of substructure components is assured.

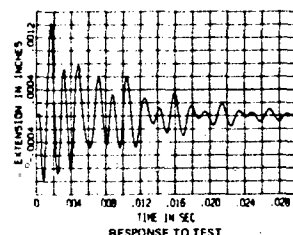
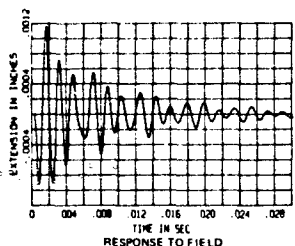


a. Acceleration Response of Mass 2

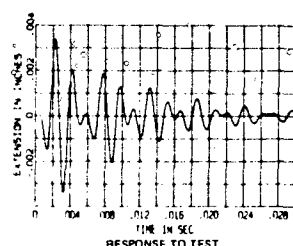
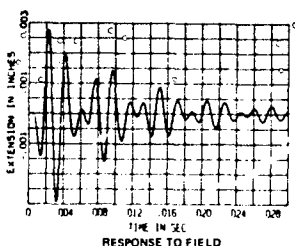


b. Acceleration Response of Mass 3

Figure 14. Acceleration Response of the Substructure Components to the Field Excitation and to the Excitation (Figure 13a) Applied as an Acceleration to Mass 1 of the Substructure



a. Linear Extension of K2 in Inches



b. Linear Extension of K3 in Inches

Figure 15. Displacement Response of the Substructure Elastic Elements to the Field Excitation and to the Excitation (Figure 13a) Applied as an Acceleration to Mass 1 of the Substructure

In the example shown in Figures 14 and 15, the test specification was derived in terms of damped oscillatory functions from the ESD of the acceleration response of Mass 1 to the field environment. It was demonstrated that component responses to the resulting excitation corresponded quite closely to those observed in the field simulation. If, instead of the table acceleration, the excitation voltage of the exciter amplifier is specified to be a superposition of damped oscillatory function, the acceleration response of the exciter table will again be of a decaying oscillatory nature and the corresponding ESD or SRS will be prominent at the frequencies of the component waveforms. The regions between prominent points are affected by the sign associated with the immediately adjacent components, and, furthermore, the frequency region of interest may usually be adequately covered by five or fewer superimposed functions. Thus, with the aid of an SRS or ESD analyzer, an operator may adjust the gain, damping, and sign so that the specified ESD or SRS is obtained with the same assurance concerning system response energy and maximum response bound as if the table acceleration had been specified. The SRS (5 percent damping) of the exciter table acceleration resulting from such an excitation voltage is shown in Figure 16. The load in this case was a 500-lb complex test specimen. Frequencies and damping of the components comprising the excitation voltage were 150 Hz and 0.10; 840 Hz and 0.02; and 1550 Hz and 0.02.

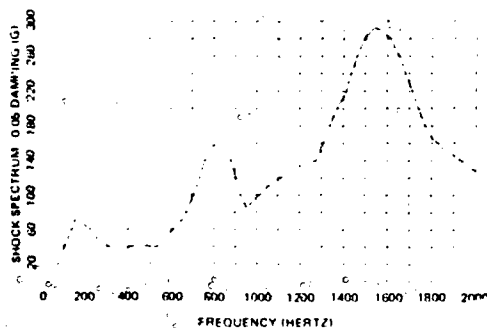


Figure 16. Five Percent Damped SRS of Resulting Table Acceleration for an Excitation Voltage Consisting of Superposition of Three Decaying Oscillatory Waveforms

CONCLUSIONS

Damped oscillatory excitation has been shown to be a realistic, as well as a realizable, simulation of the excitation experienced by a structure subjected to pyrotechnic shock. Significant features of the technique are as follows:

1. If the ESD or the undamped SRS of the recommended excitation envelops the corresponding description of the environment, it is guaranteed that the "energy" of the response of all system parts will be at least as great as that experienced in the field.
2. If the excitation of the exciter-specimen system is judiciously chosen, a reasonable bound exists on the maximum system response.
3. The excitation may be specified in a straightforward manner by the use of existing spectral descriptors.
4. Sophisticated generation and equalization equipment is useful but not required.

REFERENCES

1. John D. Favour and J. M. LeBrun, "Transient Waveform Control of Electromagnetic Test Equipment," The Boeing Company, Shock and Vibration Bulletin, No. 40, pt. 2, pp. 157-171, 1969.
2. J. V. Otts and N. F. Hunter, "Shock Testing on Vibration Machines by Digital Techniques," Sandia Laboratories, SC-TM-72-0304, June 1972.
3. D. O. Smallwood, "An Extension of a Transient Vibration Technique Using Least Favorable Responses," Sandia Laboratories, SC-RR-72-0735, November 1972.
4. D. O. Smallwood and A. F. Witte, "The Use of Shaker Optimized Periodic Transients in Matching Field Shock Spectra," Sandia Laboratories, SC-DR-71-0911, May 1972.

5. R. C. Yang, "Development of a Waveform Synthesis Technique," The Ralph M. Parsons Co., prepared for U. S. Army Engineer Division, Huntsville, Corps of Engineers, Contract No. DACA01-67-C-0010, document No. SAF-64, August 28, 1970.
6. G. W. Painter and H. J. Parry, "Simulating Flight Environment Shock on an Electrodynanic Shaker," Shock and Vibration Bulletin, No. 33, Pt. 3, 1964, pp. 85-96.
7. R. T. Fandrich, "Shock Pulse Time History Generator," Proceedings of the Institute of Environmental Sciences, 1969.
8. L. Meirovitch, Analytical Methods in Vibrations, N. MacMillan Co., New York, 1967.
9. R. Bracewell, The Fourier Transform and its Applications, McGraw Hill, Inc., New York, 1965.
10. P. A. McCollum and B. F. Brown, Laplace Transforms Tables and Theorems, Holt, Rinehart and Winston, Inc., New York, 1965.
11. M. C. Van Valkenberg, Introduction to Modern Network Synthesis, John Wiley and Sons, Inc., New York, 1960.
12. V. K. Gabrielson and R. T. Reese, "Shock Code User's Manual: A Computer Code to Solve the Dynamic Response of Lumped-Mass Systems," SCL-DR-69-98, November 1969.

DEVELOPMENT OF A PYROTECHNIC SHOCK TEST FACILITY

Dan R. Powers
McDonnell Douglas Astronautics Company - West
Santa Monica, California

A total of 24 high energy pyrotechnic shock tests were performed in the process of developing a pyrotechnic shock test facility. The concept employs a 4- by 8-foot flat metal response plate to which items to be tested are mounted. The response plate is driven by the energy released from detonating flexible linear shaped charge which cuts a separation sheet. Capabilities of the facility and results of numerous firings are discussed. Data presented are used to answer some of the typical questions arising in the prediction of shock environments and in the conduct of shock tests.

INTRODUCTION

Qualification of equipment which must survive the shock environment caused by pyrotechnic devices has long been a problem. Producing pyrotechnic environments by performing ground tests utilizing flight separation hardware has two main disadvantages: cost, and the inability to obtain qualification margins. Electrodynamic shakers controlled by shock synthesizers have been used successfully to qualify equipment for service in some of the less severe shock environments; inherent shaker limitations in acceleration obtainable, frequency response, and specimen weight restrictions have prevented their use in simulating environments whose shock spectra specifications exceed 5,000 g's or 10,000 Hz [1]. Because of unrealistic simulation, there is a current trend to write shock spectra specifications to exclude the use of synthesizers whose outputs resemble sine packets rather than high frequency transients typical of pyrotechnic events.

The facility described in this paper was developed in order to produce higher accelerations and achieve more realistic simulation of pyrotechnic shock environments. The final design incorporates desirable features from several types of existing fixtures; one of these features is the reusable joint concept, presently used on barrel testers, which has proven to be very successful [2]. In order to achieve high accelerations and greater versatility, a thick flat plate was chosen for the response member rather than a thin cylindrical shell typical of barrel testers.

After the fixtures were built, a comprehensive test program was carried out in order to determine the relationships between the various changeable parameters of the fixtures and the accelerations produced. Since the program consisted of 24 firings, it provided

an excellent opportunity to investigate some of the problems associated with the pyrotechnic shock phenomena.

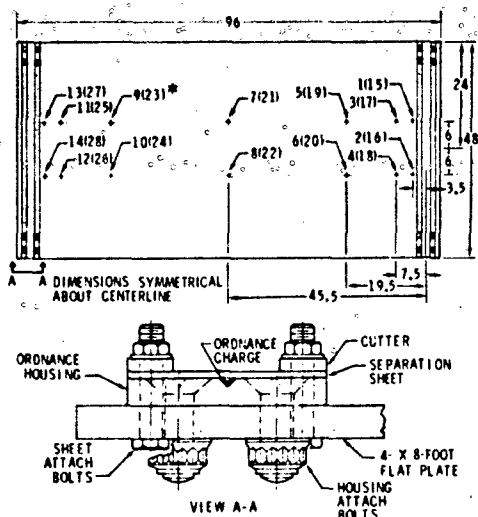
Although this paper will describe and discuss the facility and its capabilities, it is also hoped that the information presented can be used to answer some of the typical questions arising in the prediction of shock environments and in the conduct of shock tests.

DEVELOPMENT PROGRAM

The objective of the program was to design, build, and test a facility capable of producing pyrotechnic shock environments over a wide range of magnitudes in a predictable, repeatable, and inexpensive manner.

Two flat plates were chosen as the fixtures to which the components to be tested would be attached. The plates were suspended vertically, from the ceiling of a blockhouse, with nylon slings. Both plates measured four feet by eight feet. One was 1/2-inch-thick steel and the other was 1/4-inch-thick aluminum. At each end of both plates, a high strength steel ordnance housing was attached (Figures 1 and 2).

Different size cavities in the ordnance housings allowed for a wide selection of charge sizes to be used. Separation sheets of various thicknesses were bolted to the top of the ordnance housings. Shocks were generated by detonating flexible linear shaped charge inserted in the ordnance housings and severing the separation sheets. Combinations of charge sizes, ranging from 7 grains/foot to 50 grains/foot, and separation sheets ranging in thickness from 0.030 inch to 0.250 inch were used to generate shock spectra levels from 5,000 to 100,000 g's (5 percent damping). A total of



*UNBRACKETED NUMBERS, 0.5 INCH STEEL PLATE ACCELEROMETER LOCATIONS
BRACKETED NUMBERS, 0.25 INCH ALUMINUM PLATE ACCELEROMETER LOCATIONS

Fig. 1 - Pyrotechnic flat plate

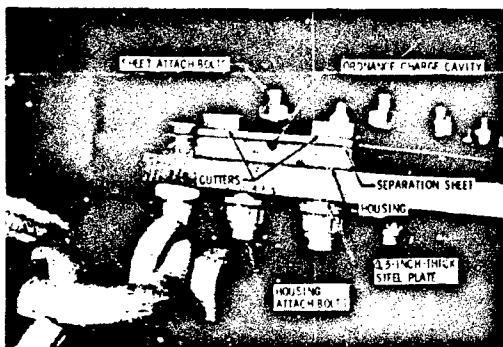


Fig. 2 - One-half-inch steel plate ordnance housing assembly

24 firings were made and shock spectra were generated from the outputs of 13 accelerometers for each firing.

Program objectives were satisfactorily met. Predictability and repeatability of shock spectra are excellent. Cost per test is considerably less than tests utilizing flight hardware to produce the shock. Material costs to conduct a flat plate test are less than \$50 per shot. One-inch-diameter flight-type pyrotechnic separation bolts are \$1,200 each, and skin cutting separation systems, similar to the one used on the Spartan missile, are in excess of \$20,000.

INSTRUMENTATION

Transducers

Fourteen Endevco Model 2225-M5 accelerometers were mounted on each plate (Figure 1). The method that was used to mount the accelerometers is described in detail since various mounting techniques can alter data considerably. Figure 3 shows the mounting stud and method of attachment. Figure 4 shows the actual installation. Note that the stud and base of the accelerometer, as well as the Microdot connector, have been coated with an epoxy (3M Company EC-2216) to prevent loosening. Cable movement has been prevented by securing the cable to the body of the accelerometer with tie cord and taping it down to the plate. On one test, the 3001 connector attached to the Endevco Model 2291 accelerometer came loose, resulting in the loss of signal; so it too was covered with epoxy (subsequent to the taking of the photograph, Figure 4).

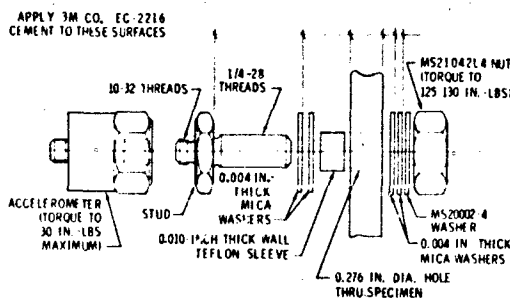


Fig. 3 - Accelerometer attachment

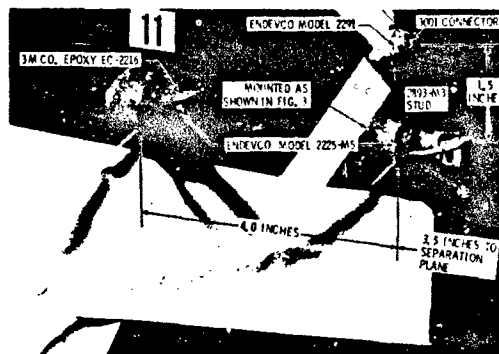


Fig. 4 - Accelerometer mounting technique

Data Acquisition

The data acquisition system consisted of Endeavor Model 2225-M5 accelerometers, 100-foot Microdot cable leads, Unholtz-Dickie Model D11 charge amplifiers, and an Ampex CP-100 recorder operated at 60 inches per second in the FM mode (108 kHz center frequency). System checkout was performed by ganging the amplifiers together and inserting voltages at appropriate amplitudes and frequencies and recording the signals. All channels were flat ± 1 dB over the frequency range from 20 to 20,000 Hz, linear ± 1 dB from 5 percent to 100 percent full scale, and had a dynamic range greater than 35 dB.

Data Reduction

Immediately after each firing, the recorded data were played back and displayed as oscillograms. Honeywell Model M5000 galvanometers used with a recorder tape speed reduction of 4/1 yielded flat response to 12 kHz. The data were examined for dc shifts, clipping, and proper band edge settings.

Valid data were then played into an MB Electronics Model N982 shock spectrum analyzer. Positive and negative shock spectra plots were generated using 5 percent damping (magnification factor $Q=10$) for analysis. For ease of interpretation, much of this raw data was re-plotted as maximax spectra (maximum envelope of positive and negative spectra).

RESULTS AND DISCUSSION

In general, results were as expected with higher accelerations occurring near the cutting plane. As the shock wave traveled down the plate, attenuation, edge reflections, and plate response increased data scatter. For this reason, most of the data presented has been restricted to locations within 20 inches from the cutting plane.

Figure 5 shows the envelope of the maximax spectra generated from the outputs of accelerometers 1 through 4 for shots 1 and 3. An approximate ± 3 dB scatter band is shown for each shot. Shot 1 was fired with 15 grains/foot, aluminum sheathed, flexible linear shaped charge (FLSC RA15J). Shot 3 used the identical charge and material type except the separation sheet thickness was increased to 0.125 inch. A 75 percent sheet thickness increase produced a 50 percent shock spectrum amplitude increase.

The maximum capability of the facility is presented in Figure 6, which shows the maximax spectra from the outputs of accelerometers 11 through 14 for shot 5. A sheet of 2014-T651 0.250 inch thick and a charge of FLSC RA50J were used. Note that the sheet thickness is double that used in shot 3 (Figure 5), and the mean amplitude of the shock spectra is twice

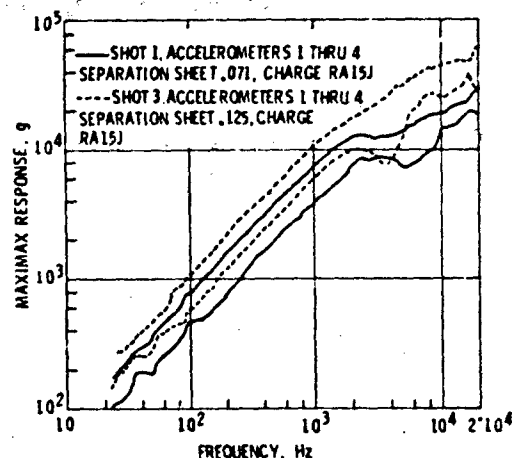


Fig. 5 - Envelopes of maximax spectra from two shots showing change in spectra amplitudes due to variation in separation sheet thickness

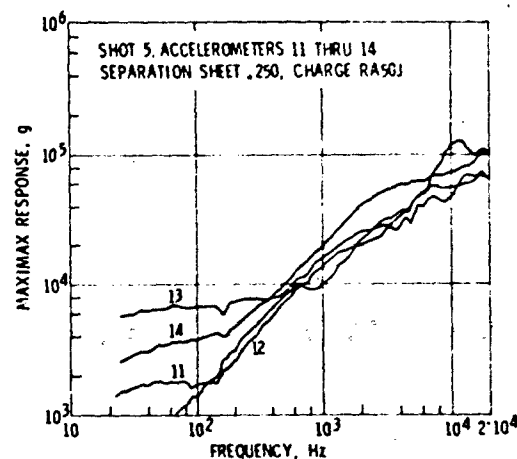


Fig. 6 - Maximum facility capability

that obtained in shot 3; however, in order to accomplish adequate separation, the charge size was changed from 15 grains/foot to 50 grains/foot.

Figure 7 presents spectra envelopes from shot 3 and shot 6. The conditions for both shots were identical except for the covering of the flexible linear shaped charge. Shot 3 used 15 grains/foot aluminum sheathed FLSC and shot 6 used 15 grains/foot lead sheathed FLSC. Differences, if any, are hidden in the data scatter band.

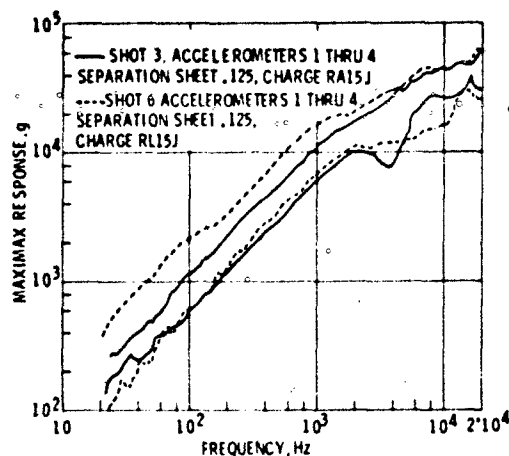


Fig. 7 - Envelopes or max/max spectra from two shots showing effect on spectra amplitudes due to changing the covering of the flexible linear shaped charge

Shots 13 and 14 were made to determine the effect on spectra amplitudes by varying the mechanical properties of the separation sheets. Both shots used a charge of RL15J and a separation sheet thickness of 0.125 inch. Shot 13 used 2014-T6 (ultimate tensile strength = 67,000 psi; Brinell hardness = 135) and shot 14 used 6061-0 (ultimate tensile strength = 18,000 psi; Brinell hardness = 30). Figure 8 shows very little difference in spectra amplitudes. This result was not as predicted.

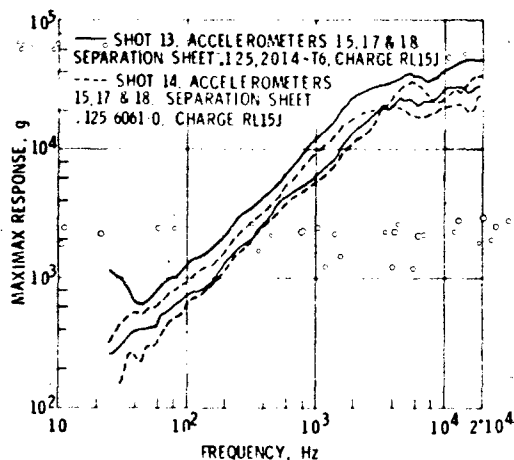


Fig. 8 - Envelopes of max/max spectra from two shots showing effect on spectra amplitudes due to changing the mechanical properties of separation sheet

Flexible linear shaped charge scaling laws include the Brinell Hardness Number showing that harder materials require a greater quantity of charge to achieve adequate cutting. This implies that harder materials absorb more energy prior to failure and would, therefore, transmit more energy into the response plate. After the firings, the separation sheets were examined and compared. The 2014-T6 sheet separated as two strips, failing at the center by the cutting action of the charge (80 percent penetration) and at the contact point of each of the cutters (Figure 1). The 6061-0 sheet failed only at the center, cut completely through by the charge and bent back over the cutters. Perhaps one reason that differences in spectra amplitudes were not noted is that the ordinance housing design used is very dependent upon charge size as explained later in the discussion of Figure 10.

Some experimenters have voiced the opinion that the thickness of the material being cut is the major factor in the changing of spectra amplitudes and that charge size has negligible effect as long as the material is satisfactorily severed [3,4]. These conclusions were based mainly on data obtained from ground tests utilizing flight separation systems. However, it is difficult to make generalized statements since there are so many configurations in use. For instance, one common stage separation system employs a rubber charge holder with a fiberglass backup ring. Upon detonation, the rubber and fiberglass are destroyed and the shock transmitted through the charge holder to the vehicle skin is minimal. For this type of system, the thickness of the skin is probably far more important than the quantity of charge. This is not true for systems using mild detonating fuse (MDF) where the charge holder is usually an integral part of the vehicle structure.

Figure 9 shows the effect that varying the charge size has upon spectra amplitudes of the aluminum response plate. Shot 16 used a charge of RL7J and shot 17 used a charge of RL10J. A separation sheet 0.030 inch thick was used for both shots. A 40 percent increase in charge size nearly doubled the resulting shock spectra.

The results from shots 16 and 18 are presented in Figure 10. Both shots used the same charge RL7J. Shot 16 used a separation sheet of 0.030 inch and shot 18 was fired without a separation sheet. Very little difference in spectra amplitudes are indicated.

Figure 11 shows the spectra obtained from shots 18 and 19. Neither shot used a separation sheet. The charge size for shot 18 was 7 grains/foot (RL7J) and for shot 19 was 25 grains/foot (RL25J). The 3.6 times increase in charge size resulted in an approximate 2.8 times increase in spectra amplitude.

Questions have arisen in the past regarding the effect of a high intensity sound field upon

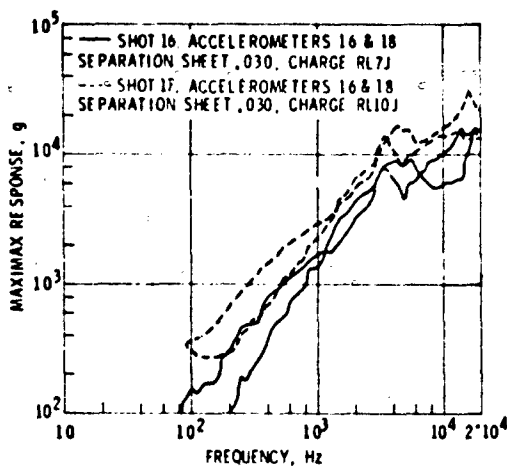


Fig. 9 - Maximax spectra from the outputs of two accelerometers for two shots showing the effect on spectra amplitudes due to changing charge size (separation sheet thickness constant)

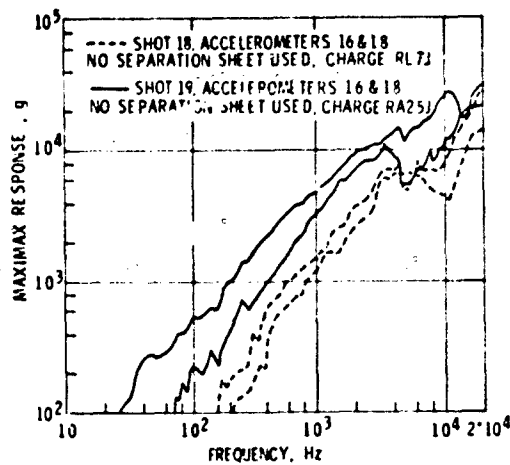


Fig. 11 - Maximax spectra from the outputs of two accelerometers for two shots showing the effect on spectra amplitudes due to changing charge size (no separation sheet used)

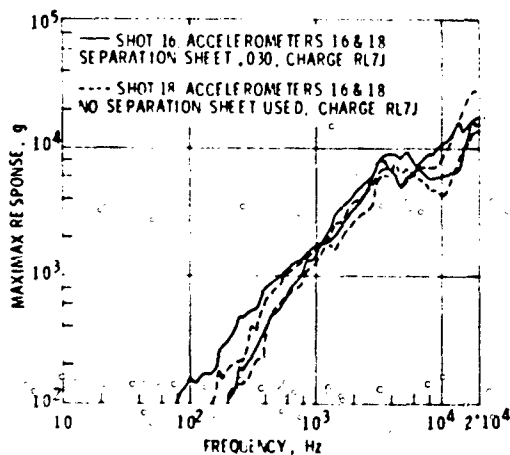


Fig. 10 - Maximax spectra from the outputs of two accelerometers for two shots showing the effects on spectra amplitudes due to elimination of the separation sheet

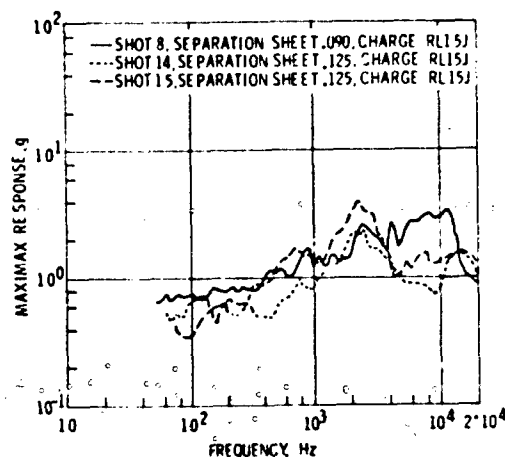


Fig. 12 - Maximax spectra from the outputs of an accelerometer exposed to the high intensity acoustic field associated with charge detonation

the outputs of accelerometers [6]. Figure 12 shows the maximax shock spectra generated from an acoustically excited accelerometer (Pulsar 200-11). The accelerometer was suspended from the ceiling with a piece of tie cord 4 feet long and was positioned 10 inches away from the

charge. Some response is indicated; however, it is negligible compared to the full-scale ranges of plate mounted accelerometers.

Unquestionably, the most important element in the data acquisition system used in the conduct of pyrotechnic shock tests is the

transducers. Many so-called shock accelerometers produce completely erroneous data when exposed to a pyrotechnic environment even though the actual acceleration is less than the manufacturer's published acceptable limits. The two most widely accepted pyrotechnic shock accelerometers in use today are the Endevco Models 2225 and 2225-M5 [6,7,8]. A new generation accelerometer, the Endevco 2291, is currently being recommended as a replacement for the 2225-M5. Since so many specifications and predictions have been based on data obtained from the earlier models, it is important to recognize that there are variations in outputs between the designs.

Six shots were made in which the output of 2225-M5 was compared with the output of a 2291. Representative shock spectra from two of these shots are presented in Figure 13. Note that the spectra amplitudes are generally higher for the 2225-M5 than the 2291, especially at the higher frequencies. This characteristic was also true for the other four shots from which comparisons were made. Both accelerometers were mounted in the same 1/4-28 tapped hole on opposite sides of the response plate as shown in Figure 14. A photograph of the mounted 2291 is presented in Figure 4. Acceleration histories for the two shots are shown in Figures 15 and 16. It is of interest to examine and compare the transients produced from the two shots. For shot 5, the 2291 indicates a peak acceleration of 47,500 g's, and the 2225-M5 indicates a peak of 65,000 g's (Figure 15). For shot 6, the peak accelerations are closer to each other, but the wave forms differ considerably (Figure 16).

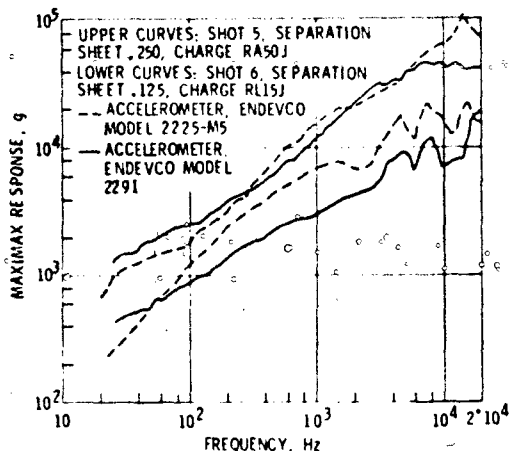


Fig. 13 - Maximax spectra from the outputs of two different model accelerometers mounted on opposite sides of the response plate in the same hole (see Fig. 15 and 16 for acceleration histories)

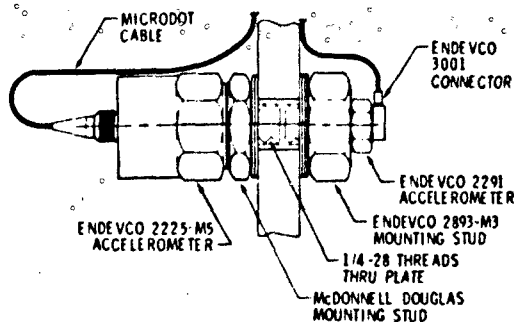


Fig. 14 - "Back to back" mounting procedure

As mentioned earlier, the accelerometers on the response plate were mounted as shown in Figure 3. This rather elaborate mounting procedure has been adopted at McDonnell Douglas as standard practice for all pyrotechnic shock tests because of bad experiences with other methods of attachment. Namely, accelerometers spinning loose or flying off, and problems with grounded accelerometers such as severe reduction of dynamic range and complete loss of data from amplifier saturation if a short to the mounting structure occurs.

Figure 17 is a plot of the maximax spectra from the outputs of two 2225-M5 accelerometers located 1 inch apart, both located 3-1/2 inches from the cutting plane. One accelerometer was mounted as shown in Figure 3 and the other was mounted to a stud that was screwed directly into the response plate as shown in Figure 14. Figure 17 shows that the spectrum generated from the accelerometer on the stud screwed in the tapped hole is approximately 3 dB higher, in the region above 10 kHz, than the spectrum from the accelerometer on the insulated stud.

There are numerous opinions about the effects of mass loading on the response of a structure transmitting a pyrotechnic transient [3,6,9]. This, of course, was a critical issue in the development of the facility. It was very desirable to be able to test electronic boxes and components. If mass loading had a significant effect on the response plate, it would not only limit specimen weight, but also ruin the predictability feature of the facility.

Figure 18 shows the configuration used to determine mass loading effects. An 8-pound section of a Spartan missile fairing, which was used as a backup structure for a previous shock test, was attached to the steel response plate by four bolts which were torqued to

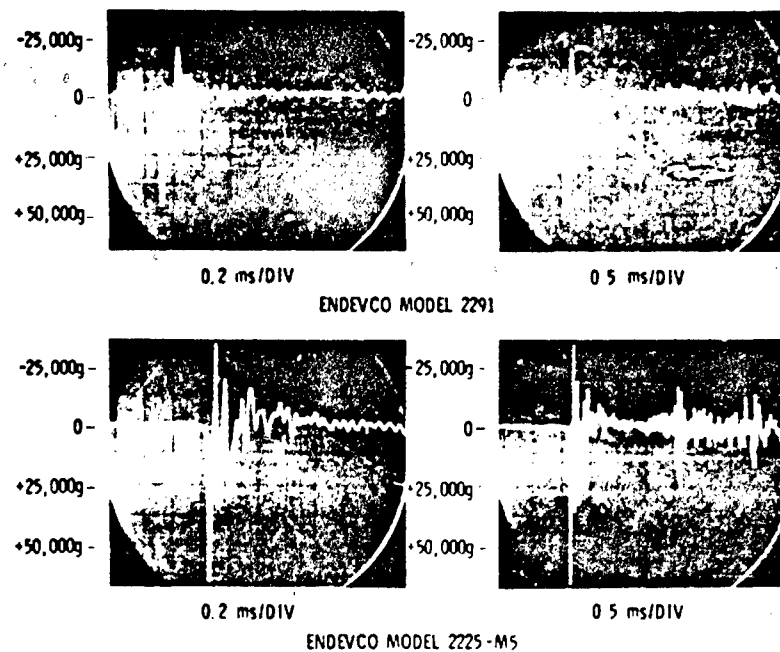


Fig. 15 - Acceleration histories from the outputs of two different model accelerometers mounted on opposite sides of the response plate in the same hole (see Fig. 13 for shock spectra)

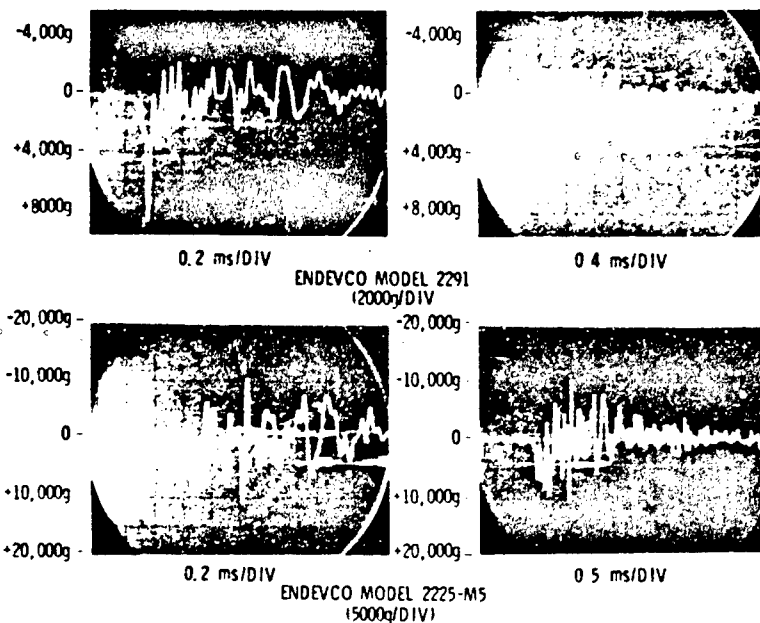


Fig. 16 - Acceleration histories from the outputs of two different model accelerometer mounted on opposite sides of the response plate in the same hole (see Fig. 13 for shock spectra)

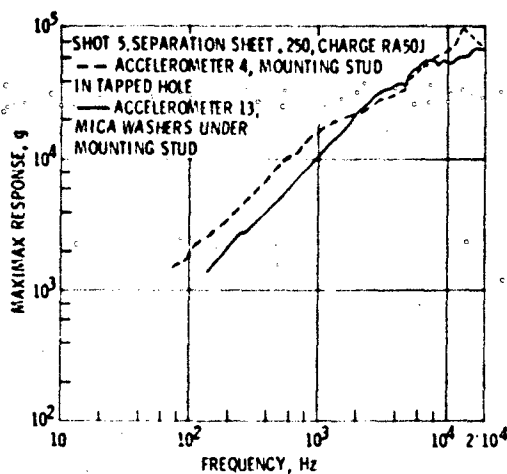


Fig. 17 - Maximax spectra from the outputs of two accelerometers mounted 1-inch apart, one mounted on a stud in a tapped hole, the other mounted as shown in Fig. 3

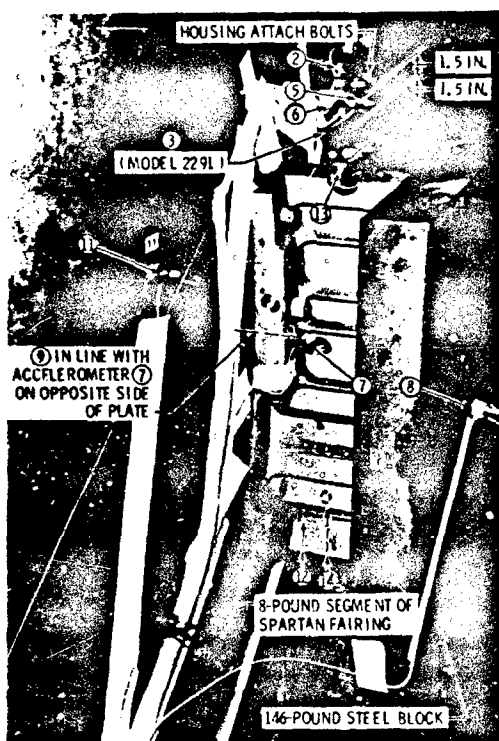


Fig. 18 - Steel plate with 154-pound mass

121 foot-pounds. On top of the fairing, a 146-pound steel block was attached. Accelerometer number 8 was attached to the center of the steel block as shown.

Figure 19 shows the results of shot 20 which used a separation sheet 0.190 inch thick and a charge of RA50J. Unfortunately, dc shifts invalidated the outputs from accelerometers 11, 13, and 14. Maximax spectra from the outputs of accelerometers 3, 9, and 12 are shown. Accelerometer number 3 was the Endeveco 2291 shown in Figure 4, and was located 1.5 inches from accelerometer 13. Note that, even though accelerometer number 9 was located on the response plate directly under the attach point of a 154-pound mass, the spectrum generated from its output is still within the spectra band formed from the outputs of accelerometers 3 and 12. The envelope formed by 3, 9, and 12 compares very closely with the envelope obtained from the unloaded plate in shot 5 (Figure 6). Note when comparing the two shots that not only was a large mass attached for shot 20, but also that the separation sheet thickness was decreased. Both of these changes would imply a reduction in spectra amplitudes. Such was not the case, and it appears that the addition of the mass had very little effect on plate response.

A significant reduction in spectra amplitudes is indicated at locations 7 and 8. The difference between spectra at locations 7 and 9 is attributed to the joint loss occurring at the interface between the response plate and the fairing. The difference between spectra at locations 7 and 8 is attributed to the fairing, steel block interface. Note that this reduction occurs mainly above 5 kHz, while at locations 9 and 7 the reduction occurs over the entire frequency band.

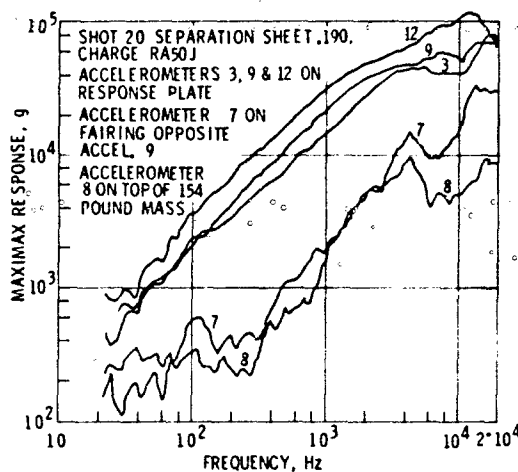


Fig. 19 - Maximax spectra from the outputs of 5 accelerometers to show the effect of mass loading and joint losses

There has been much discussion as to the meaning and/or validity of tri-axial measurements in a pyrotechnic environment. Figure 20 is presented for general information only; no attempt is made to explain or justify data presented. Accelerometers 2, 5, and 6 were attached to a 1-inch aluminum cube as shown in Figure 18, each reading response in mutually perpendicular directions. Note the difference between the spectrum generated from the output of accelerometer number 5 which was mounted on the 1-inch block and the spectra from the outputs of accelerometers 3, 9, and 12 (Figure 19) mounted in the same general area but directly to the response plate.

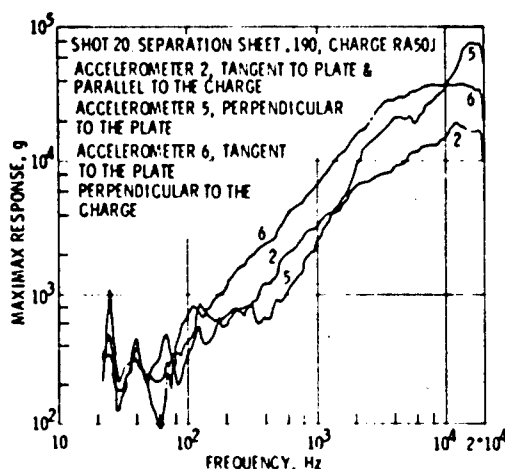


Fig. 20 - Max. max spectra from the outputs of 3 accelerometers mounted on a one-inch aluminum cube (tri-axial)

CONCLUSIONS

Based on our experience in the use of the pyrotechnic shock test facility and tests conducted to date, the following conclusions have been drawn; caution should be exercised, however, in extrapolating the test results presented in this paper to configurations differing from those tested.

1. The facility, through actual usage, has proved to be a reliable, repeatable, and cost-effective method of qualifying parts for usage in pyrotechnic shock environments.
2. Increasing the thickness of the separation sheet increases the amplitude of the resulting shock spectra (Figure 5). Mathematical relationships between sheet thickness and spectra amplitudes are not easily derived since the quantity of charge used also affects spectra amplitudes.

3. Spectra amplitudes are a function of the quantity of flexible linear shaped charge used when the charge holder is rigidly attached to, or is a part of, the main structure (Figures 9 and 11).
4. Figure 7 shows that the covering of flexible linear shaped charge does not significantly alter the response spectra.
5. Alteration of the mechanical properties of the separation sheet does not significantly change the response spectra (Figure 8). The effect of this change may have been hidden by the fact that the housing used was so dependent upon the charge that even the complete elimination of the separation sheet did not significantly reduce the spectra amplitudes, as shown in Figure 10.
6. Accelerometer outputs are not significantly affected by the high intensity sound field that accompanies a pyrotechnic event (Figure 12).
7. The outputs of the Endevco 2225-M5 and 2291 accelerometers differ, particularly in the region above 10 kHz, with the 2225-M5 indicating the higher values.
8. Using the accelerometer mounting technique shown in Figure 3 will reduce resulting shock spectra plots by approximately 3 dB in the regions above 10 kHz (Figure 17).
9. Mass loading does not significantly alter high frequency pyrotechnic shock transients traveling through structural members. Large attenuations are shown at mounting interfaces and structural joints (Figure 19).

REFERENCES

1. Driskill, P.H. "Investigation of Increased Mechanical Shock Testing Capabilities Employing Electrodynmic Shakers," TM-GEN-ENV-R7127, McDonnell Douglas Astronautics Company, Santa Monica, California. 1973.
2. Ikola, A. L. "Simulation of the Pyrotechnic Shock Environment," Shock & Vibration Bulletin 34, Part 3, pp 267-274. December 1964.
3. Hines, D. D. "Generations and Propagation of Stage Separation Shocks in Missile and Space Vehicles," Institute of Environmental Sciences, 1964 Proceedings, pp 681-689.
4. Paul, V. R. "Mechanical Shock From Frangible Joints," Shock & Vibration Bulletin 33, Part 4, pp 63-71. March 1964.
5. Roberge, H. J. and S. Rybacki. "Shock Environments Generated by Pyrotechnic Devices," Shock & Vibration Bulletin 33, Part 4, pp 73-81. March 1964.

6. Olsen, J. R. et al. "Mechanical Shock of Honeycomb Structure From Pyrotechnic Separation," Shock and Vibration Bulletin 35, Part 6, pp 15-42. April 1966.
7. Noonan, V. S. and W. E. Noonan, "Structural Response to Impulsive Loading (Pyrotechnic Devices)," Shock & Vibration Bulletin 35, Part 6, pp 265-284. April 1966.
8. Kacena, W. J. III, et al. "Aerospace Systems Pyrotechnic Shock Data (Ground Test and Flight)," Martin Marietta Corporation, Denver, Colorado. March 1970. Distributed by National Technical Information Service, U.S. Dept. of Commerce, Springfield, Va.
9. Noble, E. C. and R. L. Batten. "Shaped Charge Shock Environment for Centaur Vehicle Components," Shock & Vibration Bulletin 35, Part 6, pp 331-351. April 1966.

DISCUSSION

Mr. Chapman (Jet Propulsion Laboratory): What instrumentation did you use to obtain the data that we saw?

Mr. Powers: The data acquisition system consisted of 14-2225 accelerometers. The microdot cable leads went approximately 100 ft. to an Unholtz-Dickie D11 charge amplifier. The amplifier signal went into the recorder. Prior to running the test a frequency response check was made on the system which showed that there was no rolloff up to 20,000 Hz; that is the system was flat to 20,000 Hz; and insert voltages were used to prove that it was linear within + 1 db, and the signal to noise ratio was in excess of 35 db. On the playback side, the data reduction side, the signal was played back through an MB N 982 shock spectrum analyzer and the plots out of the analyzer were condensed in form into maxi-max shock spectra, and the greatest and the least maxi-max spectra from each accelerometer were put on this plot to form an envelope.

Mr. Chapman: It has been our experience that in measuring slew rates of impulse type functions into the charge amplifiers and tape recorders that we get different responses depending upon the rise time of the pulses. You mentioned your recorder, who is the manufacturer of the recorder and what is the model number?

Mr. Powers: I believe it was a CP 100.

Mr. Chapman: Many of the tape recorder manufacturers have two modes of operation on their tape decks, a transient mode and a sine wave or steady mode; the pulses that you used are the means of determining that your data channel was flat to 20,000 Hz. What mode of operation did you use?

Mr. Powers: That was a pure sinusoidal input out of an oscillator. The paper will show you the transients that were used at least for the 2225 and 2291 accelerometer comparisons, and they were taken directly off the scope and directly from the tape recorder.

Mr. Peete (Naval Undersea Center): What did you use in your calibration technique between the 10,000 and 20,000 Hz area, was it based on a standard comparison, or what was your absolute traceable standard?

Mr. Powers: 10,000 to 20,000 Hz. How do I know that is the true frequency of the input oscillator?

Mr. Peete: No, the true acceleration in that frequency band.

Mr. Powers: Perhaps an Endevco representative could answer your question. Endevco publishes calibration data up to about 20,000 g's.

Mr. Ensor (Endevco): The traceability that we have above 10,000 Hz is a bit nebulous, but we use a calibration shaker that has a resonant frequency of approximately 55,000 Hz and the standard inside has a resonance at approximately 80,000 Hz. We run a number of types of accelerometers whose resonant frequencies are known by excitation on this shaker and shock excitation and so forth. So above 10,000 Hz we have an electrical filter which takes out the resonant frequency of the standard or the rise due to the standard in the shaker; so we don't really know the accuracy of the calibration above 10,000 Hz to any great extent. We do know that we have comparisons between two types of accelerometers, up to 50,000 Hz. When you have a very high resonant frequency accelerometer of 10,000 Hz, like the 2291, then you can make comparisons of that accelerometer relative to lower resonant frequency instruments.

STUDY OF AN EXPERIMENTAL TECHNIQUE FOR APPLICATION
TO STRUCTURAL DYNAMIC PROBLEMS

R. F. Snell
McDonnell Douglas Astronautics Company
Huntington Beach, California

An experimental program was conducted to determine the feasibility of using subscale Lexan plastic models to determine the response of full-scale aerospace structural components to impulsive, pyrotechnic loadings. A Lexan monocoque cylinder was impulsively loaded around the circumference of one end, causing a compressive stress wave to propagate in the axial direction. The resulting structural responses of two configurations of the cylinder (with and without a cutout) were recorded by photoelasticity, strain gages, and accelerometers. A maximum dynamic stress concentration was photoelastically determined and the accelerations calculated from strain-gage data were in good agreement with those recorded by accelerometers. On the basis of results from these tests, it is concluded that reliable, quantitative structural response data can be obtained by the experimental techniques described in this report.

INTRODUCTION

Pyrotechnic devices are commonly used today in space vehicles for several purposes, e.g., stage separation, bay removal, and fairing removal. The detonation of these devices imparts shock loading to the vehicle structure and to the components attached to this structure. For a given application, the pyrotechnic devices must be designed in conjunction with the vehicle structure and components such that the integrity of the vehicle and its mission are not compromised by the shock loading. Unfortunately, limited information is available to the designer on shock levels generated from pyrotechnic detonations and on the effects that these shock loadings have on the vehicle structure and components. There is therefore a need both for more powerful analytical techniques and for less expensive, more versatile experimental techniques for investigating shock loading and the response of structures to shock loading. McDonnell Douglas Astronautics Company (MDAC), under the sponsorship of NASA Contract NAS9-12873, conducted an experimental program, described in this report, to investigate the feasibility of one improved experimental technique, that of an

electromagnetic, stress-wave generator augmented by dynamic photoelastic, strain gage, and accelerometer instrumentation techniques for the determination of dynamic response in models of proposed vehicles.

This technique can be divided into three areas, that of the loading device, that of the model, and that of instrumentation for determination of the response of the model to the loading. The loading device employs the energy stored in a high-energy, high-voltage capacitor bank to produce uniform impulsive loads that simulate shock loads from the detonation of pyrotechnic devices. The test specimen models proposed vehicle configurations and is made of Lexan polycarbonate plastic. Lexan, a photoelastic material, allows the determination of the states of strain in the model by use of a dynamic polariscope. The model can also be instrumented with strain gages and low-mass accelerometers to further characterize the model response. As a final step in this technique, the dynamic response of the model must be related to the dynamic response of an actual prototype by the use of appropriate similitude relationships.

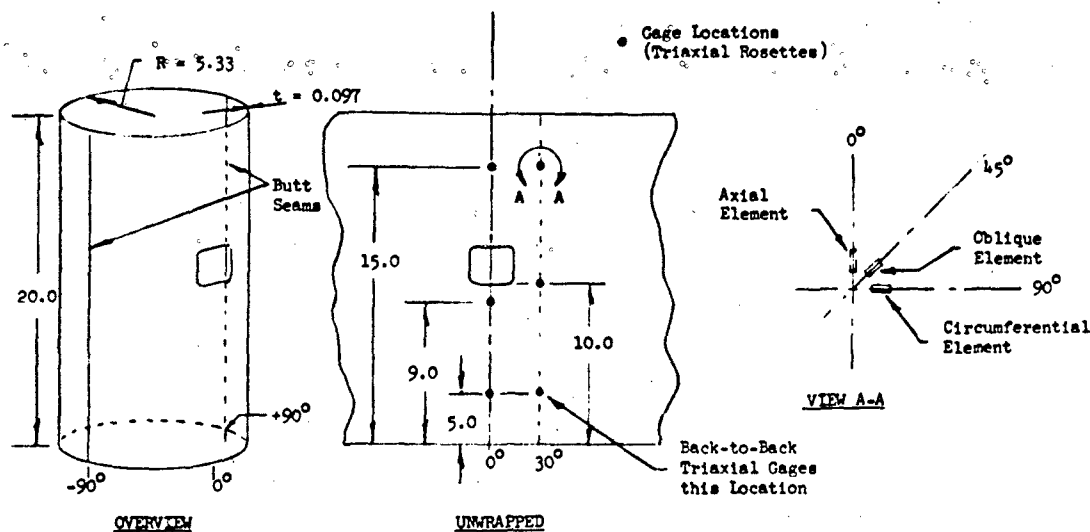


Fig. 1 - Configuration and dimensions of Lexan cylinder

This experimental technique has two principal advantages. First, the technique is relatively inexpensive in comparison to full-scale pyrotechnic testing and, second, the technique allows the determination of the states of strain in the model. This is in contrast to the information normally available from actual hardware tests in that results from hardware tests are generally limited to determining if the part does or does not fail under shock loading.

MODEL DESCRIPTION

A cylinder of Lexan polycarbonate plastic was fabricated to the dimensions shown in Figure 1 for an r/t ratio of 54.2. The length of the cylinder was arbitrarily established as 20 inches, a length that was approximately four times the radius of the cylinder. Fabrication of the cylinder was accomplished by thermoforming two sheets of Lexan of the appropriate dimensions into half cylinders by the use of a male mold. These two half cylinders were subsequently butt-joined with ethylene dichloride, a solvent of Lexan commonly used as a bonding agent, to form a complete cylinder. Lexan was used as the material for the cylinder model because Lexan is easily thermoformed into complicated shapes and is a sensitive photoelastic material. In

addition, Lexan is an extremely tough material and, as such, survives well in a high-shock environment. The final cylinder with strain gages attached is shown in Figure 2.

EXPERIMENTAL PROCEDURE

Loading Device

For this experimental program, the existing MDAC stress-wave generator was modified to accept a cylinder of the type and dimensions previously described. The stress-wave generator utilizes the discharge of a high-energy, high-voltage capacitor bank to produce a magnetic pulse which, in turn, produces a relatively short-duration, high-intensity pressure pulse. Reference 1 gives a complete description of this stress-wave generator and its principle of operation. Numerous tests have shown excellent repeatability of the pressure pulse (on the order of 3 percent) and the generator therefore allows the production of repeatable high-pressure, short-duration pulses over flat or curved surfaces. For the experiments of this program, the pressure pulse had a sine squared shape with a duration of approximately 25 microseconds and a peak magnitude of approximately 2000 psi.

the equation

$$\sigma_x - \sigma_y = \frac{nK}{d} \quad (1)$$

where σ_x and σ_y are the principal stresses, n is the fringe order, d is the thickness of the model, and K is a constant of the particular photoelastic material called the stress optical coefficient. At a free edge of a model, one of the principal stresses is zero and the other principal stress, lying tangent to the edge, can be directly determined from Equation 1. This is fortunate because the maximum stresses occur at a surface location for the vast majority of static problems and, therefore, photoelasticity may be used to directly determine these maximum stresses.

The experimental program at hand, however, involved a dynamic condition of stress-wave propagation and, although the validity of Equation 1 still holds, maximum stresses do not necessarily occur at a free boundary. Principal stresses can be determined at free edges, as in the static case, but the resolution of internal stresses can only be accomplished with additional information about the stress field, e.g., the existence of a uniaxial stress field allows such a resolution. For the dynamic case, photoelasticity does, however, produce a dramatic qualitative indication of the stress state.

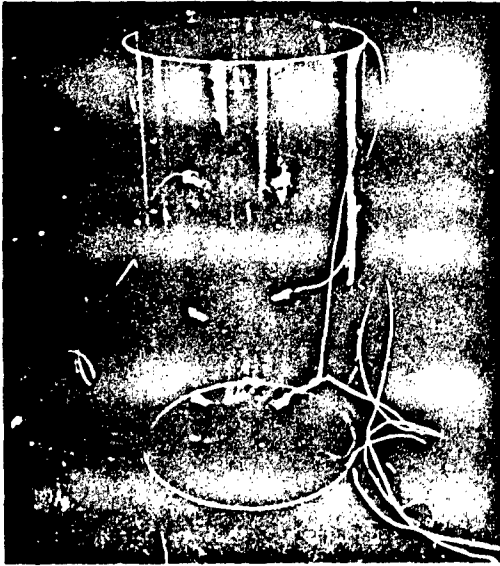


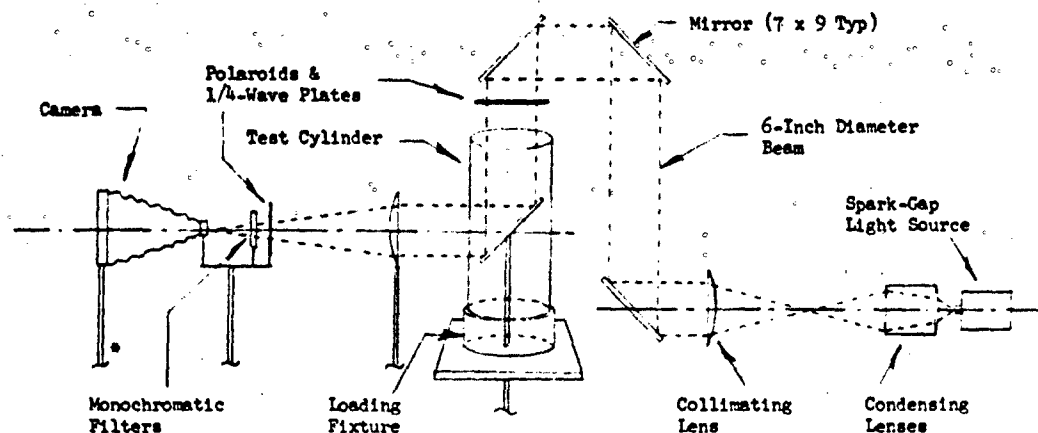
Fig. 2 - Lexan cylinder with strain gages attached

Instrumentation

Response of the cylinder to the passage of the stress wave was determined by photoelastic, strain gage, and accelerometer techniques. The three techniques, as applied to this test program, are described in the following paragraphs.

Static photoelasticity generally involves the fabrication of a two-dimensional model of the part to be analyzed from a photoelastic material. This model is appropriately loaded and observed with a circular polariscope. Basically, a circular polariscope is a device that allows the observation of the birefringence of the model and, for photoelastic materials, this birefringence can be directly related to the state of stress or strain that exists in the model. An observer will see a series of dark and light bands which are collectively called the fringe pattern and the fringe order for a given point is determined by counting the fringes to that point. This fringe order may be related to the difference in principal stresses at that point by

The photoelastic fringe patterns that result from a propagative stress-wave cannot be directly observed because of their high velocity of propagation (approximately 5000 ft/sec). In the stress-wave generator, this problem has been overcome by the use of a camera in conjunction with a high-intensity, short-duration (0.5 μ sec) light source to photographically stop the movement of the wave. The time at which the light source is activated relative to the initiation of the stress wave at the end of the cylinder is controlled by a time-delay circuit. For a given passage of the stress wave, this experimental setup allows the taking of only one photoelastic fringe pattern. Consequently a number of discharges of the stress-wave generator, each with a different light-source delay time, are required to map completely the passage of the stress wave through the model. The validity of this approach rests upon the excellent repeatability of the load history by the generator plus the operation of the generator at a load level that assures an elastic response of the model. In this manner, the photoelastic manifestation of the



*Termination of support shafts indicate adjustability of these shafts.

Fig. 3 - Dynamic polariscope

interaction of stress waves in models have been recorded in past test programs as well as in the model of this test program.

The optical path of the polariscope used for this experimental program is shown in Figure 3.

One biaxial strain gage and seven triaxial strain gage rosettes were applied to the cylinder model during the course of this test program. The location of the triaxial gages are shown in Figure 1. In the case of the biaxial gage, one element was oriented in the direction of the cylinder axis and the other in the circumferential direction. Two of the three elements of the triaxial rosettes were also oriented in the axial and circumferential directions, with the third element located between the other elements at an angle of 45 degrees. All elements had active gage lengths of 0.062 inch, a size small enough relative to the wave length to prevent distortion in the gage readout [2]. A standard wheatstone bridge was employed to read the strain gages in conjunction with a dual-beam Tektronic 555 oscilloscope.

In the tests of this experimental program, two types of piezoelectric accelerometers were used, the Endevco

2291 and the Endevco 2292. Both accelerometers are designed for the measurement of shock accelerations, both attach to the structure by 1/4-inch diameter holes tapped with 28 threads per inch, and both have masses of 1.3 grams. The 2291 is nominally rated for a peak acceleration of 100,000 g with a resonant frequency of 250 kHz and a sensitivity of 0.00385 picocoulomb/g. The 2292 is designed for a somewhat less severe environment, having a peak acceleration rating of 20,000 g, a resonant frequency of 100 kHz and a sensitivity of 0.130 picocoulomb/g. Data from the accelerometers were recorded with a dual-beam Tektronic 555 oscilloscope in both voltage-mode and charge-mode instrumentation schemes.

TEST SEQUENCE, RESULTS, AND DISCUSSION

First Test Series

The first test series was conducted on the monocoque cylinder to determine the response of the configuration to an axially propagating stress wave. The results of this test series served as the baseline for subsequent tests and provided insight into the difference in response between that of a cylinder and that of a flat plate, both without inclusions or cutouts. The initial loadings of the monocoque cylinder were

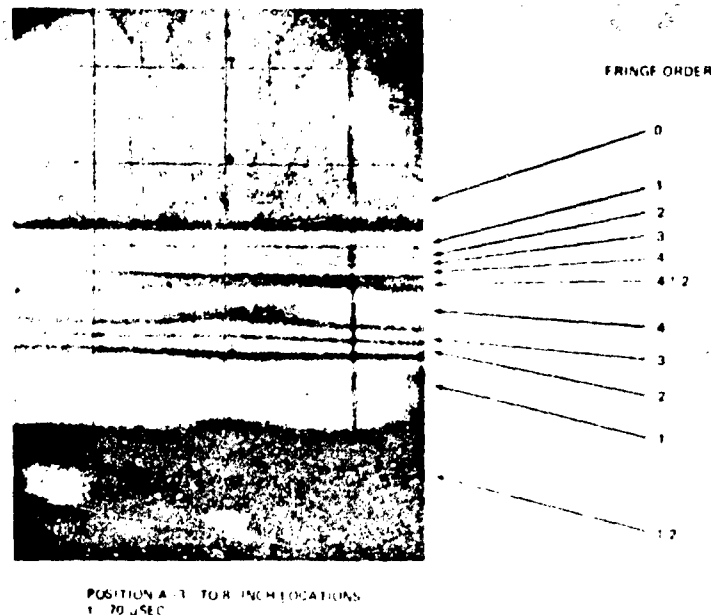


Fig. 4 - Typical photoelastic fringe pattern of first test series

used to obtain photoelastic data on the cylinder. Photoelastic pictures were taken prior to the installation of strain gages and accelerometers to provide a basis for determination of the effects that these other two types of instrumentation had on the response of the cylinder. Examination of these fringe patterns, e.g., Figure 4, show that the propagating stress wave was uniform in magnitude and velocity of propagation with a velocity of propagation of 0.063 in/usec and a pulse length of 1.6 inches for a pulse duration of 25 usec. Furthermore, these patterns indicated that attenuation and dispersion of the wave as it propagated up the cylinder was insignificant.

After completion of the initial photoelastic mapping, seven strain gage rosettes were placed on the cylinder at the locations indicated in Figure 1. The subsequent photoelastic fringe patterns indicated that the strain gages had only a localized effect on the strain field.

Each element of all the rosettes was subsequently read on an oscilloscope

to determine the strain history from the passage of the stress wave. The oblique (45°) gages gave peak strain values that were approximately one half of the peak axial strain values while the transverse gages showed that circumferential strain remained at zero throughout the wave passage. The geometry of the model (large r/t ratio) makes the application of plane stress relationships valid. The readings of the oblique and transverse gages indicate that the conditions are more restrictive than plane stress in that the circumferential strain is zero. The stress-strain relationships therefore become

$$\sigma_x = \frac{E \epsilon_x}{1-\nu^2} \quad (2)$$

$$\sigma_y = \frac{\nu E \epsilon_x}{1-\nu^2} = \nu \sigma_x \quad (3)$$

where σ_x and σ_y are the axial and

circumferential stresses respectively, E is Young's modulus, ν is Poisson's ratio, and ϵ_x is the axial strain.

The back-to-back triaxial rosettes at the 5-inch, 30-degree location (Figure 1) gave identical readings, within experimental accuracy for all elements. There was therefore no bending in the walls and no radial displacement. This indicated that, for the stress-wave length of these tests, the wall of the cylinder responded in the same manner as a flat plate of the same thickness would have responded. Generally speaking, the geometry of the cylinder would probably not affect the stress-wave response unless the length of the wave were equal to, or greater than, the circumference of the cylinder.

Shock responses of aerospace vehicles are usually described in terms of acceleration as a function of time for various points on the vehicle or in terms of a shock spectra consisting of response representations obtained by reduction of acceleration histories. In order for model data to be readily used by the aerospace industry, it is necessary that the raw model data be reduced to acceleration histories or reduced to shock spectra. The last test series of this experimental program determined accelerations directly by accelerometers. The disadvantage of such an approach for model application is that the available accelerometers are large relative to the structure of the model. One then has the classic case of altering the response one wishes to measure by the very act of making that measurement. For this study photoelasticity and strain gage techniques were investigated for the feasibility of reducing these types of data to accelerations of the model. The following paragraphs describe how this was accomplished.

For a plane wave traveling in the direction of increasing x , displacement as a function of position and time may be written as

$$u = f(c_0 t - x) \quad (4)$$

where u is displacement, f represents the function, c_0 is the propagation velocity, and t is time. Separate differentiating of Equation 4, first with respect to x and then with respect to t , will yield

$$\frac{\partial u}{\partial x} = -f'(c_0 t - x) \quad (5)$$

$$\frac{\partial u}{\partial t} = c_0 f'(c_0 t - x) \quad (6)$$

Solving both equations for $f'(c_0 t - x)$ and equating the results gives

$$\frac{\partial u}{\partial t} = -c_0 \frac{\partial u}{\partial x} \quad (7)$$

As $\partial u / \partial t$ is the particle velocity (v_x) and $\partial u / \partial x$ is the strain in the x direction (ϵ_x) Equation 7 becomes

$$v_x = -c_0 \epsilon_x \quad (8)$$

Differentiation of Equation 8 with respect to time will yield the acceleration

$$A_x = -c_0 \frac{\partial \epsilon_x}{\partial t} \quad (9)$$

where A_x is acceleration. Equation 9 simply states that the acceleration is equal to the propagation velocity times the instantaneous slope of the strain history for any given time. It should be realized that the foregoing argument is valid only for the case of the propagation of a plane stress wave. In practice Equation 9 means that a strain history may be reduced to an acceleration history by a point-by-point measurement of the slope of the strain history. The disadvantage of this approach is that small variations in the strain history may result in large variations in the slopes. For the present study, however, the strain histories are smooth curves and such a reduction as herein described is both straightforward and accurate.

Maximum acceleration is then determined by measurement of the maximum slope. For example, Figure 5 shows a typical strain history from the gages used in these tests. The maximum strain rate for this history is measured as -754 in/in/sec. This value, along with the velocity of propagation of

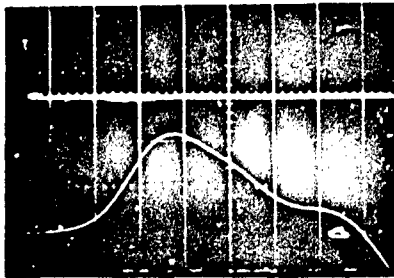


Fig. 5 - Typical strain gage trace for axial gage (2500 $\mu\text{in/in/cm}$, 5 $\mu\text{sec/cm}$, sweep delay = 115 μsec)

0.063 in/lsec, results in a maximum acceleration of 126,000 g.

In like manner the slope of the strain may be obtained from the photoelastic data. This is accomplished by determining the fringe order at a given point as a function of time. Such a determination requires a series of photographs of the fringe patterns at the point, each taken at slightly different times. The data obtained from these photographs would be a series of discrete points plotted as a function of time and connection of the points would yield a continuous curve of fringe order versus time. Application of Equation 1, for conversion of fringe order to difference in principal stress, and Equations 2 and 3, for conversion of difference in principal stress to strain, results in a plot of strain versus time. The procedure for obtaining acceleration from this stage onward is then identical to that employed with the strain gage data.

There are certain difficulties in the reduction of photoelastic data to obtain accelerations. First, a large number of photographs are required to accurately record the changing photoelastic pattern and the minimum time separation between these photographs would be a function of the maximum strain rate. Second, determination of exact fringe order in most cases would require extrapolation to non-integral values of fringe orders. These non-integral values must be estimated from the photographs and such estimation could give rise to inaccuracies. Finally the reduction of differences in principal stress to axial strain requires additional information as to

the type of stress field that exists at the point of interest. In the monocoque configuration, for instance, it is known that the conditions are that of plane stress with zero circumferential strain. Without such additional information the photoelastic data cannot be reduced to accelerations. Accelerations determined from strain gages were used in the data reduction for the test series of this program, rather than those determined from photoelastic data, because of the relative ease with which strain gage data may be reduced to accelerations.

The assumption that the pressure applied to the loaded edge is a sine-squared function of time gives an interesting check on the validity of the maximum acceleration measured with strain gages. Again assuming classical wave propagation theory, it can be shown that the maximum acceleration for a strain pulse having a sine-squared shape is

$$A_{\max} = - \frac{C_0 \epsilon_M \pi}{P} \quad (10)$$

where C_0 is as previously defined, ϵ_M is the maximum strain ($\sim 5500 \mu\text{in/in}$) and P is the strain duration time (25 μsec). Substitution of these values will result in a maximum acceleration of 115,000 g, a value very close to the measured value.

Second Test Series

A rectangular cutout was machined into the cylinder wall to constitute the model configuration of the second test series. Figures 1 and 6 show the location and dimensions of this cutout. As in the first test series, model response was determined by the taking of photoelastic pictures and the recording of strain gage outputs.

As was expected the photoelastic fringe patterns taken prior to the arrival of the stress wave at the cutout are identical to those patterns taken on the uncut cylinder. The interaction of the stress wave with the cutout are shown in Figure 7. Three phenomena are readily apparent in this figure. First, the reflection of the compression wave at the lower edge of the cutout results in the propagation of a tension wave in the opposite direction from the initial compression wave. Second, the interaction of the stress wave with the cutout results in a stress concentration at the corners of the cutout. This is manifested in the large increase in fringe order that occurs at these corners.

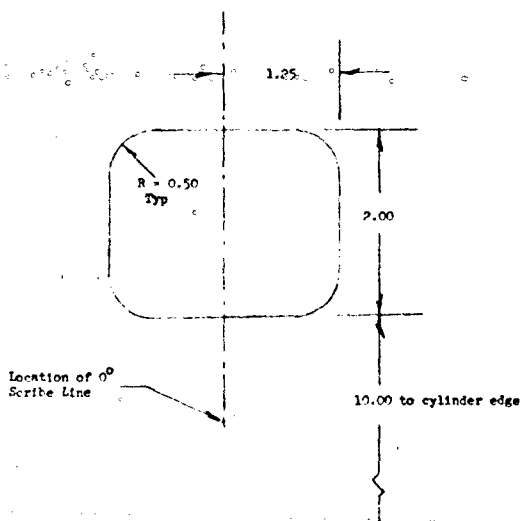


Fig. 6 - Dimensions of cylinder cutout

Figure 7B indicates that the maximum fringe order at these corners is 10, compared to a maximum fringe order of 4-1/2 at a location away from the cutout. These fringe orders, together with the assumption that a plane stress, uniaxial-strain field exists in the cylinder wall and that a plane stress field exists at the edge of the corner, results in a strain concentration value of 1.62 and a stress concentration of 1.40. For this program strain and stress concentrations were defined as the maximum values of such quantities at the location in question, e.g., the edge of the cutout, divided by the maximum values of such quantities in the free field of the cylinder.

Finally, the photographs indicate the formation of oblique relief waves, (shown in Figure 7C) on both lateral edges of the cutout, that propagate into the remainder of the cylinder at an angle of approximately 45 degrees. As previously mentioned the strain field of the stress wave, prior to the arrival at the cutout, has no strain component in the circumferential direction and, hence, there exists a biaxial stress field. For a free edge, however, there can exist no stress component perpendicular to this free edge, and when the stress wave arrives at the cutout, the circumferential component of the biaxial stress field is relieved at the edge of the cutout. This relief propagates into the

remainder of the cylinder and gives rise to the oblique relief waves.

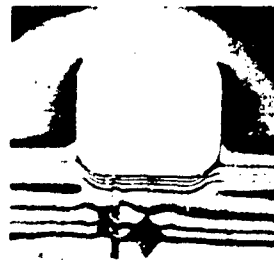
Figure 7D shows the bending of the stress wave around the back of the cutout. The subsequent reunification of the wave components results in a fringe order considerably reduced from the free-field fringe order. As can be seen in Figure 7F this reduction is by a factor of approximately two when the peak of the wave has propagated a distance away from the cutout equal to the height of the cutout.

Third Test Series

The third test series was for the determination of the axial acceleration of the cylinder by the use of accelerometers. As previously mentioned, the reason for obtaining accelerometer data was for a comparison of this data for cylinder response with the data obtained by strain gages and by photoelasticity. Such a comparison would be facilitated if the measurements were made in a uniform field away from the wave disturbance that results from the cutout. For this reason, the accelerometers were mounted on the cylinder in a position diametrically opposite that of the cutout. As the accelerometers are large relative to the wall thickness of the cylinder, it was necessary to design and install a mount for the accelerometers. The mount was also made from Lexan and bonded to the cylinder with ethylene dichloride. Its geometry and location are shown in Figure 8.

As mentioned previously, two types of accelerometers were each employed in two different types of data acquisition modes to measure the acceleration of the cylinder wall. The acceleration histories, shown in Figure 9, indicated that in all cases that the measured acceleration was approximately 62,000 g. This value is considerably less than the acceleration of 126,000 g determined by the reduction of the strain histories obtained from the strain gages. The mount to which the accelerometers were attached had a depth of 0.375 inch compared to the underlying wall thickness of 0.097 inch. With this large difference in thickness, a reduction in acceleration is not surprising. The task then became that of correlating the acceleration measured on the mount with that calculated from the strain gage outputs. Two approaches were taken to resolve this issue.

First, photoelastic pictures were taken of the stress wave as it propagated into, through, and beyond the



A - 150 μ SEC



C - 170 μ SEC



E - 200 μ SEC



B - 160 μ SEC



D - 190 μ SEC



F - 210 μ SEC

Fig. 7 - Fringe patterns in region of cutout for second test series

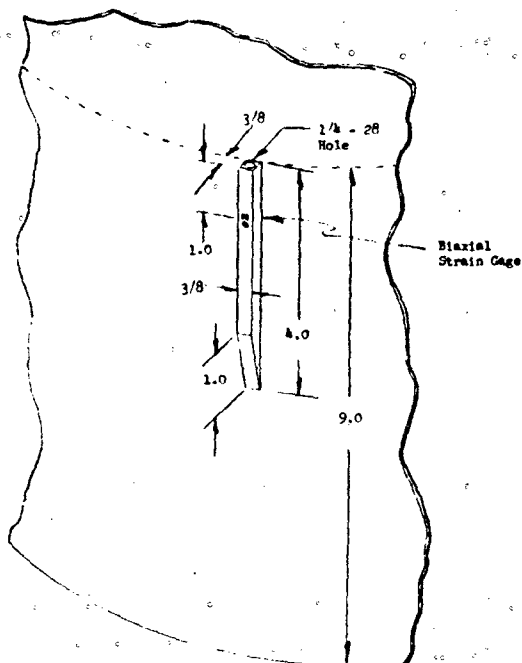


Fig. 8 - Dimensions and location of accelerometer mount

accelerometer mount. One such picture is shown in Figure 10 and, as can be seen, the mount resulted in considerable disturbance to the free-field photoelastic pattern. This pattern also allows an assessment of the average strain in the mount and cylinder wall directly under the mount relative to the strain in the cylinder wall in a region

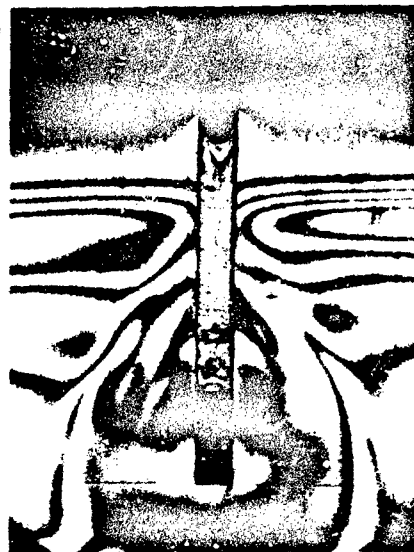
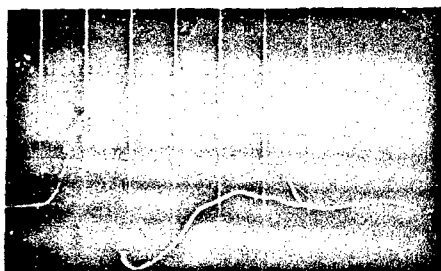
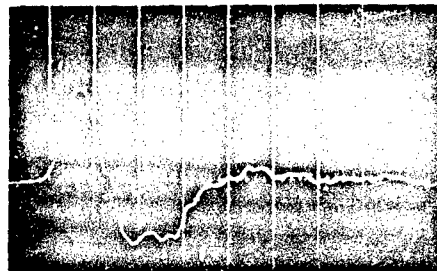


Fig. 10 - Photoelastic fringe pattern in accelerometer mount at $t = 120 \mu\text{sec}$

undisturbed by the mount. Such an assessment is accomplished by comparison of the maximum fringe orders in each position in conjunction with certain assumptions concerning the stress-strain field in these two regions. The stress-strain relationship for the cylinder are given in Equations 2 and 3. These two equations may be combined to give the following expression for the axial strain



A 2291 ACCELEROMETER



B 2292 ACCELEROMETER

Fig. 9 - Accelerometer readings in charge mode (30,000 g/cm, 20 $\mu\text{sec/cm}$, sweep delay = 120 μsec)

$$\epsilon_x = -\left(\frac{1+\nu}{E}\right) (\sigma_x - \sigma_y) \quad (11)$$

Because the length of the wave is long compared to the cross-section dimensions of the mount, a condition of uniaxial stress is assumed to exist in the mount. The applicable stress-strain relationships are therefore

$$\sigma_x = E \epsilon_x \quad (12)$$

$$\sigma_y = 0 \quad (13)$$

For later convenience Equations 12 and 13 are rewritten as

$$\epsilon_x = \frac{1}{E} (\sigma_x - \sigma_y) \quad (14)$$

The division of Equation 14 by Equation 11 will result in an expression for the ratio of the axial strains. This expression reduces to

$$\frac{(\epsilon_x)_1}{(\epsilon_x)_2} = \frac{(\frac{1}{1+\nu})}{(\frac{1}{1+\nu})} \frac{(\sigma_x - \sigma_y)_1}{(\sigma_x - \sigma_y)_2} \quad (15)$$

where the subscripts 1 and 2 refer to the mount and cylinder respectively. These differences in principal stress are determined by the photoelastic fringe patterns as applied to Equation 1. The ratio of the differences in principal stresses may be written

$$\frac{(\sigma_x - \sigma_y)_1}{(\sigma_x - \sigma_y)_2} = \frac{n_1 d_2}{n_2 d_1} \quad (16)$$

where n is the maximum fringe order (17 fringes and 4-1/2 fringes for the mount and cylinder wall respectively) and d is the optical thickness (0.472 inch for the combined thickness of the mount and cylinder wall and 0.097 inch for the cylinder wall alone). The application of these values plus the value for Poisson's ratio of 0.37 to Equation 15 and 16 results in a ratio for the axial strains of 0.56. The strain in the mount is therefore 56 percent of the strain in the cylinder wall. This result can be applied to determine the ratio of the maximum accelerations if it is assumed that the axial strain histories of the mount and

cylinder wall are of the same shape, differing only in magnitude. If such a condition exists, then the ratio of the maximum accelerations equals the ratio of the maximum strains. The maximum accelerations in the mount should therefore be 56 percent of the maximum acceleration of the cylinder wall. Assuming that the wall acceleration is 126,000 g (as determined by strain gages) then the acceleration in the mount would be 71,000 g. Considering the assumptions made in the foregoing analysis, this value is reasonably close to the accelerometer value of 62,000 g; this difference amounting to 14 percent.

As a second approach to the determination of the validity of the accelerometer readings, a biaxial strain gage was placed on the accelerometer mount in the position shown in Figure 8. The reduction of the axial strain history from this strain gage gave a maximum strain rate of -357 in/in/sec corresponding to a maximum acceleration (Equation 9) of 59,000 g, a value approximately 4 percent below that obtained with the accelerometers.

A summary of the values obtained by the three instrumentation techniques for accelerations is given in Table 1.

A comparison of the accelerometer trace of Figure 9A for the 2291 with that of Figure 9B for the 2292 shows that the positive portions of the traces are nearly identical. The negative portions are different, however, in that local oscillations occur in this portion in the trace from the 2292 accelerometer but do not appear in the trace from the 2291 accelerometer. Figure 9B shows that five cycles of local oscillation occur for the 2292 in 36 microseconds, corresponding to a frequency of 139 kHz. This frequency is close to the manufacturer's stated resonant frequency of 100 kHz for this transducer and these local oscillations are probably the excitation of this resonance. No such oscillations appear in the traces for the 2291 at a frequency of 139 kHz nor are there oscillations at 250 kHz, the resonant frequency of the 2291 accelerometer.

For a further characterization of the shock pulse, the outputs obtained in the charge mode of both accelerometers were reduced to produce shock spectra. As would be expected, the shock spectra, shown in Figures 11 and 12 are very similar for the 2291 and 2292. The peak of both occur at about 150,000 g. This value is about 2-1/2 that of the peak acceleration of the acceleration histories and such a ratio

TABLE 1
Summary of Acceleration Data

	Photoelastic	Strain Gage	2291 Accelerometer	2292 Accelerometer
Acceleration (kg)	71	59	62	63
Percent of Acceleration* in Cylinder Wall	56	47	49	50
Percent of 2291 Accelerometer Reading	114	96	100	102

* Maximum acceleration in cylinder wall = 126,000 g

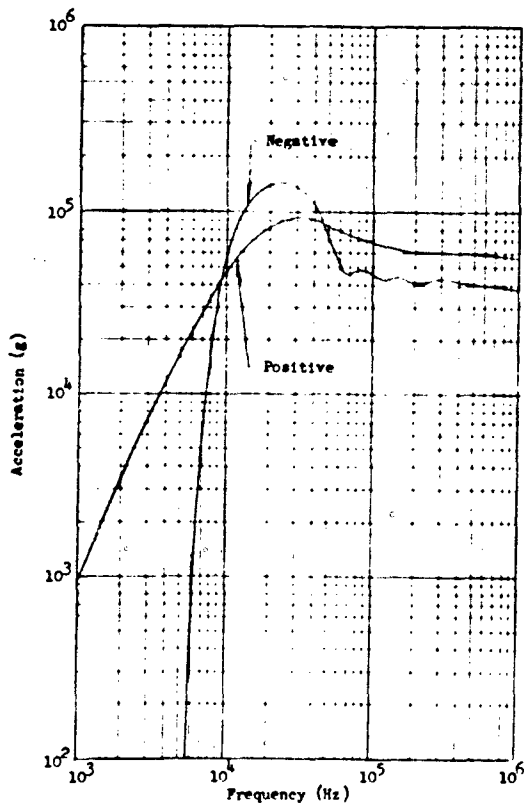


Fig. 11 - Shock spectrum from 2291 accelerometer data

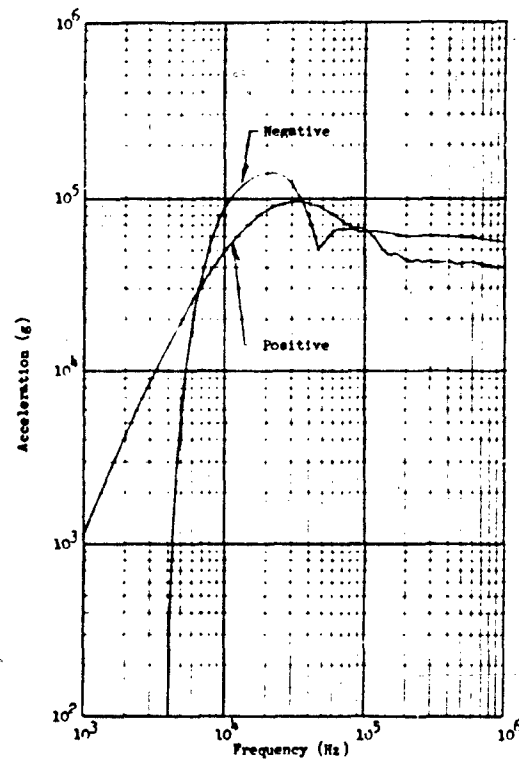


Fig. 12 - Shock spectrum from 2292 accelerometer data

is characteristic of shock spectra. It is interesting to note the local peak in the negative response portion of the shock spectra of the 2292 in the region of 100,000 kHz. This local peak is apparently from the resonance excitation, and as such does not appear in the spectrum of the 2291.

SIMILITUDE FEASIBILITY STUDY

Introduction

The feasibility of scaling model data to determine the dynamic response of full-size prototypes depends fundamentally on what physical parameters are important in the response problem. At one end of the spectrum are linear elastic response problems for homogeneous, one-dimensional structures that are insensitive to strain rate and that are undamped. At the other end are response problems for structures whose material constitutive relationships are of such complexity as to make scale modeling extremely difficult if not impossible. The present study is concerned with metallic structures of isotropic materials and scale models of plastic materials. It is helpful to first review the modeling requirements of three-dimensional elasticity for an isotropic body. Next the feasibility of scale modeling when stress depends on strain rate as well as strain will be investigated and, finally, model fabrication problems will be reviewed.

Model Requirements for an Isotropic Body

Consider an isotropic, homogeneous, linear elastic body that occupies a volume V bounded by a surface B as shown in Figure 13. The undeformed body is initially at rest in a uniform gravitational field g . The body is subjected to body forces $f_i(\bar{z}, t)$ in the interior, surface tractions $S_i(\bar{z}, t)$ on a portion of the bounding surface B_S , and the displacement vector $u_i(\bar{z}, t)$ is prescribed zero on the remaining portion of the bounding surface, B_U . The coordinates z_i of a point \bar{z} are with respect to an orthonormal Cartesian frame that can be considered an inertial frame. The field equations for infinitesimal displacements are

$$\frac{\partial \sigma_{ij}}{\partial z_j} + f_i = \rho \frac{\partial^2 u_i}{\partial t^2} + \rho g d_i \quad (17)$$

$$\sigma_{ij} = 2\mu \epsilon_{ij} + \lambda \delta_{ij} \epsilon_{kk} \quad (18)$$

$$\epsilon_{ij} = 1/2 \left(\frac{\partial u_i}{\partial z_j} + \frac{\partial u_j}{\partial z_i} \right) \quad (19)$$

where σ_{ij} and ϵ_{ij} are respectively the components of the stress and strain tensors of classical elasticity; u_i are the components of the displacement vector; d_i are the direction cosines of the gravitational field; λ and μ are the Lamé constants of the material, and ρ is the mass density. The initial conditions are

$$u_i(\bar{z}, 0) = 0 \quad (20)$$

$$\frac{\partial}{\partial t} u_i(\bar{z}, 0) = 0 \quad (21)$$

and the boundary conditions are

$$\sigma_{ij} n_j = S_i(\bar{z}, t); \bar{z} \in B_S \quad (22)$$

$$u_i(\bar{z}, t) = 0; \bar{z} \in B_U \quad (23)$$

where n_j are components of the outward unit normal \bar{n} to B_S at the point \bar{z} on

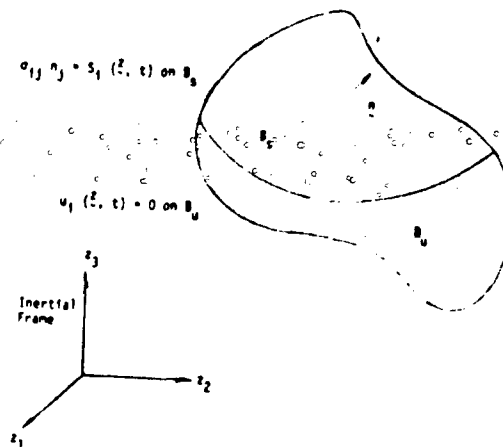


Fig. 13 - Elastic body and coordinate system

this surface. These conditions and the field equations completely determine the response $u_i(z, t)$, $\sigma_{ij}(z, t)$ and $\epsilon_{ij}(z, t)$ and hence identify all the physical parameters important in the response problem. In general it is not necessary to know the governing equations to identify the important physical parameters in the response problem. In fact, having identified the important physical parameters, the modeling requirements can be determined using the Buckingham Pi theorem without recourse to the governing equations. Counting the components of a vector or tensor as only one parameter, there are eleven physical parameters that determine the response which implies there are eight dimensionless Pi terms that are sufficient to describe the response. The eleven parameters* are σ_{ij} , f_i , g , u_i , t , S_i , λ , μ , ρ , l , and z_i , and a convenient set of Pi terms is

$$G\left(\frac{\sigma_{ij}}{\mu}, \frac{f_i l}{\mu}, \frac{\rho g l}{\mu}, \frac{z_i}{l}, \frac{u_i}{l}, \frac{t}{l} \sqrt{\frac{\mu}{\rho}}, \frac{\lambda}{\mu}, \frac{S_i}{\mu}\right) = 0 \quad (24)$$

The quantity l is any convenient characteristic length.

These are not unique but are a commonly used set of dimensionless parameters. Equation 24 can also be written

$$\frac{\sigma_{ij}}{\mu} = F\left(\frac{f_i l}{\mu}, \frac{\rho g l}{\mu}, \frac{z_i}{l}, \frac{u_i}{l}, \frac{t}{l} \sqrt{\frac{\mu}{\rho}}, \frac{\lambda}{\mu}, \frac{S_i}{\mu}\right) \quad (25)$$

The scaling laws that are implied by Equation 25 can be stated as

$$\left.\begin{aligned} \left(\frac{\sigma_{ij}}{\mu}\right)_m &= \left(\frac{\sigma_{ij}}{\mu}\right)_p \\ \left(\frac{f_i l}{\mu}\right)_m &= \left(\frac{f_i l}{\mu}\right)_p \\ \left(\frac{\rho g l}{\mu}\right)_m &= \left(\frac{\rho g l}{\mu}\right)_p \\ \left(\frac{z_i}{l}\right)_m &= \left(\frac{z_i}{l}\right)_p \end{aligned}\right\}$$

* Strain ϵ_{ij} and the direction cosines d_i are already dimensionless.

$$\left(\frac{u_i}{l}\right)_m = \left(\frac{u_i}{l}\right)_p \quad (26)$$

$$\left(\frac{t}{l} \sqrt{\frac{\mu}{\rho}}\right)_m = \left(\frac{t}{l} \sqrt{\frac{\mu}{\rho}}\right)_p$$

$$\left(\frac{\lambda}{\mu}\right)_m = \left(\frac{\lambda}{\mu}\right)_p$$

$$\left(\frac{S_i}{\mu}\right)_m = \left(\frac{S_i}{\mu}\right)_p$$

Where the subscript m denotes model and p denotes prototype. The strains ϵ_{ij} and direction cosines d_i must also be equal. It should be emphasized that the relations of Equation 26 are not dependent on the governing equations; they depend only on the Buckingham Pi theorem. The strain-displacement equations and stress-strain equations can be nonlinear for example. The interpretation of the relationships given in Equation 26 is relatively straightforward. For instance, the first relationship of Equation 26 means that stresses in the prototype can be determined simply by multiplying the stresses measured in the model by the ratio μ_p/μ_m , provided that all the other conditions of Equation 26 are satisfied. The satisfaction of Equation 26 can, however, require stringent model design, especially if gravity forces are important. When the model and prototype are of the same material, simulation of these forces requires either a full-scale model or requires the changing, somehow, of the magnitude of these force fields. The problem could be further compounded if the model and prototype were made of different material. Even when gravity forces are unimportant, Equation 26 requires replica modeling and requires the use of materials that have the same Poisson's ratio, i.e., $(\lambda/\mu) = 2\nu/(1-2\nu)$.

The use of models that have Poisson's ratios different from the prototype require an examination of the influence of Poisson's ratio on response. Past experience in photoelasticity for static loadings of models have shown that differences in Poisson's ratios generally have insignificant

effects in the prediction of stresses in the prototype [3, 4, and 5]. As the similitude relationships for the static case are the same as those of the dynamic case (Equation 26), with the exception that the relationship $(t/l \sqrt{\mu/\rho})_m = (t/l \sqrt{\mu/\rho})_p$ need not be satisfied, it is possible that the effect of different Poisson's ratios may also be insignificant for the dynamic case. An indication of the effect for the dynamic case can be obtained by an examination of the equations of motion (Navier's Equations). First a change of variables will be made to non-dimensionalize the equations per Equation 26.

$$\xi_1 = z_1/l, u_1^* = u_1/l$$

$$\tau = (t/l) \sqrt{\mu/\rho}, f_1^* = f_1 l/\mu, g^* = \rho g l/\mu$$

and the dilatation, $e \equiv \epsilon_{kk}$, defined so that the equation can be written

$$\left(\frac{1}{1-2\nu}\right) \frac{\partial}{\partial \xi_1} (e) + \nabla^2 u_1^* + f_1^* = g^* d_1 + \frac{\partial^2}{\partial \tau^2} (u_1^*) \quad (27)$$

The only term explicitly dependent on Poisson's ratio is the dilatation term (i.e., hydrostatic stress term). The value of ν for Lexan is near 0.37 while ν for aluminum is near 0.30 and, in this range, the coefficient $1/(1-2\nu)$ does change significantly. One manner to determine if this distortion will in turn produce a significant effect on dynamic response is that of the employment of a two-dimensional computer simulation code to predict response for a reference shape using different values of Poisson's ratio. Should the response change significantly, a prediction factor to correct this distortion could possibly be determined empirically for the actual structural shape. This would require the testing of several plastic models with different values of ν_m and plotting, for example, the strain (or any of the nondimensional parameters of Equation 26) versus ν_m . The ratio of the non-dimensional strain at the correct ν and the distorted ν would be interpolated from this graph and used directly to predict prototype response. Although the determination of a prediction factor is a standard engineering procedure [6], the need to fabricate and

test several models, plus the difficulty or impossibility of adequate variation of Poisson's ratio in these models, make the application of this procedure questionable for the type of tests described in this report. In any event should the effects of difference in Poisson's ratios prove unacceptable, there still remains to the experimenter the use of models made from the same materials as the prototype.

Strain-Rate Effects

In the present study the loading conditions are impulsive in nature and the physical parameters affecting structural response must be re-examined. This will be done using the simple Voigt viscoelastic model and a more general viscoelastic model [7] that satisfies fundamental thermodynamic considerations. The Voigt model traditionally has been applied to describe viscoelastic behavior because of its relative simplicity. However, as shown in Reference 7, the Voigt model exhibits implausible thermodynamic behavior. This is unimportant at low-strain rates but, for high-strain rates, use of the Voigt model is questionable. The more general viscoelastic model has no such inherent limitations and consequently is valid at high as well as low-strain rates. In an effort to be comprehensive both models are considered and it will be shown that the scale modeling requirements for the more general model are quite different from those obtained for the Voigt model.

Consider first the one-dimensional Voigt relation for stress as a function of strain and strain rate ($\dot{\epsilon}$).

$$\sigma = E \epsilon + \eta \dot{\epsilon} \quad (28)$$

This identifies one new physical parameter, η , that must be considered to determine the structural response. The units of this parameter are $FL^{-2} T$ and using the Buckingham Pi theorem again we obtain the additional modeling requirement

$$\left(\frac{\eta}{l \sqrt{\mu \rho}}\right)_m = \left(\frac{\eta}{l \sqrt{\mu \rho}}\right)_p \quad (29)$$

This requirement is similar to that obtained for body forces and gravitational forces in that the rate constant η must be changed in proportion to l . The only manner in which this could be satisfied would be to determine the

parameters of η , μ , and ρ for both the prototype and model materials, apply these values to Equation 29, solve for the ratio λ_m/λ_p , and apply this ratio to the scaling of the model relative to the prototype. It is unlikely that the ratio would be of a suitable value. Furthermore, if the prototype and model are of the same material, the ratio is one and the model would be identical to the prototype. In fact a small model of the same material will accentuate strain-rate effects according to the Voigt model since

$$\left(\frac{\eta}{\mu}\right)_m > \left(\frac{\eta}{\mu}\right)_p \quad (30)$$

These differences will be small if the condition $E \epsilon_{\max} \gg \eta \dot{\epsilon}_{\max}$ holds.

Reference 8 indicates this is true of metals and plastics at structural-response strain rates ($\dot{\epsilon} \sim 10^3$ in/in/sec) but that it is not true of plastics at shock-response rates ($\dot{\epsilon} \sim 10^6$ in/in/sec). The strain rates associated with the Lexan models of the present study were all under 10^3 in/in/sec. If higher strain rates are necessary, empirical correction curves obtained with different model materials offer one possible solution. This assumes of course that the materials are all governed by the Voigt model.

The validity of a Voigt model is questionable at very high strain rates for most engineering materials in that these materials possess an initially elastic response not predicted by a Voigt model. Valanis [7] demonstrates that "contrary to expectation the rate of irreversible entropy production increases with the square of the rate of strain according to [the Voigt] theory." The effect of strain rate will now be reconsidered on the basis of a model exhibiting behavior that is thermodynamically plausible. This model is based on a viscoelastic potential that includes thermodynamic coordinates and leads to the stress response at a point as

$$\sigma_{ij}(t) = C_{ijkl} \epsilon_{kl}(t) + \int_{-\infty}^t C_{ijkl}^1(t-a) \frac{\partial \epsilon_{kl}}{\partial a} da \quad (31)$$

C_{ijkl} and C_{ijkl}^1 are elastic and viscoelastic response functions respectively

and a is a dummy variable of integration. For isotropic materials

$$\begin{aligned} \sigma_{ij}(t) = & \lambda \epsilon_{kk}(t) \delta_{ij} + 2 \mu \epsilon_{ij}(t) \\ & + \delta_{ij} \int_{-\infty}^t \lambda^1(t-a) \frac{\partial \epsilon_{kk}}{\partial a} da \quad (32) \\ & + 2 \int_{-\infty}^t \mu^1(t-a) \frac{\partial \epsilon_{ij}}{\partial a} da \end{aligned}$$

This identifies two new physical parameters $\lambda^1(t)$ and $\mu^1(t)$, both functions of the history of deformation, that must be considered to determine structural response. The units of these parameters are FL^{-2} and using the Buckingham Pi theorem we obtain

$$\begin{aligned} \left[\frac{\lambda^1(t_m)}{\mu} \right]_m &= \left[\frac{\lambda^1(t_p)}{\mu} \right]_p \\ \left[\frac{\mu^1(t_m)}{\mu} \right]_m &= \left[\frac{\mu^1(t_p)}{\mu} \right]_p \quad (33) \end{aligned}$$

where model time and prototype time are related as in Equation 26. These requirements indicate that if the model and prototype are of the same material, the nondimensional response will be the same provided the nondimensional deformation history in model time is the same as the nondimensional deformation history in prototype time. Equation 33, in conjunction with Equation 26, therefore indicate the feasibility of accurately determining prototype strain rate effects from measured strain rate effects in a model.

Fabrication Effects

In the previous discussion the possibility of replica scale modeling of all important dimensions was tacitly assumed. In actuality the fabrication of a true geometrical model could be difficult in that some portions of the prototype often are relatively small compared to the overall dimensions of the prototype. The construction of a model of reasonable overall size would then require that these portions be extremely small. A serious manifestation of this problem occurs in the case of models of vehicles that have very large r/t values. For example, a vehicle with an r/t of 500 would require a wall thickness of 0.010 inch in a 10 inch diameter model, in contrast to the

0.097 inch wall thickness of the model of the test program described in this report. The wall thicknesses required on such models may be too small for an accurate geometrical reproduction. One possible solution to such a situation, is to construct a distorted model, distorted in the sense that the thickness dimensions of the model violates a true geometrical scaling. The major difficulty of using a model distorted in the thickness dimension occurs when the response of the model to bending forces and to in-plane forces are both of importance. In such cases the ratio of the dynamic response of the distorted model to the dynamic response of the prototype will be a continually varying quantity. Hence there will be no set multiplier to convert model response to prototype response.

The use of distorted models in static testing is not an uncommon practice [6] and has previously been outlined in this report concerning the violation of the Buckingham Pi relationship (Equation 26) involving Poisson's ratio. In all probability, however, the dynamic aspects of a dimensionally distorted model will not in general be compensatable.

Consequently it appears that it will be necessary to adhere to strict geometrical models. The consequence to the experimenter of strict adherence to true geometrical models may not be as serious as it first appears. Although the diameter of the model used in this test program was just over 10 inches, there is nothing inherent in the technique which prohibits the use of larger models. A diameter of 20 inches, for instance, would result in a wall thickness of 0.020 inch for an r/t of 500. Fabrication of a model cylinder of this thickness is within the present state-of-the-art.

There are other problems involved in true geometrical modeling that, although not as important as a violation of the r/t ratio, must nevertheless be considered. Actual flight hardware often has irregular construction detail that may make it impossible to achieve truly replica modeling. This is particularly true of joints and fasteners but it could also include such things as residual stresses caused by fabrication. Consider for example a welded part that has very thin gages when scaled. If the scale model is also welded, the resulting joint may have vastly different properties because of thermodynamic differences in the two welding

processes. If a substitute mechanical joint or no joint at all is used, the vibration characteristics of the model and prototype may differ considerably. Perhaps the most noteworthy example of the problems that can arise from joint and fastener differences is the 1/10 scale replica model of the Apollo/Saturn V, described in Reference 9. This was a quality model in which serious efforts were made to replica model practically the entire structure. In spite of this there were obvious differences in bolted flange joints because, as Reference 10 describes it, "the thin-flange ring frames used in the scale model would not hold their planar shape." In addition to these differences, the gravity forces on the structure could not be scaled and this allowed some joints to open during vibration testing.

Another fabrication difference that can be important in scale model construction is caused by tolerances. In most instances these differences are unimportant but, if the response is sensitive to imperfections, then these differences can be significant. Buckling of thin walled shells is an example of a structural response sensitive to imperfections.

CONCLUSIONS

The tests of this program showed that photoelastic cylindrical models may be successfully fabricated and loaded with short duration, uniform loads in a stress-wave generator. Both photoelastic and strain gage techniques can be used to determine the response of such models to the resulting stress wave as this wave propagates through the model. The photoelastic data give quantitative information on stress and strain concentrations at free edges of the model and qualitative information in the remaining areas of the model. Strain histories from the strain gage data can be readily reduced to accurate acceleration histories. Accelerometers may also be used to get accelerations that occur in the model and the accelerations indicated the excellent accuracy with which accelerations may be obtained by reduction of the strain gage data. The experimental portion of this program also showed that shock spectra for the model response may be obtained by reduction of the acceleration histories.

The modeling requirements for general isotropic structures given by Equation 26 indicate the feasibility of model testing for dynamic response if body forces and gravitational forces

can be neglected. The use of substitute isotropic materials with different Poisson's ratios may cause response differences. In this event it will probably be necessary to restrict model materials to the same materials as used in the prototype, although there does exist the possibility of determining empirical correction curves based on tests with different plastic materials.

The most efficient use of plastic scale models is in design trade studies where a number of concepts can be evaluated using inexpensive models. The feasibility of such testing was established provided (a) that body forces can be neglected and (b) that response differences that result from differences in Poisson's ratio between the prototype and model materials are insignificant or that correction factors can be obtained to compensate for these differences. The feasibility of prototype prediction by model testing was also established subject to certain fabrication limitations. As a practical matter, structures with complex joints and fasteners or imperfection sensitivities will be difficult to simulate in a scale model. An awareness of this situation is important but it does not limit the basic capability of scale model testing. Furthermore, it may be necessary to construct relatively large models in order to conform to strict geometrical scaling in the case of models that model vehicles having large r/t ratios.

It is well to note that the unresolved problems associated with dynamic model testing, which are discussed in this report (body forces, Poisson's ratio, and exact scaling), are not unique to dynamic modeling but rather are general problems associated with all model testing.

ACKNOWLEDGEMENTS

The work described in this report was conducted under NASA Contract NAS9-12873 and the Program Monitor was D. K. McCutchen, Structures Branch, NASA-JSC.

A special note of acknowledgement is due Dr. E. L. Stanton who conducted the similitude study described in this report.

REFERENCES

1. R. F. Snell, D. C. MacKaller, and R. Guernsey, "An Electromagnetic, Plane Stress-Wave Generator," *Experimental Mechanics*, Vol. 13, No. 11, November 1973.

2. M. G. Pottinger, "Gage Length Effects on Strain Measurements," *Instruments and Controls*, September 1970, pp. 115-116.
3. M. Clutterbuck, "The Dependence of Stress Distribution on Elastic Constants," *British Journal of Applied Physics*, Vol. 9, August 1958.
4. H. Fessler and H. Lewin, "A Study of Large Strains and the Effect of Different Values of Poisson's Ratio," *British Journal of Applied Physics*, Vol. 11, July 1960.
5. B. Kenny, "Effect of Poisson's Ratio on Stress Distributions," *The Engineer*, October 30, 1964.
6. G. Murphy, "Similitude in Engineering," Roland Press, 1950, Chapter 6.
7. K. S. Valanis, "Unified Theory of Thermomechanical Behavior of Viscoelastic Materials," Published in "Mechanical Behavior of Materials under Dynamic Loads," U.S. Lindholm Editor, Springer-Verlag, 1968.
8. J. D. Colton, and H. E. Lindberg, "Mechanical Breakup of Reentry Vehicles Under Flood and Spot Loads (U)," Vol. 1: Mechanical Breakup of Reentry-Vehicle-Type Shells Under Spot Loads, (Secret) DNA-01-72-C-0062, 1972.
9. S. A. Leadbetter, H. W. Leonard, and E. J. Brock, Jr., "Design and Fabrication Considerations for a 1/10-Scale Replica Model of the Apollo/Saturn V," NASA TN D-4138, 1967.
10. P. J. Grimes, L. D. McTigue, G. F. Riley, and D. I. Tilden, "Advancements in Structural Dynamic Technology Resulting from Saturn V Programs," NASA CR-1540, 1970.

TIMewise OUTPUT OF PYROTECHNIC BOLTS

V. H. Neubert
The Pennsylvania State University
University Park, Pennsylvania

and

R. P. Parker
Uniroyal Research Center
Middlebury, Connecticut

The paper describes experimental results of measurement of output axial force versus time of explosive bolts. A Hopkinson bar arrangement was used with strain gauges located along the length of the bar to trace the force-time pulse, which was found to be a compressive pulse about twelve microseconds long. The pulse was sufficiently short that dispersion of the wave occurred in the one inch diameter bar. Results of some computations using the simple wave equation and the Love equation are included to help confirm the conclusions regarding the measurements. Some devices fabricated using primuline as the explosive are also briefly discussed.

INTRODUCTION

Vibrations and impact due to pyrotechnic shock are an important part of the environment which must be considered for equipment on spacecraft. On some missions, over one hundred pyrotechnic devices are detonated, including such items as nuts, bolts and pin-pullers. One of the most severe loading conditions appears to be that due to the tearing of a circumferential V-band joint, using primacord, to separate two stages of a rocket. Many acceleration spectra have been measured, usually up to 20,000 Hz, with some to 50,000 Hz, but it is not clear how one would use these spectra in a design analysis. Therefore, much proof-testing has been done; the best such device appears to be a full-scale barrel tester where actual pyrotechnics are used. For analysis and improvement of basic understanding, it was felt that a useful approach would be to measure the force-time output of some typical pyrotechnics and this force-time loading could then be used as a design loading.

The loading was measured with a Hopkinson bar arrangement, which is a long, thin elastic bar, traditionally used to measure axial loads applied at one end [1]. If the wave lengths of

the components of the applied transient load are long compared to the diameter of the bar, say by at least a factor of ten, the resulting stress wave travels along the length of the bar without changing shape. Longitudinal strain could then be measured at any point along the bar and the end loading deduced. As the ratio of wave length to bar diameter becomes small, dispersion of the stress wave occurs and the wave changes shape as it travels along the bar.

Two types of pyrotechnics were tested. The present report shows and discusses primarily the output from explosive bolts. Some preliminary work was also begun to determine resultant forces generated during the tearing of metal using primuline, which is a milder, string-like explosive than primacord.

Experiments and the associated analysis show that because the pulse is only ten to twelve microseconds long, frequencies at least to 80,000 Hz should be considered. The associated wave length in steel would be 2-1/2 inches, which is not long compared to the one inch diameter of the Hopkinson bar used for measurements, and dispersion of the stress wave occurred. Therefore, the simple one-dimensional wave equation and the more exact Love equa-

tion, which accounts for radial inertia effects in the Hopkinson bar, were used in analysis. Also in the bar, the particle acceleration is proportional to the time derivative of the strain or pressure-time pulse. Analysis indicated that the instrumentation available was not adequate to measure acceleration, and no acceleration measurements were attempted.

Since this work was completed, a similar apparatus was developed at NASA Langley and used to measure the output of explosive nuts. The resultant pulses appeared to be longer than those for the bolts. Strain and acceleration measurements were successfully made on the bar and results presented in Ref. [2].

EXPERIMENTAL ARRANGEMENT FOR BOLTS

Explosive bolts are available in many of the standard sizes from Halex, Inc. The studies reported here involved 1/4 inch and 3/8 inch diameter bolts. A typical 3/8 inch-24 bolt is shown in Fig. 1. The bolts are designed to fracture circumferentially at a specified "break line", 13/16 inch from the bolt head. The total charge, explosive plus primer, is 440 milligrams for the 1/4 inch and 450 milligrams for the 3/8 inch bolts. The bolts were detonated by touching extensions of the two wires to the terminals of a 12 volt automobile battery. The battery was found superior to a blaster's plunger or twist-type detonators, which produced considerable electrical noise.

In Fig. 1, the details of the attachment of the bolt to the end of the Hopkinson bar are shown. The Hopkinson bar was 100 inches long and one inch in diameter. It was supported at the quarter-points by piano wires in a pendulum arrangement. The end of the bar was drilled and tapped so the break line of the installed bolt would be flush with the end of the bar. The hole was countersunk 1/8 inch deep to a specified diameter to allow for expansion and tearing of the bolt at the break line. The bolt was inserted through a washer and chamber. The outer diameter of the chamber was one inch, but one of the first chambers fractured radially, so on subsequent tests the chamber used had a 1-1/2 inch outside diameter. The end of the chamber was also countersunk at the bolt expansion line. Typically, after the test, the bolt head and shank would remain stuck in the chamber and fly free from the bar. For safety, a five-sided box of 2 inch pine was slid over the end of the bar to catch the flying pieces. The threaded end would remain stuck in the bar. The threaded end was easily removed using a pliers and an easy-out tool so the same bar could be used for more than one test. All the tests of 3/8 inch diameter bolts were performed using this arrangement. Several tests were made with 1/4 inch diameter bolts with corresponding changes in dimensions of holes in the chamber and bar.

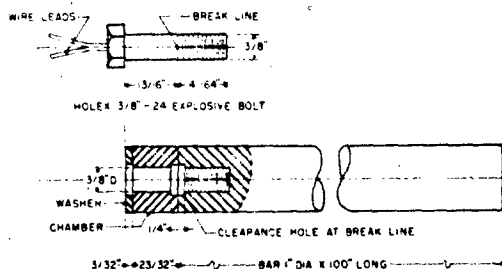


Fig. 1 Experimental Arrangement for Explosive Bolts

EXPERIMENTS WITH PRIMALINE

Another form of pyrotechnic, primaline, was studied briefly, and the preliminary results are presented here. Primaline is a miniaturized detonating fuse with approximately four grains/foot of explosive and a diameter of about 0.010 inch. It was furnished by the Ensign-Bickford Company. It is detonated with a standard electrical blasting cap. The detonation travels about 21,000 feet per second along the primaline.

At first it was not known what thickness of metal could be torn by primaline. In Fig. 2, an arrangement is shown by which four thicknesses of brass shim stock were tried at one time, each piece 3 inches by 1-7/8 inches. A heavy steel back-up plate 1/2 inch x 1-7/8 inch x 12 inches had a 1/8 inch x 1/8 inch groove machined along its length to receive the primaline and the thin brass plates were clamped to this plate. It was found that the primaline was capable of tearing all four thicknesses. No timewise measurements were made during this test. It appeared that the tearing action occurred in two steps--first a neat, 1/8 inch wide cut was made in the shim stock, then the gas pressure bent the remaining shim stock up against the face of the clamp. Since the primaline successfully cut brass plate as thick as 0.010 inches, this thickness was used on later tests with primaline.

The purpose of the third experimental arrangement was to measure the output of a 5/8 inch diameter ring of primaline during the tearing of brass material 0.010 inch thick, see Fig. 3. A brass end cap of 1-1/2 inch outer diameter was made to be screwed onto the end of

a 100 inch long, one inch diameter bar. A circular groove $1/8$ inch wide x $1/8$ inch deep and $5/8$ inch diameter was machined on the inside of the cap to hold the primaline. The thickness of material left to be cut was 0.010 inches. The primaline was fed in through a hole in the cap. The other end of the string of primaline was detonated using a standard electric cap which was exploded inside a box, made of two inch thick wood, to catch the pieces of the cap. After the test, a neat circular hole of $3/4$ inch diameter was left in the end cap. The circumferential length of contained primaline was nearly two inches, so the total pressure rise time should have been at least 9 microseconds, the time for the detonation to travel 2 inches along the cord.

The purpose of the fourth experimental arrangement was to excite beam bending vibrations. Again, a 100 inch long, one-inch diameter steel rod was used, supported at the quarter-points, but free to swing in the lateral direction. A brass jacket was made of 0.010

inch thick shim stock 2-1/2 inches long, see Fig. 4. The jacket was cylindrical except for a lengthwise bulge to receive the 0.01 inch diameter primaline. By using 2-1/2 inches of primaline, it was felt that the minimum rise time for the loading would be at least 11 microseconds. Again, the primaline cut the material neatly. Apparently an instant later, the diametrically opposite soldered joint failed, and two separate pieces of brass shim stock were found in the "collecting" box which is always placed over the bar end for safety purposes to catch debris.

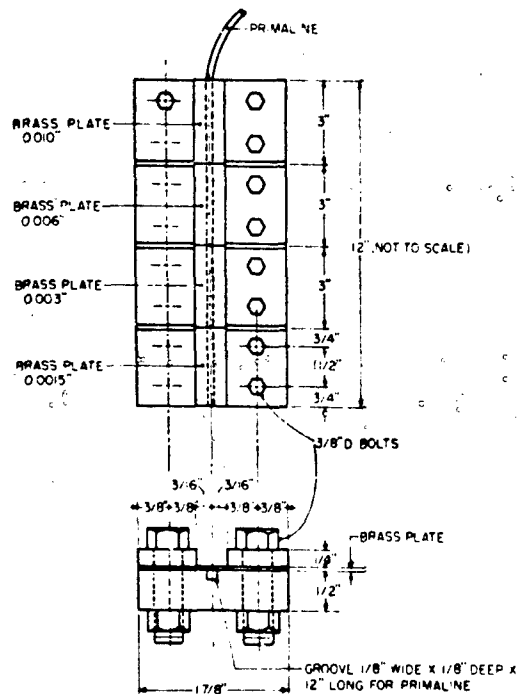


Fig. 2 Test Device for Tearing Various Plate Thicknesses with Primaline

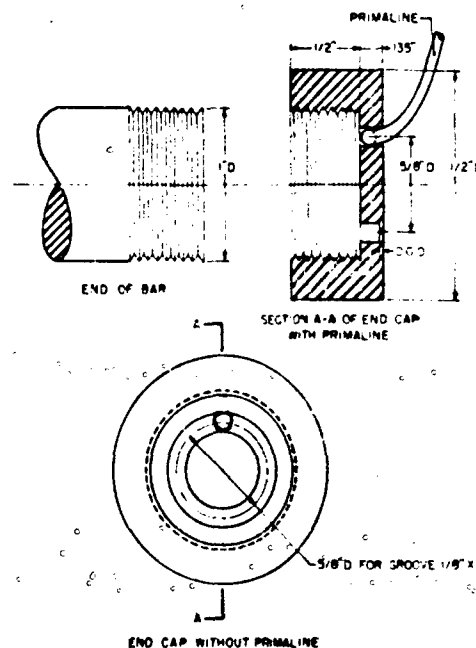


Fig. 3 Experimental Arrangement for Axial Excitation of Bar Using Primaline

ELECTRONIC EQUIPMENT

The pick-ups used were Micro-Measurement foil, resistance-type, strain gauges $1/8$ inch long. Each of these was connected to one arm of an Ellis BAM-1 bridge amplifier. Five bridge amplifiers were used. Two of these have DC to 100,000 Hz capability while the response of the other three begins to drop off at 25,000

Hz. The signals from the amplifiers were recorded on a Sangamo 3560 tape recorder, which on FM has a range of 0 to 80,000 Hz with a rise time of 5 microseconds. Signals were recorded at 120 inches per second and played back at 3-3/4 inches per second, giving a ratio of record-to-playback speed of 32.

Gauges were located at stations 5 inches, 10 inches, 20 inches and 50 inches from the end of the bar. Two strain gauges were located at each station, on diametrically opposite sides of the bar. The axis of the strain gauges was parallel to the axis of the bar, to measure axial strain. By having two gauges at each station, bending as well as axial deformation could be detected.

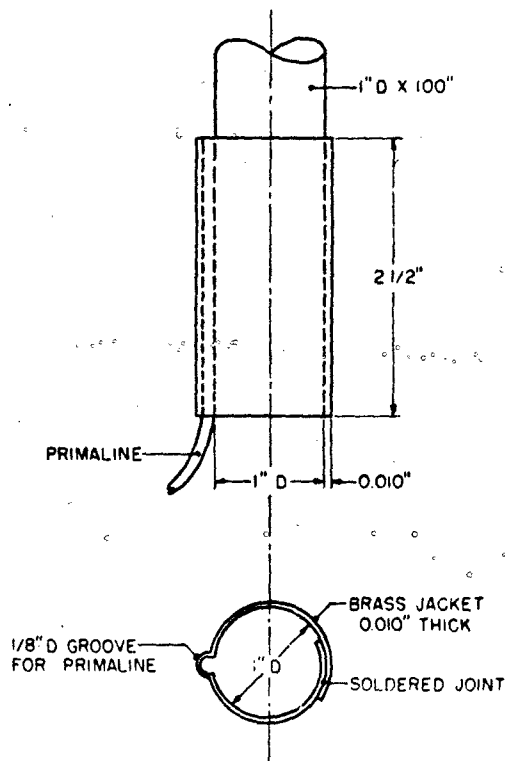


Fig. 4. Experimental Arrangement for Lateral Excitation of Beam Using Primuline

TEST RESULTS

The test results for a certain size bolt were quite repeatable. Typical experimental records are shown in Figs. 5 and 6. The records from two strain gauges located 20 inches from the explosion and on diametrically opposite sides of the bar are shown for the test of a 1/4 inch diameter bolt. Also shown is a 100,000 Hz timing signal. The strain signals should be of the same magnitude and phase if the pulse is axial, without bending. If there were pure bending the signals would be of the same magnitude but 180 degrees out of phase. The top set of records in Fig. 5 corresponds to an oscilloscope playback sweep speed of 5 milliseconds/major division. Multiplying by 1/32 for the relative tape speeds gives 156 microseconds/major division. A primarily compressive pulse first occurs at time t_1 , which is seen, reflected as a tensile pulse, again at time t_2 after travelling 160 inches. It then appears again as a compressive pulse at t_3 after travelling 40 more inches, after being reflected from the initially loaded end of the bar. Relating the distances travelled to the elapsed time between pulses indicates a wave speed of about 210,000 inches per second, which is close to the expected elastic wave speed for steel. The two lower playbacks of Fig. 5 correspond to 500 microseconds/division divided by 32 = 15.6 microseconds per division, which is confirmed by the timing trace. The central and lower set of signals show the first compressive pulse at time t_1 on the expanded time scale.

The two strain signals are seen to be almost perfectly in phase, indicating little bending. The difference in height is due to difference in amplification. Taking into account the calibration, the peak strain for the upper trace is 1140 microinches/inch and, for the lower trace, is 1190 microinches/inch. If the material is elastic, with $E = 30 \times 10^6$ psi, the corresponding peak stress is 35,700 psi. No permanent set was recorded by the gauges, so it is assumed that this is a reasonable estimate of peak stress at a distance of 20 inches from the explosion.

In Fig. 6, the playbacks were made with different amounts of time delay to show, in more detail for the same test as in Fig. 5, reflections of the initial pulse during its second and third appearances. The central display shows the first reflected tensile pulse at time t_2 , which indicates that an attenuation of about 45% occurred during the 160 inches of travel in the solid bar. The lower display shows again the tail of the same pulse as well as the first reflected compressive pulse at time t_3 , which appeared to right of center in the top display in Fig. 5. The top display shows this same reflected compressive pulse to a time scale expanded by a factor of two. It should

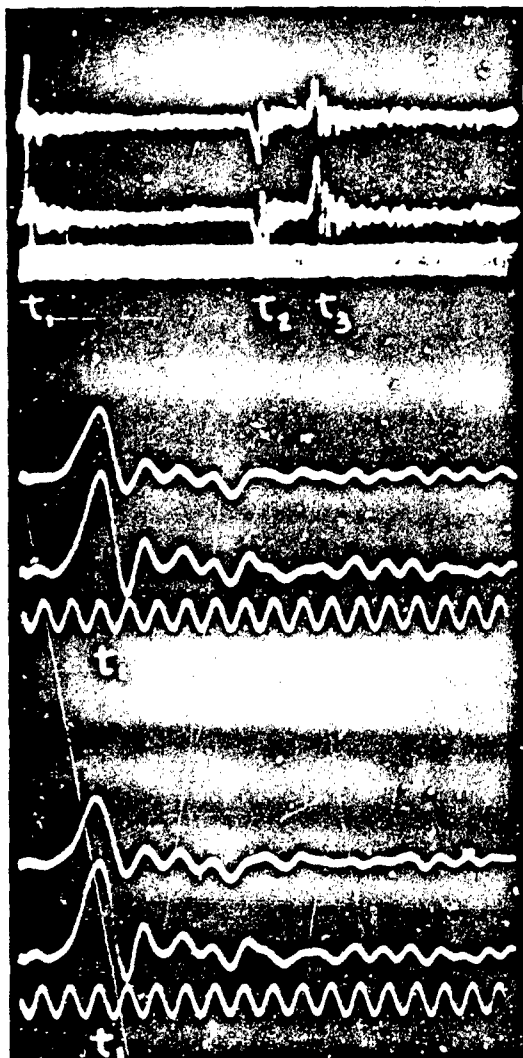


Fig. 5 Strain Records at $x = 20$ Inches Showing Long Term Response and Details of First Compressive Pulse, 1/4" Bolt

be noted that the pulse continues to decrease in magnitude and lengthen in duration, which indicates dispersion. Also the peaks immediately after the major peak tend to become relatively larger.

The pulses shown are typical in shape to

those obtained some distance from the explosion with different size bolts and also from the primeline in the end cap. Closer to the explosion, at the 5 inch and 10 inch stations, the initial strain signals showed tension as well as compression. The explosion and tearing process of the bolt is obviously complex. Initially, inside the bolt, a pressure would de-

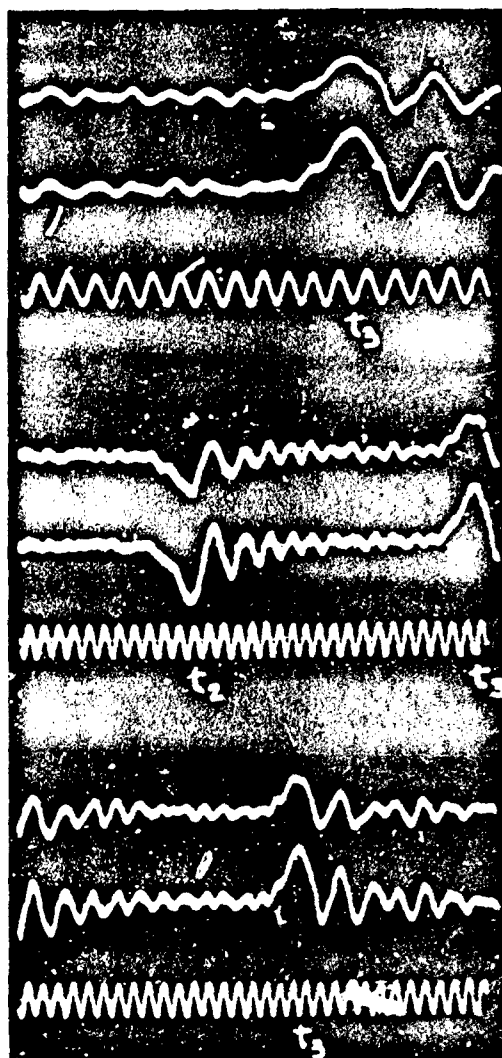


Fig. 6 Strain Records Showing Details of First Reflected Tensile and First Reflective Compressive Pulses, 1/4" Bolt

velop. The bolt cross-section would tend to be in tension, to contain the explosion, until it breaks. Thus the loaded end of the bar would feel a compression while the outer circumference, at the threads, would be in tension. The end of the bar is submitted to a complex stress distribution, and the waves must travel some distance before they can be considered nearly plane waves. Also, the length of the initial pulse compared to the bar diameter indicates dispersion should be expected.

Although no precise displacement measurements were made, it was observed that the bar, supported in a pendulum arrangement, swung about 8 to 10 inches. From this, the impulse delivered to the end of the bar checks well with the area under the load time curve.

THEORETICAL ANALYSIS FOR BAR

The purpose of the theoretical analysis for the bar is primarily to determine if the force-time input over the cross-section can be deduced from measurements at various stations along the bar. Once the net force-time output is known, presumably this could be applied as a load for analysis of other configurations.

For the elastic bar, analysis was performed using the simple wave equation in one dimension

$$E \frac{\partial^2 u}{\partial x^2} = \rho \frac{\partial^2 u}{\partial t^2} \quad (1)$$

in comparison with the Love [3] equation

$$E \frac{\partial^2 u}{\partial x^2} = \rho \frac{\partial^2 u}{\partial t^2} - \rho v k^2 \frac{\partial^4 u}{\partial x^2 \partial t^2} \quad (2)$$

where ρ = mass density

E = Young's modulus

v = Poisson's ratio

k = radius of gyration of the cross-section about a longitudinal axis

The assumed force-time input to the end of the bar was

$$F(t) = F_0 \sin \omega t \quad 0 \leq t \leq \frac{\pi}{\omega} = t_0$$

$$= 0 \quad t > \frac{\pi}{\omega} = t_0$$

Theoretical pulse lengths of 10 and 25 microseconds were used, corresponding to $\omega = 100,000$ and $40,000$ respectively.

A.) One-Dimensional Wave Equation

Since much practical structural analysis is performed using a normal mode approach, the solution for Eq. (1) was first carried out by that method. It is well known that the pulse travels the bar without change in shape according to this theory, so the convergence of the normal mode solution could be checked against the exact solution.

In Fig. 7, the result of summing 50, 100, 200 and 500 modes is shown for a 10 microsecond half-sine pulse with $P_0 = 30,000$ pounds, which corresponds to a stress of 38,200 psi, or a strain of 1,270 microinches/inch. The curves show the predicted strain pulse at $x = 20$ inches and 50 inches. The 200 mode solution still involves about a 5 percent error in prediction of peak strain and a 15 percent error in pulse length. Use of 500 modes results in very negligible error.

In Fig. 8, the predicted acceleration is shown at $x = 50$ and at $x = 100$ inches, for the first wave, and again at $x = 50$ inches for the first reflection.

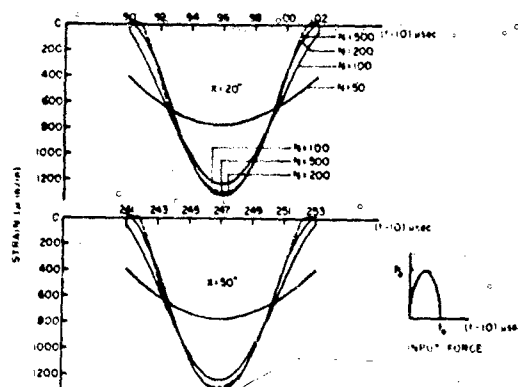


Fig. 7 Strain Versus Time, Elementary Bar Analysis, $t_0 = 10 \mu\text{sec}$, $P_0 = 30,000 \text{ lb}$.

The one-dimensional theory indicates that the following should be true:

If $u = f(x-ct)$ for a wave travelling in the positive x -direction,

$$\text{strain} = \frac{\partial u}{\partial x} = f'(x-ct)$$

$$\text{particle velocity} = \frac{\partial u}{\partial t} = -cf'(x-ct)$$

$$\text{particle acceleration} = \frac{\partial^2 u}{\partial t^2} = c^2 f''(x-ct)$$

$$\begin{aligned} \text{strain rate} &= \frac{\partial^2 u}{\partial x \partial t} = -cf''(x-ct) \\ &= -\frac{1}{c} \frac{\partial^2 u}{\partial t^2} \end{aligned}$$

The particle acceleration time curve would be proportional to the slope of the strain curve. For a 10 microsecond strain pulse, the particle acceleration is as shown. Peak acceleration is about 83×10^6 in/sec² or 215,000g at the center of the bar. Due to reflection at the free end of the bar, it is doubled. The solutions for 50 and 500 modes are shown.

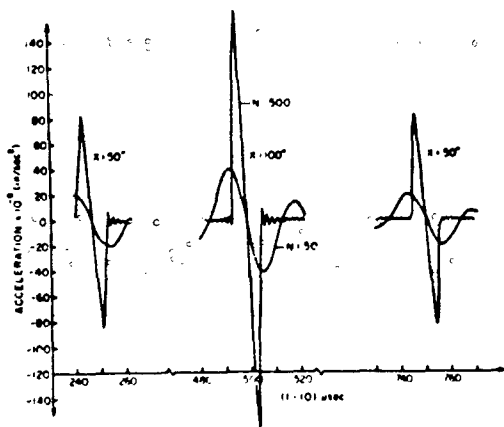


Fig. 8 Acceleration Versus Time, Elementary Bar Analysis, $T_0 = 10$ μ sec, $P_0 = 30,000$ lb.

In Fig. 9, the convergence of the acceleration-time solution for the first reflected pulse is shown for the various number of modes. Straight lines are shown if sufficient points were not computed to trace a curve. Since acceleration is proportional to the derivative of the strain, it converges less rapidly. Note that the 200 mode solution has a precursor wave which should not exist, but this is eliminated by taking more modes.

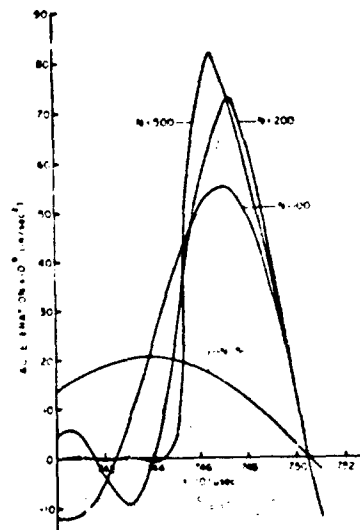


Fig. 9 Acceleration Versus Time, $x = 50$ inches, Elementary Bar Analysis, $T_0 = 10$ μ sec, $P_0 = 30,000$ lb.

B.) Love Equation

In Fig. 10, the stress pulse is shown at $x = 5$ inches, 10 inches and 50 inches as predicted by the Love theory. Dispersion is indicated by the fact that the peak stress decreases in magnitude as the wave travels, the apparent pulse length increases, and a tension "tail" begins to develop. A longer pulse should show less dispersion for the same diameter bar. This is demonstrated in Fig. 11, where the pulse shape at 50 inches is compared for a 25 microsecond half-sine pulse compared to a 10 microsecond half-sine pulse. The pulse shape at various stations for a 10 microsecond pulse agrees fairly well with that predicted by the Love theory. The experimental pulse also lengthens with distance travelled.

decreases in magnitude, and tends to develop the "tail".

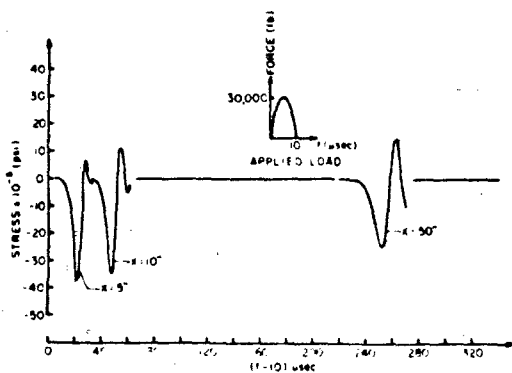


Fig. 10 Stress Versus Time, Love Theory, $t_0 = 10 \mu\text{sec}$, $P_0 = 30,000 \text{ lb}$.

THEORETICAL ANALYSIS FOR A BEAM

In order to determine if the $P(t)$ derived from the bar tests could be used for more complex structures, one test was performed to excite the 100 inch bar in bending using the apparatus of Fig. 4. The analysis of the bar as a free-free Timoshenko beam submitted to a lateral half-sine pulse of a 10 microsecond duration was completed by Parker [4]. However, it appears that the tearing of the sleeve in Fig. 4 does not produce a sharp lateral pulse because the pressure wave quickly tears, folds and blows the entire sleeve away, so the end of the bar is quickly engulfed in the air pressure wave. A stiffer sleeve would probably be better, but the added mass may effect the beam vibrations. Further work is necessary here.

SUMMARY AND SUGGESTIONS FOR FURTHER STUDY

Results to date may be summarized as follows:

1. The measurement of strain in a solid bar five or more inches from the explosion appears to present no experimental difficulty with the equipment used. The rise time is about 10 microseconds which is within the capability of the amplifiers and recorders used. The measurement of acceleration is more difficult, because

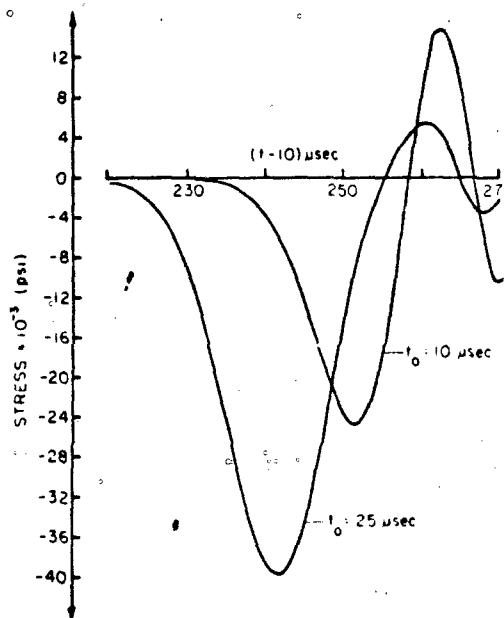


Fig. 11 Stress Versus Time at $x = 50"$, Love Theory $t_0 = 10$ and $25 \mu\text{sec}$, $P_0 = 30,000 \text{ lb}$.

of the more rapid rise time and the high acceleration involved.

2. The example given here showed a peak stress of 35,700 psi from a 1/4 inch bolt at the 20 inch station, with no permanent set. Nearer the explosion, apparent stresses of 55,000 psi were measured in the mild steel bar with no permanent set. This is assumed to be due to increased yield strength associated with the high rate of loading.

3. The net impulse is compressive even though the pressure-time variation over the cross-section at the bolt threads must be quite complex. Initially the pressure would increase causing compression. The bolt wall is in tension as it attempts to contain the explosion. Thus there might be first a net compressive phase and then a tensile phase, although the compressive phase seems to dominate for the

bolts. At the 5 inch station, for the primaline axial loading, a tensile phase appeared first, followed immediately by a compressive pulse. This may be due to the fact that the threaded portion is on the outside of the bar for that test. At greater distances from the explosion, the compressive pulse dominates for the primaline, too. Thus it is felt that 5 or 10 inches from the explosion, the strain at the surface is not representative of the strain distribution over the cross-section.

The fact that the net impulse is compressive was also shown by the fact that the bar, supported like a ballistic pendulum, swung away from the explosion in every case. The net impulse was checked by observing the amount of the swing on several tests.

4. The prediction of strain or acceleration due to pyrotechnic shock is not at all hopeless. Elastic wave theory is adequate for the configurations used. Normal mode solutions were attempted because there is great interest in the number of modes excited. This interest is associated with the use of finite elements and related grid spacing. Summing of many modes for a bar or Bernoulli-Euler beam is accurate and inexpensive. The Timoshenko beam normal mode solution for a free-free beam became much more difficult. More experimental work needs to be done with beams. After that, shells should be investigated, since analysis would save much present expensive prooftesting. Response of shell-mounted equipment is of primary interest. It would appear that some techniques may be used based on mechanical impedance and Fourier transform to avoid summing many modes.

5. A principle result of the study is the conclusion that significant high frequency accelerations exist above 10,000 Hz and that efforts should be made to measure accelerations to higher frequencies. As capability of instrumentation extends to higher frequencies so does the interest in structural and material response. It is recognized that in many aerospace structures, pyrotechnic disturbances lose high frequency content rapidly as they are transmitted through complex structures. This is confirmed in data presented by Rader and Bangs [5], who show shock spectra to 10,000 Hz. The same data also shows that there is a possibility of amplification by the structure. A shock spectrum is shown in which the level 35 inches from the source is almost twice as great as the level 3 inches from the source, at 1600 Hz. In a separate report [6], data for response of a stiffened shell, shows very little attenuation with distance along a longeron, but there is attenuation around the circumference of the shell. In reference [6], some shock spectra are presented to 30,000 Hz.

6. Careful design and prooftesting has apparently minimized the problem of structural and electronic equipment damage due to pyrotechnic

shock. However, the improvement of design analysis procedures still represents considerable challenge. Shock spectra are of limited usefulness, in part because of the well-known weakness that associated phase information is lost. It is felt that the study of effective force-time outputs is more basic and useful for design purposes and should be pursued further.

REFERENCES

1. Davies, R. M., "A Critical Study of the Hopkinson Pressure Bar", Phil. Trans. Royal Society, series A, Vol. 240, 1948.
2. Bement, Laurence J. and Neubert, V. H., "Development of Low-Shock Pyrotechnic Separation Nuts", Proceedings of the Eighth Aerospace Mechanisms Symposium, NASA Langley Research Center, October 18-19, 1973.
3. Love, A. E. H., "The Mathematical Theory of Elasticity" 4th Edition (1st American Edition) Cambridge University Press, 1944.
4. Parker, R. P., "High Frequency Response of Bars and Beams", Ph.D. Dissertation, Department of Engineering Mechanics, The Pennsylvania State University, March 1973.
5. Rader, W. P. and Bangs, W. F., "A Summary of Pyrotechnic Shock in the Aerospace Industry", Shock and Vibration Bulletin 41, Part 5, p.9, Naval Research Laboratory, Washington, D. C. 1970.
6. McGrath, Michael B. and Rader, E. Paul, "Shock Propagation in Aerospace Structures" Task No. 85838, Martin Marietta Corporation, January 1969.
7. Neubert, V. H. and Parker, R. P., "High Frequency Shock of Spacecraft Systems", Final Report, NASA Contract NGR 39-009-146, November 24, 1971.

ACKNOWLEDGMENTS

The work was carried out under NASA Contract NGR 39-009-146, which resulted in a final report dated November 24, 1971 [7]. A doctoral thesis [4] has also been published which resulted from the studies. The initial interest of Mr. Homer Morgan and Dr. J. P. Raney of NASA, Langley is greatly appreciated. The suggestions of Mr. Robert Hayduk and Dr. E. T. Kruszewski were also very helpful.

DISCUSSION

Mr. Chapman (Jet Propulsion Laboratory): We have long speculated about the frequencies generated from pyrotechnic devices and your paper is very enlightening in that respect. Your concern over the high frequency would depend upon your mode of business. If you were a semiconductor manufacturer you would be interested in the frequency range that you talk about based upon your 12 microsecond primary pulse. I was very surprised to see that the duration of time was that small. On the other hand if you are designing spacecraft and if you are interested in primary members you are worried about the lower frequencies, but in any case it seems as if the biggest problem is in measuring these events accurately. In your case you used an oscilloscope so the data are realistic; when you just put it into a commercial charger amplifier and then into a tape recorder that has a bandwidth of 80,000 Hz, and is running at 120 inches per second you may not be getting the results that you think you are getting. It is my opinion that in many cases, depending on how close your transducer was to the actual event, you may be seeing the impulse response of the electronics rather than what actually physically occurred in the detonation of the device.

Mr. Parker: I think the fact that we have fed in 100,000 timing signals, and it came out is some indication that we were seeing what we think we were seeing.

Mr. Prescott (Jet Propulsion Laboratory): In these tests, both of the Halex Bolt and of the Primaline you are dealing with an impulse input from a high explosive with a detonation velocity of maybe 6,000 meters per second. This is a different class than an explosive device that would use a power cartridge that would be essentially a pressure generation device, where the pressure would build up in perhaps a quarter to a half millisecond. It might be that the frequencies involved in something like that might be considerably lower.

Mr. Workhoven (Sandia Laboratories): Could elaborate on the mounting techniques of the strain gages that you used, and perhaps the problems that you had?

Mr. Parker: We didn't use Eastman 910 cement on that job; as I recall it we used a heat cureable epoxy that was manufactured by Baldwin-Lima-Hamilton. We used the same bar for several tests since they were not destructive, and there was no evidence that the gages were coming loose after eight or ten tests.

PYROTECHNIC SHOCK REDUCTION*

S. N. Prescott
Jet Propulsion Laboratory
Pasadena, California

The pyrotechnic shock output from electro-explosive release devices has been reduced by changes in the separation mechanism designs. State-of-the-art hard point release devices were tested on an instrumented simulated spacecraft structure. The accelerometer data were reduced by computer analyses to shock spectra. Comparisons were made between shock spectra and actual degradation or damage to spacecraft equipment. Theories of shock generation mechanisms were propounded. Devices were designed and fabricated to incorporate shock mitigation features suggested by theory. These devices were fired on the instrumented structure and the shock spectra obtained were compared with those taken from the previous devices. Significant reduction in shock output was noted.

INTRODUCTION

Pyrotechnic shock can be defined as the complex vibration and shock transient generated by the actuation of an explosive or pyrotechnic device. Pyrotechnic shock differs from other mechanical shocks by the predominance of high frequency excitation with intermediate peak accelerations. These peaks may occur at the local resonant frequencies of the structure.

The actual amount of mechanical shock introduced into the structure by a space vehicle type pyrotechnic device is very small when compared with the kind of shocks which you find in military applications both in the operation of weapons and the effect of someone operating weapons against you. But these relatively small shocks are important to people in the spacecraft design business because spacecraft are relatively small and therefore the pyrotechnic devices are necessarily close to all the mechanisms and equipment aboard. Spacecraft contain delicate components which have been found to be sensitive to shock. New spacecraft designs have intensified the effects

of the mechanical shock output from pyrotechnic devices. Miniaturized electronics and sophisticated experiment devices are more sensitive to damage from high frequency inputs of relatively low total energy. Hard point structural separation joints provide direct pyrotechnic shock paths. The rigid structure transmits high frequencies of shock. The requirements for pyrotechnic redundancy call for the use of dual squibs. This doubles the explosive energy input. Heavier spacecraft require higher preload on attachment devices with a resultant increase in stored energy. These increases in pyrotechnic shock cause increased cost in design constraints, shock mounting, testing of components and systems, and failure analysis.

If we do have failures, they are not usually of a predictable type. They include migration of particles within integrated circuits causing random shorts, or brittle failures of small components which have the appearance of fatigue failures. Gyro drift has been induced up to one half of the total allowable drift from spacecraft separation device initiation.

*This paper presents the results of one phase of research carried out at the Jet Propulsion Laboratory, California Institute of Technology, under Contract No. NAS7-100, sponsored by the National Aeronautics and Space Administration.

Changes in frequency of radio crystals has been seen after pyro shocks.

The conventional method of assessing the effects of pyrotechnic device shock on a particular spacecraft is to assemble all subsystems on a "developmental test" or "pyrototype test model" spacecraft and fire all pyrotechnic devices. The electronic subsystems are monitored during the test for transient effects or examined after the test for evidence of permanent damage. Obviously, this test can be performed only after the design and fabrication of the initial spacecraft is complete. Attention to the reduction of shock generating mechanisms in the design of pyrotechnic devices would contribute much to the successful outcome of spacecraft pyro shock tests.

In general, there are three approaches to the problem of pyrotechnic shock: shock isolation of components; shock attenuation in structures; and the reduction of the shock produced at the source. This last approach was used in the research described here.

This investigation of pyrotechnic shock mitigation was initiated as a part of the Outer Planets Grand Tour spacecraft Technical Development Continuation program. After cancellation of this project, the information which had been obtained was collected in this report.

These data are presented for information only and do not constitute endorsements or evaluation of the specific devices tested or of their manufacturers.

RATIONALE

The shock output of conventional pyrotechnic devices of a variety of types and from various manufacturers were to be characterized by tests on a typical spacecraft structure. This characterization was to be correlated with damage indications on actual spacecraft components. A model of the shock production mechanism was to be developed. Pyrotechnic devices which eliminated or greatly reduced pyro shock effects were to be demonstrated. Design criteria were to be established for reliable, low shock devices.

INITIAL DEVICES TESTED

To keep the investigation within manageable limits, it was restricted to hard point release devices installed with an axial preload of 10,000 pounds. The mounting provisions were kept as similar as possible. The stored energy

in the structure external to the release device itself thus remained constant.

The purpose of these initial tests of off-the-shelf devices was to provide a baseline against which to compare the effects of design changes. Pyro shock data were obtained on the devices described as follows:

Type A - Pyrotechnic release nut

Type B - Explosively actuated bolt

Type C - Explosive nut

Type D - Dual piston separation bolt

Type E - Explosive nut

The Type A release device consists of a segmented nut retained by a locking piston encased in an external housing. The firing of an explosive squib displaces the piston and releases the nut segments. An inner piston expels the attaching bolt. (Figure 1.)

The Type B/C explosively actuated bolt/nut assembly has two different modes of separation. The bolt is separated in the shank area on firing by actuation of a piston against elastomer pads. The nut contains a special threaded collet which opens on firing releasing the grip of the bolt. The device was tested in each mode and in simultaneous release but instrumentation difficulties prevented the recording of usable data in all but the nut release mode (Figure 2).

The Type D dual piston separation bolt has one separation plane and is separated by the pyrotechnic actuation of one or both of two internal pistons (Figure 3). Data were obtained

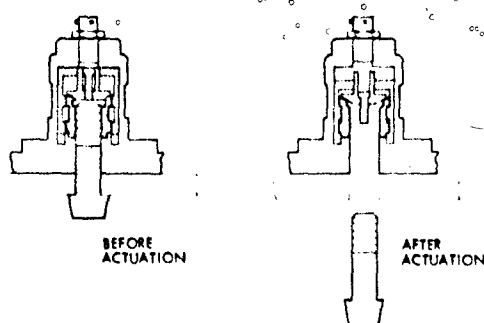


Fig. 1 - Segmented nut

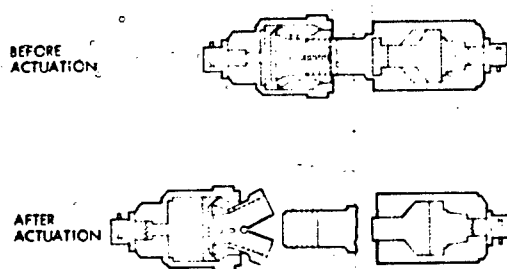


Fig. 2 - Bolt/nut assembly

on actuation of both pistons in individual and simultaneous firings.

The Type E explosive nut assembly contains a threaded and slotted nut which is deformed by a piston to release a bolt similarly to the Type C device.

A number of other devices were scheduled to be tested. A reduction of scope required by funding constraints prevented further state-of-the-art tests.

Test Structure and Instrumentation

The test structure consisted of half of an actual Mariner spacecraft. It was attached rigidly to a metal floor plate (Figure 4). The spacecraft structure was of semimonocoque construction with longerons and shear web skin. There were simulated electronic chassis "black boxes" attached in the same manner that would be used on the actual space vehicle. Relays and other circuit components mounted in these boxes were electrically monitored for shock effects. High frequency crystal shock

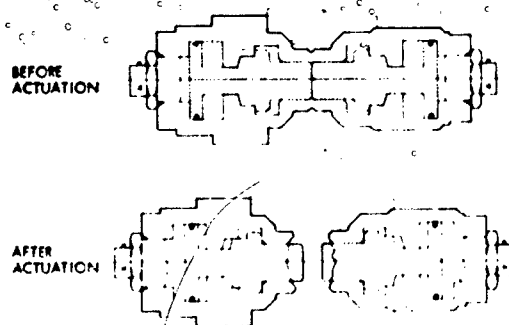


Fig. 3 - Dual piston bolt

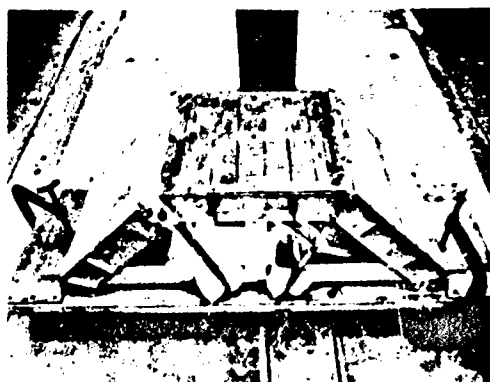


Fig. 4 - Test structure

accelerometers were mounted at twelve points on the structure and chassis (Figure 5). Therefore, data were obtained, both on nearby shock effects and on the shock transmitted through realistic structural paths [1].

Each release device was mounted on an aluminum plate (Figure 6) and attached to a similar plate which was mounted on the spacecraft structure by three one-quarter inch cap-screws. Thereby the structural preload external to the device consisted of a ten thousand pound load between two one-half inch aluminum plates.

Data Conversion

The data were recorded on 12 channel, 20 kilohertz, FM tape at 60 inches per second. To allow direct comparison of shock damage potential, the acceleration data were converted to shock spectra [2].

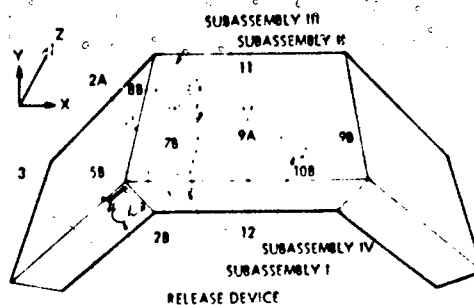


Fig. 5 - Accelerometer locations

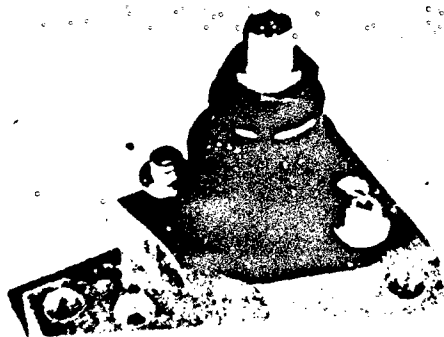


Fig. 6 - Device mounting

The conversion of analog data from the accelerometers to shock spectra was accomplished by digitizing the data in the selected time interval, and transforming the data from the acceleration-vs-time domain to the acceleration-vs-frequency domain by a Fortran program [3] adapted for the Univac 1108 computer. The transformation was assigned a Q value representative of the structure. The shock spectrum of a transient at a point on the structure was taken to be the maximum response of a massless oscillator placed at that point where the transient was applied to the transducer. Both "primary" and "residual" shock spectra were obtained and printed by a Stromberg-Carlson 4200 plotter (Figure 7).

The primary shock spectra in the region between 20 Hertz and 20,000 Hertz were plotted on a log-log scale of acceleration values from 10 "g"s to 100,000 "g"s. All spectral data were obtained with a Q of 20. As a check on the conversion effect of an assigned Q value, the data from one accelerometer was converted into shock spectra with Q values of 5, 10, and 20. As would be expected, the magnitude of the digitally generated shock spectral "g" levels was a direct function of Q. The relative intensity versus frequency remained the same.

For budgetary reasons, all data were not converted to shock spectra. Representative accelerometer locations were chosen and comparative shock spectra were generated for the various types of devices.

Mechanism of Shock Production

An examination was made of the apparent shock generation mechanism of each device. The predominant causes of high shocks were estimated to be:

- impact of moving parts which had been accelerated by pyrotechnics
- energy released by the fracturing of separation device parts

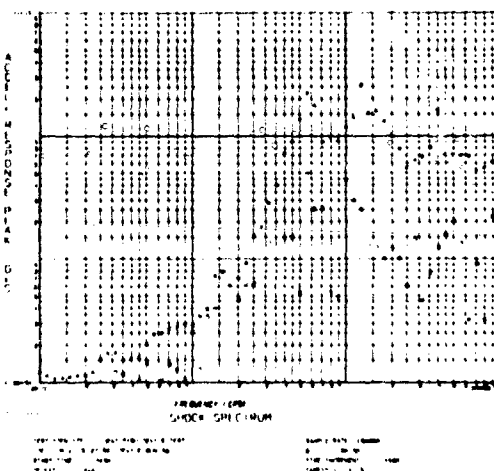
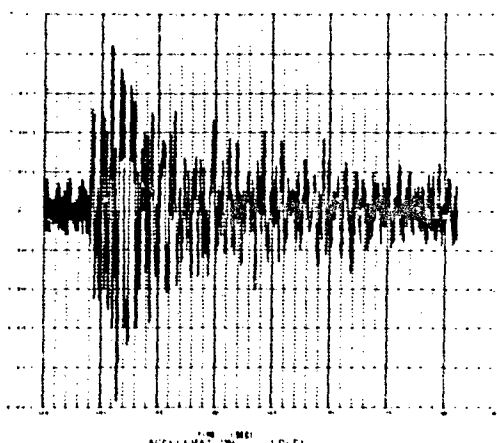


Fig. 7 - Plotter output

- sudden release of the preload energy in the device and in the attached structures.

As all of the devices mentioned in this report were actuated by deflagrating squibs (metal-oxydant mixes) no high explosive detonation phenomena were considered.

The reasoning behind this selection of pyrotechnic shock mechanisms started with the observation of device squib tests. Pressure versus time measurements were made at the Jet Propulsion Laboratory on production lots of the explosive squibs which are used to actuate pyrotechnic devices. These squibs were fired in constant volume test bombs and the pressures generated were recorded with pressure transducers. An accelerometer was attached to the test bomb in an attempt to get a time indication of squib initiation. Examination of the "g"s output of the accelerometer revealed that a much lower output was recorded than was recorded on pyrotechnic device shock tests. This indicated that "pyrotechnic shock" was not primarily caused by squib firing. Obviously, energy transfer mechanisms other than the simple pressurization of the device body, were responsible. Relating the textbook treatment of impact to an actual design problem can be difficult. But exact answers are not always necessary [4]. Examination of the function of each type of device provided insight into the major causes of shock generation. (Figure 1)

The Type A device has a locking piston which was accelerated by the squib pressure. When this piston reached the point in its travel where the corners of the nut segments no longer were restrained, the pre-load on the bolt was released. This produced a sudden relaxation of the deflected components, modified by the sixty degree ramp provided by the mating screw threads. The piston continued to move until it impacted the housing which was in contact with the structure. The primary shock generation mechanism was estimated to be impact of moving parts. The stored energy released was a secondary shock source as the internal deflections in the device due to loading were small.

The Type B explosively actuated bolt shown in Figure 2 is broken in tension when an internal piston accelerated by an explosive squib strikes an elastomer pad. The kinetic energy of the piston, augmented by the residual pressure against it is partially transferred into hydrostatic shock in the elastomer. The high transient stress breaks the bolt at the minimum cross-section plane. The remainder of the

piston energy is expended in impact with a conical retaining surface. Pyrotechnic shock energy was generated by fracturing separation device parts, and impact of moving parts. Stored preload energy was estimated to be small from visual examination of the bolt.

The Type C explosively actuated nut shown in Figure 2 releases the bolt when an explosively accelerated piston strikes a slotted nut and deforms it to disengage the threaded collet. The primary shock generation mechanism is estimated to be the impact of moving parts with sudden release of preload energy as a secondary effect. The Type D dual piston separation bolt shown in Figure 3 presents the same apparent shock generation mechanism as the Type B bolt.

The Type E nut assembly was similar to the Type C nut in function and shock generation mechanisms.

Principles of Low Shock Device Design

Pyrotechnic shock is characterized by sudden transfer of energy to structure. The same energy released over a longer period of time can be absorbed without the generation of high frequency shocks. Momentum exchange between the pyrotechnic device and the structure is caused by the center of gravity shift during actuation. Shocks induced in the same direction that structural loads are carried are transmitted into surrounding structure more efficiently. Shock pulses are generated by the fracturing or impact of pyrotechnic device parts. Based on these rather obvious points, the following preliminary principles of low-shock device design were proposed:

- gradual release of stored energy
- cancellation of external momentum exchange
- management of primary shock direction
- eliminating impact of moving internal parts

Revised Pyro Devices Tested

Modified and redesigned devices were made in-house or were submitted for test by outside manufacturers. These designs incorporated provisions for reducing the internally stored mechanical energy, eliminating the impact of moving internal parts, and reducing the rate of release of stored preload energy.

Each device was mounted on the test structure with the same plates and preload as that used in the first series of tests. The instrumentation was unchanged. Pyro shock data were obtained on the devices described as follows:

The Type F release device was modified from a v-band release mechanism to provide solid mounting of the housing. The stud is released when a pyrotechnically-actuated piston moves up to free captive rollers which allow a collet to spread. The end of the stud is released as a gradual release of stored energy (Figure 8).

The Type G release device consists of a segmented nut with a shallow acme-type thread. It is retained by a collar which is displaced by the firing of an explosive squib. The collar incorporates pins which act in tapered grooves to separate the nut segments and provide a gradual release of stored energy (Figure 9). This design also reduces the radial loads and thus the actuation energy required for release should be lessened.

The Type H release device contains a spool-shaped threaded segmented nut which is held in place by two grooved pistons in a common housing. Pressure from an explosive squib is ducted to the opposite ends of the two pistons, forcing them together. The spool ends of the nut segments fall into the grooves in the pistons and release the bolt. All internal impact is between opposed pistons not directly coupled to structure (Figure 10). This eliminates the external momentum exchange.

The Type I release device consists of a clevis with a pin passing through a hole in the loaded stud. The pin has an integral piston which travels in an enclosed housing. Upon the firing of a squib, the piston withdraws the pin

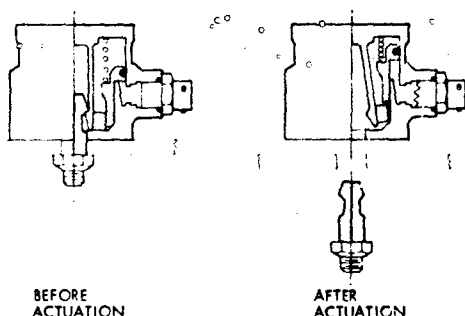


Fig. 8 - Collet release

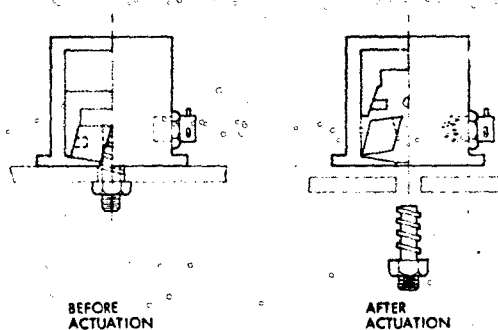


Fig. 9 - Acme-type nut

and releases the stud. The piston moves at right angles to the load axis and provides management of the primary shock direction (Figure 11).

The Type J release device consists of a segmented nut and locking piston similar to the Type A device. The piston, however, is displaced in the opposite direction and impacts the free end of the housing, thus loading it in tensile rather than compressive shock. This is another example of the management of primary shock direction.

The Type K release device is similar to the Type J except that there are two pistons which move in opposite directions until the pressure between them is equalized by internal venting. The pistons do not contact each other. This eliminates the impact of moving internal parts. (Figure 12)

TEST RESULTS

The shock spectra for the baseline tests are shown for selected accelerometer locations on Figures 13 through 20. Device Type A was of most interest on the spacecraft program and was used as the baseline standard against which to compare candidate low-shock devices.

The transducer locations chosen for comparison provide a selection of structural conditions.

Location 1 is on the device mounting plate and in the axis of preload and separation.

Location 2B is on the nearest electronics sub-chassis and in the separation axis.

Location 9A is on a more remote sub-chassis and is oriented at right angles to the separation axis.

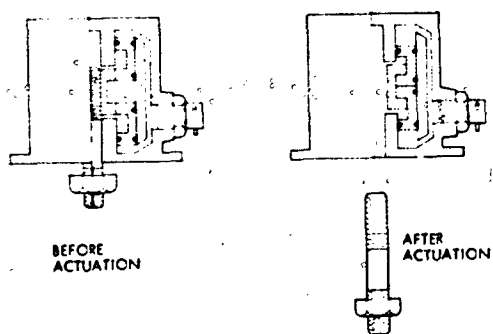


Fig. 10 - Dual piston nut

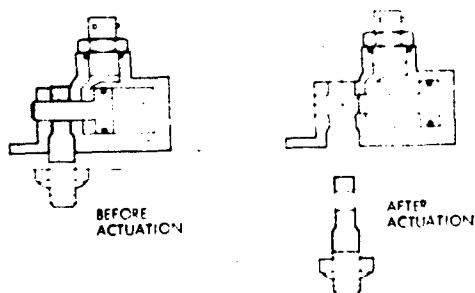


Fig. 11 - Pin puller

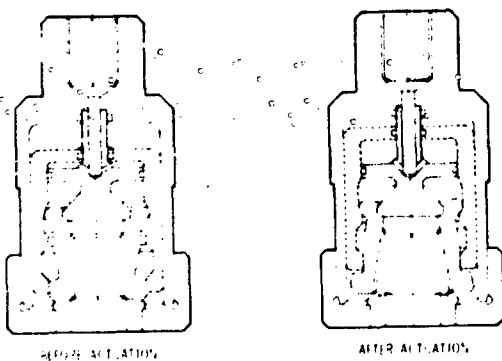


Fig. 12 - Floating piston release device

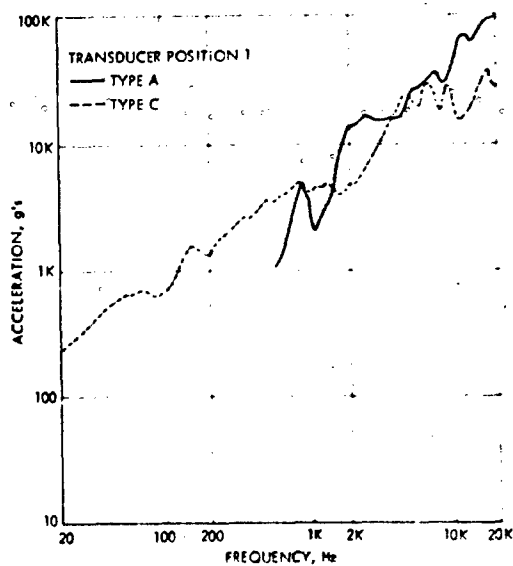


Fig. 13 - Baseline spectra

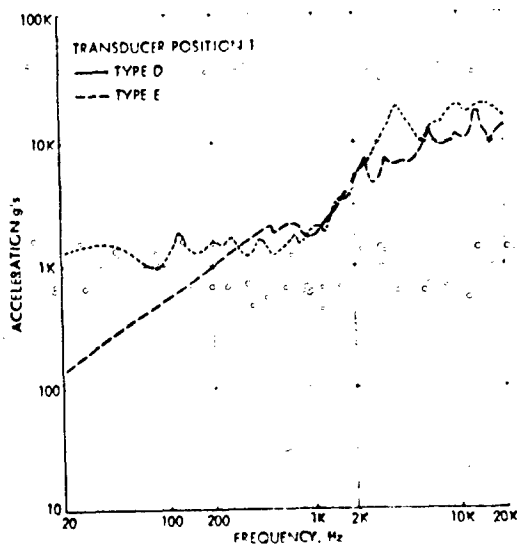


Fig. 14 - Baseline spectra

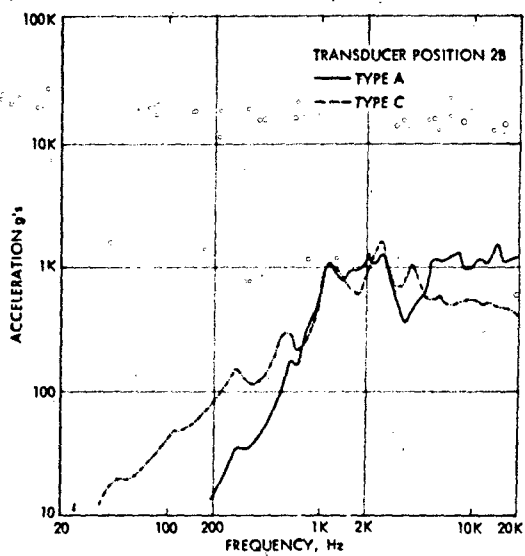


Fig. 15 - Baseline spectra

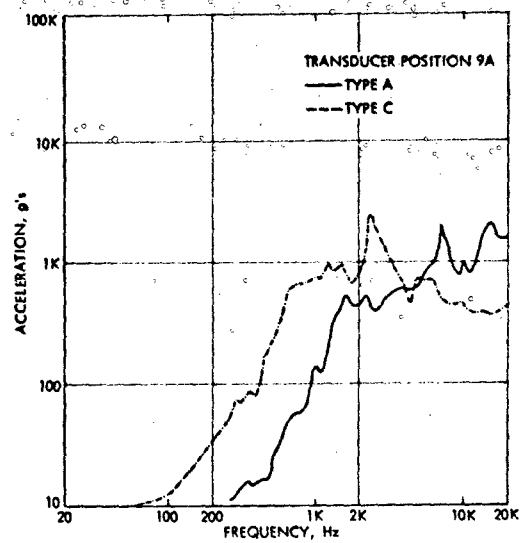


Fig. 17 - Baseline spectra

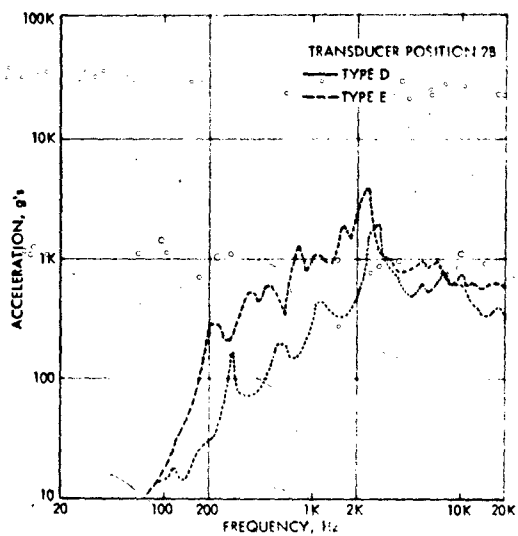


Fig. 16 - Baseline spectra

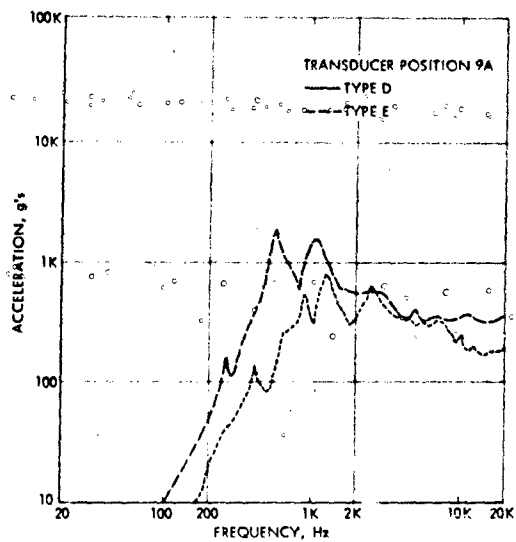


Fig. 18 - Baseline spectra

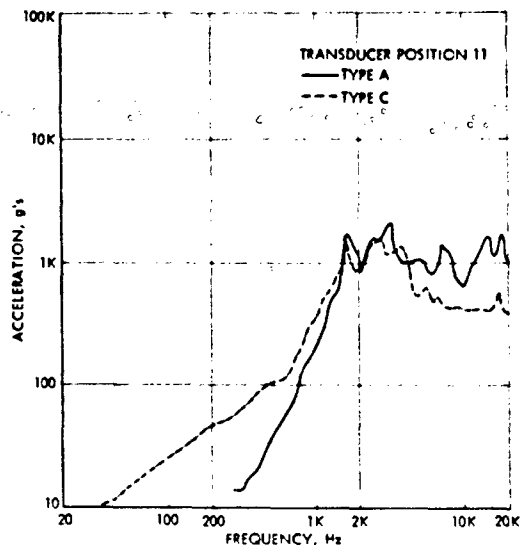


Fig. 19 - Baseline spectra

Location 11 is in the middle of a shear plate over the central chassis rail of the central bay of the simulated spacecraft. It is oriented at right angles to both the separation axis and to transducer number 9A.

The shock spectra for the low-shock design device tests are shown on Figures 21 through 32. The shock spectra are shown for the same transducer locations as presented for the baseline devices. Device Type A is shown for comparison purposes on all spectral plots.

The residual shock spectra (shown as squares on Figure 7) were in general, lower in "g" level than the primary spectra and are not shown on these combined spectral plots.

The indications of relay chatter (from components mounted on the electronics sub-chassis) correlated with the peak "g" readings taken at the same points on the structure. Of thirty-eight relay contacts which were monitored during pyrotechnic device firings, fourteen sets of contacts transferred or chattered during a Type A device test. Five sets of contacts transferred or chattered during the firing of the "low-shock" collet release device Type F. Only one set of contacts chattered during the pinpuller Type I test.

The comparisons between conventional pyrotechnic devices and low-shock devices

were made on the basis of shock spectra induced in the test structure at the same accelerometer positions.

A broad study of aerospace pyrotechnic shock test results has concluded that failure data has not been sufficient to relate the shock environment to damage potential [5]. Present functional design requirements for spacecraft pyrotechnic shock environments are, however, specified in terms of shock spectra [6]. With a frequency description of a shock that is likely to occur in service, an equipment designer knows what his natural frequencies should be, in order to avoid damage. The shock spectrum at a point on a structure describes what a particular shock pulse does to an idealized mechanical system [7].

The reduced scope of the test program did not allow rigorous experimental proof that pyrotechnic shock spectra envelopes have more than a general positive correlation with component malfunction or damage. However, there appears to be enough precedent in print to use a reduced shock spectrum level as an indication of a reduced potential of shock damage to equipment at a particular point.

Shock spectral envelopes of devices were generated for mounting plate (transducer 1) (Figure 33) and chassis (transducer 2B) (Figure 34) locations. The shock spectra of the

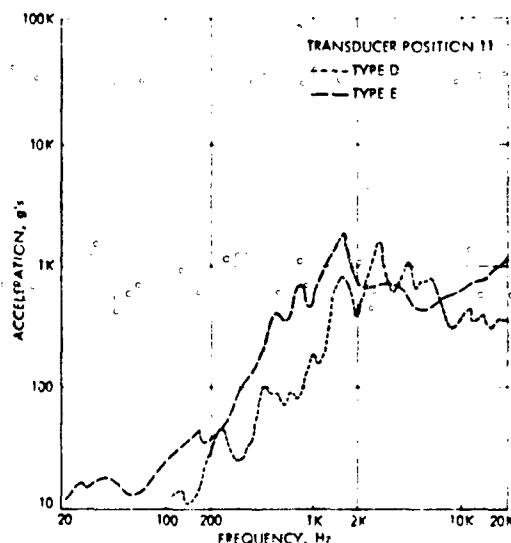


Fig. 20 - Baseline spectra

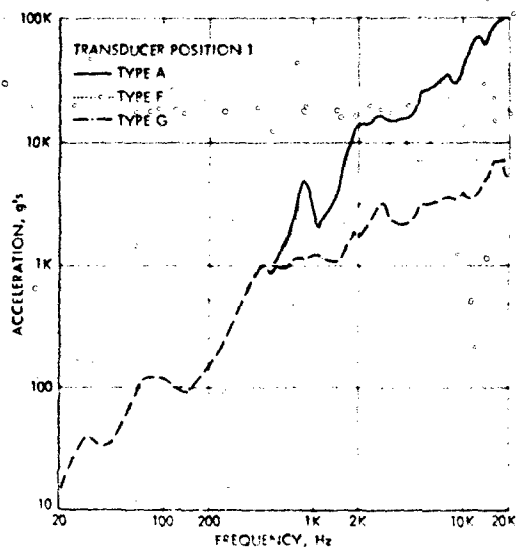


Fig. 21 - Low-shock spectra

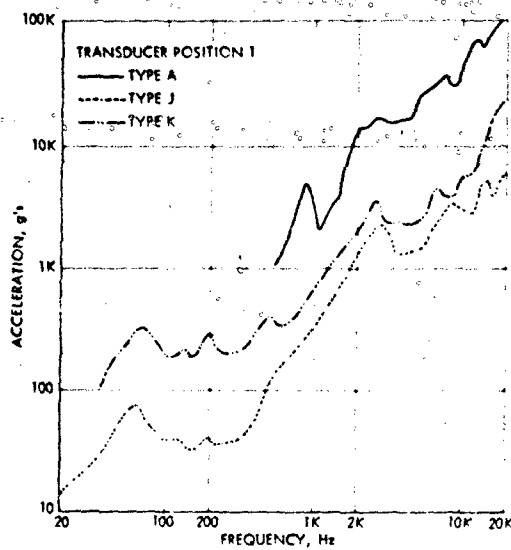


Fig. 23 - Low-shock spectra

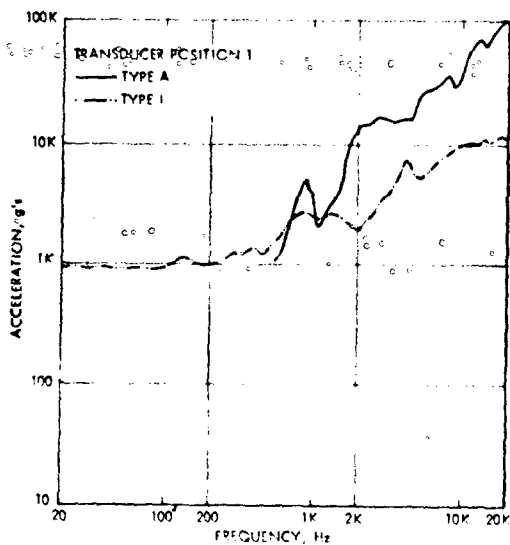


Fig. 22 - Low-shock spectra

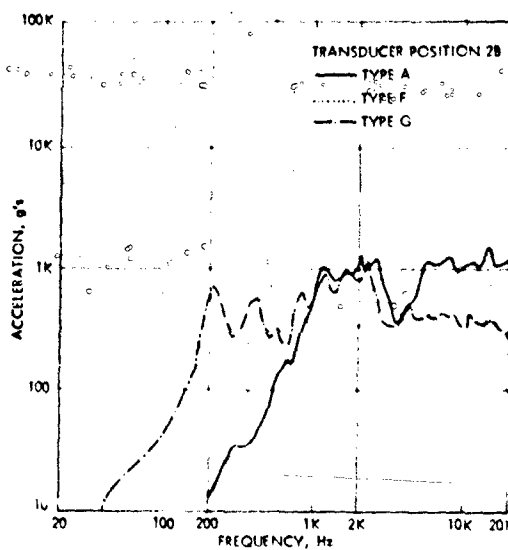
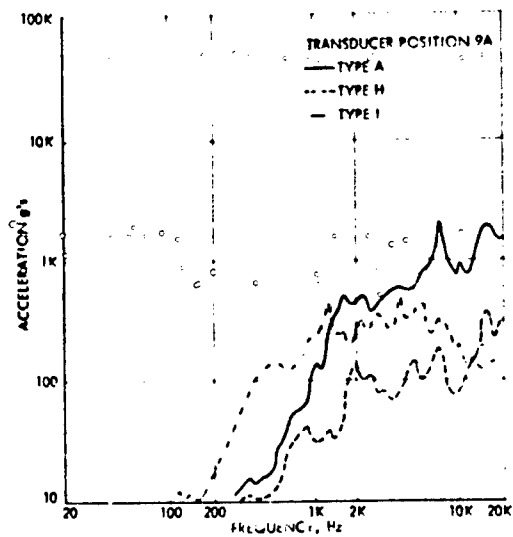
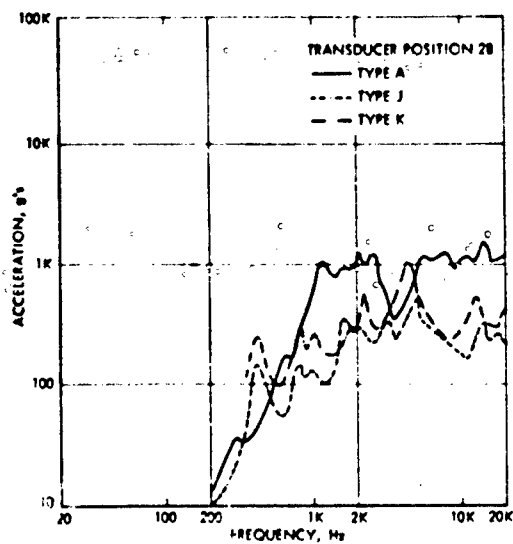
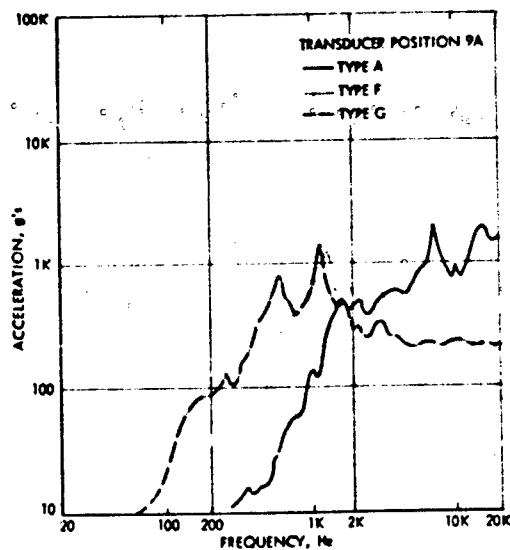
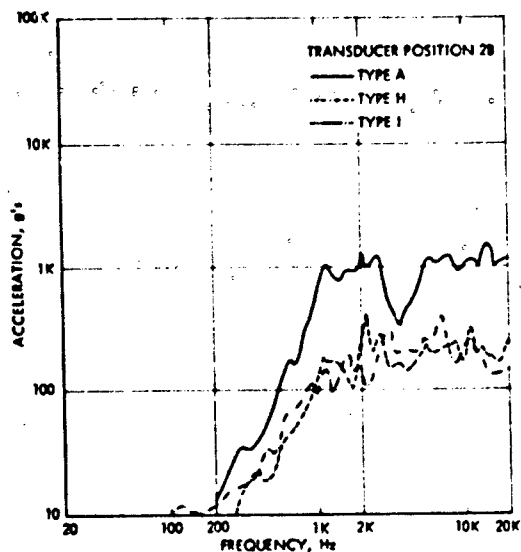


Fig. 24 - Low-shock spectra



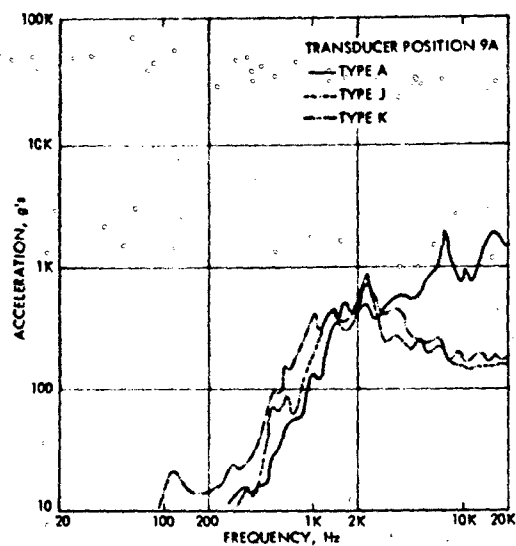


Fig. 29 - Low-shock spectra

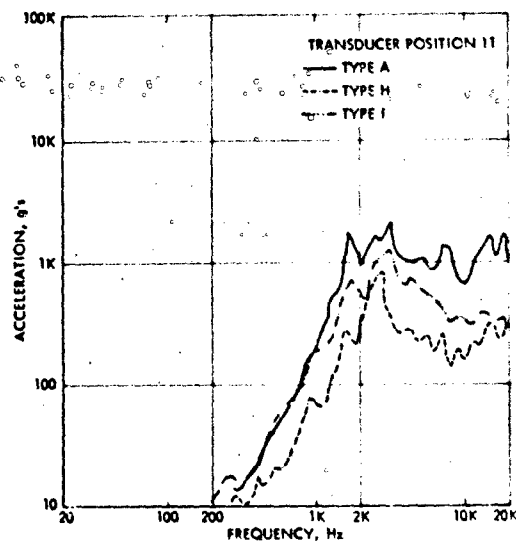


Fig. 31 - Low-shock spectra

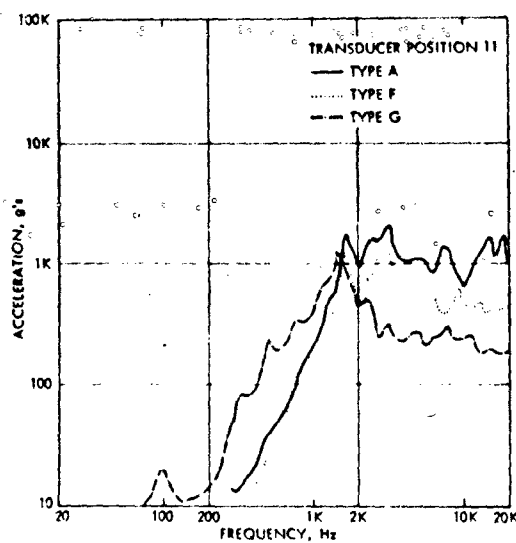


Fig. 30 - Low-shock spectra

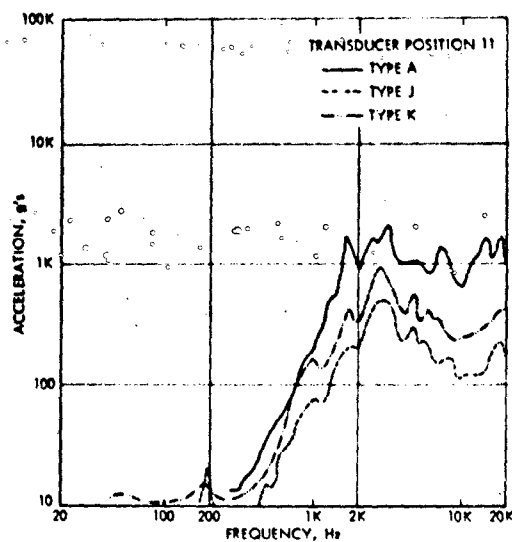


Fig. 32 - Low-shock spectra

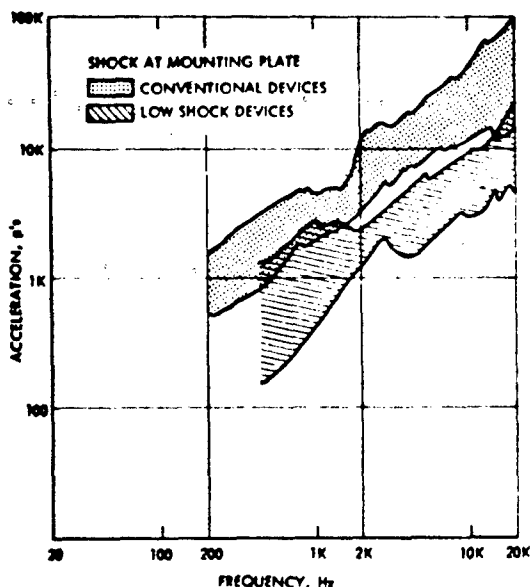


Fig. 33 - Mounting plate spectra

conventional devices were, in general, from two to five times as severe as the spectra from the modified or redesigned devices. An exception was found in the modified V-band release device (Type F) which, although it produced less shock than the standard (Type A) device, fell into the conventional device envelope.

CONCLUSION

The preliminary results have been encouraging. Further analysis of the test data and comparisons with prospective tests of actual spacecraft equipment should be performed. Theories of shock generation should be refined. Improved explosive release devices should be designed and fabricated to test these theories.

The shock output from conventional pyrotechnic devices can be characterized by pyro shock spectra.

Correlation of shock spectra with damage to or degradation of spacecraft components is a major task which should be pursued on a more general level.

The shock production mechanisms were estimated to be:

- impact of moving parts
- fracturing of device parts

- sudden release of preload energy.

Other factors were the amount of stored energy in the device and in the structure (deflections for a given preload), the direction of energy release (into the structural load paths), and momentum transfer from the device to the structure.

The examination of pyrotechnic shock causes led to the establishment of preliminary principles of low shock device design:

- gradual release of stored energy
- cancellation of external momentum exchange
- management of primary shock direction
- elimination of impact of moving parts

Devices which incorporated one or more of these principles generated less shock as indicated by shock spectral plots.

Pyrotechnic shock is designed into pyrotechnically actuated devices and can be reduced by design changes. A systematic approach to these changes would be applicable to many types of devices. Based on the information generated by these experiments, the phenomenon of pyrotechnic shock is amenable to

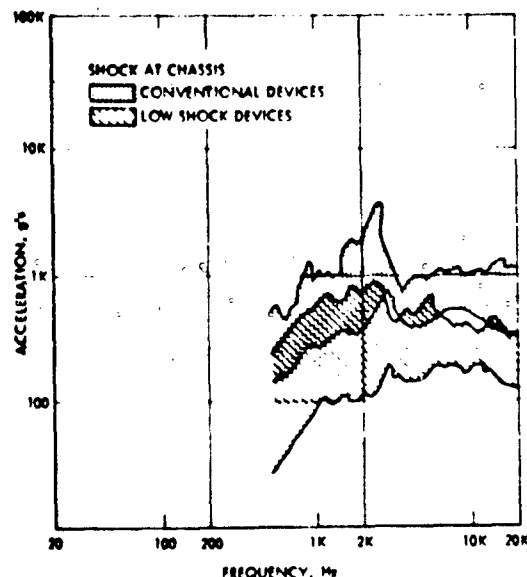


Fig. 34 - Chassis spectra

mitigation by mechanical design changes in the devices.

REFERENCES

1. S. N. Prescott, "Investigation of Pyrotechnic Shock" 20th Annual Instrumentation Symposium, Instrument Society of America, 1974.
2. C. T. Morrow, "The Shock Spectrum," Electrical Manufacturing, C-M Technical Publications Corp. August 1959.
3. W. Phelps, "Shock and Vibration Data Analysis Programs-User's Guide" Document 2941-302, Jet Propulsion Laboratory, Pasadena, California. (JPL Internal Document)
4. J. H. Bickford, "How to Make the Most - Or the Least - Out of Impact," Machine Design, Penton Publications, Cleveland, Ohio, May 9, 1968.
5. W. J. Kacena, M. B. McGrath, W. P. Rader, "Aerospace Systems Pyrotechnic Shock Data," MCR-69-611, Martin Marietta Corporation, Denver, Colorado, 1970.
6. T. Glendorf, "MJS'77 Environmental Design Requirements" FR3-240, Jet Propulsion Laboratory, Pasadena, California, 1973. (JPL Internal Document)
7. W. Tustin, "Shock Measurement and Analysis," Tustin Institute of Technology, Santa Barbara, California, 1971.

IMPACT TESTING WITH THE 35-FOOT CENTRIFUGE

J. V. Pitts
 Canale Laboratories
 Albuquerque, New Mexico

(U) An impact test technique whereby the tangential velocity of the 35-foot centrifuge is used to create the required impact environment is described. The technique involves impacting a test item into stationary targets and the reverse, moving a target into a stationary test item. The accuracy, flexibility, low cost, and efficiency offered by this technique make it highly competitive for future impact test series.

Key Words: Centrifuge; Impact; Velocity

INTRODUCTION

The 35.5-foot-radius centrifuge is an outdoor test facility located in Canale Laboratories' Area III. The basic function of this centrifuge is to provide "radial" acceleration environments up to 250*g*, which corresponds to 145 rpm at the 35.5-foot-radius. The centrifuge structure can support a maximum test weight (test item plus fixture) of 15,000 pounds and a normal acceleration x test-weight product of 450,000 *g*-pounds.

The angular velocity, ω , of the centrifuge is controllable to less than $\pm 1\%$ error between 2 and 145 rpm. Therefore, a test item mounted near the tip of the rotating arm can be subjected to accurate, tangential velocities up to 331 feet/second.

The developed technique consists of releasing the test item from the centrifuge arm and allowing it to "free fly" into the target.

The technique, capabilities, instrumentation and applications are presented below. Implications, potential centrifuge impact test techniques are suggested.

ILLUSTRATION

Upon release, a test item will "free fly" along a path tangent to the orbit of the centrifuge arm at a velocity of (neglecting drag)

$$V = \frac{2\pi}{60} R \omega \text{ ft/sec} \quad (1)$$

where V = tangential, free flight velocity (ft/sec)

R = radius of test item mounted to centrifuge (ft)

ω = angular velocity of centrifuge (rpm)

The technique is illustrated in Figure 1. Note that the test item free-flies into a target located beyond the orbital path of the arm/test item combination.

(See next page for Figure 1)

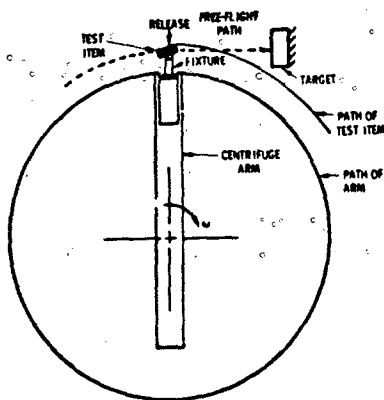


Figure 1. Free-Flight Impact Test Technique

Prerelease Environment

Prior to release from the centrifuge, the test item experiences the following acceleration environments: (Reference Figure 2)

1. Tangential Acceleration

The test item must be accelerated to its specified impact velocity. In the case of the 35.5-foot centrifuge, a small release mechanism driving torque and moment of inertia results in a maximum angular acceleration less than 0.2g. For example, 270 seconds is the minimum time required to accelerate from 0 to 145 rpm (639 ft/sec @ 35.5 feet).

2. Radial Acceleration

$$G = \frac{a}{32.2} = 3.41 \times 10^{-4} \omega^2 \quad (2)$$

The maximum radial acceleration corresponding to 35.5-foot-radius and 145 rpm is 254 G.

Postrelease Environment

During free flight, the test item will rotate about its axis at ω rpm. The angular velocity, ω , is equal to that of the centrifuge arm at the time of release.

The prerelease and postrelease environments prior to impact may be detrimental to the test item and/or the test objectives.

Figure 2 depicts sequential positions of the test item up to the time of impact.

Fixture Requirements

The fixture required to adapt the test item to the centrifuge is simple and inexpensive. The basic requirements include the following:

1. The test item must be restrained at a static load of WG , where W is the weight of the test item and G is the radial acceleration on the test item prior to release.
2. The fixture cannot interfere with the test item after release from the rotating arm.
3. The fixture should allow adjustable radius of the test item.
4. The fixture must allow adjustable release angle for the test item in order to compensate for test item rotation during free flight. This angle offset is a function of impact angle, centrifuge speed, and free-flight distance to impact.

A typical fixture is shown in Figure 3. Basically, a support cradle and steel cable are mounted on a fixture plate which bolts to the centrifuge arm. The radius and the release angle are adjustable by manipulation of this plate.

Release Mechanism

Timely release of the test item is accomplished by cutting the support cable (Figure 3). Required accuracy has been obtained with a Holec guillotine 1/2-inch-diameter cable cutter where firing time is controllable to less than 1 millisecond.

(See next page for Figures 2 and 3)

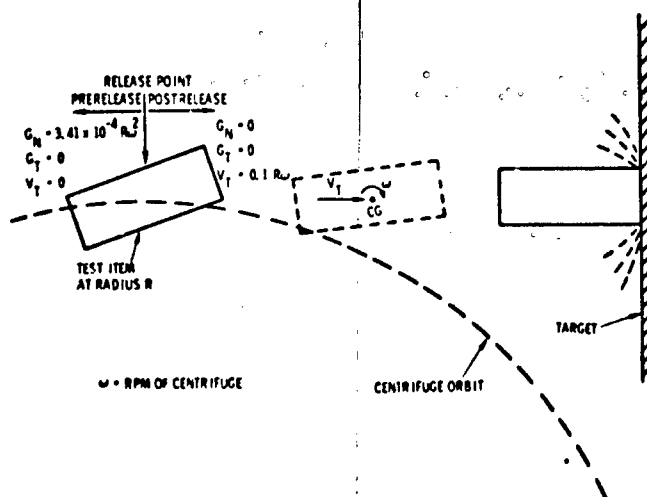


Figure 2. Free-Flight Environment of Test Item

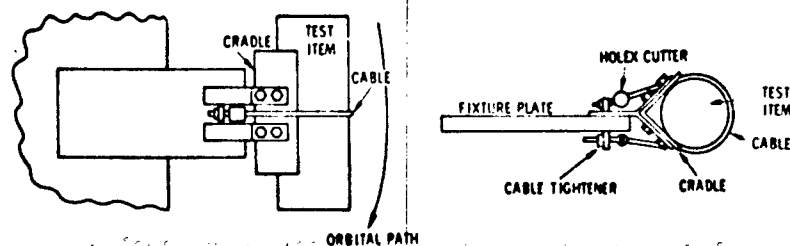


Figure 3. Typical Fixture for Impact Testing

A schematic of the Holes firing circuit is shown in Figure 4. A microswitch is mounted to the centrifuge base (nonrotating). The position of the microswitch is adjustable to allow for selective firing location. A contact plate (runner) is mounted to the rotating arm and, therefore, closes the microswitch during revolution of the arm (See Figure 5). A minimum of 9 milliseconds is required to insure closure of the trigger relay. This time is obtained through the length of the runner which closes the microswitch. Once the required centrifuge rpm is reached, the cutter is activated by a manually controlled safety switch. After the safety switch is

set manually, the cutter is activated by a 28-VDC, 6-ampere source the next time the microswitch is closed. The time delay between microswitch closure and Holes firing is 32 ± 1 milliseconds. The accuracy of this release mechanism, coupled with built-in adjustment of microswitch position, allows nearly precise selection of impact location and test item angle of impact. Also, this release technique has proved to be reliable through 125 impact tests conducted to date (no release failures).

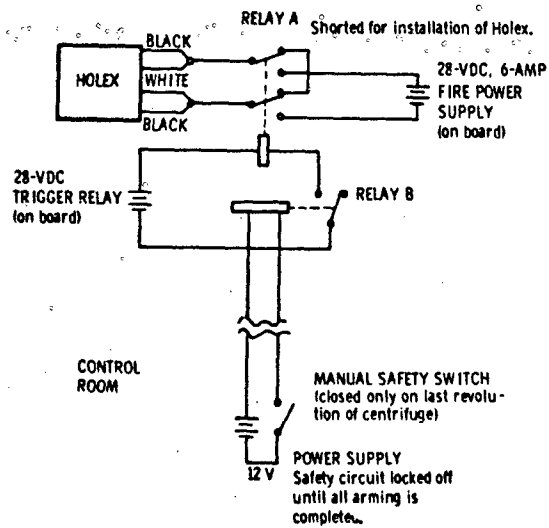


Figure 4. Schematic of Horex Cable Cutter Firing Circuit

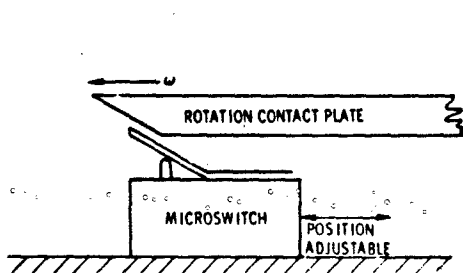


Figure 5. Switch Closure Technique

Target

The major restrictions on target location are as follows:

1. The orbital path of the rotating arm, with test item, cannot intersect the target.
2. The target cannot be allowed to interfere with the rotating arm as a result of the impact.

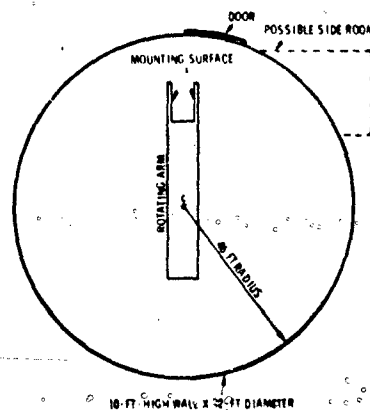


Figure 6. Physical Layout of 35-Foot Centrifuge Facility

The weight, size, and complexity (steel, concrete, water, etc) of the stationary target are essentially unrestricted. At present, the physical size of the centrifuge pit area (see Figure 6) must be considered. However, a side room, as shown in Figure 6 or an opening in the pit wall would be entirely feasible for future testing.

Control of Impact Angle

The test item/target impact angle can be controlled through one or more of the following:

1. Test item release angle
2. Free-flight distance
3. Target angle

The angular velocity, ω (RPM) tangential velocity V (ft/sec) and release point are accurately known. Therefore, impact angle is a very simple calculation. For a free-flight distance L (ft), the test item rotates $\omega \cdot L$ revolutions.

$\frac{6}{65} \quad \frac{5}{7}$

Data Acquisition

Impact data from transducers mounted on the test item are transmitted by trailing cables between the test item and centrifuge arm. Signal conditioners and amplifiers are located at the center of the arm, intermediate to the slip rings, through which data are transmitted to FM tape recorders located in the control room. The slip rings available for data or miscellaneous requirements are outlined below.

Slip Ring Ratings on 25' Control Page

<u>Quantity</u>	<u>Characteristics</u>
12	250 V x 100 amp
24	250 V x 5 amp
150	32 V x 0.85 amp

Fortunately, long lengths of trailing cable are not required because the relative distance between the test item and centrifuge arm will normally be small. This distance can be approximated by

$$d = X_T (\csc \theta - \cot \theta), \quad (3)$$

where d = relative distance between
impact point and centrifuge
arm tip

X_T = free-flight distance of test item

θ = angle between release and impact points.

On-board recorders or telemetry techniques were not available for consideration.

Figure 7 depicts the distance, d , as well as target/test item miss distance before release. As an example, a 6' long trailing cable has been adequate for past tests where free-flight distance was approximately 14 feet.

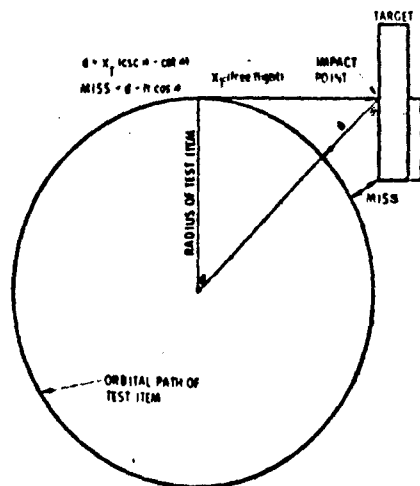


Figure 7. Space Relationship Between
Target and Exit Item

Alyssa: 100%

1. Accurate and repeatable impact velocity ($\pm 1\%$).
2. Velocity control in the range of 10 to 500 ft/sec.
3. Accurate and repeatable impact location on target.
4. Accurate and repeatable impact angle with target.
5. Nonflexible tangential acceleration (<0.2 g) prior to impact.
6. High confidence in obtaining data as a result of a minimum of trailing wire.
7. Inexpensive handling the target and trailing wire.
8. Inexpensive fixturing.
9. Fast setup and turn-around time.
10. Minimal test personnel requirements (two people).
11. Sequential or simultaneous firing of multitest item arrays.

Disadvantages

1. Test item undergoes high radial acceleration.

2. Test item undergoes rotation ω during free-flight and impact.

3. Rebound of test item must be treated with caution.

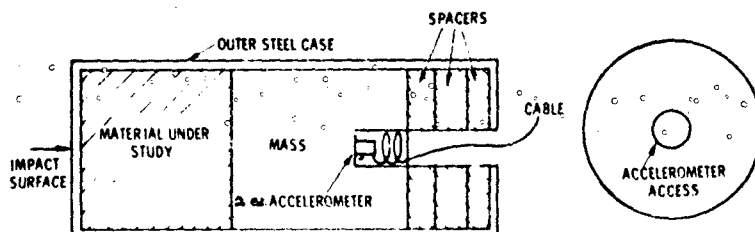
Free-Flight Impact Test Capabilities

Impact Velocity	10 to 539 ft/sec ($\pm 1\%$)
Weight (Test item plus fixture)	10,000 pounds maximum
Force in Centrifuge Arm (weight x g)	450,000 g-pounds
Target	Optional
Impact Angle	Optional
Free-Flight Distance	Optional
Test Temperature	-65 to 300° F

Application

A long-term program is currently underway to determine the absorption capability of various materials being considered for accident resistant containers. Figure 8 details the basic test configuration used in the initial material evaluation. The free-flight technique was used to impact the test item (#50#) into a steel target weighing 14,000 pounds. The impact velocity and impact angle were normally 275 ft/sec and 0° respectively.

Instrumentation consisted of 2 each Endevco 2264 accelerometers mounted side by side on the impacting mass. As mentioned previously, these were hardwired between the flying mass and the rotating centrifuge arm. Typical impact data are shown in Figure 9. To date, more than 125 tests have been conducted at a very high success rate.



NOTE: Not to scale

Figure 8. ARC Test Item Layout (axial impact)

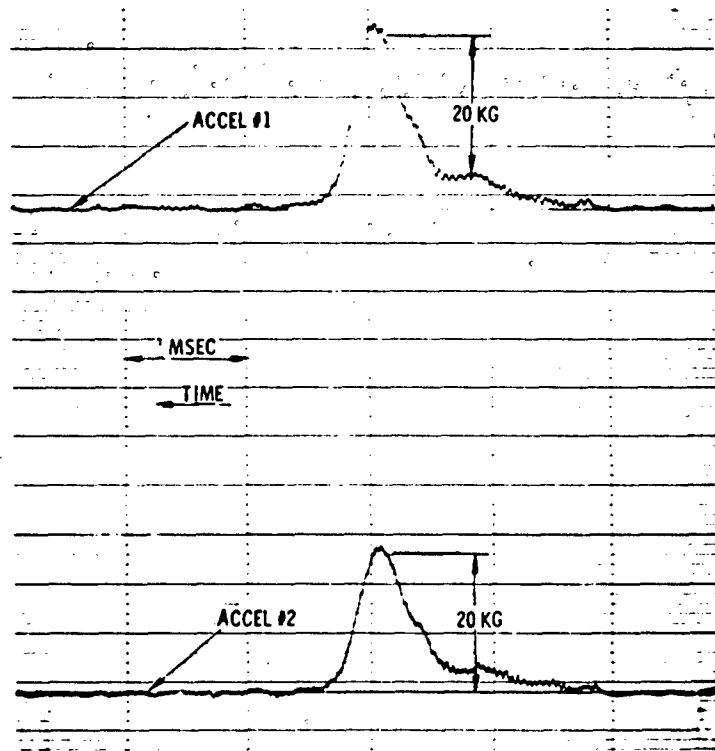


Figure 9. Axial Impact Data - ARC Test Series

Alternate Centrifuge Impact Techniques

1. Throw target into stationary test item.
2. Move test item into orbital path of target.
3. Move target into orbital path of test item.
4. Accelerate test item radially outward along centrifuge arm to impact target mounted on the end of the arm.

Conclusions

An impact test technique whereby the tangential velocity of the 35-foot centrifuge is used to create the required impact environment has been described. The options include impacting a test item into stationary targets and the reverse, moving a target into a stationary test item.

The accuracy, flexibility, low cost, and efficiency offered by this technique make it highly competitive for future impact test series.

DISCUSSION

Mr. Storey (Army Missile Command): Have you ever considered building an impact carriage and putting pads on the anvil to shape the shock pulse or not to allow the specimen to break up during testing?

Mr. Otts: We have the technique and if the type of requirement were to come along it would certainly be worth considering. To this point, we are just developing it as the need arises and we have not tried to expand it; we have a number of impact test techniques and I am not trying to out do one another. Also you might realize that you have other options that are available; you can move, push, or drop the item into the path of the target which would be on the centrifuge, or vice versa, you could flip these around.

Dr. Mains (Washington University): You had a velocity noted at $1/10$ R W. Do you mean this?

Mr. Otts: It is approximately .1 something and it works out that way.

Dr. Mains: Then you have some kind of units in there? You have a radius in feet and omega in radians per second?

Mr. Otts: RPM. This takes care of the factor. You saw a distance per time and it works out that I use this .1 when I use RPM as RPM and feet for the radius, it works out quite well.

Mr. McWhirter: What are you going to use for a vertical water base for water impact?

Mr. Otts: We are going to use a very cheap 100 plus dollar culvert, put a diaphragm over the front, fill it full of water, and it will be sitting in vertical position.

Mr. McWhirter: You are saying that the diaphragm be the water interface.

Mr. Otts: Yes.

FRAGMENT VELOCITIES FROM EXPLODING LIQUID PROPELLANT TANKS

R. L. Bessey
Southwest Research Institute
San Antonio, Texas

An extension of analytical techniques used to describe bursting gas reservoirs is applied to a geometrically simplified model of the exploding liquid propellant tank problem. The model is capable of predicting fragment velocities produced by the internal pressure of the explosion when a mixture of fuel and oxidizer is detonated in the confined-by-missile configuration and no drag effects are considered on the resulting fragments of the tankage. Fragment velocities near liquid propellant tank explosions have been obtained by analysis of high-speed films from Project PYRO. These results are compared to those predicted by the model.

INTRODUCTION

Hazards produced by exploding liquid propellant tanks include those associated with the blast wave, those associated with thermal effects, and those associated with the missile produced by fragmentation of the tank. In a recent study for the Aerospace Safety and Data Research Institute (ASRDI), Nasa Lewis Research Center [1], the author has had the opportunity to investigate some of the phenomena associated with the fragmentation hazard. In order to assess the range and degree of hazard of fragments emanating from a propellant tank explosion, ballistic equations and energy equations depend on a knowledge of the initial velocity of the fragments. Obviously, determination of these fragment velocities is a complex problem both empirically and analytically. This is especially so when an analytic model is developed capable of predicting fragment velocities for quite general conditions, i.e., a variety of tank geometries, propellants, etc.

An analytical model is developed in this paper which attempts to predict initial fragment velocities from exploding liquid propellant tanks based on a gross simplification of the geometric factors and assumptions about the thermodynamic state of a hypothetical sphere of "gaseous explosion products" which represents the conditions within the tank at the

instant the explosion occurs. Mathematically, the initial fragment velocities are obtained by an extension of the techniques described by D. E. Taylor and C. F. Price [2], and G. L. Grodzonski and F. A. Kukanov [3] in their papers on bursting gas reservoirs.

Additionally, empirical data on fragment velocities were obtained from high-speed films taken of the events of Project PYRO. Project PYRO was a series of tests consisting of detonations of liquid propellant tanks with a considerable amount of documentation on each test. From these films, data on fragment velocity versus yield were obtained. The analytical model attempts to predict these same values for the test conditions described.

ANALYTICAL MODEL

The geometry of the model chosen to simulate the missile within which a propellant explosion is occurring is shown in Figure 1. The salient features of this model are that the explosion is initially contained by the missile tankage (CBM case); the reacting fuel and oxidizers are perfectly mixed in the stoichiometric ratio and react completely to form gaseous explosion products (contained in a spherical volume initially of radius R_0); and the missile tankage and non-reacting propellants are approximated by an incompressible concentric spherical outer shell about the

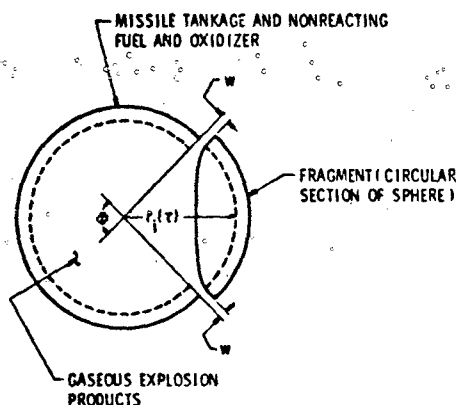


Fig. 1. Schematic of Idealized CBM Liquid Propellant Explosion

sphere of gaseous explosion products. The shell is assumed to fragment into n fragments of equal surface area, A_i , all of which are circular sections of the shell. The fragments move radially and are at a distance $r_i(\tau)$ at any time τ from the center of the original sphere. The solid angle formed by a fragment at $\tau = 0$ at the sphere's center is Ω . Each fragment is characterized by a mass M_i and a circular periphery Γ_i . The total shell mass is M_t .

The sphere of gaseous explosion products is characterized by a pressure, $P_0(\tau)$, sound speed, $a_0(\tau)$, temperature, $T_0(\tau)$, volume, $V_0(\tau)$, mass, $M(\tau)$, and density, $\rho_0(\tau)$ at any time τ , as well as a ratio of specific heats, κ . The initial conditions are

$$r(0) = R_0, \quad \frac{dr(0)}{d\tau} = 0, \quad P_0(0) = P_{00},$$

$$a_0(0) = a_{00}, \quad \rho_0(0) = \rho_{00}, \quad T_0(0) = T_{00},$$

$$M(0) = M_{00}, \quad V_0(0) = V_{00} \quad (1)$$

It is assumed that the entire shell could be divided into the n fragments; thus,

$$A_i = 4\pi R^2/n \quad (2a)$$

and

$$n = M_i/M_t \quad (2b)$$

The equation of motion for a fragment is

$$M_i \frac{d^2 r_i(\tau)}{d\tau^2} = F P_i(\tau) \quad (3)$$

where F is the fragment's projected area, which from Eq. (2) is

$$F = 4\pi R_0^2 \left[\frac{1}{n} - \frac{1}{n^2} \right] \quad (4)$$

The equation of state for the gaseous explosion products is taken as

$$P_0(\tau) V_0(\tau) = R M(\tau) T_0(\tau) \quad (5)$$

A crack of width, w , appears around the periphery of each fragment at time, τ , through which the gaseous explosion products escape until $P_0(\tau)$ approaches ambient pressure. From one-dimensional flow equations [2]:

$$P_i(\tau) = P_0(\tau) \left[1 - \left(\frac{\kappa - 1}{2a_0^2(\tau)} \right) \left(\frac{dr(\tau)}{d\tau} \right)^2 \right]^{\frac{\kappa}{\kappa - 1}} \quad (6)$$

$$\frac{dM(\tau)}{d\tau} = -k \rho_* a_* \Omega w \quad (7)$$

$$\rho_* = \rho_0(\tau) \left(\frac{2}{\kappa + 1} \right)^{\frac{1}{\kappa + 1}} \quad (8)$$

$$a_* = a_0(\tau) \left(\frac{2}{\kappa + 1} \right)^{1/2} \quad (9)$$

where k is a discharge coefficient and the other variables have been defined.

The volume of the sphere of gaseous products of explosion at any time τ , is

$$V_0(\tau) = (4/3)\pi r^3(\tau) \quad (10)$$

and the adiabatic case is assumed where

$$\frac{P_0(\tau)}{P_{00}} = \left(\frac{\rho_0(\tau)}{\rho_{00}} \right)^{\frac{\kappa}{\kappa - 1}} = \left(\frac{T_0(\tau)}{T_{00}} \right)^{\frac{\kappa}{\kappa - 1}} = \left(\frac{a_0(\tau)}{a_{00}} \right)^{\frac{2\kappa}{\kappa - 1}} \quad (11)$$

The equations will be non-dimensionalized by setting

$$P_0(\tau) = P_{00} P_*(\xi), \quad \tau = \theta \xi, \quad r(\tau) = Xg(\xi) \quad (12)$$

where g is the dimensionless distance coordinate, ξ is the dimensionless time coordinate, and P_* is the dimensionless pressure. From Eqs. (6) and (3) and non-dimensionalizing with Eq. (12), we obtain

$$M_t \frac{X}{\theta^2} g'' = F P_{\infty} P_* \left[1 - \frac{(n-1)}{2a_0^2} (g')^2 \frac{X^2}{\theta^2} \right]^{\frac{n}{n-1}} \quad (13)$$

where primes denote derivatives with respect to θ . Using Eqs. (3), (11), and (12) in (13), we obtain

$$g'' = n P_* \left[1 - \frac{(g')^2}{(P_*)^{\frac{n-1}{n}}} \right]^{\frac{n}{n-1}} \quad (14)$$

where we have chosen the non-dimensionalizing parameters X , θ^2 .

$$X = \frac{M_t a_{\infty}^2}{F P_{\infty}} \left(\frac{2}{n-1} \right) \quad (15)$$

$$\theta = \frac{M_t a_{\infty}}{F P_{\infty}} \left(\frac{2}{n-1} \right)^{1/2} \quad (16)$$

From Eq. (5) and its derivatives with respect to τ , we obtain

$$\begin{aligned} \frac{dP_0(\tau)}{d\tau} &= \frac{P_0(\tau)}{\rho_d(\tau) V_0(\tau)} \frac{dM(\tau)}{d\tau} \\ \frac{P_0(\tau)}{T_0(\tau)} \frac{dT_0(\tau)}{d\tau} &= \frac{P_0(\tau)}{V_0(\tau)} \frac{dV_0(\tau)}{d\tau} \end{aligned} \quad (17)$$

The area of a crack around a fragment is

$$(\Omega w)_i = \left(\frac{1}{2} r_i^2(\tau) - A_i \right) \quad (18)$$

and the total crack area for n fragments is

$$\Omega w = 4\pi R_0^2 \left(\frac{r^2(\tau)}{R_0^2} - 1 \right) \quad (19)$$

From Eqs. (7) through (12) and (19), we may write Eq. (17) as

$$\begin{aligned} g^3 \frac{P_*'}{P_*} &= \frac{3k\mu a_{\infty} \left(\frac{2}{n-1} \right)^{\frac{n+1}{2}}}{X} \\ P_* \frac{\frac{n-1}{2k} \left(\frac{R_0^2}{X^2} - g^2 \right)}{X^2} &= 3\mu g^2 g' \end{aligned} \quad (20)$$

If we define

$$C_1 = 3k\mu \left(\frac{2}{n-1} \right)^{\frac{n+1}{2}} \left(\frac{2}{n-1} \right)^{-1/2} \quad (21)$$

and

$$C_2 = R_0^2 \left(\frac{2}{n-1} \right)^{-2} \frac{F^2 P_{\infty}^2}{M_t^2 a_{\infty}^4} \quad (22)$$

or using Eq. (4),

$$C_2(n) = \left(\frac{2}{n-1} \right)^{-2} \frac{P_{\infty}^2}{M_t^2 a_{\infty}^4} \left[\frac{1}{n} - \frac{1}{n^2} \right]^2$$

Then, Eqs. (15), (16), (21), and (22), Eq. (20) becomes

$$g^3 \frac{P_*'}{P_*} = \left[-C_1 g^2 + C_1 C_2 \right] P_* \frac{n-1}{2k} - 3\mu g^2 g' \quad (23)$$

This equation can be solved simultaneously with Eq. (14) for the initial conditions of Eq. (1), which for Eq. (12) are given in dimensionless form as

$$g(0) = \frac{R_0}{X}, \quad g'(0) = 0, \quad P_*(0) = 1 \quad (24)$$

NUMERICAL SOLUTIONS

The solution of Eqs. (14) and (23) was obtained numerically for the initial conditions, Eq. (24), using the Runge-Kutta method. Table 2 is an example solution for the conditions of Table 1. The maximum velocity of a

TABLE 1.
Condition for Solution of Table 2

μ	$= 1.4$
a_{∞}	$= 1.352 \times 10^4 \text{ ft./sec}$
P_{∞}	$= 8 \times 10^3 \text{ psi}$
n	$= 100$
R_0	$= 27 \text{ in.}$
M_t	$= .455 \text{ lb-sec}^2/\text{in.}$
k	$= 1.0$

fragment is obtained as g' approaches zero, i.e., no drag effects are considered. Figure 2 shows how the maximum fragment velocity varies with n for two example cases of particular R_0 , μ , P_{∞} , and a_{∞} and M_t . P_{∞} and μ are the same, for both cases, and a_{∞} , R_0 , and M_t differ widely between the two cases. The figure indicates that, for sufficiently large n , the maximum fragment

TABLE 2.
Example Solution

INITIAL CONDITIONS			
SW = .000E+01	G = .001E+01	G' = .000E+01	P-NORM = .100E+01
CHARACTERISTICS OF MOTION OF FRAGMENTS (NORMALIZED)			
T-NORM	G	G'	Q'
.000E+02	.491E+01	.001E+00	.657E+02
.100E+01	.517E+01	.543E+00	.144E+02
.150E+01	.540E+01	.600E+00	.682E+01
.200E+01	.576E+01	.633E+00	.282E+01
.250E+01	.608E+01	.632E+00	.112E+01
.300E+01	.639E+01	.630E+00	.600E+00
.350E+01	.671E+01	.637E+00	.124E+00
.400E+01	.703E+01	.640E+00	.279E+01
.450E+01	.735E+01	.633E+00	.107E+02
.500E+01	.767E+01	.630E+00	.104E+00
PRESSURE (NORMALIZED)			
T-NORM	P-NORM		
.000E+02	.001E+00		
.100E+01	.700E+00		
.150E+01	.510E+00		
.200E+01	.367E+00		
.250E+01	.250E+00		
.300E+01	.181E+00		
.350E+01	.127E+00		
.400E+01	.907E+01		
.450E+01	.632E+01		
.500E+01	.476E+01		
		TIME	.927E+01 SEC
		DISTANCE	.144E+01 DYS
		VELOCITY	.141E+04 FT/SEC
		ACCELERATION	.124E+02 IN/SEC-SEC
		PRESSURE	.576E+01 PSI

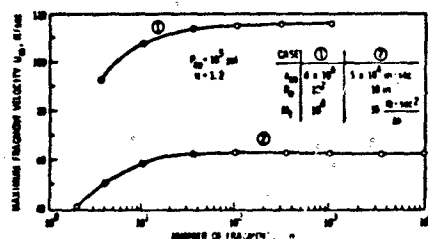


Fig. 2. Maximum Fragment Velocity as a Function of Number of Fragments

velocity is constant, independent of n . For low n , Eq. (2) is a poor approximation. Figure 3 shows the dependence of maximum fragment velocity on α and the initial gaseous explosion products mass to shell mass ratio, M_0/M_t , for a particular R , n , P_{00} and a_{00} .

Results obtained from this model may be compared to those obtained from other analytical and experimental work on fragmenting spherical results as a result of high internal pressure.

The results of this method are compared to the cases described by Taylor and Price [2] in which:

$$\alpha = \frac{P_{00} V_{00}}{M_t a_{00}^2} = 2.55, 0.1436 \quad (25)$$

in Figure 4. Generally it can be seen that our results predict somewhat lower fragment

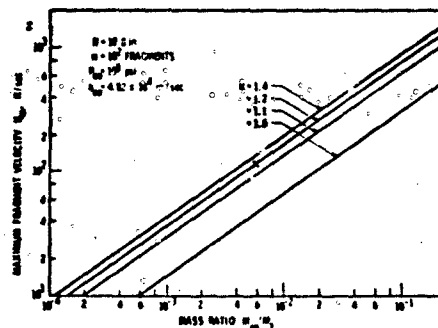


Fig. 3. Maximum Fragment Velocity Versus Mass Ratio

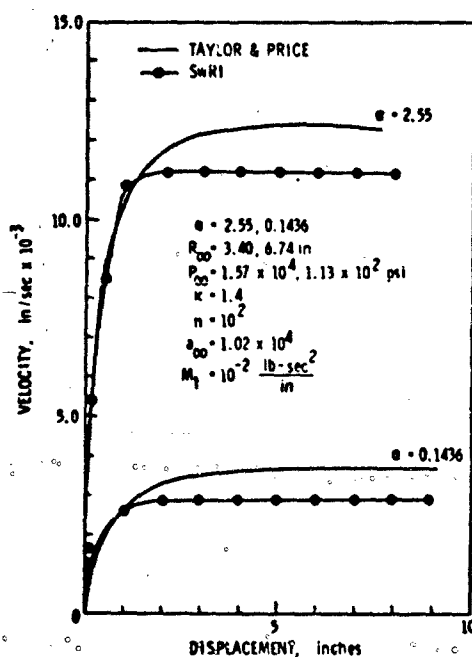


Fig. 4. Comparison of Taylor-Price to SwRI Solutions for Adiabatic Case

velocities than they do. Some discrepancy is to be expected because our assumptions on geometry were not as precise as theirs. This is especially true where we assumed that the surface area of a spherical volume could be divided into n equal circular areas; they assumed only two hemispherical fragments whose projected areas were well defined. Nonetheless, the agreement is relatively good, especially for the greater α .

Table 3 gives a comparison between fragment velocities measured in experimental work relating to hazards from bursting high-pressure tanks and predicted velocities using our model. The experimental values of Pittman [4] were obtained by pressurizing spherical metal tanks with N_2 until they burst. Fragment velocities were measured by use of a breakwire. Where the experimental values were not precisely determined in tests D and E, limits were assigned to the fragment velocity on the basis of the data obtained. Input data to our program were based on the tank geometry and burst pressure, described in Reference [4] and the properties of N_2 .

TABLE 3. Comparison of Predicted Fragment Velocities with Pittman's Data [4]

Test	P_0 (psf)	R_0 (in.)	M_0 (lb.-sec./in. ²)	Measured V_f (ft/sec)	Predicted V_f (ft/sec)
C	8×10^3	6.2	1.43×10^{-2}	1.2×10^3	1.201×10^3
D	8×10^3	27.0	6.94×10^{-3}	1.3×10^3	1.61×10^3
E	8.15×10^3	27.0	6.43×10^{-3}	1.17×10^3	1.46×10^3

CORRELATION OF PREDICTED FRAGMENT VELOCITIES WITH PROJECT PYRO DATA

High-speed films were taken of explosions of liquid rocket propellant tanks in project PYRO [5-7]. Films from 94 of these tests were analyzed (to provide data on initial fragment velocities) [1]. Fragment positions were recorded frame by frame, and the same fragment was identified between films of a given event taken by cameras located radially about the explosion center at different azimuth angles. Although it was impossible to determine a true initial fragment velocity because of the obstruction of fragment motion by the fireball, average fragment velocity values were obtained close to the explosion center for many of these tests.

Since our fragment velocity prediction method is based on a spherically symmetric containment vessel, it is reasonable to take the cylindrical test geometry of the PYRO tests which most closely approximated spherical symmetry for purposes of comparison with data from the analytical model, i.e., only tests with $L/D = 1.8$ (the smallest L/D ratio) are considered. Furthermore, only confined-by-the-missile (CBM) cases are considered. (Confinement-by-the-ground-surface (CBGS) cases do not represent internal explosions.) To simplify the assumptions made about the gaseous explosion products, only

tests where LH_2/LO_2 was the propellant are considered.

The data for these PYRO tests appear in Table 4, and the mean fragment velocities are plotted versus measured yield in Figures 5 and 6 for tests involving a total propellant weight, W_t , of 200 and 1000 lb, respectively. The weight of reactants, W_r , involved in the explosion is given by

$$W_r = Y \cdot W_t \frac{H_{TNT}}{H_r} \quad (26)$$

where H_{TNT} and H_r are the heats of explosion per unit mass of TNT and LO_2/LH_2 , and Y are a percentage yield for a given test obtained from blast line peak overpressure measurements. Using the ratio for the heats of explosion, Y_m is

$$Y_m = 0.27 Y \quad (27)$$

Our method of fragment velocity prediction is relatively insensitive to the value of n and x as we have seen; accordingly, we picked reasonable values ($n = 100$, $x = 1.2$) for these parameters to describe the number of fragments and the gaseous explosion products of the PYRO tests. The energy produced in the explosion of the reacting propellant obtained from these tests is

$$E = W_r \cdot H_r \quad (28)$$

Based on the calculated density of a mixture of LH_2/LO_2 (mixed in the stoichiometric ratio), we obtained a volume for the sphere of gaseous explosion products related to W_r for each test from

$$V_r = \frac{W_r}{\rho} \quad \text{where } \rho = \frac{V_H \rho_H + V_{OX} \rho_{OX}}{V_H + V_{OX}} \quad (29)$$

and

$$8 V_H \rho_H = V_{OX} \rho_{OX} \quad (30)$$

ρ and V are density and volume, and the subscripts H and OX refer to LH_2 and LO_2 . The energy can be expressed in terms of the initial pressure within the sphere of gaseous explosion products as

$$E = \frac{V_r}{\gamma - 1} \left[P_{00} - (14.7) \frac{\gamma - 1}{\gamma} (P_{00})^{1/\gamma} \right] \quad (31)$$

This was solved for P_{00} by the Newton-Raphson iteration technique, using Eqs. (28) through (30), to give $P_{00} \approx 14^4$ psf.

TABLE 4. PYRO Test Data.

Test No.	Total Prop. Wt. W_t (lbs)	Measured Yield Y_m (%)	Reactants Weight W_r (lbs)	Reactants Energy E (ft-lb $\times 10^{-5}$)	Mass of Non-Reactants $M_0 = M_v + M_t - M_r$ (lb-sec ² /in)	Radius of Reactants Sphere R_0 (in.)	Calc. Max. Fragment Velocity U_f (ft/sec)	Measured Mean Velocity U_f (ft/sec)
053	200	1.08	2.08	3.35	.633	8.0	358	362
091	200	7.83	15.63	15.63	.564	15.5	975	1500
118	200	5.41	10.82	17.4	.589	13.7	790	710
199	200	2.16	4.32	6.95	.623	10.2	543	660
200	200	4.59	9.18	14.8	.597	13.0	786	880
210	1000	1.89	18.9	30.4	2.49	16.12	540	650
212	1000	7.29	72.9	117.0	2.21	25.35	1020	790
213	1000	9.46	94.60	150.8	2.11	27.15	1110	990
265	1000	2.70	27.0	43.5	2.45	17.85	636	690

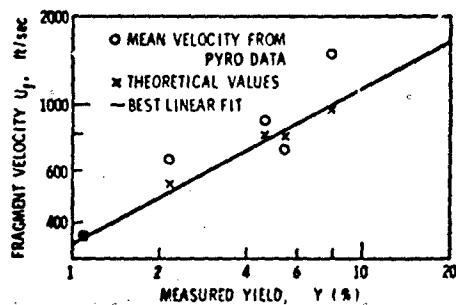
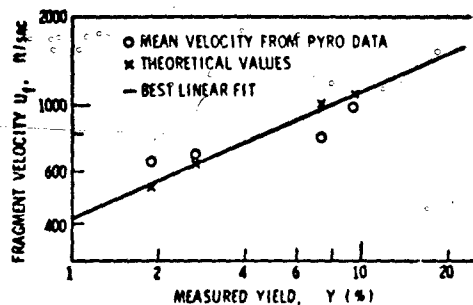
Fig. 5. Fragment Velocity: Correlation of Data from PYRO LH₂/LO₂ Tests with Theoretical Values, $W_t = 200$ LbsFig. 6. Fragment Velocity: Correlation of Data from PYRO LH₂/LO₂ Tests with Theoretical Values, $W_t = 1000$ Lbs

Figure 7 is a plot of fragment velocity, V_f , as a function of a_{00} and R_0 , as obtained from our analytical method. From this figure, it can be seen that V_f is relatively insensitive to a_{00} but very sensitive to R_0 . We chose $a_{00} = 14^4$ in./sec as a reasonable value for the initial sound speed for the gaseous explosion products of the PYRO tests since information such as this on the thermodynamic state of the explosion at $\tau = 0$ was not available for these tests. Values for R_0 were obtained by taking a lower limit based on Eqs. (10), (29), and (30) and an upper limit based on the radius of a sphere with the same volume as the particular confinement vessel tank for each test.

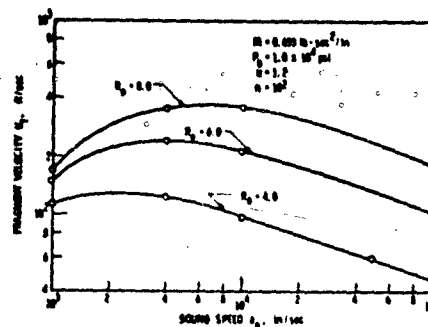


Fig. 7. Fragment Velocity as a Function of Sound Speed in the Explosive Products

Within these limits, an R_0 was chosen to give a reasonable value for initial fragment velocities for one PYRO test for each of the tank sizes. R_0 was then varied as the cube root of the measured blast yield for the other tests, and a corresponding V_f was calculated. Values for R_0 are given in Table 4. Figures 5 and 6 show the comparison of the measured and calculated fragment velocities for the 200-lb and 1000-lb tests.

CONCLUSIONS

An analytical model based on a spherical vessel containing a gas under high pressure which bursts into n fragments was used to predict the initial fragment velocities from liquid propellant rocket explosions (Project PYRO) and from NOL bursting pressure vessel data. Results from the model were generally insensitive to the number of fragments and many of the thermodynamic properties of the confined gas, but depended strongly on the initial radius of the vessel and the initial pressure of the gas. Comparison of fragment velocity data obtained from high-speed films of PYRO events with the analytical predictions could only be made by taking reasonable values for the thermodynamic parameters and assigning limits to the initial radius of explosion. Agreement was generally good under these conditions, but the model needs to be validated by tests which provide more information about what is occurring inside the confinement vessel at the time of explosion. Analytical predictions of the NOL data were good. These experiments provided more complete information on the initial conditions, which are required by the model, and used test vessels which were geometrically similar to those assumed by the model.

REFERENCES

1. Baker, W. E., Parr, V. B., Bessey, R. L., and Cox, P. A., "Assembly and Analysis of Fragmentation Data for Liquid Propellant Vessels," NASA CR Report (to be published), Southwest Research Institute, San Antonio, Texas, 1973.
2. Taylor, D. B., and Price, C. F., "Velocities of Fragment from Bursting Gas Reservoirs," ASME Transactions, *Journal of Engineering for Industry*, Nov. 1971.
3. Grodzowski, G. L., and Kukanov, F. A., "Motion of Fragments of a Vessel Bursting in a Vacuum," *Soviet Engineering Journal*, Mar/Apr, 1965.
4. Pittman, J. F., "Blast and Fragment Hazards from Bursting High Pressure Tanks," NOLTR 72-102, May 1972.
5. Willoughby, A. B., Wilton, C., and Mansfield, J., "Liquid Propellant Explosive Hazards, Final Report - Dec. 1968, Vol. I - Technical Documentary Report," AFRPL-TR-68-92, URS-652-35, URS Research Co., Burlingame, California.
6. Willoughby, A. B., Wilton, C., and Mansfield, J., "Liquid Propellant Explosion Hazards, Final Report - Dec. 1968, Vol. II - Test Data," AFRPL-TR-68-92, URS 652-35, URS Research Co., Burlingame, California.
7. Willoughby, A. B., Wilton, C., and Mansfield, J., "Liquid Propellant Explosion Hazards, Final Report - Dec. 1968, Vol. III - Prediction Methods," AFRPL-TR-68-92, URS 652-35, URS Research Co., Burlingame, California.

SHOCK ANALYSIS

PIPING DESIGN FOR HYDRAULIC TRANSIENT PRESSURE

Charles C. Huang and Richard J. Bradshaw, Jr.
U.S. Army Engineer Division, Huntsville
Huntsville, Alabama

and

Howard H. Yen
Sperry-Rand Corporation
Huntsville, Alabama

Designing fluid-filled piping systems in protective structures requires determining the severity of the transient pressures produced in piping by strong motions resulting from a nuclear detonation. When the transient pressure exceeds the allowable pressures of the pipe, or equipment in the piping system, attenuators will be required. The same problem is involved in designing piping systems in nuclear power plants to withstand earthquakes. A new computer code, HYTRAN, has been developed to assist engineers in solving these types of problems.

This paper introduces the HYTRAN code with a description of its boundary conditions and numerical solution techniques. Modeling techniques are discussed and a typical example of HYTRAN application to analyzing a large three-dimensional piping system is presented to demonstrate the utility of the code. A comparison of test data and HYTRAN computed results is also included to demonstrate the reliability of the code.

INTRODUCTION

When protective structures are subjected to the violent shaking motions produced by the detonation of nuclear weapons, transient pressures are generated in the fluid filled piping systems contained in the structures. Designers of these structures are faced with determining these transient pressures and providing necessary attenuation devices if the transient pressures exceed the allowable pressures of the piping system. In 1969, the U.S. Army Corps of Engineers initiated a R&D program to develop and verify a computer code, HYTRAN, which provides a means to calculate these pressures and to design attenuators. Since that time, HYTRAN has been used in designing all the critical piping systems in the protective structures of the SAFEGUARD Ballistic Missile Defense System. The comparison of laboratory, test data and calculated data, which are presented in this paper, indicates that HYTRAN predicts the transients pressures quite accurately.

The purpose of this paper is to present HYTRAN to engineers responsible for designing piping systems subjected to strong shaking motions which are produced by either detonation

of weapons or earthquakes. The basic formulation, numerical solution, column separation, attenuators, modeling techniques, and comparison of test and computed data are presented.

BASIC EQUATIONS

In this section the basic partial differential equations for hydraulic transient phenomena in a piping system are discussed. The physical problem is depicted in Figure 1. To formulate the governing equations which are mathematically solvable the following idealizations are introduced:

- One-dimensional flow
- Small density change
- Nonviscous fluid except at the pipe boundary
- Friction force on pipe calculated by Darcy equation
- Wave velocity calculated by considerations of the elastic properties of the fluid and pipe

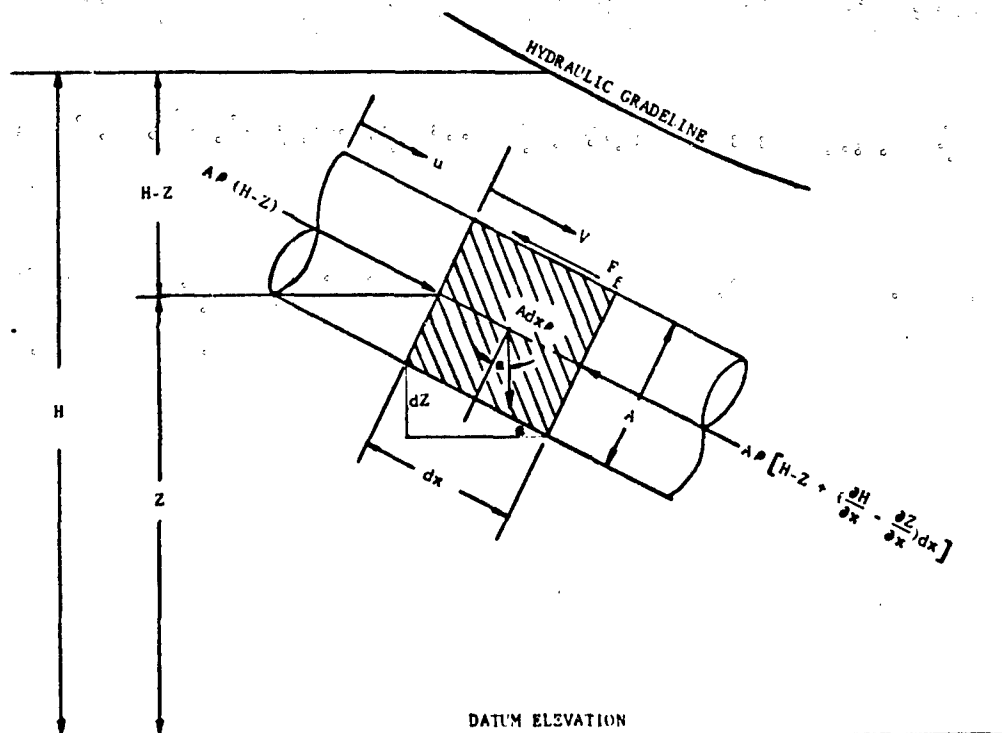


Figure 1. Forces Acting on an Element of Liquid dx in Length

- Rigid pipe segment
- Velocity head neglected.

MOMENTUM EQUATION

The condition of dynamic equilibrium can be set up for an element dx along the pipe. By considering friction force to be related to the relative flow velocity between the fluid and the moving pipe wall $(V-u)$ the balance of momentum yields Equation (1).

$$\frac{\rho A dx}{g} \frac{dV}{dt} = A_0 \left\{ (H-Z) - \left[(H-Z) + \left(\frac{\partial H}{\partial x} - \frac{\partial Z}{\partial x} \right) dx \right] \right\} - \frac{\rho A f}{2gD} (V-u) |V-u| dx + A_0 dx \sin \alpha \quad (1)$$

where $\frac{dV}{dt}$ is the acceleration of the liquid element. To preserve the direction of the pressure head drop, the absolute value of the relative velocity is used in Equation (1). Since $\sin \alpha = -\frac{\partial Z}{\partial x}$, Equation (1) may be expressed as:

$$\frac{1}{g} \frac{dV}{dt} = -\frac{\partial H}{\partial x} - \frac{f}{2gD} (V-u) |V-u|. \quad (2)$$

Expanding the total derivative into partial derivatives, Equation (2) becomes

$$\frac{1}{g} \left(\frac{\partial V}{\partial t} + V \frac{\partial V}{\partial x} \right) = -\frac{\partial H}{\partial x} - \frac{f}{2gD} (V-u) |V-u|. \quad (3)$$

Equation (3) is the momentum equation of one-dimensional wave propagation.

CONTINUITY EQUATION

A second equation relating H and V is determined from the condition of continuity [4].

$$\frac{\partial H}{\partial t} + V \frac{\partial H}{\partial x} = -\frac{C^2}{g} \frac{\partial V}{\partial x}. \quad (4)$$

Where C is the wave velocity and is expressed by

$$C = \sqrt{\frac{1}{\frac{\rho}{g} \left(\frac{1}{B} + \frac{DC_1}{Ee} \right)}}. \quad (5)$$

NUMERICAL SOLUTION BY THE METHOD OF CHARACTERISTICS

There are several numerical methods to solve partial differential equations, however, the method of characteristics is most applicable for hyperbolic partial differential equations with two independent and two dependent variables. Lister [5] shows the general mathematical development of the method and the computational procedures for digital computer solution. The application of the method to hydraulic transient analysis was first adopted by Streeter and Lai [1]. Yang [6] used the same approach as Streeter, but treated the more complicated boundary conditions.

Four characteristic equations; Equations (6), (7), (8) and (9) are obtained by combining Equations (3) and (4).

$$\begin{cases} \text{C+ Curve} \\ \left\{ \begin{aligned} dt - \frac{dx}{V+C} &= 0 \\ dv + \frac{g}{C} dH + \frac{f}{2D} (V-u) |V-u| dt &= 0 \end{aligned} \right. \end{cases} \quad (6) \quad (7)$$

$$\begin{cases} \text{C- Curve} \\ \left\{ \begin{aligned} dt - \frac{dx}{V-C} &= 0 \\ dv - \frac{g}{C} dH + \frac{f}{2D} (V-u) |V-u| dt &= 0 \end{aligned} \right. \end{cases} \quad (8) \quad (9)$$

Equations (6) through (9) are of a simple form and are satisfied, by every solution of Equations (3) and (4).

The characteristic equations may be solved by using the grid of characteristics or specified time intervals. A specified time interval in the t -direction relates the values of V and H at the beginning of the interval to those at the end by the characteristic equation. This method has several advantages over the grid of characteristics, which is used in solving supersonic compressible flow problems. The process of solving Equations (6) through (9) is illustrated in Figure 2, when t_i and t_{i+1} are the beginning and the end of the time interval Δt . Points A, C, and B are three adjacent points on the line $t = t_i$, each a distance Δx apart. Let point P fall on the intersection of $t = t_{i+1}$ and $x = x_C$. Two characteristic lines, C^+ and C^- , pass through P and intersect the line $t = t_i$ at R and S. The values of V and H at $t = t_i$ are assumed to be known, and their values at point P are to be determined.

Applying the linear approximation for small intervals to Equations (7) and (9), the following equations are obtained.

$$\begin{aligned} (V_P - V_R) + \frac{g}{C_R} (H_P - H_R) \\ + \frac{f}{2D} (V - u)_R |V - u|_R \Delta t = 0 \end{aligned} \quad (10)$$

and

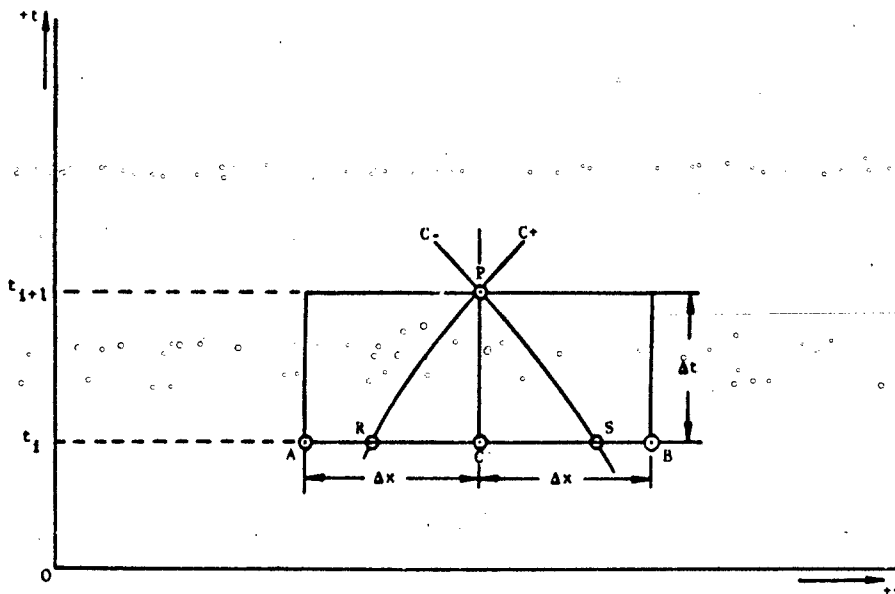


Figure 2. Positions of the Characteristic Lines in a Specified Time Interval

$$(V_p - V_s) - \frac{g}{C_s} (H_p - H_s) + \frac{f}{2D} (V - u)_s \left| V - u \right|_s \Delta t = 0. \quad (11)$$

Equations (10) and (11) contain four terms representing the value V and H at points R and S , which may be evaluated by considering the slopes of the characteristic lines given by Equations (6) and (8).

For the first approximation, the slopes of the characteristics lines at points R and S may be assumed to be the average slopes between the points A and C and C and B , respectively. Then, Equation (6) and (8) may be approximated by

$$C_+ : \frac{dx}{dt} = \frac{V_A + V_C}{2} + C \quad (12)$$

and

$$C_- : \frac{dx}{dt} = \frac{V_C + V_B}{2} - C. \quad (13)$$

Physically, Equations (12) and (13) represent the wave front velocities. Therefore, the location of the points R and S may be determined as

$$x_R = x_C - \frac{(V_A + V_C)}{2} \Delta t + C \Delta t \quad (14)$$

and

$$x_S = x_C - \frac{(V_B + V_C)}{2} \Delta t - C \Delta t. \quad (15)$$

If the velocities from A to C and C to B are assumed to be linearly distributed, then the velocities at points R and S can be approximated as

$$V_R = V_C - \frac{x_C - x_R}{\Delta x} (V_C - V_A). \quad (16)$$

and

$$V_S = V_C + \frac{x_C - x_S}{\Delta x} (V_C - V_B). \quad (17)$$

Similarly, the value of H at points R and S can be evaluated as

$$H_R = H_C - \frac{x_C - x_R}{\Delta x} (H_C - H_A) \quad (18)$$

and

$$H_S = H_C + \frac{x_C - x_S}{\Delta x} (H_C - H_B). \quad (19)$$

Once the values of V_R , V_S , H_R , and H_S are determined, Equations (10) and (11) can be solved simultaneously to obtain V_p and H_p as follows:

$$V_p = \frac{1}{2} (V_R + V_S) + \frac{g}{2C} (H_R - H_S) - \frac{f \Delta t}{2D} (V_C - u) \left| V_C - u \right| \quad (20)$$

and

$$H_p = \frac{C}{2g} (V_R - V_S) + \frac{1}{2} (H_R + H_S). \quad (21)$$

The method can now be applied to a pipe. Consider, for example, a pipe which is divided into n sections, each of Δx length. First, the values of V and H at A_0, A_1, \dots, A_n in Figure 3 are given for $t = t_0$. Then, by using Equations (16) through (21), the values of V and H at B_1, B_2, \dots, B_{n-1} can be evaluated. In similar manner, C_2, C_3, \dots, C_{n-2} can be evaluated. The computation can proceed to a point determined by the number of sections in the pipe. However, if sufficient boundary conditions on x_0 and x_n are given as a function of time, V and H at those points marked in Figure 3 by a black circle can be computed. It is evident that, once suitable boundary conditions are given at both ends of the pipe, the computation can be performed.

In order to proceed with the computation, the boundary conditions at the ends of the pipe must be established and the solution must satisfy such conditions. As shown in Figure 4, there is only one characteristic line involved at each boundary. Therefore, Equations (10) and (11) cannot be solved simultaneously to obtain V_p and H_p . At the boundary, the values of V_p and H_p must be given as a function of time, or V_p and H_p must be related by a known function. Then, Equations (10) and (11) may be solved separately for the remaining unknown variables. In the case of a boundary where more than one pipe is involved, the condition of continuity and pressure drop at the boundary must also be satisfied. For convenience, the positive direction is defined as from the left-end boundary to the right-end boundary, and the same convention is also applied to the pipe motion and flow direction in the pipe.

A three-pipe joint such as the T-joint shown in Figure 5, will be used as an example to illustrate the treatment of the boundary condition. The joint consists of three boundaries. The absolute flow velocities at the boundaries are defined as V_{p1} , V_{p2} , and V_{p3} . If there is external excitation at the joint with excitation velocities u_1 , u_2 , and u_3 , then the relative flow velocities are given by

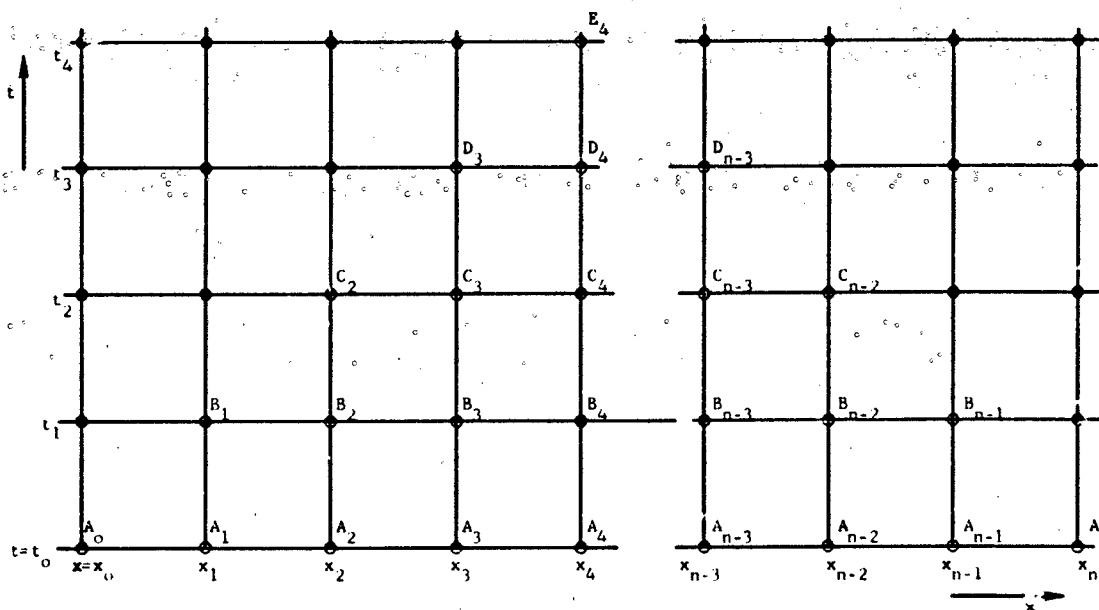


Figure 3. Computation Procedures for Interior Points

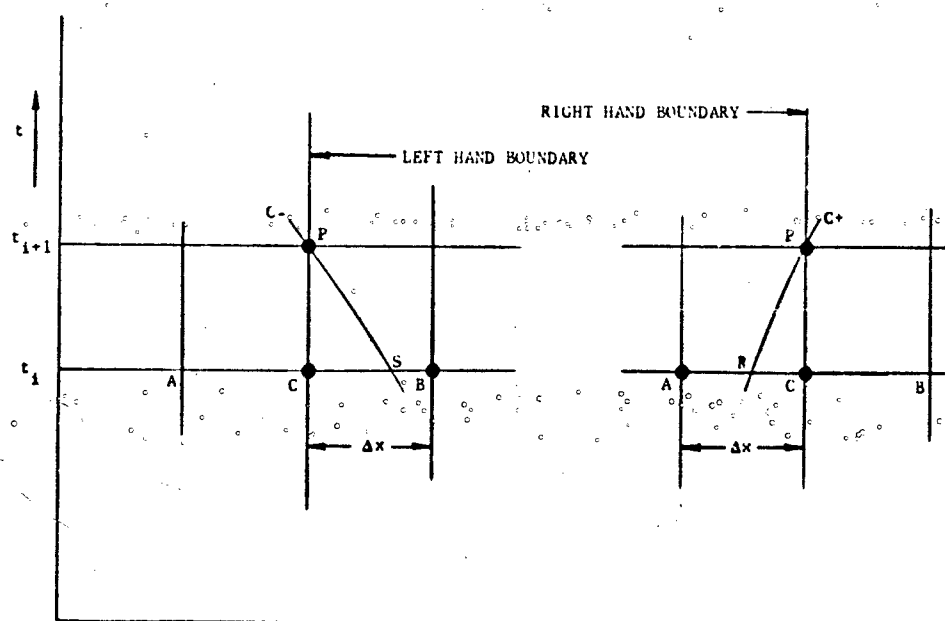


Figure 4. Positions of the Characteristic Lines at the Boundaries

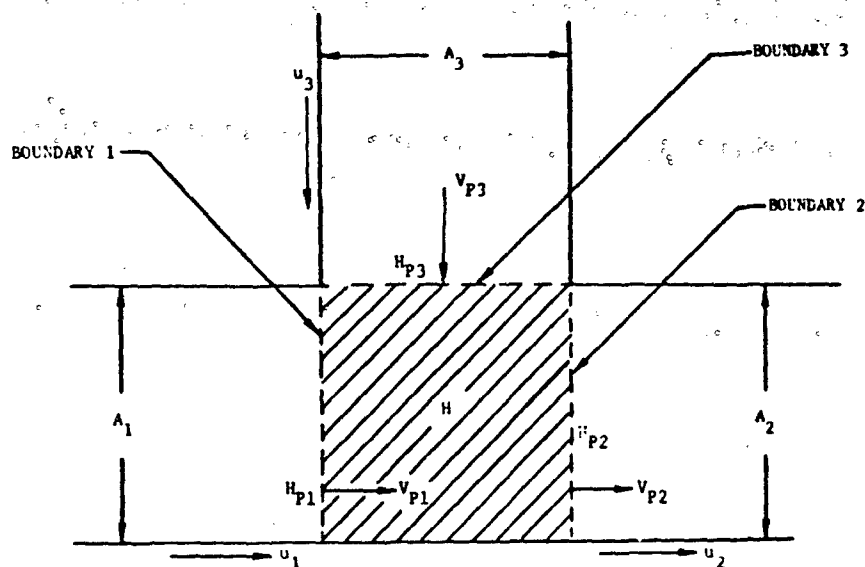


Figure 5. Boundary Conditions at a T-Joint

$$\begin{aligned}\bar{u}_1 &= v_{P1} - u_1 \\ \bar{u}_2 &= v_{P2} - u_2 \\ \bar{u}_3 &= v_{P3} - u_3\end{aligned}\quad (22)$$

To satisfy the equilibrium condition, there can be only one pressure H at the joint, and it is related to the pressures at the boundaries of the three pipes as

$$\begin{aligned}H &= H_{P1} \pm \Delta H_1 \\ H &= H_{P2} \pm \Delta H_2 \\ H &= H_{P3} \pm \Delta H_3.\end{aligned}\quad (23)$$

Where ΔH is the pressure drop across the boundary and follows the sign convention that plus indicates a left boundary and minus a right boundary. Substituting Equations (10) and (11) into Equation (23) for the values of H_P , the following six characteristic equations are obtained for a three-pipe joint:

Pipe 1

Right boundary - R:

$$\begin{aligned}H &= H_{R1} - \frac{C}{g} (v_{P1} - v_{R1}) - \\ &\frac{Cf}{2gD_1} \left| \bar{u}_1 \right| \bar{u}_1 \Delta t - \Delta H_1.\end{aligned}\quad (24a)$$

Left boundary - L:

$$\begin{aligned}H &= H_{S1} + \frac{C}{g} (v_{P1} - v_{S1}) + \\ &\frac{Cf}{2gD_1} \left| \bar{u}_1 \right| \bar{u}_1 \Delta t + \Delta H_1.\end{aligned}\quad (24b)$$

Pipe 2

Right boundary - R:

$$\begin{aligned}H &= H_{R2} - \frac{C}{g} (v_{P2} - v_{R2}) - \\ &\frac{Cf}{2gD_2} \left| \bar{u}_2 \right| \bar{u}_2 \Delta t - \Delta H_2.\end{aligned}\quad (25a)$$

Left boundary - L:

$$\begin{aligned}H &= H_{S2} + \frac{C}{g} (v_{P2} - v_{S2}) + \\ &\frac{Cf}{2gD_2} \left| \bar{u}_2 \right| \bar{u}_2 \Delta t + \Delta H_2.\end{aligned}\quad (25b)$$

Pipe 3

Right boundary - R:

$$\begin{aligned}H &= H_{R3} - \frac{C}{g} (v_{P3} - v_{R3}) - \\ &\frac{Cf}{2gD_3} \left| \bar{u}_3 \right| \bar{u}_3 \Delta t - \Delta H_3.\end{aligned}\quad (26a)$$

Left boundary - L:

$$H = H_{S3} + \frac{C}{g} (V_{P3} - V_{S3}) +$$

$$\frac{Cf}{2gD_3} \left| \bar{u}_3 \right| \bar{u}_3 \Delta t + \Delta H_3. \quad (26b)$$

Depending on the physical orientation of the pipes at the joint, there are eight possible combinations of the boundaries for a three-pipe joint. The combinations are:

1. R, R, R
2. R, R, L
3. R, L, R
4. R, L, L
5. L, R, R
6. L, R, L
7. L, L, R
8. L, L, L.

The coordinate system and a sample combination of the boundaries are shown in Figure 6 and 7 respectively. For a given combination, there are three equations which can be selected from Equations (24a) through (26b). Four variables, H , V_{P1} , V_{P2} , and V_{P3} , are involved in three equations, therefore, a fourth equation is required. The fourth equation is derived from the condition of continuity at the joint. If the three pipes have flow area of A_1 , A_2 , and A_3 , then the continuity equations for the eight boundary combinations can be expressed as follows:

$$R, R, R: A_1 \bar{u}_1 + A_2 \bar{u}_2 + A_3 \bar{u}_3 = 0 \quad (27a)$$

$$R, R, L: A_1 \bar{u}_1 + A_2 \bar{u}_2 - A_3 \bar{u}_3 = 0 \quad (27b)$$

$$R, L, R: A_1 \bar{u}_1 - A_2 \bar{u}_2 + A_3 \bar{u}_3 = 0 \quad (27c)$$

$$R, L, L: A_1 \bar{u}_1 - A_2 \bar{u}_2 - A_3 \bar{u}_3 = 0 \quad (27d)$$

$$L, R, R: -A_1 \bar{u}_1 + A_2 \bar{u}_2 + A_3 \bar{u}_3 = 0 \quad (27e)$$

$$L, R, L: -A_1 \bar{u}_1 + A_2 \bar{u}_2 - A_3 \bar{u}_3 = 0 \quad (27f)$$

$$L, L, R: -A_1 \bar{u}_1 - A_2 \bar{u}_2 + A_3 \bar{u}_3 = 0 \quad (27g)$$

$$L, L, L: -A_1 \bar{u}_1 - A_2 \bar{u}_2 - A_3 \bar{u}_3 = 0 \quad (27h)$$

Based on the given boundary combination, one of the above equations is selected with the other three equations selected from Equations (24a) through (26b) to solve for the values of H , V_{P1} , V_{P2} , and V_{P3} .

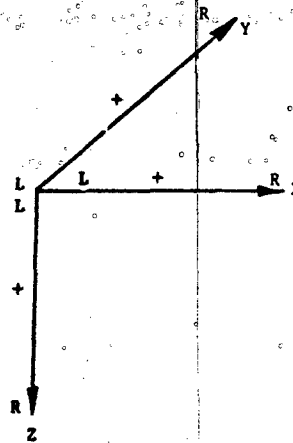


Figure 6. The Coordinate System Used in the HYTRAN

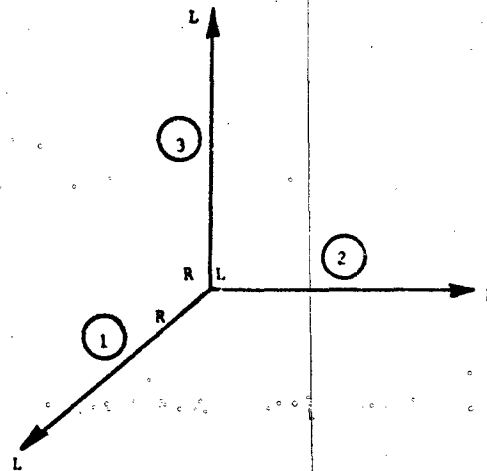


Figure 7. Sample Combination of Boundaries (R, L, R.)

Once H is determined, H_{P1} , H_{P2} , and H_{P3} are calculated from Equation (23). The pressure drop terms in Equation (23) are calculated using the usual pressure drop coefficient, K_1 , K_2 , and K_3 .

$$\Delta H_1 = \frac{K_1}{2g} \left| \bar{u}_1 \right| \bar{u}_1 \quad (28a)$$

$$\Delta H_2 = \frac{K_2}{2g} \left| \bar{u}_2 \right| \bar{u}_2 \quad (28b)$$

$$\Delta H_3 = \frac{K_3}{2g} \left| \bar{u}_3 \right| \bar{u}_3 \quad (28c)$$

The boundary conditions for a two-pipe joint or a one-pipe joint can be similarly formulated.

COLUMN SEPARATION AND PRESSURE ATTENUATOR

Although there are methods [7] of calculating the pressure generated at a boundary due to the reattachment of the separated fluid column, it is difficult to describe the detailed behavior of a two-phase system representing the cavitation and column separation phenomena. For engineering applications, it may be sufficient to predict an average pressure developed near a joint due to column separation. In predicting column separation effects in a complicated piping circuit, a practical engineering approach is used to simplify the formulation. The following assumption is employed in this analysis to indicate the occurrence of column separation.

Column separation occurs when the liquid pressure drops below its vapor pressure or $(H - Z) \leq H_{min}$.

The HYTRAN computer program has an inherent assumption that the hydraulic transient equations and the continuity relationship at a joint remain valid even when column separation occurs. When column separation at some joint is predicted in the solution, a constant pressure equal to the vapor pressure of the

liquid is imposed on the location until it is changed to a higher value by a reflected pressure wave. Employing this approach the location of column separation effects are identified in the piping circuit and estimates of their severity are made to provide a basis for the sizing of pressure attenuation devices to avoid the occurrence of this phenomenon. In view of this, it is recommended that pressure attenuation devices be used to suppress column separation at the locations where column separation may occur.

A variety of attenuator types such as quick opening valves, rupture diaphragms, and energy storage accumulators have been considered for application in protective facilities. Owing to the requirements for fast response and multiple exposures, only the energy storage type of unit is considered to be of interest here. This type of accumulator as shown in Figure 8 consists of either a piston or a bladder type of diaphragm which separates the fluid from a precharged gas container and operates on the principle that the energy of the pressure waves is stored by compression of gas in the unit and then released later at a slower rate. To establish the initial conditions of an accumulator, the precharge gas is assumed to be in thermal equilibrium with the liquid. Consider an accumulator that has a gas volume of V_0 at a precharge pressure of H_0 . Then, at the steady-state operating pressure of H_s , the accumulator gas volume is $V_s = V_0(H_0/H_s)$. Usually the precharge gas pressure is set at 80 percent of the steady-state operating pressure or $V_s = 0.8 V_0$. During hydraulic transient variations, liquid volume is either added to or removed from the accumulator. The pressure at the joint is determined by the reversible

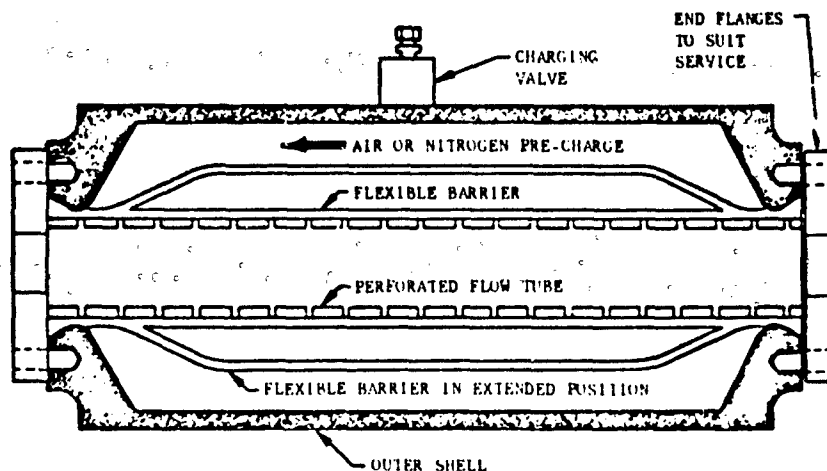


Figure 8. In-Line Accumulator With a Perforated Flow Tube (Von Manufacturing Co.)

polytropic process of the precharge gas, or

$$H_p = H_s \left(\frac{V_s}{V_s + \Delta V} \right)^\gamma \quad (29)$$

where γ is a constant of the gas which depends on the physical property and process. ΔV is the change of flow volume of the accumulator.

HYDRAULIC TRANSIENT COMPUTER PROGRAM (HYTRAN)

Based on the mathematical formulations presented in the previous section, an integrated computer program HYTRAN was developed. It consists of three subprograms for calculating initial steady-state flow conditions, hydraulic transient pressures, and for plotting the computed data. The three subprograms are:

- HYTRAN-I. Calculates initial equilibrium flow conditions for piping circuits in which the circuit parameters are estimated.
- HYTRAN-A. Calculates pressure transients in piping circuits due to support motions. Locations of column separation are indicated, but the phenomena are not treated rigorously.
- HYPLLOT. Prints and plots variations of flow velocities and pressure heads as a function of time at the left or right end of selected pipes. The result will facilitate the proper selection of accumulators.

HYTRAN-A is the basic fluid transient program and has the following features and capabilities:

- a. Calculates transient pressures in three-dimensional piping networks, with various combination of boundaries as shown in Table 1.
- b. Accepts velocity excitations at pipes; each pipe having different excitations.
- c. Accepts pressure excitations at one-pipe joints.
- d. Accounts for the effects of a variety of pipe fittings considering tee joints as three-pipe joints, valves and elbows as two-pipe joints, and reservoirs and pumps as one-pipe joints.
- e. Accounts for pipe friction and pressure drop at joints.
- f. Accepts both in-line and appendage-type pressure attenuators.
- g. Calculates wave velocities based on fluid and pipe elastic properties.

h. Calculates the flow velocities and fluid pressures as functions of time.

i. Summarizes the maximum flow velocities and maximum and minimum pressure heads in each pipe and identifies the time at which they occur.

HYTRAN-I calculates the steady-state flow. The computation for the piping circuit is completed when the flow velocities at both ends of each pipe in the circuit are equal to or less than a prescribed tolerance.

The HYTRAN-A program also detects the occurrences of column separation phenomena in a piping circuit by monitoring the liquid pressures and identifying when they drop below the vapor pressure.

HYPLLOT utilizes data from HYTRAN-A and allows the user to specify pipe numbers and location (left and/or right end of pipe) where transient velocities and pressures are to be plotted as function of time. HYPLLOT offers two options of plotting, CALCOMP pen plotter or line printer, to display information graphically.

Table 2 presents the capabilities and limitations of the HYTRAN Program.

These limits can be increased to larger numbers by changing the dimension statements of the programs as long as they do not exceed the core size of the computer system.

The present version of the HYTRAN program (HYTRAN-I, HYTRAN-A, and HYPLLOT) requires 32,000₁₀ words.

A detail description and listing of the HYTRAN programs are contained in Reference 8.

COMPARISON OF HYTRAN COMPUTER RESULTS WITH EXPERIMENTAL DATA

To verify the HYTRAN program, a comparison was made between the computed transient pressure in a complex fluid system and the recorded test data. Figure 9 shows the configuration of the fluid system. The fluid circuits which are an integral part of the equipment, carry chilled fluid through each component to keep the temperature within tolerance. The chilled fluid is supplied by and returns to an outside source. All the pipes were solidly mounted to the main frame of the cabinet.

The electronic equipment was mounted on a hydraulic shaker table capable of subjecting the equipment to a specified acceleration time history. A piping circuit located off the shaker table supplied the chilled fluid to the fluid circuits of the equipment at design pressure and flow. Pressure transducers and accelerometers were positioned in the fluid circuit

Table 1. Summary of Boundary Conditions

Boundary Condition (NBOND)		Joint Boundary Condition			H _B	V _B
Numeric	Symbolic	Pipe 1 (NP1)	Pipe 2 (NP2)	Pipe 3 (NP3)		
1	RRR	R	R	R		
2	RRL	R	R	L		
3	RLR	R	L	R		
4	RLL	R	L	L		
5	LRR	L	R	R		
6	LRL	L	R	L		
7	LLR	L	L	R		
8	LLL	L	L	L		
9	RR	R	R			
10	RL	R	L			
11	LR	L	R			
12	LL	L	L			
13	RHB	R			GIVEN	
14	RVB	R				GIVEN
15*	RHV*	R			GIVEN	GIVEN
16	LHB	L			GIVEN	
17	LVB	L				GIVEN
18*	LHV*	L			GIVEN	GIVEN
19*	R *	R				
20*	L *	L				
21*	RRB*	R	R		GIVEN	GIVEN
22*	RLB*	R	L		GIVEN	GIVEN
23*	LRB*	L	R		GIVEN	GIVEN
24*	LLB*	L	L		GIVEN	GIVEN
25	RRP	R	R			
26	RLP	R	L			
27	LRP	L	R			
28	LLP	L	L			

*These boundary conditions are not used in HYTRAN-I.

Symbols:

HV is a dead end attenuator. R indicates right end of a pipe.
 B is a in-line attenuator. HB indicates constant pressure.
 P is a pump. VB indicates constant velocity.
 L indicates left end of a pipe.

Table 2. Capabilities and Limitations of HYTRAN Program

Item	Improved HYTRAN (Sperry Rand)
No. of pipes	800 (HYTRAN-I, UNIVAC) 750 (HYTRAN-I, CDC) 600 (HYTRAN-A, UNIVAC) 500 (HYTRAN-A, CDC)
No. of joints	Same as No. of pipes
No. of section in each pipe	A function of No. of pipes in a particular problem = 3000/NPIPE (UNIVAC) = 2500/NPIPE (CDC)
NOTE: The remaining items are for HYTRAN-A only.	
No. of Velocity Excitation functions	12
No. of Pressure Excitation functions	1
No. of data points	
Velocity Excitation	650 (UNIVAC) 800 (CDC)
Pressure Excitation	650 (UNIVAC) 800 (CDC)
No. of time increments for calculations	19,200 (UNIVAC) 16,000 (CDC)
No. of data points on each plot	1000

at several locations. Then with the electronic equipment operating, it was subjected to several shock tests in each of the three orthogonal axes [3]. Test data for comparison with computed data was recorded on a tape recorder and an oscillograph recorder.

A list of the material and inside diameter of each piping segment is tabulated in Table 3. Figure 10 is the mathematical model of the test unit which was constructed using the circuitry of the system and the coordinate system defined in Figures 6 and 7. Examination of the accelerometer readings from the test results showed that each of the three main piping levels experience about the same accelerations as the base of the cabinet. Hence, the excitation input at the base of the cabinet was used to excite all the pipes in the model.

The flexible plastic tube runs are idealized by three straight segments. Since the HYTRAN formulation assumes one dimensional flow, the traveling wave water jackets of the electron tube are simulated with equivalent cross sectional area pipes. Further, the program accepts

only one modulus of elasticity so it was necessary to modify the wall thickness of the plastic pipe so that the calculation for the wave velocity would equal the predicted value.

The model of the equipment shown in Figure 10 contained several pipes with a length of 1.4 feet. The maximum Δx (Figure 2) for a 1.4 foot length of pipe is 0.7 feet. To satisfy the stability criteria of HYTRAN a Δt (Figure 2) of 0.00015 seconds was selected.

Sample plots at four locations in the test system are presented in Figures 11 through 15. The upper part of Figure 11 shows the recorded accelerometer reading. This time history was numerically integrated to form the velocity/excitation table which defined the motion of the pipes. The HYTRAN computation was performed using the mathematical model of Figure 10 and using the measured base velocity excitation to excite the pipes. Computed results are shown in Figures 11 through 15 superimposed on the measured pressure time histories. A comparison of the results indicates good correlation between the test data and computed results.



Figure 9. Actual Fluid Loop

Table 3. Tube Dimensions and Material List of AM Unit 202

TUBE NUMBERS	MATERIAL	TUBE INSIDE DIAMETER
1,49	Copper	1.25"
2,3,4,5,9,10,14,15,19,20,24,25,26, 27,28,29,33,34,38,39,43,44	Copper	1.062"
6,8,11,13,16,18,21,23,30,32,35,37, 40,42,45,47	Plastic	0.487"
7,12,17,22,31,36,41,46 (Simulated Traveling Wave Waterjackets of Electron Tube)	Steel	Simulated with 0.866" Pipe

Note: Steady State Flow Rate 32 gpm

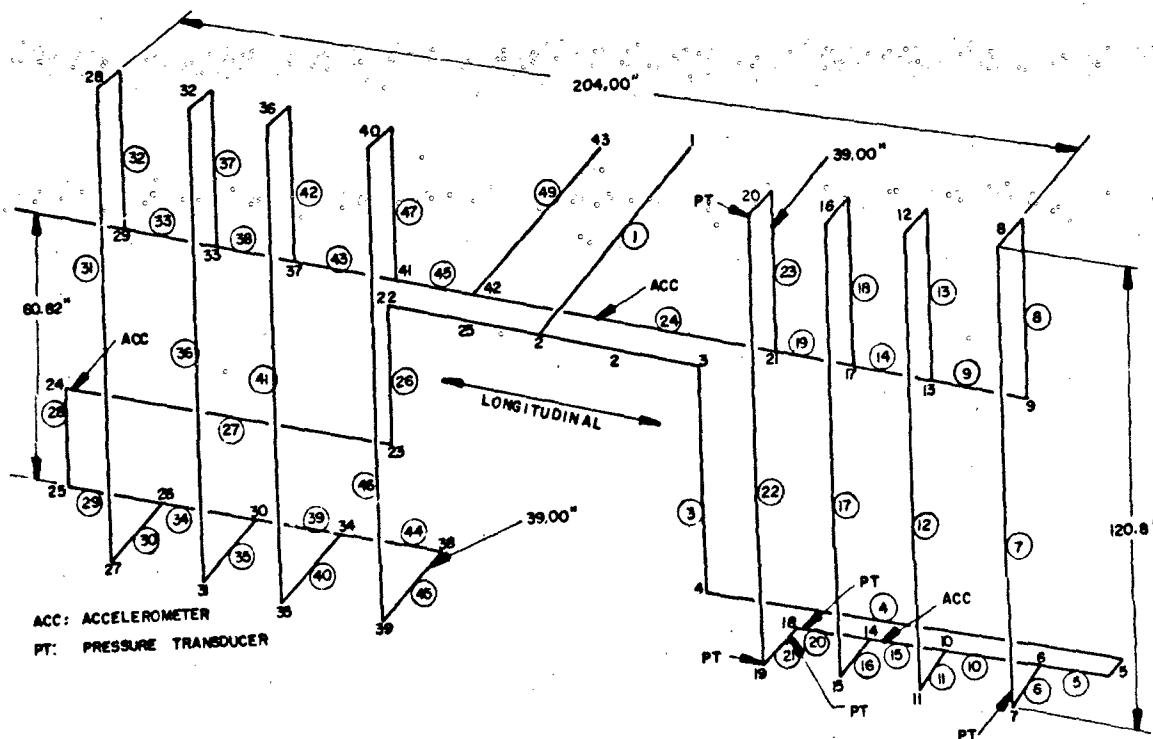


Figure 10. Mathematical Model of the Fluid System

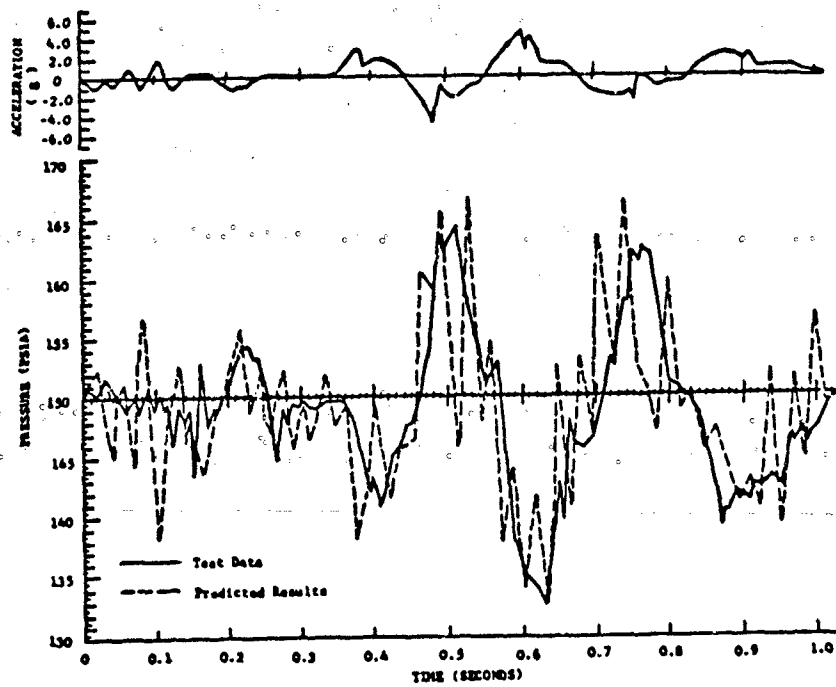


Figure 11. Pressure Time History at the Lower End of Pipe 7 for Test 39

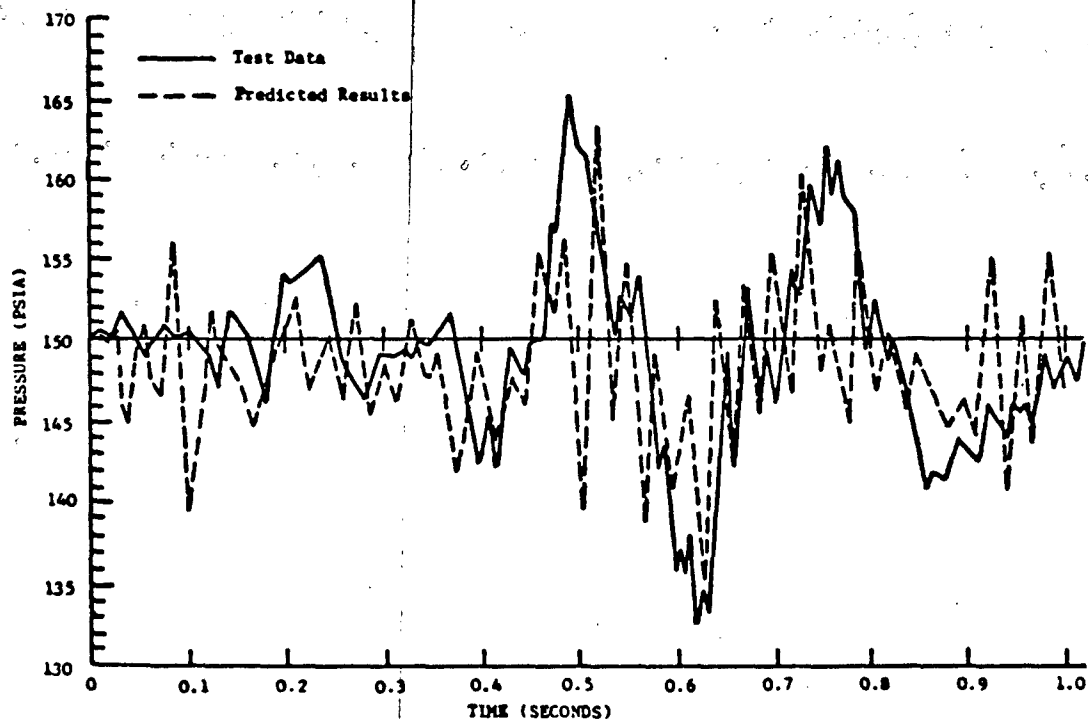


Figure 12. Pressure Time History of Pipe No. 20 for Test 39

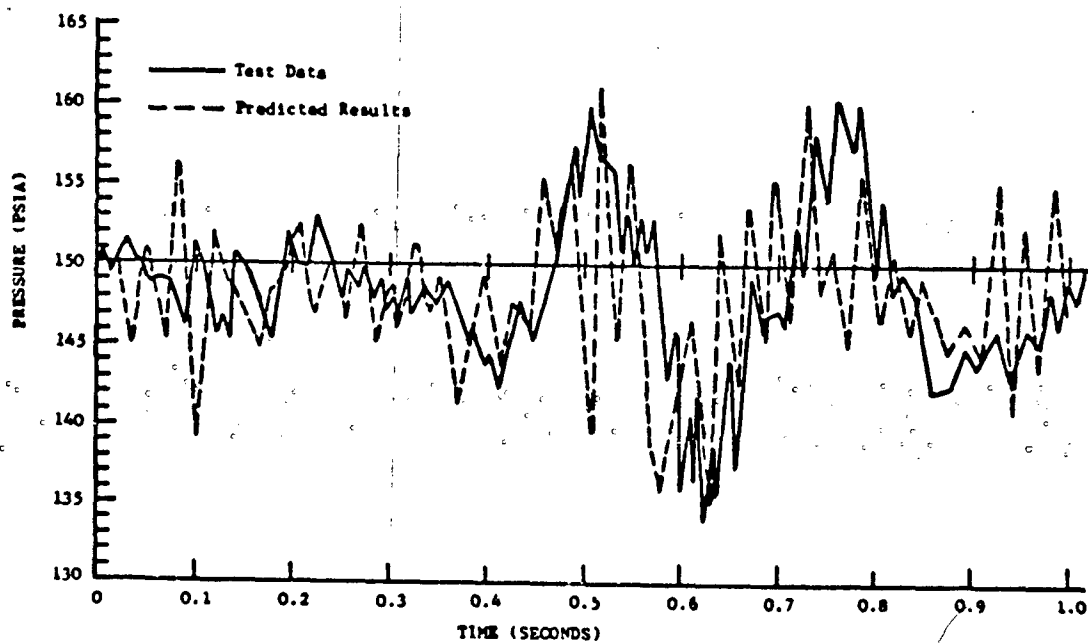


Figure 13. Pressure Time History of Pipe No. 21 for Test 39

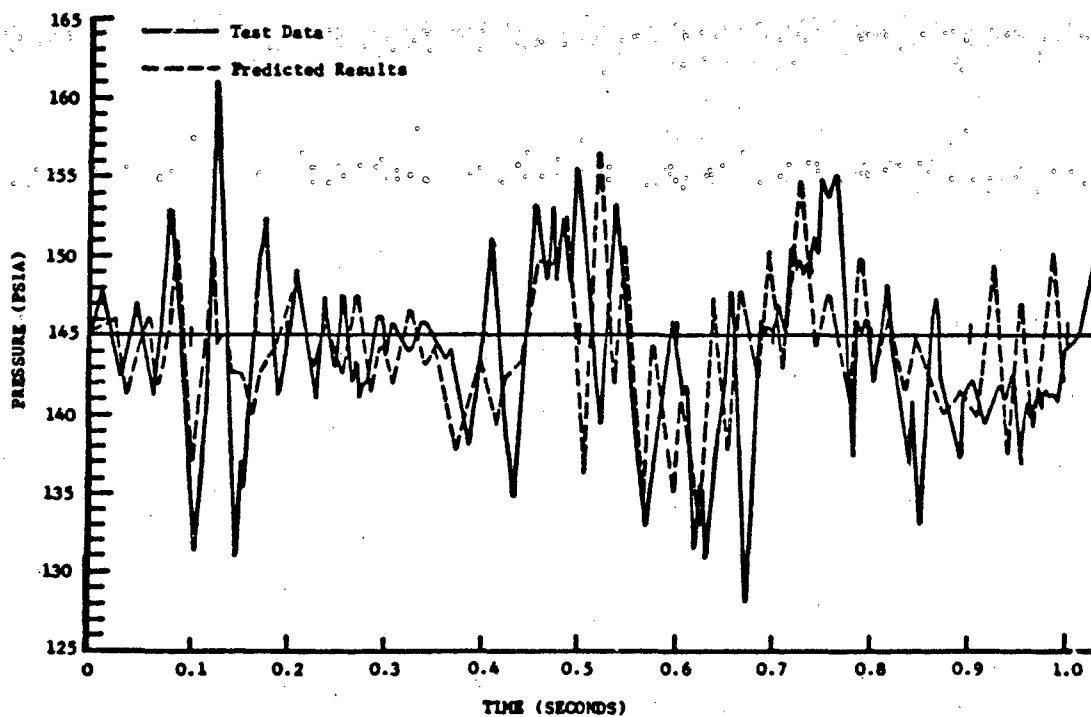


Figure 14. Pressure Time History at the Upper End of Pipe No. 22 for Test 39

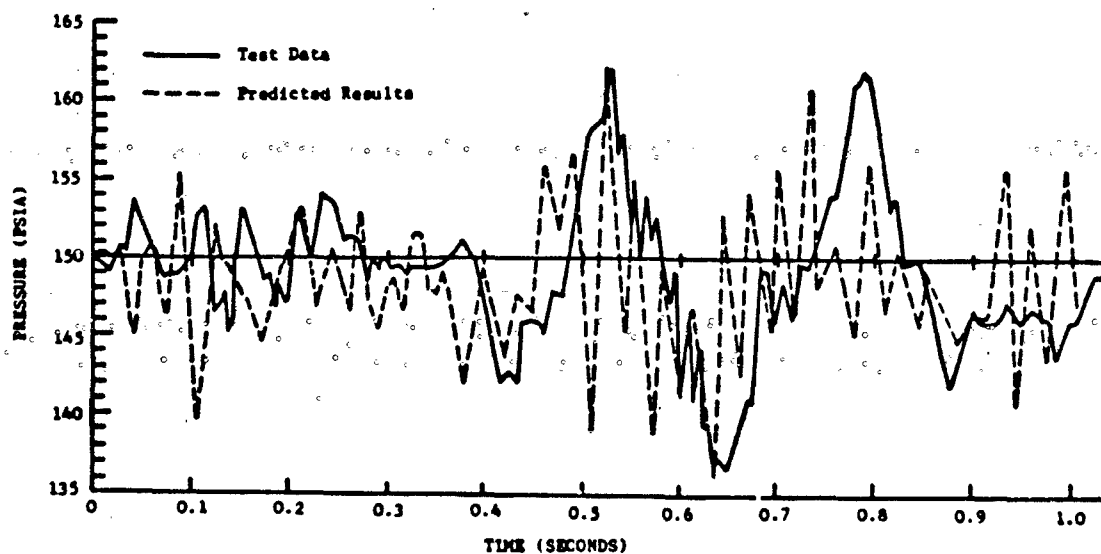


Figure 15. Pressure Time History at the Lower End of Pipe No. 22 for Test 39

Where the minor differences between test and computed data exist, they could be due to the following reasons:

- Accuracy of the test instrumentation.
- Negligence of the viscous effects of the fluid in the basic HYTRAN formulation. As discussed by DeArmond and Rouleau [9], viscous effects may be significant, especially if frequencies are high or pulse lengths short, leading to attenuation and dispersion of the propagating wave.
- Negligence of the elastic effects of the pipes (except wave velocity calculation) in the basic HYTRAN formulation.

CONCLUSIONS

Based on this study, it can be concluded that HYTRAN provides good qualitative results and that it is a usable engineering tool for hydraulic transient analyses of piping systems subjected to external excitation (base motion).

LIST OF SYMBOLS

- A Cross sectional area of a pipe
- B Bulk modulus of elasticity of the liquid
- C Wave velocity as defined by Equation 5
- C₁ Constant
- D Diameter of pipe
- E Modulus of elasticity of the pipe wall material
- e Pipe wall thickness
- f Friction factor
- g Gravitational acceleration
- x Distance along pipe axis
- ρ Density of liquid
- 1 Subscript referring to pipe 1
- 2 Subscript referring to pipe 2
- 3 Subscript referring to pipe 3

REFERENCES

1. Streeter, V. L. and Lai, C., "Waterhammer Analysis Including Fluid Friction", Transactions of American Society of Civil Engineers, Vol. 128, Part I, 1963.
2. "Experimental Evaluation of Design Methods for Hardened Piping Systems", IIT Research Institute, Report No. J6185, September 1970.
3. "Work Statement Specification PAR Prototype Hardness Verification Test Program", Bell Telephone Laboratories, June 1970.
4. Parmakian, J., "Waterhammer Analysis" Prentice Hall, Inc., New York, N. Y., 1955.
5. Lister, M. "The Numerical Solutions of Hyperbolic Partial Differential Equations by the Method of Characteristics", Mathematical Method for Digital Computers, Edited by Ralston and Wilf. John Wiley and Sons, Inc., New York, 1960.
6. "HYTRAN Computer Program User's Manual", the Ralph M. Parsons Company, Document No. SAF-41, November 1970.
7. Li, W. H., and Walsh, J. P., "Pressure Generated by Cavitation in a Pipe", Proceedings of the American Society of Civil Engineers, Vol. 90, No. EM6, December 1964.
8. "Hydraulic Transients Program", U.S. Army Engineer Division, Huntsville, HNDTR-73-9-ED-R, 30 April 1973.
9. DeArmond, R. P., and Rouleau, W. T., "Wave Propagation in Viscous, Compressible Liquid Confined in Elastic Tubes" ASME Paper No. 72-FE-23.

DISCUSSION

Mr. Welch (Westinghouse Electric Corporation):
How can private companies get a copy of this HYTRAN program?

Mr. Yen: Anybody who is interested in this program can write me in Sperry or call the U.S. Army Corps of Engineers in Huntsville, AL. Presently this program is waiting for the CDC and Univac Machines.

Mr. Welch: I think that anyone who is dealing with control problems, hydraulic control problems, or hydraulic power problems might find this program of some use to them.

POPPING MOTOR DOME SHOCK DURING FIRST STAGE SEPARATION ON POSEIDON MISSILE FLIGHTS

Lane R. Pendleton, Research Specialist
and Ralph L. Henrikson, Sr. Research Engineer
Lockheed Missiles & Space Company, Inc.
Sunnyvale, California

INTRODUCTION

Shocks as large as 34 g's peak-to-peak were measured in the re-entry bodies during first stage separation on Poseidon development flights. These shocks occurred between 60 and 120 milliseconds after second stage ignition, and excited the fundamental longitudinal modes of the missile. The significant longitudinal frequencies were in a band between 35 and 120 Hz with little response above 150 Hz. The problems resulting from this shock were large loads on the re-entry body support structure and severe shock environments for electronic and hydraulic packages attached to the aft dome of the second stage motor. The analysis effort devoted to this anomaly was considered successful in isolating the source and effecting a suitable design change to reduce its magnitude.

FLIGHT DATA

During the C3X-6 (sixth Poseidon development flight) first separation event, the accelerometers and vibration transducers located in the three instrumented re-entry bodies indicated a shock response (hereafter referred to as "mystery shock") much higher than observed on previous flights. This shock began approximately 80 milliseconds after second ignition. Since all missile body telemetry links are normally in "blackout" at this time, the re-entry body data was the only data initially available for evaluation. The data showed the mystery shock magnitude was considerably higher than any shock predicted for first separation/second ignition in pre-flight analytical studies. Subsequent flights have shown that this shock was not unique to C3X-6 and in fact it has been observed with widely varying amplitude on all Poseidon flights.

An extensive effort was initiated to determine the cause of this shock. The first and most important evidence was the measured flight data. The longitudinal, lateral, and normal acceleration-time histories measured near the re-entry body c.g. during a typical development flight (C3X-6) are shown in Fig. 1. The initial response (zero seconds in this figure) is caused by detonation of the circumferential pyrotechnic cord around the interstage which severs the structural connection between the first and second stages. During the next 50 milliseconds the two stages are held together by the

thrust tailoff of the first stage. Then, increasing pressure in the interstage, due to gas from the burning second stage, pushes the two stages apart. The resulting rigid body acceleration of the missile can be seen in Fig. 1. It reaches a peak of 5 g's at approximately 60 milliseconds after second stage ignition. The mystery shock begins at 80 milliseconds. The peak-to-peak amplitude on this flight in the longitudinal direction was 26 g's. The pre-dominant longitudinal frequencies are 35 and 100 Hz. These frequencies agree with calculated modal frequencies at this flight time. The measured transverse frequencies are 19 and 37 Hz which are re-entry body cantilever modes.

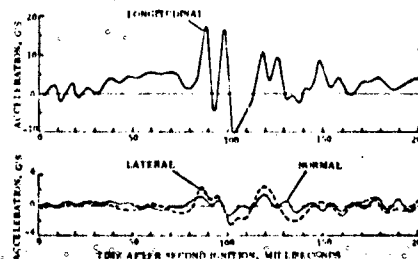


Fig. 1 - Re-entry body acceleration data measured during the C3X-6 flight

A larger mystery shock occurred on C3X-8. The re-entry body data is shown in Fig. 2. The peak-to-peak amplitude was 34 g's. The same conclusions as above can be drawn. Looking at Figs. 1 and 2, the longitudinal acceleration response is much larger than transverse, leading to the conclusion that the force which causes the mystery shock acts primarily in the longitudinal direction.

A drawing of the Poseidon missile showing locations of the segments discussed in this report is given in Fig. 3. More detail of the interstage area during the second ignition/first separation event is shown in Fig. 4.

A statistical comparison of the mystery shock magnitude at the re-entry body c.g. for all

1. No correlation was found between the shock magnitude and the re-entry body position or the number of bodies carried on a particular flight.
2. No correlation was found between the amplitude of this shock and the total velocity change of the missile during first separation. Therefore, the anomalous force-time history has little or no net impulse.

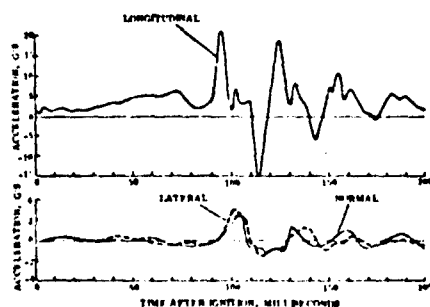


Fig. 2 - Re-entry body acceleration data measured during the C3X-8 flight

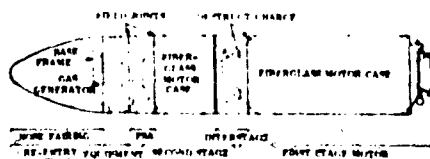


Fig. 3 - The Poseidon missile

A logical suspect for the source of this shock is the second stage motor since the shock occurs during thrust buildup. Consequently the data from twenty-four ground test firings of the second stage motor were carefully examined for evidence of a mystery shock. However, no indication of a mystery shock was found in the ground test data.

On the first six flights the only mystery shock data obtained was from re-entry body measurements. This data was transmitted independently from each

instrumented re-entry body. The missile body telemetry links had a temporary (approximately 0.14 second) blackout at this time caused by ionized gases from the second stage motor. This blackout completely masked the mystery shock event. During subsequent flights some missile data was obtained by transmitting through a redundant antenna located within the re-entry system area of the missile.

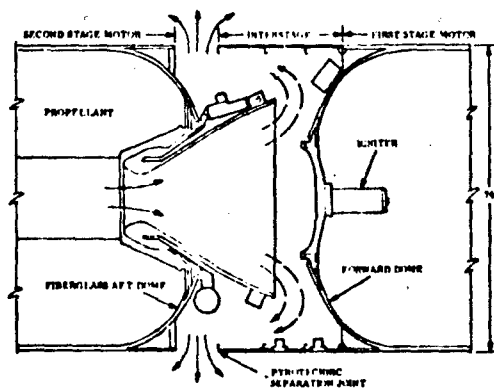


Fig. 4 - Gas flow during first separation after eleven inches of travel

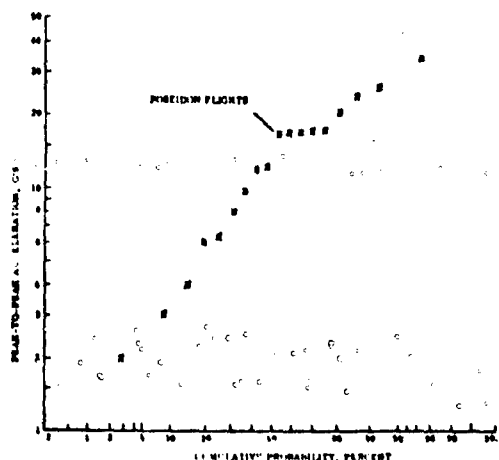


Fig. 5 - Distribution of re-entry body longitudinal acceleration

There is a lesson to be learned from this experience. Unpredicted events or malfunctions can be hidden in a very brief telemetry blackout. Delay recorders or other means must be used to fill the voids caused by T/M blackouts.

ANALYTICAL INVESTIGATION

In order to help isolate the source of this anomaly, a mathematical model of the Poseidon missile was used in an attempt to duplicate flight data. The mathematical model had a total of 123 degrees of freedom representing the missile body and re-entry system as lumped masses. Forces due to a normal separation plus forces which simulate abnormal events were applied to the model. The responses at locations of interest such as the re-entry bodies, equipment section, forward and aft domes, and nozzle were computed for each case considered. Then the computed accelerations were compared with flight data measured at the same location. Not all the possible causes of the mystery shock considered were investigated with the dynamic model since many theories could be eliminated by the flight data alone. A sketch of the structural dynamic model is shown in Fig. 6. The boxes represent lumped masses. Cylindrical shell portions of the missile were modeled as ring shaped elements. The propellant was represented by concentric cylinders connected by shear springs. The calculated response at the re-entry body c.g. due to normal ignition and separation forces is shown in Fig. 7. The measured re-entry body acceleration from a flight with a low mystery shock is also shown for comparison. The initial response shown by the flight data but not by the simulation results is due to forces from detonation of the pyrotechnic separation joint. These forces were not included in the input to the dynamic model.

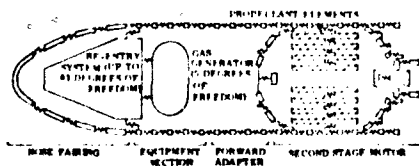


Fig. 6 - Mathematical model of Poseidon at second ignition

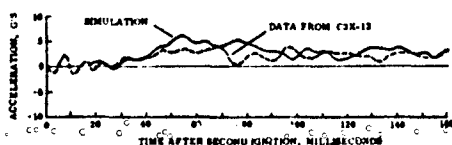


Fig. 7 - Computer simulation of second ignition/first separation, no anomalies

POSSIBLE CAUSES OF THE MYSTERY SHOCK

Many theories were offered in an attempt to explain the cause of the mystery shock. The following paragraphs give a brief description of each of these theories and outline the analysis which leads to accepting or rejecting each hypothesis.

1. Slippage of the Gas Generator

A 3000 pound, 5 millisecond terminal sawtooth pulse was applied to the base frame element of the dynamic model to simulate a loose gas generator impacting on the base frame (see Fig. 3 for gas generator and base frame locations). The calculated re-entry body response is shown in Fig. 8. The measured re-entry body acceleration data from the C3X-6 flight is also shown. It is evident that the re-entry body responses due to this event would have been considerably below those measured on C3X-6. Therefore, it was concluded that this event could not have caused the mystery shock.

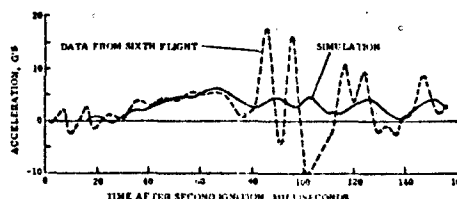


Fig. 8 - Comparison of measured data and computer simulation, gas generator slippage

2. Partial Nozzle Blockage

To determine the effect of a piece of propellant passing through the second stage nozzle, gas dynamic simulations were represented by step functions of various amplitudes and a duration of 10 milliseconds. Blockages of 60, 36, and 20 square inches were considered. The momentary blockage results in a reduction in interstage pressure and an increase in chamber pressure. Thus, the resulting second stage acceleration decreased during the blockage and sharply rose once the throat area cleared. Loads on the second stage structure resulting from this phenomenon were input to the structural dynamic model. The re-entry body acceleration-time history for the 36 square inch case is shown in Fig. 9. This blockage size produced good agreement with the C3X-6 flight data. Note that the computed response compares well with the data both in magnitude and frequency distribution. Other information however tends to discount this as a possible candidate: (1) no evidence of nozzle blockage has been recorded during second stage static firings, and (2) there would have been perturbations in the chamber pressure if this had occurred during flight. Chamber pressure measurements did not indicate any perturbations. Therefore, this theory was also eliminated.

3. First Stage Destruct Charge Detonation

The possibility of dislodging the first stage destruct charge and its subsequent auto detonation during first separation was examined. The destruct charge consists of a detonator block and a flexible linear shaped charge (FLSC) which are attached to the first stage forward dome (see Fig. 3).

Conservative force-time histories acting on the second stage nozzle and aft dome due to this event were input to the structural dynamic model. The calculated re-entry body responses are shown in Fig. 10 along with the C3X-6 flight data. Since the simulation results show considerably lower accelerations than measured during flight, it is concluded that auto detonation of the destruct charge is not the cause of the mystery shock.

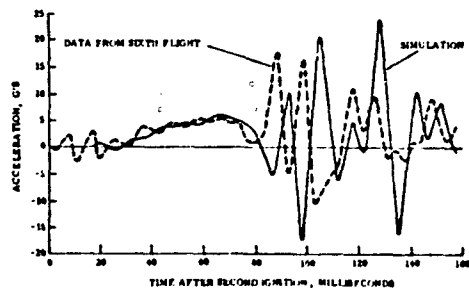


Fig. 9 - Comparison of measured data and computer simulation, partial nozzle blockage

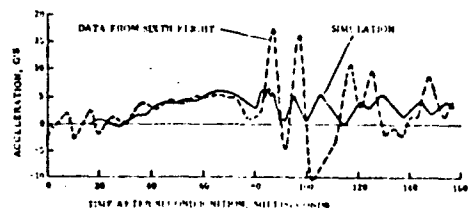


Fig. 10 - Comparison of measured data and computer simulation, detonation of the first stage destruct charge

4. Choke Plane Shifts

Consideration was given to a possible shifting of choke planes during the first separation event. A sketch of the gas flow in the interstage during the second ignition/first separation event is shown in Fig. 4. Initially, the flow chokes between the nozzle exit and the first stage forward dome. Choking also occurs at the separation gap in the interstage skin until the nozzle clears the interstage. At approximately 45 milliseconds after second stage ignition signal, the flow between the nozzle exit and first stage dome unchokes. At approximately 110 milliseconds, when the nozzle has just cleared the interstage, the separation gap choke plane shifts to a plane between the nozzle and the interstage skin. It was concluded that no flow disturbance arose from these shifts and no shift was occurring at the time the disturbance was recorded in flight. Therefore, choke plane shifting is not considered the source of the perturbation that results in the mystery shock.

5. Nozzle Flow Separation

Flow separation occurs in the second stage nozzle during the entire first separation event. The separation point moves up and down the nozzle in a continuous motion during the event. However no mechanism has been defined that would result in a rapid separation-point shift which is necessary to cause a flow disturbance of significant magnitude. The mystery shock, therefore, cannot be attributed to this event.

6. Base Frame "Oil Can"

An investigation was conducted to determine whether the base frame (see Fig. 3) which supports the re-entry bodies could "oil can" when subjected to first separation loads, thus producing the shock observed. This analysis revealed that a 25 g static load at the base frame is required to produce this phenomenon. Acceleration measurements do not indicate more than 7 g's prior to the beginning of the mystery shock, thus this event is not possible. The lack of correlation between shock magnitude and re-entry body position or number of bodies mentioned earlier also discounts this theory.

7. Slippage in the Missile Field Joints

Impact between the two sides of a loose forward skirt adapter - equipment section assembly joint was also considered as a possible cause. Since analyses showed that the entire joint is always in compression throughout the flight time of interest, this event cannot occur. The same conclusion also applies to the other field joints.

8. Combustion in the Interstage

Another theory held that secondary combustion could occur in the interstage due to fuel rich combustion gases mixing with air. To examine this theory, pressure measurements were taken in the interstage on subsequent flights. No sudden rise in interstage pressure occurred on these flights. Also, this phenomenon would produce a significant velocity increase which was not reflected in the missile acceleration data. Therefore, this theory was discarded.

9. Interstage Rupture

Some suggested that the shock resulted from interstage rupture. This theory is not credible because the interstage was designed and tested to much higher pressures than those measured in the interstage. Also, interstage rupture would have resulted in a sudden interstage pressure drop and velocity decrease which is contrary to the measured data, thus eliminating this theory.

10. Popping Motor Dome

The popping motor dome theory assumes that prior to and during the initial phase of the second stage motor ignition process a seal is formed in the unbonded area between the propellant flap and the

aft dome insulator of the second stage motor. Then the seal suddenly releases during dome expansion, allowing gas to fill the gap between the flap and insulator, resulting in a sudden redistribution of the chamber pressure forces. Illustrations depicting the positions of the aft dome and propellant before and after the "pop" are shown in Fig. 11. The propellant is not bonded to the aft dome because the large motion of the dome (1 inch) during motor pressurization would result in large propellant strain. However, to prevent propellant burning along the aft dome a flap is bonded to the propellant. Thus, there is a gap between the flap and the aft dome insulator during normal motor operation. The "pop" occurs when this gap is suddenly opened. The credibility of this theory was also explored with the structural dynamic model. The resultant forces on the propellant and aft dome that were used to simulate this event are shown in Fig. 12. The propellant force shown in this figure is the difference between the forward acting and aft acting pressure forces on the propellant. The forward dome forces are not shown. In Fig. 13 the computed responses are compared with C3X-6 flight data at the re-entry body. The agreement in magnitude and frequency distribution is excellent. It is therefore concluded that a "popping motor dome" is capable of causing the mystery shock. Additional evidence supporting this concept included the following:

- It provides an explanation for the absence of a mystery shock during static motor firings. A "popping motor dome" is not likely to occur during static firings since there is no interstage pressurization or second stage acceleration which aids the formation of the seal.
- The shock magnitude can be changed considerably from that shown in Fig. 13 by varying the pressure difference between the forward and aft domes when the seal breaks, thus accounting for the differences in shock levels from flight to flight.
- The shock from a popping motor dome would be primarily longitudinal, thus agreeing with the measured acceleration data.
- The transverse motion can be generated by assuming that the introduction of chamber pressure into the aft dome-propellant cavity does not occur symmetrically about the missile longitudinal axis.
- No velocity change results from a popping dome because it is just a redistribution of pressure forces within the second stage motor.
- No correlation of the shock amplitude with the number of re-entry bodies or instrumented body position would be expected.
- No perturbation would be expected in the motor chamber pressure because the initial volume change due to filling the gap between propellant flap and dome is small compared to the motor volume - less than 0.5 percent.

- And finally, we would not expect to see any perturbation of the interstage pressure, again because the volume change of the interstage due to second stage dome motion would be very small.

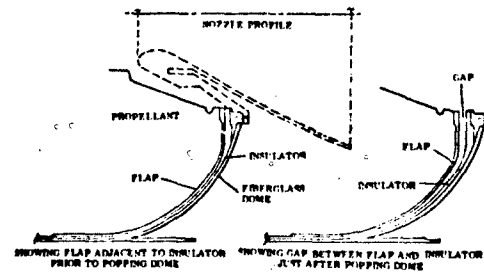


Fig. 11 - Aft dome of second stage motor, before and after popping motor dome

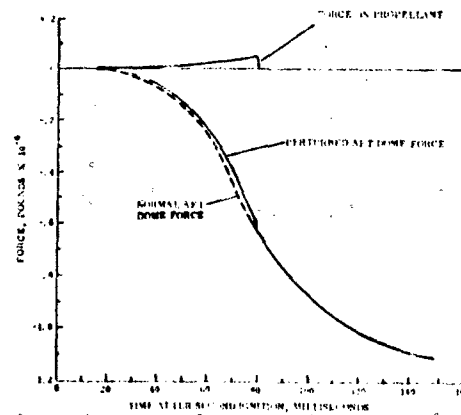


Fig. 12 - Aft dome and propellant forces used to calculate the popping dome shock

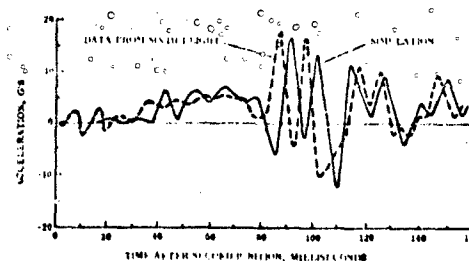


Fig. 13 - Comparison of measured data and computer simulation, popping motor dome

The popping dome theory was the only theory that matched the flight data and satisfied all the additional clues from the flight and ground test data. The theory was considered sufficiently credible to justify a design change.

DESIGN CHANGE

The chosen design change was to insert a polypropylene netting between the aft propellant stress relief flap and the aft dome insulator in order to vent this area and prevent the seal from forming. The netting has eight (.04 inch diameter) filaments per inch in a rectangular mesh. The netting has a total thickness of .08 inch because the filaments in one direction overlay those in the other direction. This netting was suggested by Hercules, Inc. (Hercules and Thiokol, A Joint Venture, Manufacture the Poseidon motors). The netting is attached to the aft dome insulator in the gap shown in Fig. 11. This netting was included in the second stage motor for all Poseidon missiles beginning with the twenty-first flight.

A statistical comparison of the shock magnitude measured at the re-entry body c.g. for all Poseidon flights where data is available is shown in Fig. 14. This data was divided into two populations: first, the initial twenty flights (data was obtained on eighteen of these) which were manufactured before the design change was installed; and, second, all flights after the initial twenty. These motors all included the plastic netting.

It can be seen from Fig. 14 that significantly lower shock levels were measured after the design change. Also, the variation from flight to flight was much smaller. The fact that the shock amplitude was significantly reduced by the netting demonstrates that popping dome was the cause of the mystery shock. Thus we were successful in determining the cause of the shock and in making a design change that reduced the amplitude. The loads and package environments based on the data measured on flights after the design change are acceptable for Poseidon missile design.

CONCLUDING COMMENT

Popping dome shock is a potential problem for any missile which uses solid propellant motors. Motor cases are frequently made of fiberglass or similar materials which experience large growth during motor ignition and pressurization. Motor dome growths of an inch or more are common. If the propellant is bonded to the dome, large bond stresses and large propellant strain results. The design solution most often used is to not bond the propellant to the dome which allows a gap between the dome and propellant when the motor is operating. This design solution can result in a "popping dome" shock. This paper described one approach which was successful in reducing the shock amplitude.

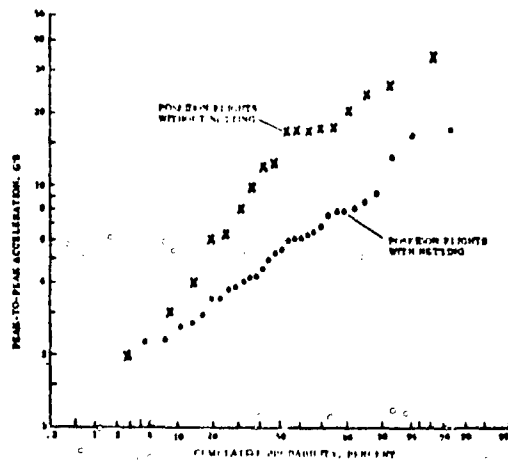


Fig. 14 - Distribution of re-entry body longitudinal acceleration

DISCUSSION

Mr. McWhirter (Sandia Laboratories): I noticed that you still had several shocks that were of quite an amplitude, did the netting fail to completely prevent bonding between the two surfaces or is there some other reason that it popped?

Mr. Pendleton: We feel it could be further reduced by putting in a thicker netting. We used roughly a 1/10 inch netting and we think that during the long time period between when the missile is built and when it is flown, the flap and the insulator can press down and form a partial seal so that we think a thicker netting would reduce it even further.

Mr. Sanders (Rockwell International): Where were your measurements made in the missile?

Mr. Pendleton: The measurements were made at the reentry body c.g in the missile, and we used that as our primary comparison because it was the only location that was available on all flights. We compared that location even though we had data at other points in the missile. We had a particular troublesome problem too in that a telemetry blackout during second ignition just coincided with the time of the shock, so had it not been for the reentry data, that did not get blacked out in this time interval, we would never have discovered it.

Mr. Sanders: How did you conclude that you had not changed the transfer function by this technique, that is pressurization of the aft dome, and hence affecting your data, rather than changing the source of the energy?

Mr. Pendleton: I presume that you are suggesting that the force comes through the aft dome somehow to the propellant in this area.

Mr. Sanders: Possibly yes.

Mr. Pendleton: If this area were actually open as it is supposed to be during this interval, there wouldn't be any way for the force to get carried across that interface so that, in either case, if shock got across the interface, it would mean that the gap was not opening as it was supposed to.

Mr. Cies (RCA): Did the time histories change with the netting, or did the peak to peak amplitude just reduce in that time area?

Mr. Pendleton: Did you say the time interval?

Mr. Cies: Yes, the time history. You showed the peaks for that 0.1 second duration; did they decrease in that area or did the complete time history change?

Mr. Pendleton: The frequencies stayed primarily the same because they were the structural frequencies of the reentry body that we were exciting, so the frequency stayed primarily the same and the amplitude dropped.

SCALING OF WATER IMPACT DATA FOR SPACE SHUTTLE SOLID ROCKET BOOSTER

R. Madden and H.A. Wright
Bolt Beranek and Newman Inc.
Cambridge, Massachusetts 02138

and

D.A. Kross
NASA - Marshall Space Flight Center
Huntsville, Alabama

A combined analytical and experimental program is performed in order to analyze the water impact environment on the space shuttle solid rocket booster (SRB). The analytical studies are intended to identify the nondimensional parameters that are principal contributors to the loading of the vehicle and thus to provide techniques for extrapolation from small-scale models to full-size vehicles. The experimental program is then conducted to verify the analysis and to indicate those parameters which require more sophisticated scaling.

Tests are conducted on a 6-in.-diameter rigid model and on 12-in.-diameter rigid and flexible models. The tests consisted of dropping the models at various impact velocities and at various entry angles without pressure scaling. The test results are analyzed to determine axial and pitch acceleration, penetration depth, and slapdown pressure as a function of impact velocity.

NOMENCLATURE

A - area
A₀ - nozzle exit area
C_g - extensional wave speed
D - diameter
E - Young's modulus
F - force
g - acceleration due to gravity
h - skin thickness
h_w - water height
I - pitch moment of inertia
k - process exponent
K - constant
l_n - nozzle length
l₀ - typical dimension
m - mass
P - pressure
P₀ - ambient air pressure
r - radial coordinate

r₀ - nozzle throat radius
R - nozzle exit radius
t - time
V - velocity
V₀ - impact velocity
x - coordinate
γ - exponent
θ - angular coordinate
ν - kinematic viscosity
ρ₀ - density of water
ω - frequency

SUBSCRIPTS

m - model
p - prototype

INTRODUCTION

This study is concerned with the effects of water impact on the space shuttle's solid rocket booster (SRB). Following its firing, the SRB encounters,

is decelerated by parachutes and/or retro-rockets, and finally lands in water. Preliminary investigations of these water impact loads indicate that they contribute substantially to the mechanical design of the booster.

Performing water impact tests on a full-scale vehicle is impractical because of the costs and time involved in constructing and testing a full-scale structure. The most feasible approach is to investigate existing theories for water entry and then to perform a number of tests on scale-model SRB's, thereby establishing appropriate scaling relationships. The loads on the full-scale vehicle may then be estimated by extrapolating the data from the scale-model tests.

The present program is composed of three phases. In the first phase, existing theoretical scaling laws are investigated for both rigid body and flexible body dynamics. In the second phase of the program, one 6-in.-diameter model and two 12-in.-diameter models are constructed from a tentative solid rocket booster configuration. The 12-in.-diameter models have different wall thicknesses in order to illustrate flexibility effects. The models are instrumented with pressure sensors and accelerometers. In the third phase, drop tests in the nozzle-first entry configuration are conducted at various impact velocities. High-speed photographs are taken of the drops.

This paper presents the theoretical analysis, a discussion of the models and the measurement scheme, and the results of the model tests.

ANALYSIS OF SCALING PARAMETERS

The model studies of water impact on the SRB during reentry are aimed primarily at extrapolating experimental observations on models of different scale. Since the physical system is extremely complex, the analyses presented here are not rigorous; however, they provide a qualitative understanding of various phenomena and serve to indicate the primary scaling parameters. In this section, the various phases of water impact are reviewed, and the dimensionless groups which appear to be important during each phase are presented. Although entries other than vertical ones can be expected for the actual SRB, this theoretical discussion is restricted to vertical entry.

Qualitatively, the following phases of motion are likely:

1. *Initial impact stage.* This stage begins with the time of initial water contact and terminates at the onset of cavity formation.
2. *Submergence stage.* This stage begins with formation of the cavity and terminates at maximum submergence; i.e., the vertical velocity is zero.
3. *Rebound stage.* This stage covers the vehicle's motion from the maximum submergence stage through resurfacing, slapdown, and final settling in the water.

In the following sections, simplified mathematical models of the physics of water impact during each of the above phases are presented. These analyses give insight into those parameters which ought to enter into a dimensional analysis that will allow the extrapolation of data from a scale-model experiment to the prototype (see, for example, Refs. 1 and 2). The quantities of interest are assumed to be the vector acceleration of the center of mass of the vehicle and the fluid pressure exerted at various points on the skin of the vehicle.

Rigid Body Scaling

Initial Impact

During the initial impact stage, the nozzle becomes filled with water which exerts pressure on the nozzle and thus decelerates the entire vehicle. Some insight into the forces on the nozzle during this phase may be obtained from an extremely simplified steady flow analysis.

Assuming a vertical entry condition, the force on the nozzle is given by

$$F = \int_0^R \frac{rP(x)dx}{\cos\theta} \quad (1)$$

where

$$\theta = \tan^{-1} \left(\frac{R-x}{r} \right) \tan\theta_0$$

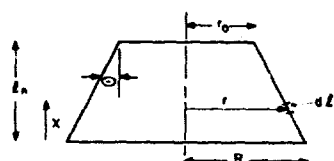
F is the total force on the nozzle

$P(x)$ is the pressure at some distance x ,

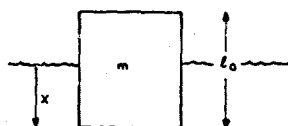
r is the radius

- r_0 is the throat radius,
 l_n is the length of the nozzle,
 θ is the nozzle half-angle.

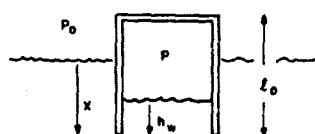
The important parameters are shown in Fig. 1a.



(a) NOZZLE CONFIGURATION



(b) BUOYANCY MODEL



(c) GAS COMPRESSION MODEL

FIG. 1. MODELS FOR THE INITIAL PHASE OF WATER IMPACT

The pressure at any point in the nozzle may be related to the initial velocity by Bernoulli's equation and the continuity equation as follows:

$$P(x) = \rho_0 \left(\frac{V_0^2}{2} - \frac{V^2}{2} - gx \right); \quad (2)$$

and

$$V = V_0 \left(\frac{A_0}{A} \right) = V_0 \left| \frac{R}{R - x \tan \theta} \right|^2; \quad (3)$$

where

V and A are the velocity and area, respectively, at some position x ,

V_0 is the impact velocity,

A_0 is the nozzle exit area,

ρ_0 is the density of water,

R is the radius of the nozzle at its exit.

When Eqs. (2) and (3) are substituted into Eq. (1) and integrated over the length of the nozzle, then the important nondimensional parameters are

$$\frac{P}{\rho_0 V_0^2 R^2}, \frac{G l_n}{V_0^2}, \frac{l_n}{R}, \frac{R}{r_0}.$$

If the force is transformed to acceleration, then two additional dimensionless groups appear:

$$\frac{a}{G}, \frac{m}{\rho_0 l_n^3},$$

where m is the mass of the nozzle. Therefore,

$$\frac{a}{G} = \psi \left\{ \frac{V_0^2}{G l_n}, \frac{m}{\rho_0 l_n^3}, \frac{l_n}{R}, \frac{R}{r_0} \right\}, \quad (4)$$

where $V_0^2/G l_n$ is the Froude number.

This analysis does not consider viscous friction effects; however, the inclusion of viscous effects aids considerably in collapsing the data as indicated in the data analysis section.

Submergence state

Submergence should be controlled by two physical factors: buoyancy and compression of the gas inside the model cavity. Two extremely simple mathematical models will be used to bound the behavior of a rigid model during the submergence stage. The first model assumes that the vehicle is a solid cylinder and that the important forces are gravity and buoyancy. The second model assumes that the vehicle is a cylinder that is closed at one end and open at the other end which contacts the water. In this model, the forces represented are a result of compression of the gas in the vehicle and gravity. The actual vehicle should be controlled by some combination of the forces utilized in these two models. These two models are also illustrated in Fig. 1.

Buoyancy model

The differential equation applicable to the solid cylinder (see Fig. 1b) impacting the water is given by

$$m\ddot{x} = mg - \rho_0 g x A, \quad (5)$$

where

m is the mass of the cylinder,

x is the penetration depth,

g is the acceleration due to gravity

ρ_0 is the density of water

A is the cylinder area.

When this differential equation is solved with the conditions that the initial velocity is V_0 and the initial penetration is zero, the following result is given:

$$x = V_0 \sqrt{\frac{m}{\rho_0 A g}} \sin \sqrt{\frac{\rho_0 A g}{m}} t + \frac{m}{\rho_0 A} \left(1 - \cos \sqrt{\frac{\rho_0 A g}{m}} t \right) \quad (6)$$

Therefore, the important nondimensional parameters are

$$\frac{x}{l_0}, \frac{m}{\rho_0 A l_0^2}, \frac{V_0^2}{g l_0}, t \sqrt{\frac{g}{l_0}},$$

and l_0 is a typical dimension of the vehicle. Note that for geometrically scaled models $A = \text{const } l_0^2$. Therefore, for the submergence stage, a buoyancy model may be represented by;

$$\frac{x}{l_0} = \psi \left\{ \frac{V_0^2}{g l_0}, \frac{m}{\rho_0 A l_0^2}, t \sqrt{\frac{g}{l_0}} \right\} \quad (7)$$

Gas compression model

The gas compression model is represented by a cylinder which is open at one end and closed at the other. As shown in Fig. 1c, it is assumed that the open end impacts the water first. It will be assumed that the gas in the open-ended vehicle is compressed according to some arbitrary process, which is defined by

$$P_0 = \left(1 - \frac{h_w}{l_0} \right) k P,$$

or

$$\frac{P_0}{P} = 1 - k \frac{h_w}{l_0}, \quad \frac{h_w}{l_0} \ll 1 \quad (8)$$

Additionally, from statics we get

$$P - P_0 = \rho_0 g (x - h_w) \quad (9)$$

where

h_w is the height of water inside the vehicle as measured from the bottom of the vehicle,

P_0 is the atmospheric pressure.

The differential equation applicable to the model is

$$m\ddot{x} = (P_0 - P) A + mg \quad (10)$$

These equations may be nondimensionalized to give the same parameters as obtained from Eq. (7) plus the additional parameter,

$$\frac{P_0}{\rho_0 g l_0},$$

which is the pressure-scaling parameter. This parameter indicates that when scale-model tests are performed, the atmospheric pressure should be scaled linearly with model size.

Rebound stage

During the rebound stage, the instability of the vertical motion causes the craft to lean over and eventually lie flat on the surface of the water. In addition to the parameters listed previously, I , the rotary moment of inertia of craft about an axis perpendicular to the axis of symmetry, is of importance. [$I_m = m/2(l_0^2/6 + r^2)$ under the assumption that the craft is a cylinder.] This introduces a new nondimensional parameter, I_m/ml_0^2 .

Flexible Body Scaling

The previous analyses rest on the assumption of rigid-body motion. The justification of this assumption clearly depends on the speed with which energy is carried away by either compressional or bending waves. Thus, two additional parameters enter into the analysis: the velocity of compressional waves in the skin C_k ($C_k = \sqrt{E/\rho}$); and the skin thickness, h . The velocity of bending waves is a function of these two parameters and of the forcing frequency, which is a dependent variable here.

In order to consider flexibility effects, two more nondimensional parameters are required:

$$\frac{C_k}{V_0} \quad \text{and} \quad \frac{h}{l_0}.$$

During the slapdown and rebound phases, the representative bending frequency ω of the vehicle will also be of importance. This adds one more dimensionless group:

$$\frac{\omega l_0}{V_0},$$

which may be recognized as the Strouhal number, S . The bending frequencies ω of the vehicle may be further reduced to

$$\omega = K \frac{C_L}{\ell_0} \left(\frac{r}{\ell_0} \right)^{3/2}$$

Under the assumption of geometric and material similarity and Froude scaling, the equations of impact reduce to

$$\frac{x}{\ell_0} = \psi_1 \left\{ t \sqrt{\frac{g}{\ell_0}}, \frac{m}{\rho_0 \ell_0^3}, \frac{P_0}{\rho_0 g \ell_0}, \frac{C_L}{V_0} \right\} \quad (11)$$

MODEL CONSTRUCTION AND INSTRUMENTATION

Three aluminum models are constructed for the program. The models are geometrically scaled with respect to overall size, weight, center of gravity, and pitch moment of inertia. The models have different wall thicknesses in order to evaluate the effects of flexibility on impact loads. However, the wall thickness and, therefore, the flexibility parameter are not scaled. The following sections discuss the construction of the models and the instrumentation used to measure and record accelerations and pressures at various points on the models.

Model Construction

6-in.-diameter models

The 6-in.-diameter model is shown in Fig. 2. The body of the model is made from a single aluminum cylinder (51.5-in. long, 6.25-in. ID, 0.062-in. wall thickness) with three fitted bulkheads. The bulkheads provided stiff platforms on which the instruments and ballast weights are placed.

The nozzle (0.080-in.-thick aluminum) is welded to the bottom bulkhead. The nose cone (0.040-in. aluminum) is secured by screws to the model body. All junctions and screwholes are sealed with RTV 732 sealant.

A 1/2-in.-ID copper tube, held by rubber bushings in the two upper bulkheads, is used to collect the data cables from the sensors. A 14-lead flexible flat ribbon cable is used to transmit the data from the model to the on-ground recording equipment. With ballast weights, the model's center of gravity is 26.3 in. below the nose cone base, its weight is 12.2 lb, and

the pitch moment of inertia is

$$I_p = 3400 \text{ lb}_m\text{-in.}^2$$

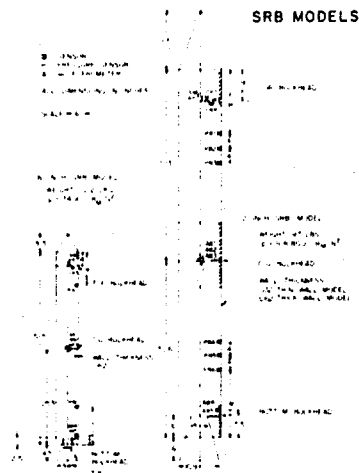


FIG. 2. SRB MODELS

12-in.-diameter models

The 12-in.-diameter models are shown in Fig. 2. Each model body is constructed from two cylindrical shells.

Three bulkheads, supported in stiffening shells, are used as instrumentation and ballast platforms. The thickness of the shells is 0.062 in. for the thick-walled model and 0.031 in. for the thin-walled model.

As in the 6-in.-diameter model, a 1/2-in. pipe, held through rubber bushings in the bulkheads, is used to collect the data wires from the different sensors and transmit them to the main data cable. All joints and screwholes are sealed with RTV 732 sealant. With ballast weights, both models' center of gravity is 52.6 in. below the nose cone base, their weight is 97 lbs, and the pitch inertia is

$$I_p = 108,800 \text{ lb}_m\text{-in.}^2$$

Model Instrumentation

Two types of sensors are used in the tests: the BBN 376M pressure sensor and the BBN 501 accelerometer. The pressure sensors measured the water pressure on the side of the models and the internal pressure inside the model.

The accelerometers measured the axial, pitch, and roll acceleration at locations shown in Fig. 2.

Figure 3 is a block diagram of the data acquisition and playback system. The 376M pressure sensors are calibrated in air and under water. The underwater calibration consisted of comparing the 376M response to that of a calibrated hydrophone. It is found that the 376M sensitivity under water is approximately the same as in air.

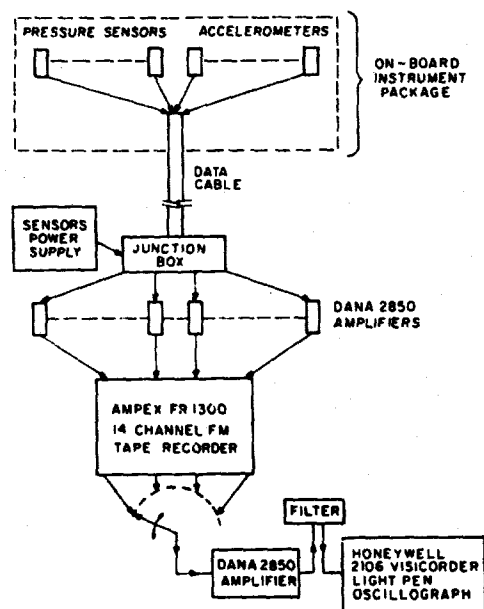


FIG. 3. DATA ACQUISITION AND PLAYBACK BLOCK DIAGRAM

EXPERIMENTAL ANALYSIS

The majority of the drop tests for this program are conducted in a 33 ft x 22 ft x 14 ft deep water tank. All drops are for the tail-first entry configuration.

The testing program consisted of 40 drops of the 6-in.-diameter model and 79 drops of the 12-in.-diameter models for a total of 119 tests. The 12-in.-diameter model drops included 66 drops of the rigid model and 13 drops of the thin skin model. Impact velocities of 7.9, 12, 16, and 22.7 fps are tested in the 6-in.-diameter model program; velocities of 11.2, 17, and 22.6 fps are used in the 12-in.-

diameter model program.

This section includes curves for scaling axial acceleration at water impact, maximum penetration depth, penetration depth as a function of time, surface pressure, and pitch accelerations at slapdown. However, the scatter in the slapdown data is so great that a large amount of data is required to give statistical significance to a scaling law. The curves do, nevertheless, illustrate the effects of varying model flexibility on resultant loads and response.

All data in the next five sections refer to a vertical entry condition. Typical data for nonvertical entry are presented in the section entitled "Non-vertical Entry." Results are presented in dimensional form or in dimensionless form in cases where this form appeared to collapse the data.

Data are recorded with a bandwidth of approximately 2 kHz; however, these wideband data exhibited an extreme amount of scatter. Therefore, we filtered our data to 50 Hz low pass in order to reduce scatter resulting from statistical variability and to eliminate misleading intense responses resulting from mechanical resonances of the instrumentation or mounting.

Axial Acceleration

Figure 4a shows axial acceleration as a function of impact velocity for the 6- and 12-in. models. The figure is a composite of all observed peak axial accelerations and includes data from both mid-model and nozzle positions. The extremum of the data is shown by a vertical line and the mean by either a circle or cross. No discernible difference is found in axial acceleration between mid-model and nozzle stations nor between rigid and flexible models. This result is to be expected, since even "flexible" models are very stiff axially. There was, however, a pronounced difference between the 6-in. and 12-in. model results.

Figure 4b shows the same data further collapsed through the use of an impact parameter which is composed of both the Froude and Reynolds numbers $(V^2/gD)^{5/6} (VD/\nu)^{2/6}$, where ν is the kinematic viscosity. This technique, which has been previously used (Ref. 3) in hydroballistic modeling, appears to be quite appropriate for water entry of the space shuttle solid rocket booster.

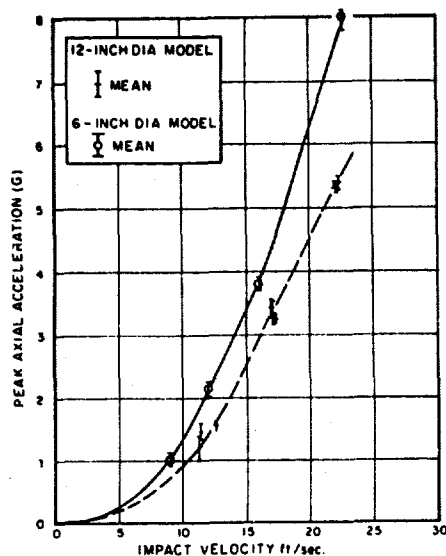


FIG. 4a. MAXIMUM AXIAL ACCELERATION DURING WATER IMPACT

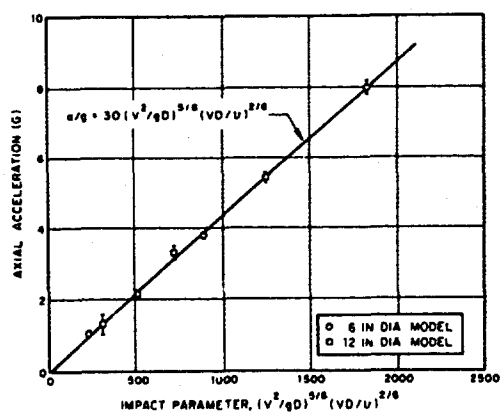


FIG. 4b. MAXIMUM AXIAL ACCELERATION AT WATER IMPACT

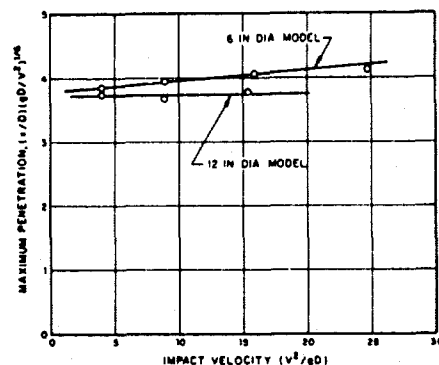


FIG. 5. MAXIMUM PENETRATION AS A FUNCTION OF IMPACT VELOCITY

Penetration Characteristics

Figure 5 presents the maximum penetration of the 6- and 12-in. diameter models as a function of impact velocity. The 12-in.-diameter model gives a constant nondimensional penetration as a function of velocity; whereas in the 6-in.-diameter model, nondimensional penetration increases with velocity. The results, similar to those for axial acceleration, show that vehicle flexibility did not contribute to the value of maximum penetration. The nondimensional penetration is divided by the sixth root of the Froude number to collapse the penetration as a function of time data. The one-sixth power is similar to that required to nondimensionalize the axial accelerations.

Since the two models differ by only 10 percent at the highest velocities and since the trend appears to be a decreasing penetration as a function of vehicle size, it is tentatively assumed that the 12-in.-diameter results will apply to larger scale models. Note that these curves do not include the effects of pressure scaling, and that, consequently, penetration of larger models may be underestimated by as much as 20 percent.

The nondimensional model penetration as a function of time is presented in Fig. 6. Time is normalized with respect to $\sqrt{g/D}$, and the data are

multiplied by the sixth power of the Froude number to compact them further. This figure is a composite of the 6-in.-diameter and 12-in.-diameter model test results as taken from high-speed photographs of the penetration.

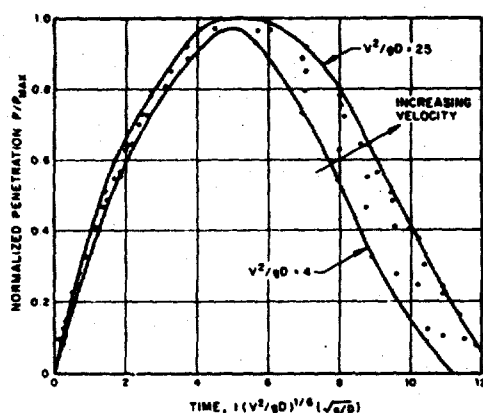


FIG. 6. NORMALIZED PENETRATION AS A FUNCTION OF TIME

Raw data points are shown on the figure in addition to a curve which encompasses all the data points. From the figure, it can be noted that during the initial penetration phase, up until maximum penetration, the scatter in the data when plotted against the coordinates chosen is minimal. Maximum penetration occurs at approximately the same nondimensional time for all tests; however, there is a slight tendency for the higher velocity models to reach maximum penetration at a later nondimensional time. As indicated on the figure, the spread in data is much greater following maximum penetration. In addition, the higher velocity models require more nondimensional time to resurface. It is well to remember, however, that the time nondimensionalization contains the Froude number, thus distorting the time scale. If data are plotted in real time, it would become clear that the higher velocity models reach maximum penetration earlier and, in addition, resurface earlier.

Surface Pressure

Figure 7 presents surface pressure as a function of penetration depth based on hydrostatic pressure considerations. Analysis of data taken during the test program showed that this is the appropriate relationship for surface pressures during near-vertical water entry. This figure may be used in conjunction with Fig. 6 to obtain surface pressure distributions over the model as a function of time during near-vertical water entry.

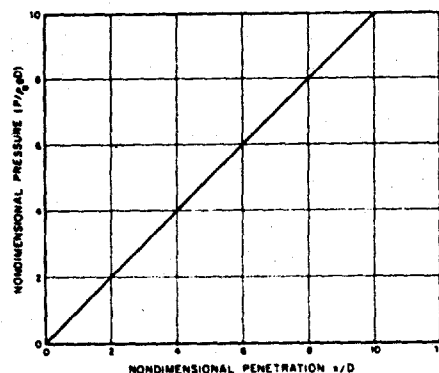


FIG. 7. SURFACE PRESSURE AS A FUNCTION OF PENETRATION

Maximum Pitch Acceleration at Slapdown

Figure 8a shows the maximum pitch acceleration observed at the top sensor position for the 12-in.-diameter model. Median points and extension are shown for both 0.062-in. and 0.032-in. wall thickness models. The top station shows the largest acceleration forces during slapdown as well as the largest scatter in the experimental data. It is found that the "rigid" (0.062 in.) model underwent peak slapdown accelerations which are virtually independent of impact velocity and which are of a magnitude of about 21 g's. Although the data are not shown in Fig. 8a, the mid-model and bottom stations were also subjected to peak pitch accelerations that were virtually independent of impact velocity but of a much lower level (7 and 4 g's, respectively).

If "rigid" (0.062 in.) and "flexible" (0.032 in.) accelerations are compared, a large decrease in acceleration as a result of flexibility is found. Because of the wide scatter bands observed (even though 50-Hz filtering was used), it is difficult to conclude that flexibility decreased peak pitch accelerations, although this is suggested by the data.

Figure 8b shows peak pitch acceleration at the mid-station for 12-in.-diameter models. A great amount of scatter is found in the data. Pitch acceleration measurements at the mid- and bottom stations showed virtually no statistically significant difference between models of differing flexibility.

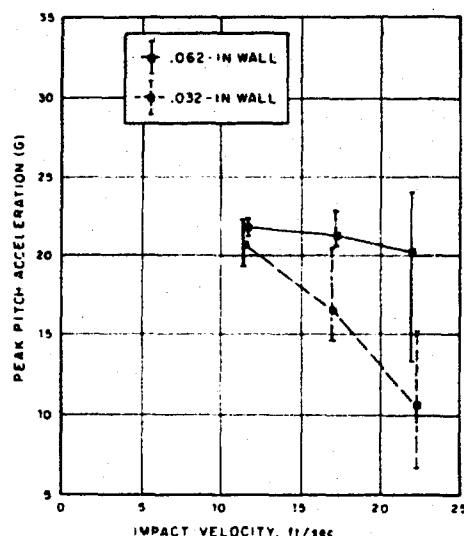


FIG. 8a. PEAK PITCH ACCELERATION
12-IN. MODEL TOP

Model Damage

Drop tests of the 6- and 12-in.-diameter models with 0.062-in. wall thickness did not result in any visible damage to the models. The 12-in.-diameter model with 0.031-in. wall thickness was, however, damaged during the slapdown phase of the first test and during each subsequent test. The damage appeared in the form of a buckle in the cylindrical section of the model between the centroid and the nose cone as shown in Fig. 9. This type of buckling is characteristic of cylinders loaded for a duration which is long compared to the shell response time (quasi-static pressure) as pointed out in Ref. 4. Although a qualitative comparison with the results of Ref. 4 can be made, a direct comparison is not possible,

since the loading functions differ considerably. For example, the loading function in Ref. 4 is nearly constant over a buckle wavelength during the time required to buckle; whereas, during slapdown, the pressure pulse propagates along the vehicle but is short compared to a buckle wavelength.

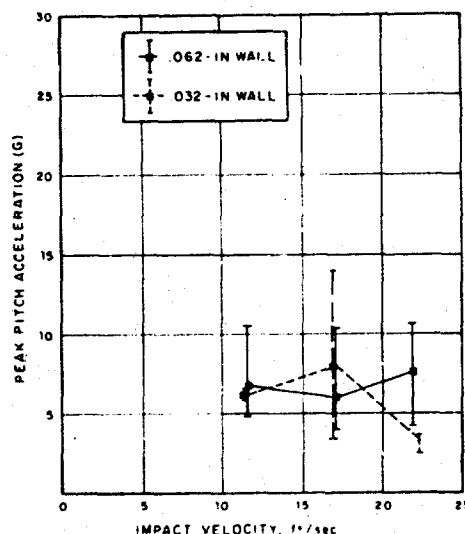


FIG. 8b. PEAK PITCH ACCELERATION,
12-IN.-DIAMETER MODEL,
MIDSTATION



FIG. 9. BUCKLE DAMAGE TO 12-IN.-
DIAMETER 0.031-IN.-THICK
MODEL RESULTING FROM SLAPDOWN

In light of the previous statements, extrapolation of model damage to full-scale structure damage would be somewhat questionable and will not be attempted at this time. Further investigation should, however, lead to a method for extrapolation.

Nonvertical Entry

The principal differences between vertical and nonvertical water impact are that the penetration decreases with increasing deviation from the vertical axis and that for angles greater than 10° a pressure pulse travels up the length of the vehicle during the primary slapdown phase. Figures 10 and 11 illustrate these trends. The data presented were obtained by NASA on a 12.5-in.-diameter model similar to the one previously discussed.

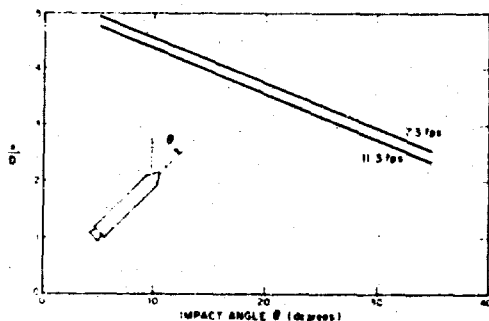


FIG. 10. PENETRATION DEPTH AS A FUNCTION OF IMPACT ANGLE

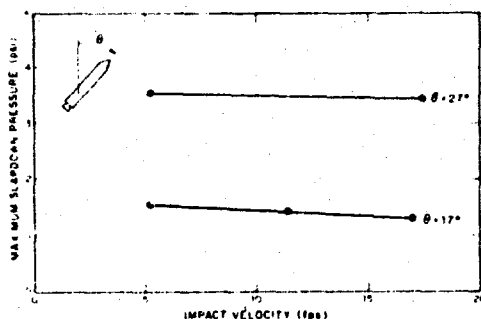


FIG. 11. MAXIMUM SLAPDOWN PRESSURE AS A FUNCTION OF IMPACT VELOCITY

Figure 10 presents penetration depth normalized by vehicle diameter as a function of impact angle for angles of 10° , 20° , and 30° from the vertical and two vertical entry velocities. The curve shows a linear decrease in penetration depth with impact angle. The data are weakly dependent on impact velocity (i.e., a factor of 2.25 increase in Froude number increases penetration depth by less than 10 percent). The curves are not normalized with respect to Froude number as previously done, since increases in impact angle attenuate the dependence on impact velocity, and normalization with respect to Froude number does not compact the data. It should be noted that these data are typical only for the models under test and that modifications to the model will result in appreciable changes in absolute magnitude of the normalized penetration. However, the decreased penetration with increased impact angle will persist.

Figure 11 presents the maximum pressure recorded along the keel for the 12.5-in.-diameter model as a function of vertical impact velocity. The two curves present data for impact angles of 27° and 17° from the vertical axis. The significant features of the data are that the maximum pressure is virtually independent of impact velocity and heavily dependent on impact angle.

CONCLUDING REMARKS

The present study consisted of a theoretical analysis of those parameters which should be important in scaling water impact data and an experimental program in which models of 6- and 12-in.-diameter were constructed and tested for comparison with the proposed scaling laws. Two 12-in.-diameter models were constructed, one with walls twice as thick as the other, in order to determine what effect model flexibility had on the resulting data. The major conclusions derived from the study are as follows:

1. Although simple theory predicts that all parameters should scale with the Froude number, axial accelerations appear to scale better with a parameter composed of both the Froude and Reynolds numbers.
2. Pitch acceleration is virtually independent of impact velocity, for the rigid models.

3. Flexibility effects are not evident in the results for axial acceleration and penetration depths. However, although there were wide scatter bands, more flexible models appear to experience significantly less pitch acceleration during slapdown and rebound.

4. Changes in impact angle are much more significant to slapdown pressures and to penetration depth than are changes in impact velocity.

REFERENCES

1. H.L. Langhear, *Dimensional Analysis and Theory of Models*, John Wiley and Sons, New York, N.Y., 1951.
2. J.G. Waugh and G.W. Sulestad, *Hydroballistics Modelling*, U.S. Government Printing Office, 1972.
3. A. May and J.C. Woodhull, "Drag Coefficients of Steel Spheres Entering Water Vertically," *J. Appl. Physics*, 19, pp. 1109-1121, Dec. 1948.
4. D.L. Anderson and H.E. Lindberg, "Dynamic Pulse Buckling of Cylindrical Shells Under Transient Lateral Pressures," *AFMA J.*, 6(4), pp. 589-593, April 1963.

IDENTIFICATION OF AN OPTIMUM SET OF TRANSIENT SWEEP PARAMETERS FOR GENERATING SPECIFIED RESPONSE SPECTRA

R. C. Rountree
The Aerospace Corporation
El Segundo, California

and

C. R. Freberg
University of Southern California
Los Angeles, California

Equation sets are described for the Transient Sweep Algorithm, and the algorithm performance is demonstrated. The algorithm identifies optimum parameters of a transient sweep for generating specified shock spectra. The specified spectra are expressed as logarithmic linear magnitude-versus-frequency test envelopes of arbitrary slopes, and two such spectra are required in order to control both the magnitude and duration of the excitation. A general class of excitations is reduced to an equation set form incorporating the transient sweep parameters in a vector. A mathematical representation is assigned to the particular form of shock spectra used in this paper, and an as yet unpublished and efficient numerical integration algorithm is described for determining oscillator response via a step size that varies only with sweep frequency. A specific error criterion function and gradient vector are identified to permit the application of a general purpose optimization technique known as the deflected gradient method. Three demonstration cases are explained and evaluated to exhibit algorithm performance and to show that the algorithm does generate optimum transient sweep parameters. Criteria are presented in graphical form for estimating initial values of the parameters. A practical and pertinent conclusion of the tabulated results is that the set of optimum parameters, in conjunction with the sweep duration, constitute a complete excitation description for implementation on a vibration test machine.

INTRODUCTION

An optimum set of transient sweep excitation parameters are identified in this paper for generating response (shock) spectra that match shock spectra specifications [1, 2]. The parameter identification is accomplished by an algorithm that applies a general purpose optimization technique known as the deflected gradient method. The algorithm generation of these optimum transient sweep parameters is functionally described in terms of overall equations in block diagram form and is also portrayed by a simple programming flow chart. The particular equations described are those used in the algorithm to define the specified response spectra, the transient sweep excitation, and the response spectra resulting from this excitation. The performance of the algorithm can be seen from the results of three demonstration cases.

The computer algorithm represents a practical nonlinear application of the deflected gradient method [3, 4] since the specified response spectra are indicative of actual vibration test conditions. The optimization involves minimizing an error criterion function that expresses a weighted squared difference between the specified response spectra and those generated by the transient sweep excitation. The specified spectra are expressed as logarithmic linear magnitude-versus-frequency test envelopes of arbitrary slope. Two shock spectra are specified in order to control both the magnitude and duration of the transient sweep excitation. The excitation is expressed in terms of four parameters that are iteratively adjusted within the algorithm until their optimum values are attained. The excitation is chosen from a class of time domain functions $\{g(t) - A(t) \sin \theta(t)\}$. The system being excited is modeled by the classical collection of tuned

oscillators (i.e., single degree-of-freedom systems) inherent in the definition of shock spectra.

This paper is presented in three technical sections following a section that states the problem being addressed. The first technical section shows the approach adopted to determine the optimum set of transient sweep parameters by means of a computer algorithm. Various equation sets called for in the blocks of the computer algorithm are described in the next section. Descriptions and results of three demonstration cases are provided in the final technical section. A summary of the findings of these three sections is then presented to conclude the paper.

STATEMENT OF THE PROBLEM

The problem addressed by this paper is the determination of a time domain excitation that generates specified response spectra (i.e., shock spectra). Determining excitation from maximized response spectra, when the system being excited is represented by a collection of oscillators, is a problem of considerable interest to environmental experts and is often referred to as the inverse shock spectra problem [5-10]. A general unique inverse has been shown to be unsolvable [7], but with application of certain constraints the inverse will be shown to be accomplished by means of a computational algorithm.

The Inverse Shock Spectra Concept

The inverse shock spectra concept is illustrated schematically in Fig. 1, which shows a collection of single degree-of-freedom (spring-mass-damper) oscillators attached to a platform. All of the oscillators have the same damping factor ζ_1 , but their natural frequencies ω_j increase from left to right. The entire platform is given a single acceleration excitation $g(t)$, and the acceleration response time history $\ddot{x}_j(t)$ of each oscillator is shown. The maximum of each of these responses is then selected.

The shock spectrum (SS) generated by the application of the particular excitation to a bank of oscillators is then plotted directly above the platform. It is a plot of the response maxima $\ddot{x}_j(t)$ max versus the oscillator natural frequency ω_j . Only the discrete frequencies are plotted, but it is customary to connect the points by a continuous curve, as represented by the dashed lines. Mathematically, the response may be expressed as

$$SS(\omega, \zeta, g) = \max_{0 \leq t < \infty} |\ddot{x}(t, \omega, \zeta, g)| \quad (1)$$

Figure 1 shows the specified or desired shock spectrum superimposed over the generated shock spectrum as a solid line. The problem is to select $g(t)$ such that the generated spectrum approaches the specified spectrum within a suitable measure.

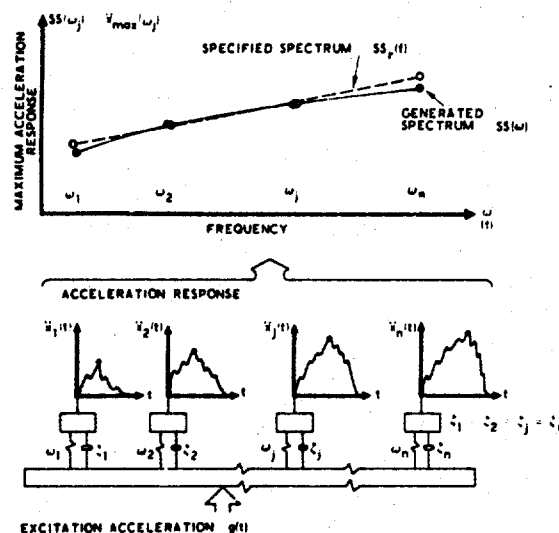


Fig. 1 - Shock spectra schematic

The selection of $g(t)$ may be accomplished by identifying key parameters of a time domain inverse shock spectrum representation for a special class of excitation functions and then adjusting these parameters until the spectra comparison is satisfied. The designated class of functions is $\{g(t) = A(t) \sin \theta(t)\}$, which is a rapid sine sweep of time varying magnitude. This form of excitation represents a wide range of real environments. The parameters are mathematically contained in a vector designated \bar{a} , which will be defined later.

The spectra comparison is refined further if a second shock spectrum is specified for control of both the magnitude and the duration of the excitation. This significance may be explained as follows.

If a different common damping factor were assigned to the collection of oscillators and the platform of Fig. 1 were again excited by the same $g(t)$, a different set of response maxima would result. For example, if lighter damping ζ_2 existed all maxima would tend to increase. The relationship of the second generated shock spectrum to the first is pertinent to the accomplishment of the complete inverse shock spectra [6, 10, 11].

Dividing the second shock spectrum (i.e., pertaining to ζ_2), point by point, by the first yields a shock spectra ratio that serves as an additional constraint as it provides a measure of the duration of the transient sweep excitation. This may be intuitively realized since under steady-state conditions the ratio will be large and under impact conditions it will be small, while for general environments the ratio will be somewhere between the two extremes. The value of the second specified shock spectrum is that, given the ratio of the shock spectra, the duration of the excitation is thereby controlled.

The approach adopted in this paper utilizes this second shock spectrum (or ratio) thereby controlling both the magnitude and duration of $g(t)$.

Optimization Algorithm Implementation

The problem is extended to the implementation of the spectra comparison and $g(t)$ selection. This implementation is accomplished via a general purpose optimization algorithm. This process emphasizes the deflected gradient [3,4] approach (also called the Fletcher-Powell method) in a discrete form. The basic concept of the discrete deflected gradient method is to iteratively adjust parameters of a mathematical function acting along lines parallel to a local search vector (i.e., the deflected gradient) until the function minimum is achieved. Each search vector is orthogonal to others previously determined during the iterative procedure. The mathematical function represents a root squared percentage difference between given or specified shock spectra and computed or response spectra from the excitation $g(t)$. The application involves a nonlinearity that arises via the transcendental nature of $g(t)$ and the maximization process inherent in shock spectra.

APPROACH UTILIZING THE DEFLECTED GRADIENT ALGORITHM

The application of the deflected gradient method to the generation of optimum transient sweep parameters will be accomplished via a computerized algorithm. The algorithm is portrayed in this section in terms of overall equations in block diagram form and also by a simple programming flow chart.

General Description of the Transient Sweep Algorithm

The desired general form of the algorithm is shown in Fig. 2. It is entitled The Transient Sweep Algorithm. All of the basic ingredients are represented in the figure, e.g., starting estimates, various individual calculations, the iterative nature, and stopping criteria. In essence, the figure suggests that a transient sweep excitation g from a designated class of functions is used to generate maximum response spectra SS , which in turn are compared to specified shock spectra SS_p . An error criterion function E and gradient vector ∇E , resulting from the comparison, are operated on by the deflected gradient methodology to drive the adjustable parameters $\bar{\alpha}$ to their optimum values (i.e., such that a user selected stop criterion is satisfied). Equation sets of the upper four blocks in Fig. 2 are summarized in the next section. Functions of each of the figure blocks and symbols are described in detail in Ref. [1].

Program Flow Chart

A simple computer program flow chart of the algorithm is shown in Fig. 3. This figure emphasizes the deflected gradient methodology by elaborating on the lower right-hand blocks of Fig. 2 and compressing the upper four blocks of Fig. 2 into steps 2 or 5. The steps of Fig. 3, which are well documented in the literature [3, 4, 12], may be summarized as follows.

Figure 3 highlights the iterative determination of a search direction vector \bar{S} and step length or gain μ along that direction. The gradient vector ∇E in Fig. 3 is modified by a positive definite matrix, denoted \bar{H} , resulting in \bar{S} . The matrix \bar{H} is iteratively computed via consecutive values of the parameter and gradient vectors. The scalar gain μ is determined by a procedure that leads to a minimum value of $E(\bar{\alpha}_k)$ along the k^{th} search direction \bar{S}_k . The procedure is Davidon's [13] cubic interpolation method, which relies on interpolation between $\bar{\alpha}_k$ and a trial value of $\bar{\alpha}_k$.

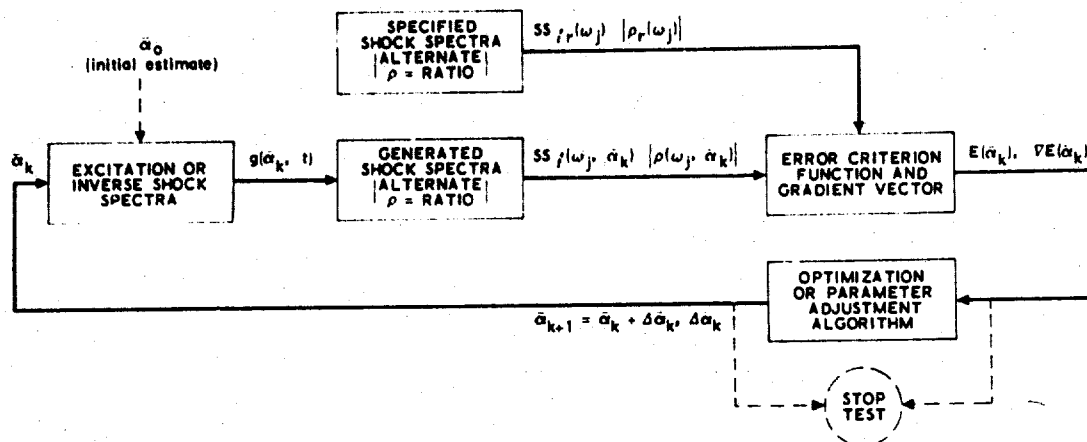
An essential step to the utilization of the deflected gradient is the definition of the error criterion function and associated gradient vector (for use in steps 2 and 5). This is accomplished in the next section.

ALGORITHM EQUATION SETS

Functions to be performed by the upper four blocks of Fig. 2 are expressed in equation form in this section. These four blocks are particularly pertinent because they represent the ingredients and the composite of the error criterion function and gradient vector required for steps 2 and 5 of Fig. 3.

Specified Shock Spectra Equations

Shock spectra specifications, which are generally presented in graphic form [5], must be translated into equation form in order to be amenable to the algorithm. These specifications are generally presented in logarithmic scales for both the ordinate and abscissa. The particular specifications of interest are restricted to those corresponding to two straight-line log-log plots representing either two shock spectra (i.e., one for each of two damping factors) or a shock spectrum for a given damping factor and its ratio to a second shock spectrum for another damping factor. Further generalization to include multiple straight line segments or notches in the specified shock spectra would involve major revisions to the algorithm; e.g., greater number of adjustable parameters, different expressions for the sweep amplitude and argument, or reinitialization during midsweep.



LEGEND

$\bar{\alpha}_k$ = PARAMETER VECTOR AT k^{th} ITERATION
 $\Delta \bar{\alpha}_k$ = CHANGE IN PARAMETER VECTOR
 $g(\bar{\alpha}_k, t)$ = EXCITATION
 $SS_i(\omega_j, \bar{\alpha}_k)$ = SHOCK SPECTRA VALUE AT j^{th} FREQUENCY, i^{th} DAMPING FACTOR
 $\rho(\omega_j, \bar{\alpha}_k)$ = RATIO OF TWO SHOCK SPECTRA (corresponding to two damping factors) AT j^{th} FREQUENCY

ω_j = j^{th} DISCRETE FREQUENCY
 SS_r = SPECIFIED OR REFERENCE VALUE OF SS
 ρ_r = SPECIFIED OR REFERENCE VALUE OF ρ
 $E(\bar{\alpha}_k)$ = ERROR CRITERION FUNCTION
 $\nabla E(\bar{\alpha}_k)$ = GRADIENT VECTOR

Fig. 2 - Transient Sweep Algorithm block diagram

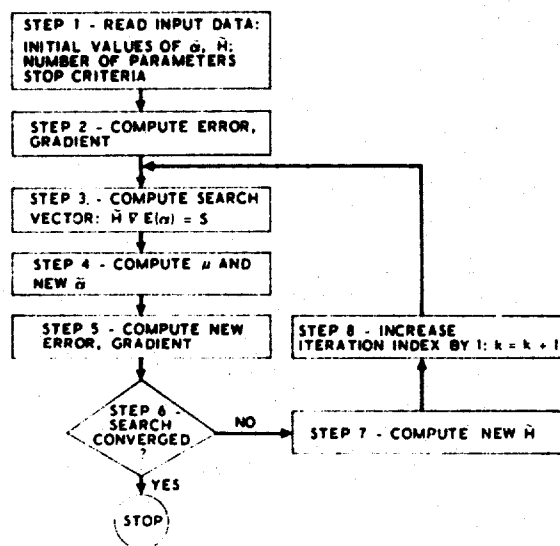


Fig. 3 - Simplified deflected gradient program flow chart

Figure 4 illustrates a linear logarithmic shock spectrum with appropriate notation. The ordinate is the natural logarithm of the shock spectrum magnitude, expressed $\ln SS(f, \zeta)$ or shortened to $\ln SS$ for convenience. The SS is expressed as a function of frequency f , rather

than circular frequency ω , as indicated earlier; this is easily accounted for by scaling. The abscissa is the natural logarithm of frequency $\ln f$. The beginning and ending points on the plot are indicated as SS_0, f_0 and SS_m, f_m . The subscripts 0 and m correspond to the original and maximum frequencies and shock spectrum magnitudes at these frequencies. The subscript m is not intended to reflect maximum or minimum magnitudes; line slope will naturally account for that.

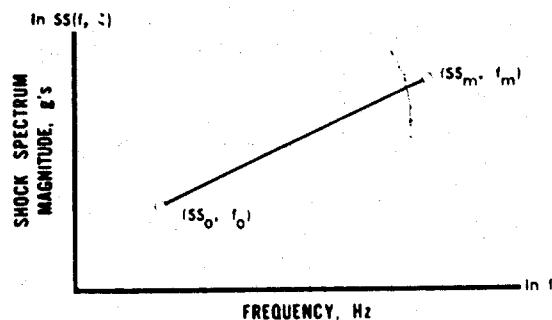


Fig. 4 - Linear logarithmic shock spectrum

The following equation provides the desired analytical expression of the specified shock spectrum shown in Fig. 4:

$$SS = SS_0 \left(\frac{f}{f_0} \right)^{b_1} \quad (2)$$

where

$$b_1 = \frac{\ln(SS_m/SS_0)}{\ln(f_m/f_0)} \quad (3)$$

The required input data would be the end point values. A discretized form is readily obtained by setting $f = f_j$ where j represents the j th frequency.

When the reference shock spectra ratio ρ appears as a straight line on a log-log plot, the procedure to express this analytically is the same as that just described. The resulting equations are analogous to Eqs. (2) and (3) with ρ replacing SS .

Transient Sweep Excitation

The general class of excitations functions $\{g(t) = A(t) \sin \theta(t)\}$ also needs to be reduced to an equation set form for incorporation into the Transient Sweep Algorithm. This is accomplished by means of the vector $\vec{\sigma}$ containing four adjustable elements designated a , β , R , γ . The elements constitute extensions of classical forms [14] of the time varying sweep amplitude $A(t)$ and time varying sweep argument $\theta(t)$. Both generalized and restricted forms of the equation set are presented. The restrictions pertain to reduction of the general form to the classical special case forms.

Generalized Forms. The generalized expressions for $A(t)$ were obtained from the following equation set:

$$\frac{d(\ln A(t))}{d(\ln f(t))} = \beta, A(0) = a, f(0) = f_0 \quad (4a)$$

$$\frac{d f(t)}{dt} = R f(t)^\gamma \quad (4b)$$

$$\frac{d \theta(t)}{dt} = 2\pi f(t), \theta(0) = 0. \quad (4c)$$

The development of these forms and their solutions (used in the algorithm) are provided in Ref. [1].

A subtle feature of the transient sweep excitation used in this paper is that it permits control of the sweep duration. Often, in tests, the sweep duration is arbitrarily selected. The expressions for f and θ are shown in Ref. [1] to yield the time to accomplish the

sweep. For the general case, solving Eq. (4b) for time t yields the sweep duration when an upper bound on the frequency is given, i.e.,

$$t_s = \frac{f_m^{1-\gamma} - f_0^{1-\gamma}}{R(1-\gamma)}, \quad \gamma \neq 1 \quad (5)$$

where

t_s = total sweep time

f_m = maximum frequency to be achieved

Restricted Forms. It is pertinent that the integrated solutions of Eqs. (4) take on special forms corresponding to the values of β and γ . Three frequency sweep methods (i.e., linear, exponential, and original transient) are historically common [6, 14, 15] and are therefore included. Each of these may be described by adoption of specific values for β or γ ; each is subsequently accounted for in the Transient Sweep Algorithm. The γ /method relationships are linear, $\gamma = 0$; exponential, $\gamma = 1$; and original transient, $\gamma = 2$. Also, in the historical usage of all three of these methods, the sweep amplitude was generally held constant. This is accomplished when $\beta = 0$.

The general form reduces to the linear frequency sweep when parameter $\gamma = 0$. This reduction pertains to both Eqs. (4) and sweep duration in Eq. (5).

Setting $\gamma = 1$ obtains the exponential frequency sweep form. Solving Eq. (4b) for t , after setting $\gamma = 1$, provides the sweep duration for the exponential, i.e.,

$$t_s = \frac{1}{R} \ln \left(\frac{f_m}{f_0} \right) \quad (6)$$

The significance of the exponential frequency sweep is that it is intended to spend an equal amount of time passing through each oscillator bandwidth during the sweep.

Setting $\gamma = 2$ yields the frequency sweep form originally intended to simulate near pulse conditions. Solving Eq. (4b) for t , after setting $\gamma = 2$, yields the sweep duration for the original transient sweep duration:

$$t_s = \frac{1}{R} \left(\frac{1}{f_0} - \frac{1}{f_m} \right) \quad (7)$$

Equation (7) has some interesting side-lights. First, it can yield an approximate sweep duration estimate that is essentially independent of f_m when $f_m \gg f_0$ (e.g., $f_0 = 5$ Hz, $f_m = 2000$ Hz, which are vibration test standards), i.e.,

$$t_s \approx \frac{1}{R\Gamma_0} \quad (8)$$

Also, the sweep time indicated by Eq. (7) represents the duration associated with maintaining a constant number of cycles while passing through the bandwidth of any oscillator excited during the sweep.

The insight gained from these special case sidelights proved to be valuable during the algorithm verification process: e.g., greater sweep times were expected to correspond to cases for $\gamma \approx 1$ than for $\gamma \approx 2$.

Generated Shock Spectra Determination

A mathematical representation is assigned to the particular form of generated shock spectra and ratio used in this paper. Determination of the oscillator response requires solution of the assigned differential equation for acceleration by means of integration. The integrand is a function of the individual oscillator frequencies and the frequency associated with the transient sweep (the latter inherently covers a broad range of frequencies). For numerical integration, it is desirable, for numerical stability, to have the integration step size independent of the oscillator frequency. An integration algorithm is described below which achieves this independence: the integration step sizes are adjusted so that they vary only with sweep frequency.

Shock Spectra Equations. Two primary equations serve to describe the oscillator response. First is the differential equation of motion treated below, and second is the maximizing equation given in Eq. (1).

The differential equation generally refers to various means of application of the excitation or to various response parameters, i.e., relative or absolute values of response motion in terms of displacement, velocity, or acceleration. The situation treated in this paper is the application of excitation to a simple oscillator by means of base motion. Absolute acceleration is selected as the parameter of interest since most shock and vibration specifications are in terms of acceleration units. The classical equation of motion associated with the relative motion r is [14]

$$\ddot{r} + 2\zeta\omega\dot{r} + \omega^2 r = -\ddot{x} \quad (9)$$

and the absolute acceleration \ddot{x} for use in Eq. (1) may be obtained by numerical integration of Eq. (9) and substitution into the following equation [14]:

$$\ddot{x} = -2\zeta\omega\dot{r} - \omega^2 r \quad (10)$$

The method of determining \dot{r} and r will be described after the formulation of the shock spectra ratio ρ .

The ratio between two shock spectra (corresponding to two fixed damping factors ζ_1 and ζ_2) is expressed as

$$\rho(\omega, \zeta_1, \zeta_2, g) = \frac{SS(\omega, \zeta_2, g)}{SS(\omega, \zeta_1, g)}, \quad \zeta_1 > \zeta_2 \quad (11)$$

Integration Algorithm. Determination of the oscillator response requires solution of the differential equation for \ddot{r} by means of integration. The integrand involved will be a function of the oscillator frequency and the frequency associated with the transient sweep, which inherently covers a broad range of frequencies. An approach to achieve integration step size independent of the oscillator frequency will be generally described in the following paragraphs. A detailed derivation is provided in Ref. [1]. This algorithm is as yet unpublished in the technical community but has been shown to be efficient [1, 2, 17].

The solution to Eq. (1) will be obtained by means of state variable techniques. These techniques require that Eq. (9) be rewritten in matrix first order form as follows:

$$\dot{\bar{Y}}(t) = A\bar{Y}(t) + \bar{U}(t), \quad \bar{Y}(0) = \bar{Y}_0 \quad (12)$$

where

$$\bar{Y}(t) = \begin{bmatrix} r(t) \\ \dot{r}(t) \end{bmatrix}, \quad (13a)$$

$$A = \begin{bmatrix} 0 & 1 \\ -\omega^2 & -2\zeta\omega \end{bmatrix} \quad (13b)$$

$$\bar{U}(t) = \begin{bmatrix} 0 \\ -\ddot{x}(t) \end{bmatrix} \quad (13c)$$

The known solution to Eq. (12) is [16, 19]

$$\bar{Y}(t) = e^{At} \bar{Y}_0 + \int_0^t e^{A(t-\tau)} \bar{U}(\tau) d\tau \quad (14)$$

Note that the integrand $e^{A(t-\tau)} \bar{U}(\tau)$ is a function of both the oscillator frequency ω entering through A and the transient sweep frequency implied by $\bar{U}(\tau)$. If a step size Δt is introduced by substitution of $t + \Delta t$ in

Eq. (14) and the excitation $\bar{U}(\tau)$ is restricted to the linear form:

$$\bar{U}(\tau) = \bar{U}(t) + \frac{\tau - t}{\Delta t} [\bar{U}(t + \Delta t) - \bar{U}(t)] \quad (15)$$

then Eq. (14) may be shown [1, 17] as

$$\bar{Y}(t + \Delta t) = T \bar{Y}(t) + M_1 \bar{U}(t) + M_2 \left[\frac{\bar{U}(t + \Delta t) - \bar{U}(t)}{\Delta t} \right] \quad (16)$$

where

$$T = e^{A\Delta t} \quad (17)$$

$$M_1 = \int_0^{\Delta t} e^{-Az} dz \quad (18)$$

$$M_2 = \int_0^{\Delta t} e^{-Az} z dz \quad (19)$$

Equation (16) has the desired integration form. It implies that, in the region where a given Δt still permits $\bar{U}(t)$ to be considered linear, the matrices T , M_1 , and M_2 need only be computed once. Therefore, the matrix A has no influence on Δt . The restriction of Eq. (15) may be readily satisfied if the step size $\Delta t < 0.1 T$ where T is the period of the input sine wave. The period continually decreases during an upward sweep; hence, some changes of step size will be required.

The exact forms of T , M_1 , and M_2 may be obtained by application of the Cayley-Hamilton theorem [18] and integration. The resulting expressions are the following:

$$T(\Delta t) = e^{-\zeta \omega \Delta t} \begin{bmatrix} C \cos(\omega_D \Delta t - b) & \frac{1}{\omega_D} \sin \omega_D \Delta t \\ \frac{-\omega^2}{\omega_D} \sin \omega_D \Delta t & C \cos(\omega_D \Delta t + b) \end{bmatrix} \quad (20)$$

$$M_1(\Delta t) = \begin{bmatrix} IC - \frac{\zeta \omega}{\omega_D} IS & -\frac{1}{\omega_D} IS \\ \frac{\omega^2}{\omega_D} IS & IC + \frac{\zeta \omega}{\omega_D} IS \end{bmatrix} \quad (21)$$

$$M_2(\Delta t) = \begin{bmatrix} IPC - \frac{\zeta \omega}{\omega_D} IPS & -\frac{1}{\omega_D} IPS \\ \frac{\omega^2}{\omega_D} IPS & IPC + \frac{\zeta \omega}{\omega_D} IPS \end{bmatrix} \quad (22)$$

where

$$\omega_D = \omega \sqrt{1 - \zeta^2}$$

$$C = \sqrt{1 + \left(\frac{\zeta \omega}{\omega_D}\right)^2}$$

$$b = \text{TAN}^{-1} \left(\frac{\zeta \omega}{\omega_D} \right)$$

$$IC = \frac{1}{\omega} \left\{ e^{+\zeta \omega \Delta t} \left(\zeta \cos \omega_D \Delta t + \frac{\omega_D}{\omega} \cdot \sin \omega_D \Delta t \right) - \zeta \right\}$$

$$IS = \frac{1}{\omega} \left\{ e^{+\zeta \omega \Delta t} \left(\zeta \sin \omega_D \Delta t - \frac{\omega_D}{\omega} \cdot \cos \omega_D \Delta t \right) + \frac{\omega_D}{\omega} \right\}$$

$$IPC = \frac{1}{\omega^2} \left\{ e^{+\zeta \omega \Delta t} \left([\zeta \omega \Delta t - (-1 + 2\zeta^2)] \cdot \cos \omega_D \Delta t + \frac{\omega_D}{\omega} [\omega \Delta t - 2\zeta] \cdot \sin \omega_D \Delta t \right) + (\zeta + 2\zeta^2) \right\}$$

$$IPS = \frac{1}{\omega^2} \left\{ e^{+\zeta \omega \Delta t} \left([\zeta \omega \Delta t - (-1 + 2\zeta^2)] \cdot \sin \omega_D \Delta t - \frac{\omega_D}{\omega} [\omega \Delta t - 2\zeta] \cdot \cos \omega_D \Delta t \right) - 2\zeta \frac{\omega_D}{\omega} \right\}$$

The resulting matrices of Eqs. (20) - (22) are more complicated than those of some available approximate forms and will require use of trigonometric subroutines for computer implementation. Nevertheless, any accuracy and stability problems, often arising from approximations, should be solved by this approach. Such problems are addressed in Ref. [1].

Step size less than 0.1 forcing function period is a general practice.

Integration Step Size. A fundamental requirement in the derivation of Eq. (16) for the response to the transient sweep excitation was that the step size Δt be considerably smaller than the period of the sweep frequency. This necessitated an evaluation of the periods associated with each of the excitation forms shown previously (i.e., the general case and the two special case forms involving $\gamma = 1$ and 2). The periods correspond to $0(t) = 2\pi i$ ($i = 1, 2, 3, \dots$).

For the general case described previously, the periods are determined by first substituting $0 = 2\pi i$ into the solution to Eq. (4c) and then solving for the times t_i , which represents the times associated with each cycle's completion. For the periods T_i , successive values of these times must be differenced, i.e.,

$$T_i = t_i - t_{i-1} \quad \text{for } t_i \leq t_s \quad (23a)$$

and

$$T'_i = t_s - t_{i-1} \quad \text{for } t_i > t_s \quad (23b)$$

Note that the parameter T'_i in Eq. (23b) is generally not a complete period. The step sizes are determined by

$$\Delta t_i = C_2 T_i \quad \text{for } t_i \leq t_s \quad (24a)$$

$$\Delta t_i = C_2 T'_i \quad \text{for } t_i > t_s \quad (24b)$$

where

C_2 = arbitrary input constant (inverse integer) ≤ 0.1

Equations (23) and (24) also apply to the excitation of the special cases for $\gamma = 1$ and $\gamma = 2$. The step size differences between the general and special cases exist in the meaning of the times t_s and t_i . The sweep durations are those of Eqs. (6) and (7) for $\gamma = 1$ and 2, respectively. The cycle times are obtained by selecting the appropriate γ , solving Eqs. (4b) and (4c) accordingly, substituting $0 = 2\pi i$, and then solving for the times t_i . These steps were performed by hand and the resulting equations programmed into the Transient Sweep Algorithm. The integration step size equations provide the information necessary to complete the integration algorithm.

Determination of Maximum Response. The maximization of \ddot{x} indicated by Eq. (1) required computer implementation. The implementation was performed by use of Eq. (10) in conjunction with the integration results of Eq. (16), i.e., $\ddot{Y}(t) = [r, \dot{r}]$. For the use of the scalar

form of Eq. (10) in a way compatible with the vector form of Eq. (16), the A matrix of Eq. (13b) is utilized. Let A be expanded as

$$A = \begin{bmatrix} 0 & 1 \\ -\omega^2 & -2\zeta\omega \end{bmatrix} = \begin{bmatrix} A_1 \\ A_2 \end{bmatrix} \quad (25)$$

The desired form of \ddot{x} represented by Eq. (10) can be obtained by a matrix multiplication of the 1×2 matrix A_2 and the vector (or 2×1 column matrix) \ddot{Y} . This appears as

$$\ddot{x} = A_2 \cdot \ddot{Y} \quad (26)$$

Equation (26) is maximized by searching the resulting matrix multiplication over the entire sweep time for the largest value. For a given transient sweep excitation, Eq. (26) will be exercised twice for each oscillator frequency, i.e., once for each damping factor. Therefore, A_2 and \ddot{Y} must be identified with respect to frequency and damping. This is done by use of subscripts j for indicating the frequency ω_j and l for indicating damping factor ζ_l . Equation (26) is then substituted into Eq. (1), which yields

$$SS(\omega_j, \zeta_l) = \max_{0 \leq t < \infty} |A_{2jl} \cdot \ddot{Y}_{jl}| \quad (27)$$

The shock spectra ratio ρ is again given by Eq. (11). Equations (27) and (11) provide the generated shock spectra/ratio information that is to be compared to the specified shock spectra data.

Error Criterion Function and Gradient Vector

A specific error criterion function and gradient vector required for the deflected gradient method are now defined. Mathematical formulations of both the error criterion function and the gradient vector are presented.

Error Criterion Function Definition. Definition of a suitable error criterion function is essential for efficient application of gradient methods to the transient sweep problem. In the present case, there are two primary comparisons to be made: (1) between the specified and generated shock spectra (i.e., SS_r and SS) for a given damping factor ζ_1 , and (2) between specified and generated shock spectra ratios (i.e., ρ_r and ρ). Various ways exist for functionally expressing the error functions resulting from these comparisons [4]. However, there are two general guidelines to be followed; i.e., the interpretation of the error function must be meaningful to the algorithm user, and the

Used to divide the period into equal parts.

error function must not allow any single component to dominate the comparison. The error function selected appears as

$$E(\bar{\alpha}) = \|\bar{E}_1(\omega_j, \bar{\alpha})\|^2 + \|\bar{E}_2(\omega_j, \bar{\alpha})\|^2, \quad (28)$$

where the individual weighted norms appear as

$$\|\bar{E}_i(\omega_j, \bar{\alpha})\| = [\bar{E}_i(\omega_j, \bar{\alpha}') W_{ij} \bar{E}_i(\omega_j, \bar{\alpha})]^{1/2} \quad (29)$$

(i = 1, 2; j = 1, n)

and

$\bar{E}_i(\omega_j)$ = column n vectors of the differences between SS_r and SS or ρ_r and ρ at n frequencies $\{\omega_1, \dots, \omega_2, \dots, \omega_j, \dots, \omega_n\}$,

W_{ij} = weighting matrices [1],

$\|\cdot\|$ = designation of a norm,

' = designation of transpose.

The weighting matrices W_{ij} are diagonal matrices with diagonal elements of W_{1j} and W_{2j} corresponding to $1/SS_r^2$ and $1/\rho_r^2$, respectively. The elements serve normalization purposes generally required for multiparameter optimization. Specific needs and tradeoffs are discussed in Ref. [1].

Gradient Vector Formulation. The formulation of the gradient vector $\nabla E(\bar{\alpha})$ is simply the four partial derivatives of $E(\bar{\alpha})$ with respect to the four adjustable parameters. These parameters were identified earlier as a , β , R , and γ . Therefore, $\nabla E(\bar{\alpha})$ is a four-element vector that appears as

$$\nabla E(\bar{\alpha}) = \left[\frac{\partial E}{\partial a}, \frac{\partial E}{\partial \beta}, \frac{\partial E}{\partial R}, \frac{\partial E}{\partial \gamma} \right]' \quad (30)$$

The gradient vector components may be obtained by an approach called the finite difference method.

The finite difference method is simple to implement because of its approximate form and has adequate accuracy: the fact that accuracy requirements are generally not prohibitive in the Transient Sweep Algorithm is explained in Ref. [1]. The finite difference method relies on an approximation to the definition of a derivative. The components of $\nabla E(\bar{\alpha})$ appear in finite difference form as

$$\frac{\partial E}{\partial a} = \frac{E(a + \delta a, \beta, R, \gamma) - E(\bar{\alpha})}{\delta a} \quad (31a)$$

$$\frac{\partial E}{\partial \beta} = \frac{E(a, \beta + \delta \beta, R, \gamma) - E(\bar{\alpha})}{\delta \beta} \quad (31b)$$

$$\frac{\partial E}{\partial R} = \frac{E(a, \beta, R + \delta R, \gamma) - E(\bar{\alpha})}{\delta R} \quad (31c)$$

$$\frac{\partial E}{\partial \gamma} = \frac{E(a, \beta, R, \gamma + \delta \gamma) - E(\bar{\alpha})}{\delta \gamma} \quad (31d)$$

where the δ increments are fixed small values or some percent C of the iterated value (e.g., $\delta a = C \cdot a$).

Equation (31) demonstrates a need for the 10 shock spectra per algorithm iteration pointed out in Ref. [1]. These 10 are required to compute a different shock spectrum for the basic and the four perturbed error criterion functions indicated in Eq. (31) for each of the two damping factors.

DESCRIPTION AND RESULTS OF DEMONSTRATION CASES

Three demonstration cases are used in this section to exhibit algorithmic performance and show that the algorithm generates optimum transient sweep parameters. The three cases represent increasing generality. The description and purpose of each demonstration case are provided, including a brief description of the algorithm input and output. Criteria are presented in graphic form for estimating initial numerical values of the adjustable parameters. The overall results of these runs are provided, as well as an evaluation of sweep duration characteristics.

Descriptions of Three Demonstration Cases

The demonstration case descriptions are given in two parts. First, the general characteristics are presented. Then the input/output (I/O) selections are given. The I/O discussion emphasizes starting estimates for $\bar{\alpha}$.

Demonstration Case Characteristics. The characteristics of the three demonstration cases are illustrated in Fig. 5 in terms of the specified shock spectra SS_r and ratios ρ_r to be satisfied. Class I represents nonconstant SS_r but constant valued ρ_r . Class II represents nonconstant SS_r but constant valued ρ_r . Class III represents the completely general case where both the SS_r and ρ_r are nonconstant. Both positive and negative slopes are implied in Cases II and III when the specification magnitudes are nonconstant.

The frequency ranges are the same for all cases, and three oscillator frequencies f_1 , f_2 , f_3 are picked between the bounds f_0 and f_m . Three oscillators are picked to reduce computer expense and because three represent the minimum number possible to ensure that a linear log-log plot is accomplished.

Numerical specification values for the three demonstration cases are presented in

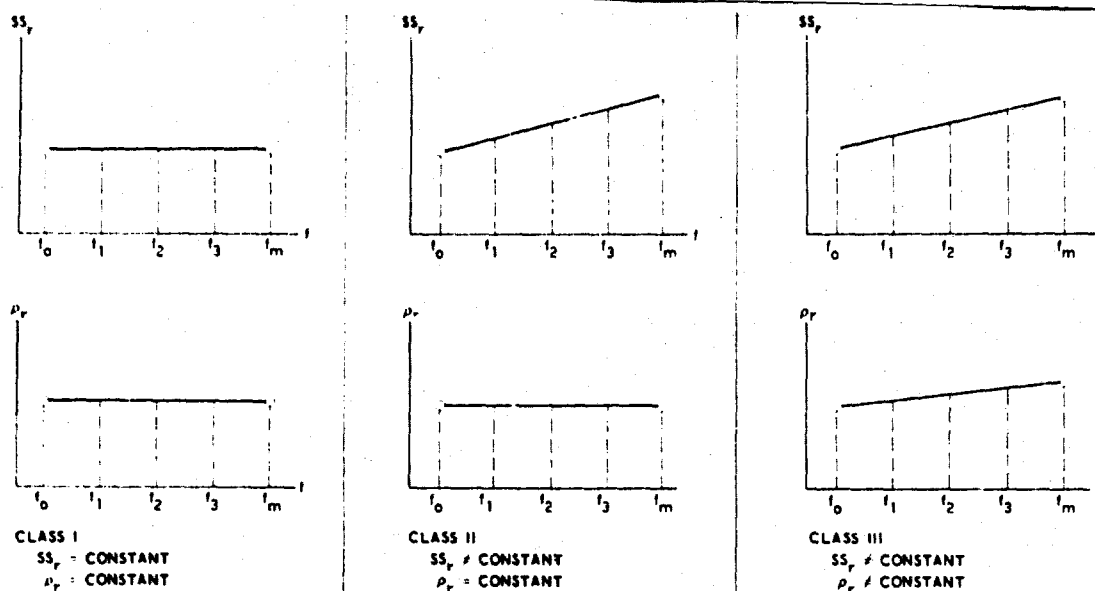


Fig. 5 - Characteristics of demonstration cases

Table 1. Individual computer runs were made for each case shown (i.e., class/run). The rationale for assigning those specification numbers are also given. A more detailed explanation of the value selection procedure is presented in Ref. [1]. Class I represents actual test specifications obtained from

industrial testing programs [6, 11] and, therefore, serves partially as a check case for Classes II and III.

Input/Output Selections. The I/O selections used during algorithm development were extended and generalized for the demonstration

TABLE I
 Selected Shock Spectra, Ratio Specifications for Demonstration Cases

CLASS, RUN	SPECIFICATION				RATIONALE
	SS_{ro}	SS_{rm}	ρ_{ro}	ρ_{rm}	
I-1	3	3	1.5	1.5	EXTENSION OF THE TEST CASE FOR 3 OSCILLATORS
I-2	3	3	2	2	MODIFICATION OF I-1 FOR SLOWER SWEEP-RATE
I-3	6	6	1.5	1.5	MODIFICATION OF I-1 FOR HIGHER AMPLITUDE
II-1	3	60	1.5	1.5	POSITIVE SLOPE SHOCK SPECTRA SPECIFICATION
II-2	3	1200	1.5	1.5	STEEPER POSITIVE SLOPE THAN II-1
III-3	3	0.15	1.5	1.5	NEGATIVE SLOPE SHOCK SPECTRA SPECIFICATION
III-1	3	60	1.5	2	GENERAL SHOCK SPECTRA/RATIO SPECIFICATIONS: BOTH WITH POSITIVE SLOPE
III-2	3	3	1.5	2	SPECIAL CASE OF III-1 WITH CONSTANT SHOCK SPECTRA SPECIFIED
III-3	3	60	2	1.5	GENERAL SHOCK SPECTRA/RATIO SPECIFICATIONS: POSITIVE SHOCK SPECTRA SLOPE, NEGATIVE RATIO SLOPE
III-4	3	3	2	1.5	SPECIAL CASE OF III-3 WITH CONSTANT SHOCK SPECTRA SPECIFIED

For all cases: Specified frequency range is $f_0 = 10$ to $f_m = 200$; oscillator frequencies are 20, 60, 100; stop criteria are 0.005 on ΔE and normalized $\Delta \bar{\alpha}$.

cases. Specific values and formats of I/O are presented in Ref. [1]. The initial $\bar{\sigma}$ estimation process is generalized in this paper, however, since optimization is generally dependent on the starting values. The effect of initial estimate accuracy on optimization convergence is discussed in Refs. [1] and [2]. Some typical output data is presented in the results discussion.

Data used to develop starting $\bar{\sigma}$ estimates were obtained from two sources. First, perturbations from a test case development provided trends in the $\bar{\sigma}$ components. Second, extrapolations were made to prior sweep rate studies [9, 15]. These sources served to establish general rules of thumb that were subsequently implemented in terms of families of curves for general use. These rules of thumb are explained in Ref. [1], and the resulting curves for the three demonstration cases are displayed in Figs. 6-8. Numerical values of the starting estimate of $\bar{\sigma}$ are presented with the results of the three demonstration cases later.

Case I starting estimate criteria are found in Fig. 6, which shows the parameters a and R . Parameters β and γ are estimated to be 0 and 2, respectively, for this case on the basis of industrial experience. Figure 6 is a curve of an amplification factor, denoted F (i.e., $F_a = SS_r/a$), versus the sweep rate constant R . Values of the specified p_r are indicated along the curve. The curve provides R directly from p_r , and a is obtained by dividing the specified SS_r by F_a . A restriction on the curve is that it was generated for oscillators whose damping factor ratios were 5 (i.e., $\delta_1/\delta_2 = 5$), as is the case selected for this paper. Similar curves for other damping factors (e.g., $\delta_1/\delta_2 = 10$) may be generated if desired. In conjunction with the present restriction, the curve suggests that both F_a and p_r are bounded above by 5 and tend below to 1, representing steady-state and impact conditions, respectively.

Case II starting estimate criteria are estimated as in Case I, with the exception of the parameter β . A straightforward estimate for β is that pertaining to the exponent b_1 shown in Eq. (3), which also represents amplitude versus frequency slope. Figure 7 shows b_1 as β versus f_m/f_0 for a family of curves representing constant values of SS_{rm}/SS_{r0} . For example, in Run II-1, $f_m/f_0 = 20$ and $SS_{rm}/SS_{r0} = 20$, so $\beta = 1$. Parameters a and R are again obtained from Fig. 6, and $\gamma = 2$.

Case III starting estimate criteria utilizes an equivalent p_r , denoted \tilde{p}_r , to enter Fig. 6 for obtaining parameters a and R in this general case. The γ estimate is found as part of the technique used to provide this \tilde{p}_r , and parameter β is obtained by means of Fig. 7 (used for Case II). The technique is portrayed in Fig. 8, which shows two correction factors, denoted CF_1 , CF_2 , versus f_m/f_0 for a family of curves

representing constant values of p_{rm}/p_{ro} . When the slope of the specified $p_r(f)$ is positive, then \tilde{p}_r is obtained by CF_1 and the γ estimate by CF_2 , as indicated on the figure. When the slope is negative, the roles of the correction factors are reversed as shown. The justification of the correction factor equation is partially explained in conjunction with the evaluation of Case III in Ref. [1].

Run III-1 starting criteria serve as an example for the Case III. Parameter $\beta = 1$ by the same steps explained for the Case II example. $p_{rm}/p_{ro} = 1.33$ and $f_m/f_0 = 20$ so that, according to Fig. 8, $CF_1 = 1.096$ and $CF_2 = 0.904$. It follows that $\tilde{p}_r = p_o \times CF_1 = 1.64$ and $\gamma = 2 \times CF_2 = 1.81$. Using \tilde{p}_r in Fig. 6 yields $R = 0.30$ and $a = 0.90$. Figure 6 was used in every case to estimate parameters a and R regardless of values of β and γ .

Results of the Demonstration Cases

Computer run results for the three demonstration cases provided verification of the method described for generating optimum transient sweep parameters. The results of these runs and an evaluation of each case are provided in the following paragraphs. An overall evaluation of sweep duration characteristics is also provided.

Summary of Results for the Demonstration Cases. A summary of the computer run results for the demonstration cases in Table 1 are shown in Table 2. The tabulated data includes the shock spectra specifications (repeated for convenience), the initial $\bar{\sigma}$ component estimates, the optimum error criterion function and parameter vector achieved, and the transient sweep duration.

Convergence within the 0.005 stop criteria (user selected) was attained for all 10 computer runs, which substantiate that optimum transient sweep parameters were generated. This criteria pertained to changes in E and normalized $\bar{\sigma}$ between iterations. It

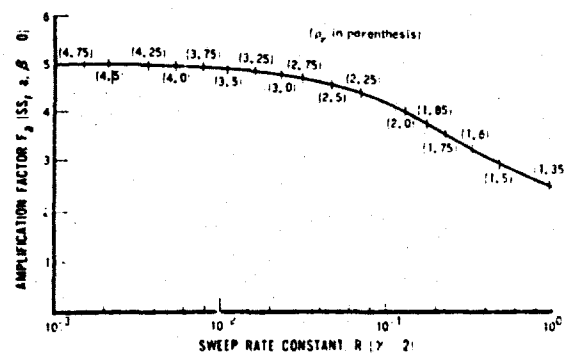


Fig. 6 - Criteria for starting estimates of $\bar{\sigma}$ (restricted to $\delta_1/\delta_2 = 5$)

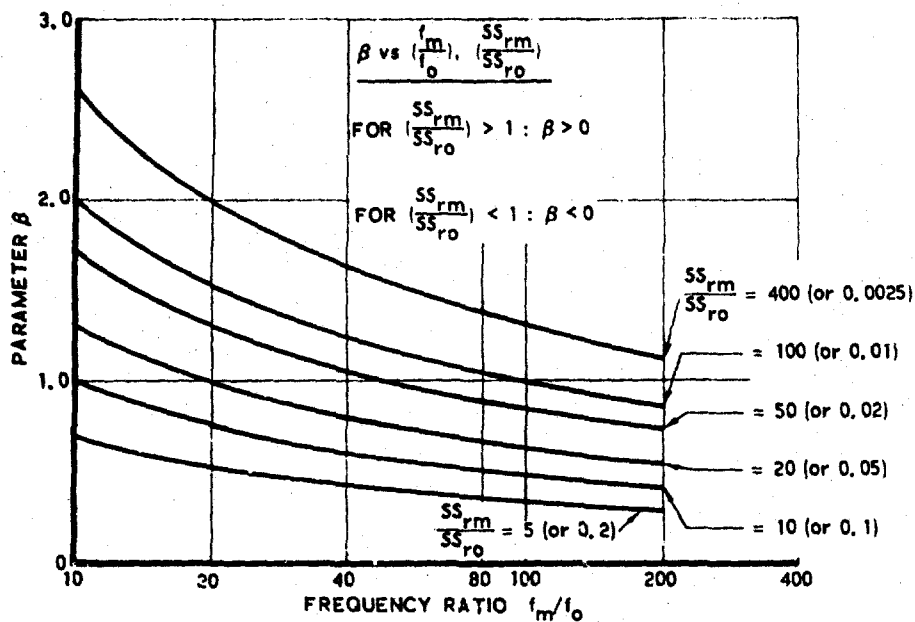


Fig. 7 - Initial parameter estimate criteria, nonconstant shock spectra

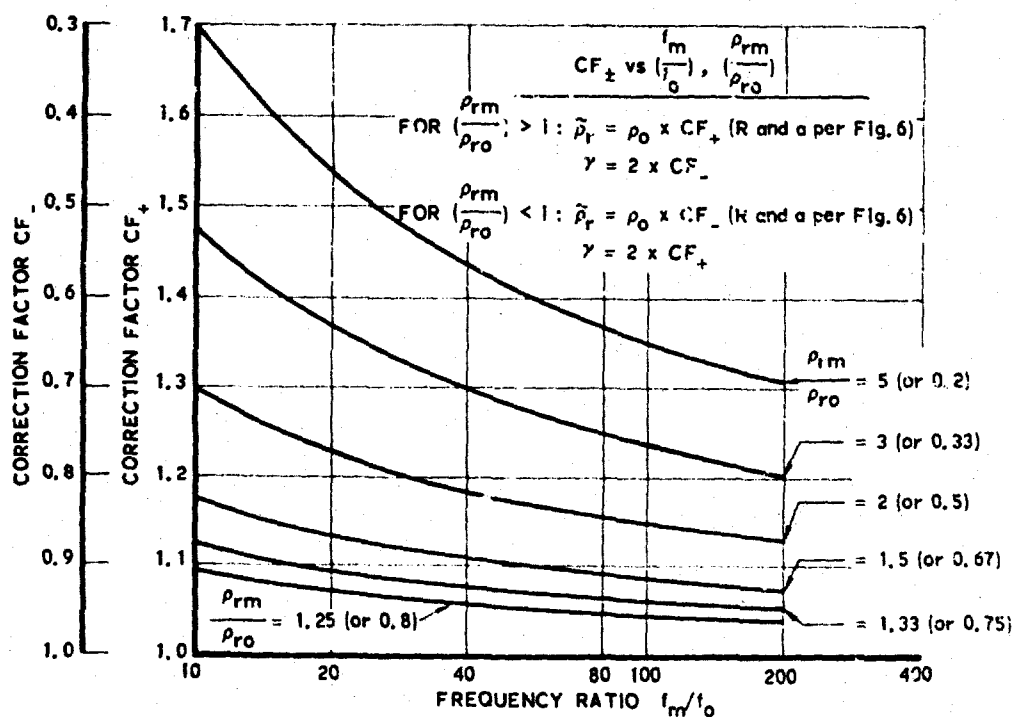


Fig. 8 - Initial parameter estimate criteria, nonconstant shock spectra ratio

TABLE 2
Summary of The Three Demonstration Cases

CLASS, RUN	REFERENCE DATA				PARAMETER ESTIMATE				OPTIMUM ERROR		OPTIMUM PARAMETERS					SWEEP DURATION t_s (sec)
	$SS_{PO}(g^2/s)$	$SS_{PM}(g^2/s)$	p_{PO}	p_{PM}	$a(g^2/s)$	β	R	γ	$E(\omega_k) \times 10^{-3}$	k	$a(g^2/s)$	β	R	γ		
I-1	3	3	1.5	1.5	1	0	0.48	2	0.509	9	1.005	-0.315×10^{-4}	0.4784	1.990	0.205	
I-2	3	3	2	2	0.75	0	0.13	2	0.291	5	0.7616	0.240×10^{-3}	0.1284	2.000	0.740	
I-3	6	6	1.5	1.5	2	0	0.48	2	0.545	6	2.006	0.1488×10^{-2}	0.4776	1.990	0.205	
II-1	3	60	1.5	1.5	1	1	0.48	2	0.389	12	0.9807	0.9967	0.5146	2.002	0.183	
II-2	3	1200	1.5	1.5	1	2	0.48	2	5.19	4	0.9872	1.982	0.4950	2.030	0.174	
II-3	3	0.15	1.5	1.5	1	-1	0.48	2	84.7	4	0.3524	-0.9881	0.5081	2.020	0.175	
III-1	3	60	1.5	2	0.90	1	0.30	1.81	0.614	4	0.7021	0.9910	0.2997	1.803	0.595	
III-2	3	3	1.5	2	0.90	0	0.30	1.81	1.53	8	0.7988	-0.764×10^{-3}	0.3461	1.871	0.402	
III-3	3	60	2	1.5	0.81	1	0.21	2.15	3.98	5	0.9315	0.9977	0.2100	2.152	0.282	
III-4	3	3	2.0	1.5	0.81	0	0.21	2.15	0.863	9	0.871	0.0368	0.1621	2.139	0.380	

n = NUMBER OF ITERATIONS

would also be desirable to minimize $E(\bar{\theta})$ itself, but the tabulated values of $E(\bar{\theta})$ indicate that some runs (e.g., Run II-3, $E(\bar{\theta}) = 84.7 \times 10^{-3}$) satisfy this condition to a considerably lesser degree. Evaluations of this condition are provided in Ref. [1].

Table 2 also shows that the initial estimates for $\bar{\theta}$ are quite close to the optimum values. This relationship suggests use of the $\bar{\theta}$ estimates as a potential replacement of the optimum values when testing tolerances permit.

Evaluation of Case I Results. The three computer runs for Case I all provided optimum error criterion function values of less than 10^{-3} and $\bar{\theta}$ components approximately equal to those estimated. Particularly, β was quite small, and γ was within one percent of the estimated value 2. Doubling the specified shock spectrum magnitude resulted in a doubling of the excitation amplitude. The effect of shock spectra ratio on sweep duration is clearly demonstrated in Table 2, since a 360 percent increase in t_s results from a 33 percent increase in p_r . Sweep duration sensitivity will be summarized later.

Evaluation of Case II Results. The $E(\bar{\theta})$ values achieved from the three computer runs for this case ranged from good to poor in terms of the margin satisfying the specified shock spectra. Run II-1 exhibited good performance; Run II-2 had mediocre performance; and Run II-3 performed poorly.

The reasons for this variation in performance are assessed in detail in Ref. [1]. Overlaid time histories of $g(t)$ and $\ddot{x}(t)$ for Run II-3 shown in Fig. 9 demonstrate I/O relationships and illustrate the cause for Run II-3 performance; i.e., the response peak occurs at the low-frequency high-amplitude portion of the sweep and is virtually independent of oscillator response.

Evaluation of Case III Results. Values of $E(\bar{\theta})$ from the four computer runs in Case III indicate reasonably good margin relative to the stop criteria, thereby verifying that

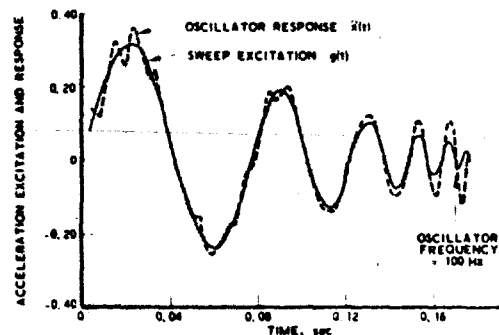


Fig. 9 - Time histories of acceleration excitation and response for Case II, Run 1

an optimum $\bar{\sigma}$ may be attained by the Transient Sweep Algorithm. Runs III-1 and III-2 investigated positive slopes of $\rho(f)$, while Runs III-3 and III-4 were for negative slope investigation. These performances are also assessed in more detail in Ref. [1].

Additional summary data for Run III-1 are provided in Figs. 10 and 11. Effectiveness of the Transient Sweep Algorithm is illustrated in Fig. 10 by comparing the specified and generated shock spectra and ratios. Tighter control was more apparent for the two shock spectra comparisons than for the ratio comparison since $E(\bar{\sigma})$ was expressed in terms of weighted differences between specified and generated values of SS and SS_2 rather than ρ . Sweep excitation $g(t)$ shown in Fig. 11 demonstrates the increasing amplitude and the number of cycles (≈ 22) associated with the sweep.

Summary of Sweep Duration Characteristics and Related Computer Time. Interpretation of data from the three demonstration cases provided sweep duration sensitivities to $\bar{\sigma}$ components R and γ and also a measure of computer time associated with the Transient Sweep Algorithm. Figure 12 shows a curve of sweep duration t_s as a function of γ and R , which can be used to evaluate the t_s sensitivity to each. The average computer run time for the 10 runs made was 1.76 minutes. The maximum computer time (3.85 minutes) was recorded for Run 1-2, where 28 sets (5 iterations requiring 23 additional trial estimates for cubic interpolation) of the 10 sweeps were made at durations approximating 0.74 seconds, shown in Table 2. Run 11-2 represented the minimum computer time; 0.77 minutes, 16 sets (4 iterations requiring 12 additional trial estimates) of 10 sweeps at $t_s = 0.174$ seconds. Computers used were IBM 360 and Univac 1108.

A practical and pertinent outgrowth of the tabulated results is that the set of optimum parameters, in conjunction with the sweep duration, constitute a complete description of the transient sweep excitation. A vibration test machine may be programmed with the $\bar{\sigma}$ and sweep duration to satisfy the particular shock spectra specification. In fact, the computerized results of Case I match those attained directly from industrial vibration testing programs [6, 11] for electromechanical equipment.

SUMMARY AND CONCLUSIONS

Several pertinent observations and conclusions serve to summarize the findings of this paper. These are the following:

- Equation sets for the Transient Sweep Algorithm have been described, and the algorithm has been utilized to prove that optima values of transient sweep parameters (i.e., an inverse shock spectra) were attainable.

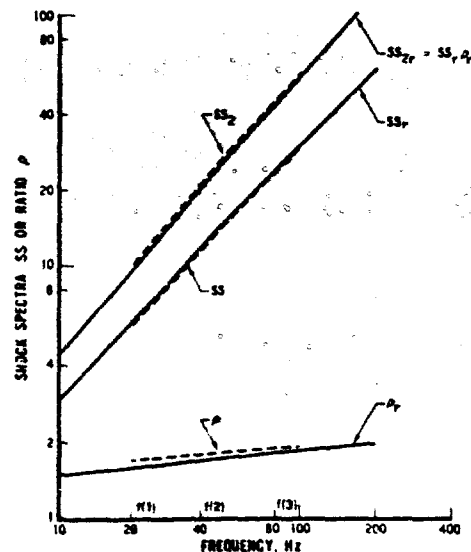


Fig. 10 - Specified versus generated shock spectra and ratio comparisons for Case III, Run 1

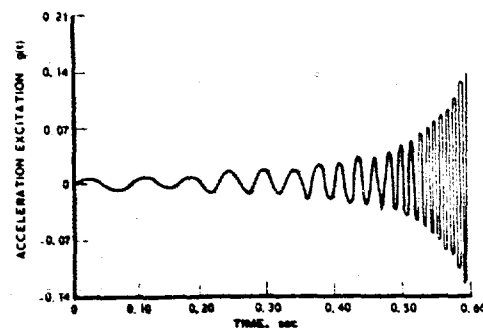


Fig. 11 - Excitation time history from Case III, Run 1

- A numerical integration algorithm is described for determining oscillator response via a step size that varies only with sweep frequency.
- Criteria have been developed in graphic form for estimating initial values of the transient sweep parameters, which lead to optimum values.
- If the vibration test tolerance to be satisfied were extremely loose (e.g., 50 percent), then the close correspondence between initial estimates and optimum transient

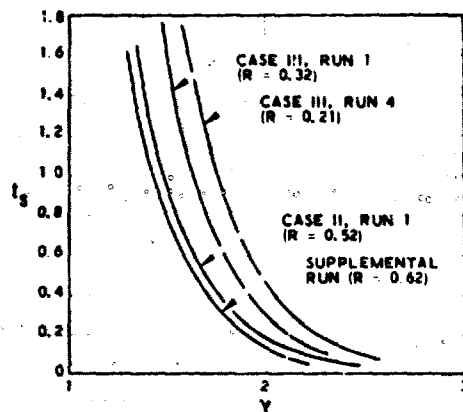


Fig. 12 - Sweep duration sensitivity to γ

sweep parameters would permit use of the estimates themselves for vibration test implementation.

- Negative slope shock spectra specifications were more difficult to match.
- The optimum transient parameters, in conjunction with the corresponding sweep duration, constitute a complete excitation description for implementation on a vibration test machine.
- The average computer run time to establish the optimum parameters was approximately 1.6 minutes when three oscillators were used (computer software overhead was negligible); hence, a rule of thumb for use in practice is approximately 0.5 minute per oscillator.

REFERENCES

1. R. C. Rountree, "Identification of Shock Environment Parameters by Optimization Techniques," Doctoral Dissertation (copy-righted), University of Southern California, June 1972.
2. R. C. Rountree, "An Optimization Technique Utilizing the Deflected Gradient Algorithm for Dynamic Testing of Electromechanical Equipment," Catalog No. 73 CHO 719-5 SWIECO, pg. 589, April 1973.
3. R. Fletcher and M. J. D. Powell, "A Rapidly Converging Descent Method for Minimization," Computer J., Vol. 6, pp. 163-168, 1963.
4. G. A. Bekey, "System Identification - An Introduction and Survey," Simulation, pp. 151-166, Oct. 1970.
5. "Specification of Shock Tests, Panel Session," Shock and Vibration Bull. No. 36, Part 2, Jan. 1967.
6. J. D. Crum and R. L. Grant, "Transient Pulse Development," Shock and Vibration Bull., No. 41, Part 5, Dec. 1970.
7. G. W. Painter and H. J. Parry, "Simulating Flight Environment Shock on an Electrodynamic Shaker," Shock and Vibration Bull., No. 35, Part 4, 1966.
8. J. P. Favour and J. M. LeBrun, "Transient Waveform Control of Electromagnetic Test Equipment," Shock and Vibration Bull., No. 40, Dec. 1969.
9. D. L. Cronin, "Response Spectra for Sweeping Sinusoidal Excitations," Shock and Vibration Bull., No. 38, Aug. 1968.
10. R. C. Rountree and F. B. Safford, "Methodology and Standardization for Fragility Evaluation," Shock and Vibration Bull., No. 41, Part 5, Dec. 1970.
11. F. B. Fay, "A Transient Test Technique," TRW Systems Group Internal Report and Presentation Summary, Redondo Beach, California, Oct. 1965.
12. L. S. Lasdon, Optimization Theory in Large Systems, The MacMillan Co., New York, 1970.
13. W. C. Davidon, "Variable Metric Method for Minimization," Argonne National Laboratory Rept. ANL-5990, Nov. 1959.
14. C. M. Harris and C. E. Crede, Shock and Vibration Handbook, Vol. 2, Chaps. 22-24, McGraw-Hill Book Co., New York, 1961.
15. R. E. Morse, "The Relationship Between a Logarithmically Swept Excitation and the Build-Up Steady-State Resonant Response," TRW Systems Group 7120-6154-R0-000, Dec. 1964.
16. D. M. Wiberg, State Space and Linear Systems, Schaum's Outline Series, McGraw-Hill Book Co., New York, 1971.
17. D. M. Trujillo, "Investigation of Techniques for Numerically Integrating Simple Systems of Differential Equations," TRW Systems Group IOC No. 69.4331.1-14, 18 Sept. 1969.
18. R. Saucedo and E. Schiring, "Introduction to Continuous and Digital Control Systems," The MacMillan Co., New York, 1968.

DISCUSSION

Mr. Favour (Boeing Company): With respect to your gradient approach iteration scheme, several years ago we conducted some independent research on a structural analysis tool where we would feed laboratory data into an analytical model, and attempt to interact through the generalized mass, stiffness, and damping matrices to come up with a new or updated model that would give us the same data out, given a specified input. We started with a gradient approach to iterate through the matrices but quite oddly we found that if we used the random ray approach we converged on the answer much faster. Have you had any similar experience or have you looked at a random ray approach?

Mr. Rountree: No. What gradient method did you use? There are a variety of gradient methods.

Mr. Favour: No, I didn't do the research myself, and I just refer to it as a random ray.

Mr. Rountree: I didn't look at that particular aspect of it but I did look at a variety of gradient methods particularly one called the deflected gradient which some of you may recognize, if you are familiar with optimization as the Fletcher Powell Method. In the past few years it is still considered to be the most efficient gradient method; it is far more efficient than anything else and it gets you there very very rapidly.

Mr. Favour: There may be a difference in the size of the problem that is being worked and that is what I was looking for.

Mr. Rountree: It very much is, because the deflected gradient method takes N number of iterations, where N is the number of parameters. I have 4 parameters so I go through 4 iterations; if you had many spring mass dampers that you are trying to adjust it could overwhelm you on the computer because you have to go through N interactions. If you are using something other than the deflected gradient method you will find that it is more like (4 or 5) N, and that is one of the beauties of the deflected gradient method, it proves that you will converge within N.

ANALYSIS OF OPEN CELL POLYURETHANE FOAM UNDER IMPACT LOADING

Valentin Sepcenko
Boeing Aerospace Company
Seattle, Washington

Analysis of elastomeric foams under dynamic loading is closely associated with testing. This paper presents the results of a program in which testing and theoretical considerations led to the development of an analytical model capable of predicting the nonlinear dynamic response of foam isolators compressed to strains up to 70% at strain rates up to 20.0 in/in-sec. The model consists of a nonlinear visco-elastic element, a series of Maxwell elements and an air spring. The responses of model elements are shown to depend on the history of past loading. The visco-elastic solution is suitable to represent the dynamic behavior of elastomeric (rubber) springs.

INTRODUCTION

This article presents the theory and the analytical technique used to represent the dynamic behavior of prismatic, open cell polyurethane foam blocks subjected to compressive loading over a wide range of strain amplitude and strain rate. Development of the theory was stimulated by the need to predict with high degree of accuracy the response of a new Minuteman missile shock isolation system where foam blocks are the primary horizontal shock attenuators. Theoretical developments were supported by an extensive testing program which provided information needed to determine a number of parameters entering into the analytical representation. These parameters were established for the range of strain and strain rate required to meet shock isolation specifications.

TESTING AND FOAM RESPONSES

The investigated foams may be described as flexible, precrushed, open cell polyurethane with a density ranging from 5.0 to 15.0 lbs/cu. ft. At an earlier stage of development a few closed cell polyurethane foams were also investigated. These were more resilient and had a narrower hysteretic loop per loading-unloading cycle than the open

cell foams. They were rejected as less suitable for this particular application.

Since the application of the foam isolators is in a temperature controlled environment, the effect of temperature on the foam parameters is not considered in this analysis. All tests were conducted at the ambient temperatures (60 to 80°F). These temperatures are sufficiently far from the glass transition temperature (about minus 30°F for polyurethane) to affect visco-elastic parameters.

Two kinds of tests are needed to define parameters in the analytical model. Low compression rate, "static", loading-unloading tests conducted at strain rates from 0.001 to 0.01 in/in-sec and with the strain amplitudes from 0.1 to 0.7 in/in provided characteristic stress-strain curves for various foams. The dimensions of the specimens in these tests do not affect stress-strain curves as long as strain rates remain sufficiently low. Figure 1 shows results of two such tests where the compression of a foam block varied in amplitude. After the second loading cycle, up to a relatively high strain amplitude, the loading branch becomes stable and it remains unchanged during the subsequent loading cycles regardless of the amplitude. Usually the first and the second

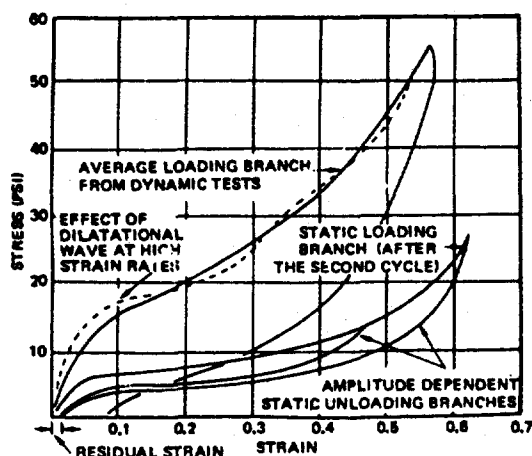


Figure 1: Hysteretic Loops From Static and Dynamic Tests for a Polyurethane Foam (Foam Density 12 Lbs/Cu Ft)

loading cycles result in somewhat higher loading branches and cycling is continued until the tests become repeatable. While the loading branch depends only upon the instant value of strain, the unloading branch depends on the strain amplitude at the time when unloading begins. It was observed that the area within the static hysteretic loop is approximately proportional to the square of the strain amplitude.

Another series of tests were conducted on an impacting sled testing machine at the strain rates from 5.0 to 20.0 in/in-sec and with strain amplitudes from 0.3 to 0.6 in/in. The results of these tests depend upon the dimensions of the specimens, the strain rates and the amplitudes. Both force and displacement time histories were recorded during these tests. A typical result of dynamic tests normalized to the stress-strain plane is shown on Figure 1 as a comparison with the static data.

During some tests conducted with the long specimens and at the upper end of the strain rates, there was observed a formation of a dilatational wave at the impacting side of the specimen. High speed motion pictures taken during these tests provided insight into the mechanism of wave propagation. The wave reached the opposite end of the specimen and bounced back and forth about twice before the peak strain amplitude was reached. The loading branch in these tests is oscillating with a decaying amplitude about an average value. Formation of the dilatational wave had no apparent effect on the unloading branch which remained smooth. Longer specimens and

denser foams were more prone to form such dilatational wave. Although the analytical treatment of propagating waves does not present a problem to the developed method of analysis, it would introduce additional dynamical degrees of freedom into the system which are hardly justified by the overall effect these waves have on the response.

Another phenomenon observed on long specimens was buckling. It was found that at the ratios of length to the smaller side below 1.5 for all prismatic specimens with the densities above 10 lbs/cu. ft. the buckling did not occur even at the highest strain rates and amplitudes used in these tests. Lower density foams were not sufficiently tested to establish safe limits against the buckling.

ANALYTICAL CONSIDERATIONS

For the purpose of the analytical treatment, the dynamic response of the foam isolators must be viewed as being twofold. A part of the response including that at low, static, strain rates is attributed to an essentially visco-elastic behavior of the material which should include microscopic phenomena associated with the local buckling of the cell walls and some irrecoverable, probably plastic effects which are indicated on the static stress-strain curve of Figure 1. This part of the response is independent of the dimensions of the foam block and can be expressed as a stress-strain-strain rate relation.

Another part of the response is associated with the air flow in and out of the block during loading and unloading. This part depends upon the size and the shape of the specimen. Although constitutive equations are presented in a normalized form containing stress and strain terms, they also contain a dimensional factor related to the size of a particular foam block.

SOLUTION FOR VISCO-ELASTIC EFFECTS

The general expression for the stress σ at a time t can be written in the form of a convolution integral

$$\sigma(t) = \int_0^t E(\epsilon, t-\tau) \frac{\partial \epsilon}{\partial \tau} d\tau \quad (1)$$

where $E(\epsilon, t)$ is both strain and time dependent relaxation function defined for foam in compression. The dependence of the relaxation function on strain should account for the nonlinearities which occur at large strains. Equation (1)

should match both static and dynamic tests when the air flow effects are excluded. We attempt to separate $E(\epsilon, t)$ into two parts

$$E(\epsilon, t) = K(\epsilon, t) + G(t) \quad (2)$$

$K(\epsilon, t)$ corresponds to the long term relaxation effects, such as those encountered in the static tests.

$G(t)$ corresponds to the short duration dynamic effects which are assumed to be linear in terms of visco-elasticity.

Equation (1) becomes

$$\sigma(t) = \sigma_s(\epsilon) + \int_0^t G(t-\tau) \frac{\partial \epsilon}{\partial \tau} d\tau \quad (3)$$

$$\text{where } \sigma_s(\epsilon) = \int_0^t K(\epsilon, t-\tau) \frac{\partial \epsilon}{\partial \tau} d\tau \quad (4)$$

$\sigma_s(\epsilon)$ is a double-valued function of strain with separate loading and unloading branches. For a particular strain amplitude it coincides with the static test data for this amplitude. Formally $\sigma_s(\epsilon)$ remains also a time-dependent function which should include such effects as long term creep. However, creep considerations were outside of the scope of this analysis, and were not necessary for the application being considered.

For numerical computations one could store test data for unloading branches at various amplitudes and interpolate as needed. It was found to be more convenient and without sacrifice of the accuracy to use an algorithm which utilizes static test stress-strain curve obtained for the maximum test amplitude from which it derives the unloading branch for any intermediate amplitude. The algorithm was derived from geometric considerations using designations from Figure 2.

$$\sigma_u(\epsilon) = \sigma_L^0(\epsilon) - \left[\sigma_L^0(\epsilon_0) - \sigma_U^0(\epsilon_0) \right] R \left(\frac{\epsilon_{max}}{\epsilon_1} \right)^p \quad (5)$$

$$\text{where } \epsilon_0 = \frac{\epsilon_1}{\epsilon_{max}} \epsilon$$

$$R = 1 - 0.5 \left\{ 1 - \cos \left[\pi \left(\frac{\epsilon}{\epsilon_{max}} \right)^q \right] \right\} \left(\epsilon_1 - \epsilon_{max} \right)^r$$

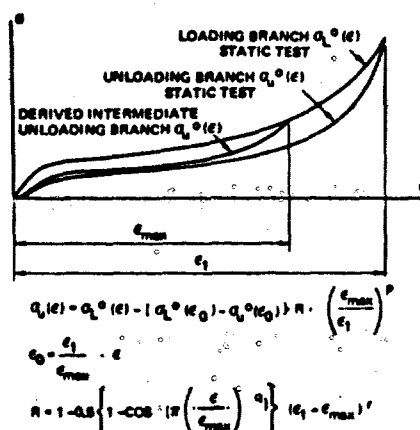


Figure 2: Algorithm for Intermediate Unloading Branch

The parameters p , q and r were found to be

$$\begin{aligned} 0.8 &\leq p \leq 1.2 \\ 2.5 &\leq q \leq 4.0 \\ 0.03 &\leq r \leq 0.06 \end{aligned}$$

The dynamic part of Equation (3) is known to be a limiting case of response of a large number of Maxwell elements connected in parallel. The constitutive equation for the i -th such element is:

$$\tau_i \frac{d\sigma_i}{dt} + \frac{1}{\tau_i} \sigma_i = G_i \frac{d\epsilon}{dt} \quad (6)$$

where G_i and τ_i are constant.

For zero initial conditions $\sigma_i(0) = 0$ and $\epsilon(0) = 0$, the solution of Equation (6) is

$$\sigma_i(t) = G_i \epsilon(t) - \frac{G_i}{\tau_i} \int_0^t \epsilon(x) e^{-(t-x)/\tau_i} dx \quad (7)$$

The integral in Equation (7) can be conveniently calculated from the following:

$$\begin{aligned} \int_0^t \epsilon(x) e^{-(t-x)/\tau_i} dx &= e^{-\Delta t/\tau_i} \int_0^{t-\Delta t} \epsilon(x) e^{-(t-\Delta t-x)/\tau_i} dx \\ &+ \int_{t-\Delta t}^t \epsilon(x) e^{-(t-x)/\tau_i} dx \quad (8) \end{aligned}$$

which leads to the recurrence formula

$$I_n = e^{-\Delta t/\tau_1} I_{n-1} + e^{-\Delta t/\tau_1} G(t) \Delta t \quad (9)$$

For acceptable convergence of Equation (9) the computational step Δt should be at least an order of magnitude smaller than τ_1 .

Thus, the convolution integral in Equation (3) is substituted by a series of discrete Maxwell elements with parameters G_i and τ_i which may be obtained from the relaxation function $G(t)$ by

$$G_i(\tau_i) = \int_{t_1}^{t_2} G(t) dt \text{ with } t_1 < \tau_i < t_2 \quad (10)$$

The relaxation function $G(t)$ must satisfy $\frac{\partial G}{\partial t} < 0$ for all t .

Thus, $G(t)$ is a decaying function for all t . When plotted on log/log scale it may be approximated by a straight line, at least within a few decades (Figure 3). Data on Figure 3 is for filled elastomers, taken from References 2 and 3.

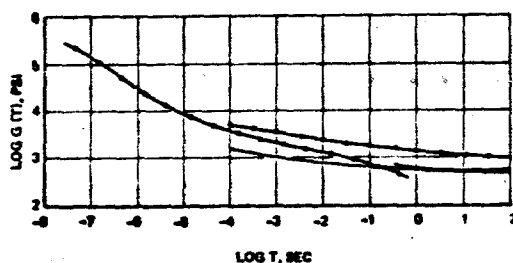


Figure 3: Relaxation Functions for Filled Elastomers

$$\log G(t) = m \log t + \log c \text{ with } m < 0 \quad (11)$$

$$G(t) = ct^m$$

For calculation of a discrete spectrum $G_i(\tau_i)$ it is convenient to use $t_2 = 2t_1$ which provides sufficient distinction between adjacent Maxwell elements. In order to plot a discrete spectrum τ_1 was assumed to be:

$$\tau_i = \sqrt{t_1 t_2} \quad (12)$$

Substituting Equation (11) into Equation (10) and integrating we obtain the distribution for the discrete relaxation spectrum $G_i(\tau_i)$

$$G_i(\tau) = c \frac{m+1-1}{m+1} \tau_i^{m+1} \text{ for all } m \neq -1 \quad (13)$$

$$G_i(\tau) = c \ln 2 \text{ (constant) for } m = -1 \quad (14)$$

Within the analyzed range of relaxation times the values of m for elastomers lie within $-1 < m < 0$ which renders $G_i(\tau_i)$ an increasing function or a constant. Considering Equation (3) we conclude that at the higher values of τ_i the discrete spectrum $G_i(\tau_i)$ must become a decreasing function and taper off since at longer relaxation times the response of the foam is described by $\sigma_2(\epsilon)$. Various shapes of the discrete spectra and their effect on the dynamic part of the foam response were investigated using twelve Maxwell elements spaced one octave apart along the τ -axis. For a foam with the density of 12.0 lbs/cu. ft. the best match was obtained using the shape shown on Figure 4. The contributions to the total

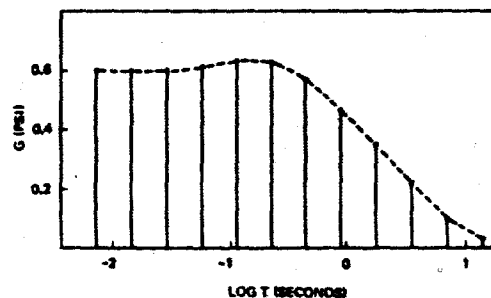


Figure 4: Discrete Relaxation Spectrum Used to Match Response of 12 Lbs/cu Ft Polyurethane Foam

response from the Maxwell elements at both ends of the spectra are small. Relaxation times of the elements located at the left end of the spectrum are too short for significant contribution to the response within the range of available tests. The most noticeable contribution is made by the group of elements from the middle part of the spectrum.

Once the shape of the spectrum and the number and spacing of the Maxwell elements is assumed there remain only two independent parameters to be determined by matching the test data: the magnitude along the G axis and the location of the spectrum with respect to τ axis.

SOLUTION FOR AIR SPRING EFFECT

The solution for the part of the response associated with the air flow in and out of the foam was derived using the model of a foam block shown on

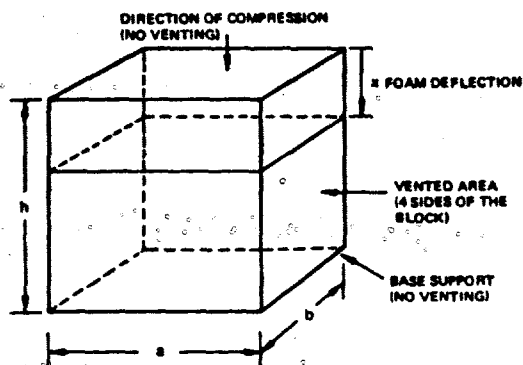


Figure 5: Model for the Analysis of Air Flow Effects

Figure 5. The following nomenclature is used in the derivation in addition to the designations given on Figure 5.

$A=ab$	cross-section area of the foam block
$V=abh$	foam block volume
$V_{air}=\gamma \cdot V$	initial volume of the air contained within the foam block at atmospheric pressure
γ	initial porosity
$\epsilon=x/h$	strain
$\beta=(V_{air}-A \cdot x)/V=\gamma-\epsilon$	instantaneous porosity
$V(\epsilon)=\beta V$	instantaneous volume of the air within the compressed block
$p(0)=14.7 \text{ psi}$	atmospheric pressure
$p(\epsilon)$	instantaneous air pressure at the center of the compressed foam block
$A_0(\epsilon)=2(a+b)h(\gamma-\epsilon)$	area of the pores within the four vented sides of the compressed foam block
v_0	average velocity of the air escaping from the compressed foam block
ΔV	volume of the escaped air from $t=0$ to time t corresponding to $x=x(t)$

$n=1.38$ for adiabatic case

Adiabatic condition for the air relates

$$p(0) V_{ref}^n = p(\epsilon) V(\epsilon)^n \quad (16)$$

$$\text{where } V_{ref} = V_{air} - \Delta V = V \gamma - \Delta V$$

The peak overpressure at the center of the block is

$$p(t) = p(\epsilon) - p(0) = p(0) \left\{ \left[\frac{\gamma - \Delta V/V}{\gamma - \epsilon} \right]^n - 1 \right\} \quad (17)$$

The expression for ΔV is assumed in the form:

$$\Delta V = \int_0^t A_0(\epsilon) v_0 dt \quad (18)$$

In order to calculate v_0 consider theoretical expressions for the air flow thru orifice. In the following subscript 1 refers to the conditions on the side of the orifice with higher pressure while subscript 2 refers to the conditions on the other side. Flow thru the orifice with large velocity changes is given by:

$$v_2^2 - v_1^2 = c(p_1 v_1 - p_2 v_2) \quad (19)$$

where c is a constant independent of friction.

Then

$$v_2^2 = cV(\gamma - \epsilon) \left[p(\epsilon) - p_2 \frac{v_2}{V(\gamma - \epsilon)} + \frac{v_1^2}{cV(\gamma - \epsilon)} \right] \quad (20)$$

In order to satisfy condition $v_1=0$ when $p(\epsilon)=p(0)$ the last two terms within the square brackets must equal to $p(0)$. Using Equation (17) it follows that

$$v_2^2 = cV(\gamma - \epsilon) p(t) \quad (21)$$

which is simply a statement that the square of the velocity through the orifice is proportional to the instantaneous volume of the air, $V(\epsilon)$, and the pressure differential across the orifice. When related to the foam one must consider friction which depends on the foam characteristics as well as the state of the foam in compression. Such a friction function, $F(\epsilon)$, was derived in the Reference (3) from the pressure gradient tests. Consequently, the equation for v_0 takes the form:

$$v_0^2 = F(\epsilon) v_2^2 \quad (22)$$

where

$$F(\epsilon) = \frac{\delta}{\lambda \epsilon^3} \frac{B^3}{1-B} = \frac{\delta}{\lambda \epsilon^3} \frac{(\gamma - \epsilon)^3}{1 - \gamma + \epsilon} \quad (23)$$

δ = average pore diameter

λ = basic friction factor

ϵ = average length of the air path during venting. The choice of ϵ defines location of the peak pressure $p(\epsilon)$ within the foam block.

The importance of $F(\epsilon)$ in this context is to provide the shape of the friction function for a compressed foam block relative to the initial value of air friction for an unstrained foam block; such an approach does not rely on the reported values for δ and λ .

$$\text{Let } B = 2(a+b) h \left[\frac{\gamma - \epsilon}{1 - \gamma + \epsilon} \right]^{1/2} \quad (24)$$

From Equations (24), (23), (24) and (18) it follows

$$\frac{\Delta V}{V} = B \int_0^t (\gamma - \epsilon)^3 \left[\frac{\gamma(t)}{1 - \gamma + \epsilon} \right]^{1/2} dt \quad (25)$$

The system of Equations, (17) and (25), completes the solution for the peak air pressure within the foam block. The numerical solution of this system is straight forward: the value of $\epsilon(t)$ entering Equation (25) is calculated one computational step behind that entering Equation (17). Whenever the values of $\epsilon(t)$ are significant for the analysis, the system of Equations, (17) and (25), is stable. When $\epsilon(t)$ is approaching zero at a slow rate, computational oscillations may occur and the computational step must be decreased accordingly.

Finally, the average overpressure applied to the support of the foam block is calculated by

$$\sigma_a(t) = \alpha \gamma \sigma(t) \quad (26)$$

The coefficient α is introduced to represent the average overpressure since $p(\epsilon)$ was defined at the center of the block. The initial porosity, γ , is introduced to account for the area of the pores in contact with the base support.

There remain two parameters, the venting factor B and the shape factor a , to be determined by matching the test data. The range of these parameters was found to be $12 < B < 50$ and $0.65 < a < 0.95$. The lower values of B and a correspond to denser foams.

CONCLUSIONS

The total stress acting on the support of a foam block subjected to a strain $\epsilon = \epsilon(t)$ is calculated by summing up the results given by the Equations (4), (7) and (26).

$$\sigma_t = \sigma_s(\epsilon) + \sum_{i=1}^{i=k} \sigma_i(t) + \sigma_a(t) \quad (27)$$

where the number of Maxwell elements, k , may be varied depending on the available range of tests. Numerical computations were made using test data for the loading branch of $\sigma_s(\epsilon)$ and the algorithm, Equation (5), for the unloading branch. The effect of Maxwell elements was calculated using Equation (7), the recurrence Equation (9) and a variable computational step for each element depending on τ_i . A separate algorithm was developed to solve the system of Equations (17) and (25) entering into computations of $\sigma_a(t)$.

Computations presented within this article are inconceivable without the use of computer programs. One such program was developed in the form of a subroutine to be used in conjunction with the programs solving equations of motions for large dynamical systems. Other programs were developed to vary parameters and to obtain the best matching of the test data. Figures 6, 8 and 10 show examples for matching 3 tests conducted with different specimens made of the same type foam with a density of 12 lbs/cu.ft. Figures 7, 9 and 11 show

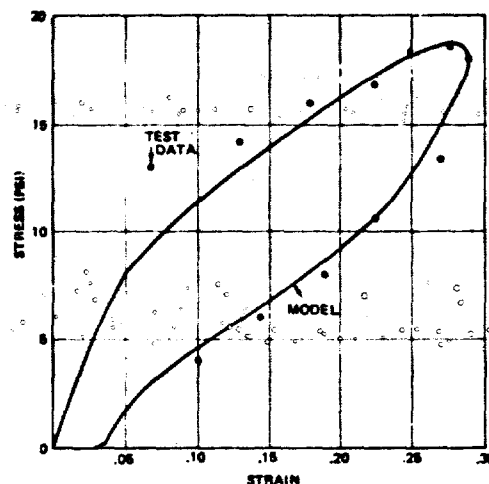


Figure 6: Foam Response at Low Strain Amplitude
Impact Rate 9.0 In./In. Sec

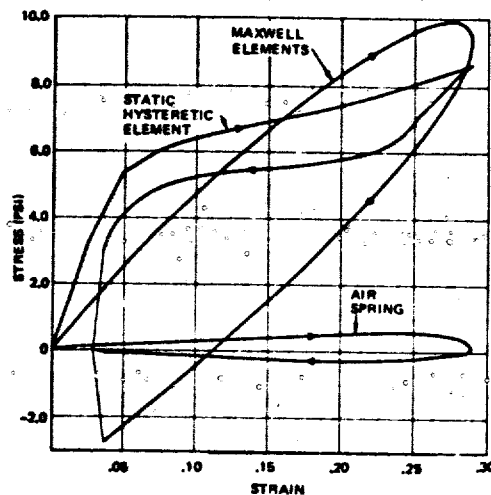


Figure 7: Contributions to the Total Stress Shown on Figure 6 From the Model Elements

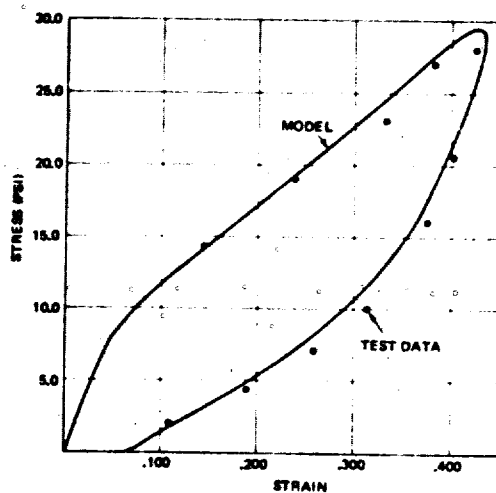


Figure 8: Foam Response at Intermediate Strain Amplitude
Impact Rate 12.0 In./In. Sec

theoretical contributions of various elements in the model to the total stress. These three tests cover a wide range of strain rates and amplitudes.

Analytical solutions contain a number of parameters. Some of them are established directly from the tests; others require trial and error procedures. In this respect presented analytical solutions may be regarded as influence functions containing parameters which can vary the shape of these functions. The wider is the range of the tests the narrower becomes the range of parameters. A single test can be matched well by a few combinations of

these parameters. The dispersion of the test results obtained from a number of foam specimens, even when the specimens are coming from the same production batch, is of such an order that the analytical match must be obtained for the statistical averages.

The visco-elastic solution was successfully used in the analysis of shaped ethylene-propylene monomer elastomeric springs which contained buckling elements. Static loading-unloading curves for these springs resemble those of a foam. These springs

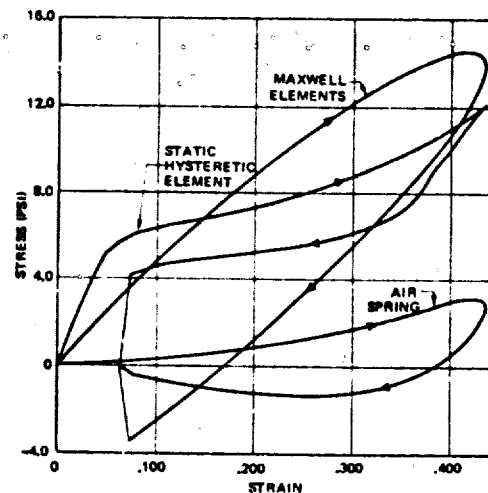


Figure 9: Contributions to the Total Stress Shown on Figure 8 From the Model Elements

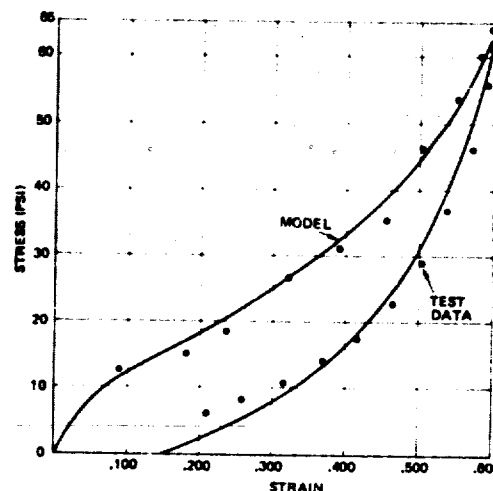


Figure 10: Foam Response at High Strain Amplitude.
Impact Rate 18.0 In./In. Sec. Loading Branch of Test Data is Affected by the Propagating Dilatational Wave

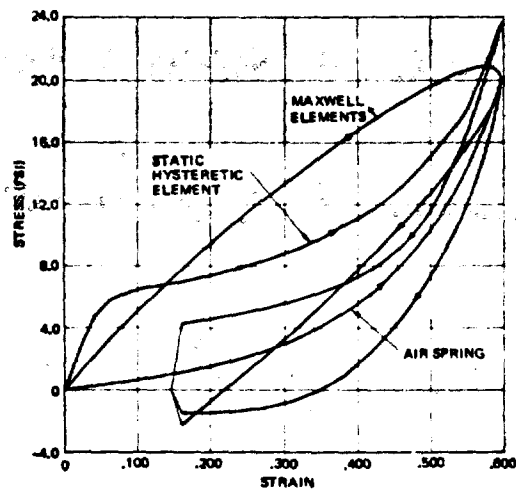


Figure 11: Contributions to the Total Stress Shown on Figure 10 From the Model Elements

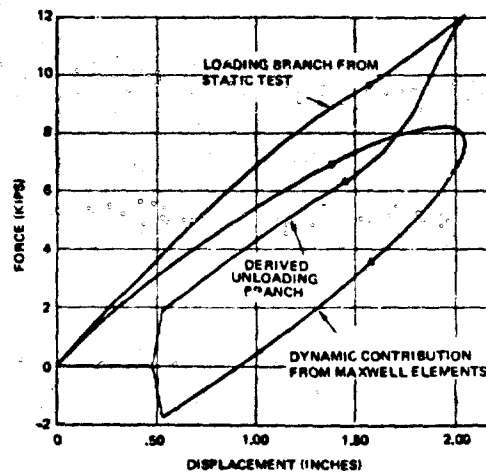


Figure 13: Contributions to the Total Force of a Shaped Elastomeric Spring From the Model Elements

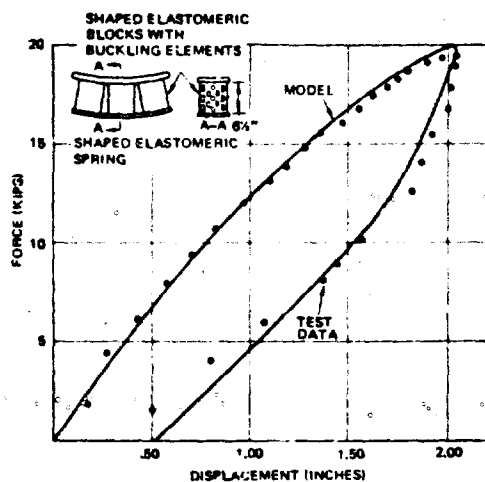


Figure 12: Hysteretic Loop of a Shaped Elastomeric Spring. Impact Velocity 48.0 In./Sec

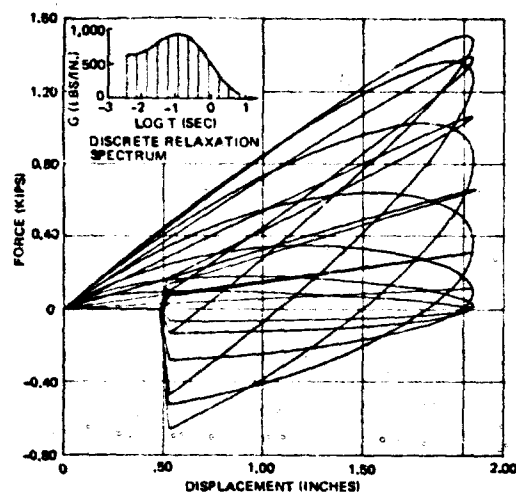


Figure 14: Contributions to the Total Dynamic Effect By the Separate Maxwell Elements

form a part of the missile isolation system. Both dynamic and static tests yield consistent data which enabled a high degree of accuracy when matching these tests. An example is shown in Figures 12, 13 and 14. The shape of the discrete relaxation spectrum used in this match and shown on Figure 14, is different from that on Figure 1 matching form tests.

REFERENCES

1. T. Nichols and A. M. Freudenthal, "The Mechanical Behavior of a Filled Elastomer at High Strain Rates." Department of Civil Engineering and Engineering Mechanics, Columbia University. Contract Nonr 266(78). Project NR 064-466. Report No. 35. August 1966.
2. T. Nichols and R. A. Heller, "Determination of the Complex Shear Modulus of a Filled Elastomer from a Vibrating Sandwich Beam." Department of Civil Engineering and Engineering Mechanics, Columbia University. Nonr 266(78). Project NR 064-446. Technical Report No. 30. June 1965.
3. W. A. Voltz, E. T. Barakauskas, and R. H. Strong, "Foam Shock Isolation System Feasibility Study Phase I and Phase II Summary Report," BSRD-TR-66-11, February 1966; Air Force Contract AF01(694)-568. Westinghouse Company.

DISCUSSION

Mr. Pakstys (General Dynamics/Electric Boat Division): What were the physical characteristics of the first foam for which you had the most comparison?

Mr. Sepcenko: That was a rectangular foam block; it is a fire resistant polyurethane, foam it weighs 12 lb. per cubic foot, and the approximate porosity is in the range of about 83%. In working with an analytical model and matching test data you really need the test data to have a match, although in the paper, we presented some data on flexible polyurethane foams ranging from about 5 lbs. to 15 lbs. per cubic foot and with different associated porosities.

Mr. Wolf (Kaman Sciences): I am aware that your effort was primarily to describe the mechanical properties of foams and that there are large varieties of foams, and that polyurethane foams are used in many applications, some of which involve areas where there are people. Have you had an opportunity to assess the fire hazard and the toxic gas situation in any more detail?

Mr. Sepcenko: In this particular application we are compelled to use the so called fire resistant or fire retardant foams. I could say that this foam survives a launch environment where the temperature is approximately 5000 degrees. The surface is charred, the foam block remains intact after launch, and the penetration of the heat, in effect the charring of the surface, is on the order of 1/8th of an inch. I would expect that some of these foams may produce some poisonous gases if subjected to a longer time heating.

Mr. Pakstys: You mentioned that there is the potential of applying this method to closed cell geometries. Have you actually done this, and have you discussed this in your paper?

Mr. Sepcenko: We did not discuss the possibility of the application to closed cell foams very much in the paper. We investigated closed cell foams at an earlier stage however they were significantly more resilient, and the hysteretic loops associated with these foams were not as wide as the ones for the open cell foams, which is to be expected, because they don't have the air flow effects.

Mr. Paz (University of Louisville): Do you use these only in the compressive form? Could they be used in a shear type of mode?

Mr. Sepcenko: In this particular type of application we used it only in compression; however shear, it would show a very similar effect, although the hysteretic loop is a little less and we ran some tests for this response. We did not use it in tension; there are some disadvantages to of using this foam in tension. It is very sensitive to a notch, if a notch occurs it begins to propagate throughout the foam and the block breaks very quickly. In our application, in the particular case of the launch tube, we had to reinforce the tensile zone in order to survive launch environment tension.

MEASUREMENT OF PEAK PRESSURES PRODUCED
AT THE GROUND SURFACE BY SHALLOW BURIED EXPLOSIVES

Bruce L. Morris
U.S. Army Mobility Equipment Research and Development Center
Fort Belvoir, Virginia 22060

(U) An experimental program was conducted to measure the peak pressures produced at the ground surface by the detonation of shallow buried explosive charges. Pressures were measured in both C-7 epoxy and soda-lime glass targets, and predictions of peak stresses in both steel and aluminum targets were made. Experimental results were compared with hydrodynamic computer code calculations.

INTRODUCTION

The rational design of equipment expected to operate and survive in a blast environment requires accurate knowledge of the forces to be encountered. This program was conducted to measure the peak pressure produced in a target on the ground surface above a shallow buried explosive charge. The prototype explosive charges were chosen as 20 lb. Pentolite cylinders and spheres with 2", 6", and 12" of soil cover to the top of the charge. Past work in the field of explosion-produced overpressure and effects has indicated that the use of replica models will produce reliable results. A replica model simulates compressibility effects and inertial effects by fabricating both model and prototype from the same materials. Geometric similarity is required, and the energy release is sealed as the cube of the geometric scale factor. Thus by using a geometric scale factor of .423, a 1.5 lb. charge weight and burial depths of .85", 2.55", and 5.1" were selected for the experimental program.

INSTRUMENTATION

The instrumentation system used is shown schematically in Figure 1. The electric blasting cap was detonated with a standard ten-cap blasting machine and the detonating cord (three feet of 6125 meters/second speed tested cord) gave a delay of approximately 150 μ -seconds between triggering of the break wire and detonation of the main charge. The break wire triggered the signal generator which in turn triggered the oscilloscope and power supply after a suitable delay time based on the charge burial depth. The shock wave in the gage causes a change in resistance in the manganin wire sensing element which, under the constant current imposed by the power supply, produces a

change in the voltage which is recorded by the oscilloscope.

The method used to interpret the data is that developed by Keough.³ The relationship between the observed relative change in voltage $\frac{\Delta V}{V}$ and the actual relative resistance change

$\frac{\Delta R}{R}$ is a function of the shunt resistance of the measuring circuit and the changing current through the gage as the change in gage resistance becomes an appreciable percentage of the blast resistance. This relationship is charted in the reference and was taken as

$$\frac{\Delta R}{R} = 1.04 \frac{\Delta V}{V} \quad (1)$$

for these tests. This value of $\frac{\Delta R}{R}$ is then

related to stress by means of the piezoresistive coefficient of manganin:

$$P(\text{Kbar}) = \frac{\Delta R}{R} [(0.29 \pm 0.01) \times 10^{-2}]^{-1} \quad (2)$$

This equation is valid for $P \leq 170$ Kbar, and pressures reported in this paper are those calculated without the uncertainty term.

Tests were conducted using the manganin wire gage embedded in both C-7 epoxy and soda-lime glass matrix materials, characteristics of which are given in Table 1. In either case the gage element is assumed to be in equilibrium with the surrounding material and the pressure measured is assumed to be that in the matrix. The Hugoniot data for the materials must be known to permit extrapolation of the results to other materials through impedance match procedures. This data is usually displayed in the form of pressure-particle velocity ($P - u$) plot, and these curves for C-7 epoxy,

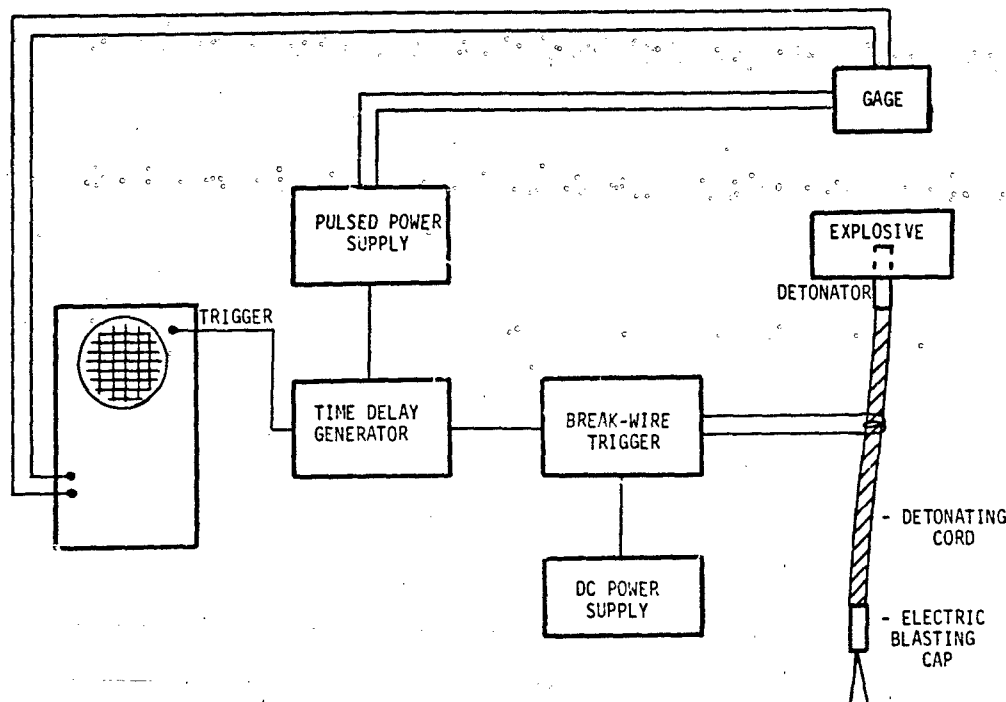


FIGURE 1. INSTRUMENTATION CIRCUIT

soda-lime glass⁵, iron⁶ and aluminum⁷ (the latter two for extrapolation purposes) are given in Figure 2. The curve for soda-lime glass has been extrapolated as shown assuming no phase changes or discontinuities. The aluminum curve is that of 24ST aluminum.

The explosive used in this program was 50/50 Pentolite (50% TNT, 50% PETN) with a density of 1.67 grams/cc. It was cast by the Ballistics Research Laboratory into spheres of 1.8 inch (4.6 cm) radius and cylinders of 4.57 inches (11.6 cm) diameter and 1.52 inches (3.86 cm) height, each charge weighing 1.5 lbs. nominally. Each charge was predrilled to allow insertion of a blasting cap to permit central initiation.

EXPERIMENTAL PROCEDURE

A total of 36 test shots yielded data in a nominally dry soil (average density = 1.758

gr/cc, sonic speed = .0336 cm/μ-sec, water content = 13.2%). The relative locations of the explosive charge and the gage are shown in Figure 3. All tests were conducted using the local soil, a sandy clay. The hole was dug approximately 2-3 inches too deep and back-filled. The charge was placed and its center-line location determined. The hole was filled with the removed soil and the gage was placed along the center-line of the charge. The soil sonic speed was determined using a seismic tunnel detector to measure the transit time of a sound disturbance over a measured distance. Soil density and water content measurements were made with a Troxler radiation soil meter.

EXPERIMENTAL RESULTS

The results of these tests are summarized in Table 2 and displayed in Figure 4. A few

TABLE 1. Gage Matrix Characteristics

	C-7 Epoxy	Soda-Lime Glass
Identification	Pulsar Md1 741 manganin	Pulsar Md1 G41M
Diameter	3.9 inches	3.9 inches
Height	1.8 inches	1.1 inches
Element Depth	.020 inches	.090 inches

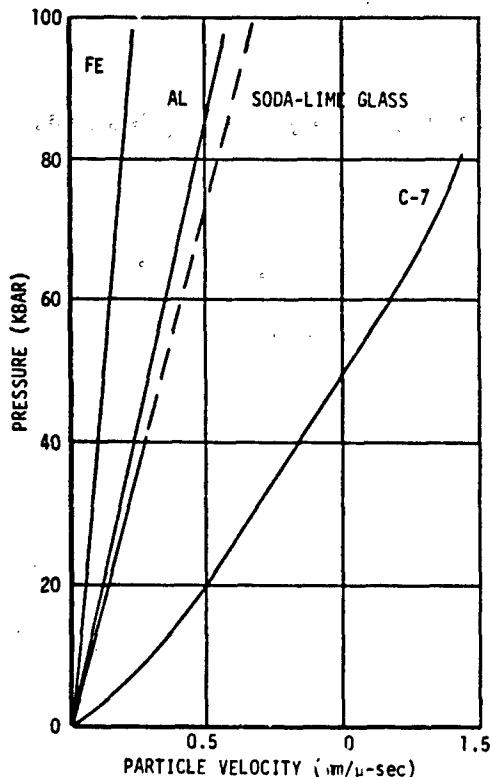


FIGURE 2. PRESSURE VS PARTICLE VELOCITY CURVES FOR C-7 EPOXY, SODA-LIME GLASS, IRON, AND 24ST ALUMINUM

qualitative comments are in order here. It was expected from impedance match considerations (acoustic impedance is defined as the product of the initial density and the sonic speed, being .31 grams/cm³ - μ sec for C-7 epoxy and 9.46 grams/cm³ - μ sec for soda-lime glass) that the pressure measured in the glass would be greater than that measured in the C-7 for each combination of charge configuration and burial depth. The increase in pressure from the cylindrical over the spherical charge was also expected and has been experimentally observed elsewhere in similar type test¹. For a given burial depth to the top of the charge, the scaled distance, defined as the distance from the center of the explosive in feet divided by the cube root of the explosive weight in pounds, is less for a cylindrical charge than for a spherical one, being given by

$$Z_{Cyl} = \frac{b + 0.053}{1.14} \text{ FT/LB}^{1/3} \quad (3)$$

for the cylinder and by

$$Z_{Sph} = \frac{b + 0.15}{1.14} \text{ FT/LB}^{1/3} \quad (4)$$

for the sphere, where b is the burial depth and $1.14 = 1.5^{1/3}$. In addition, the cylindrical charge provides a good deal of focusing of the shock wave along its cylindrical axis.

COMPUTER SIMULATIONS

As further verification of the experimental results and to improve reliability of calculations of this type of blast environment, the TOODY-A computer code was used to simulate a portion of the experimental program. The combination of the cylindrical charge and C-7 epoxy matrix material at three burial depths was selected for modelling.

The accuracy of solution given by finite difference computer code such as TOODY depends mainly on the equations of state (relating internal energy and compression to pressure) used for the materials and on the size of the computational grid used. A typical grid (that for simulating the cylindrical charge, C-7 target, .85" burial depth) at 1/4 scale of the tests is shown in Figure 5. The pentolite was modelled using the JWL⁸ equation of state with parameters as shown:

$$P = 4.91123(1 - \frac{3\eta}{4.4})e^{-\frac{4.4}{\eta}} + .090606(1 - \frac{3\eta}{1.1})e^{-\frac{1.1}{\eta}} + .30E \quad (5)$$

where η = compression = $\frac{\rho}{\rho_0}$, ρ = density, E = internal energy, and ρ_0 = initial density = 1.67 gr/cm³ for pentolite.

Both the soil and C-7 epoxy were modelled using an elastic-plastic-hydrodynamic equation of state of the form

$$P = P_H(1 - \frac{\Gamma\eta}{2}) + \Gamma\rho E \quad (6)$$

where P_H = Hugonott pressure

Γ = Gruneisen ratio

$\eta = \frac{\rho}{\rho_0} - 1$ = excess compression

E = internal energy per unit mass

The Hugonott pressure was of the form

$$P_H = \frac{\rho_0 C_0^2 \eta^2}{(1 - S\eta)^2} \quad (7)$$

for the soil where $\eta = 1 - \frac{\rho_0}{\rho}$ and

S = slope of the shock velocity-particle velocity curve = 1.3

An expansion of equation (7) in the form

$$P_H = \rho_0 C_0^2 \eta (1 + 3.5038\eta + 8.84175\eta^2 + 18.1332\eta^3 + 32.93989\eta^4) \quad (8)$$

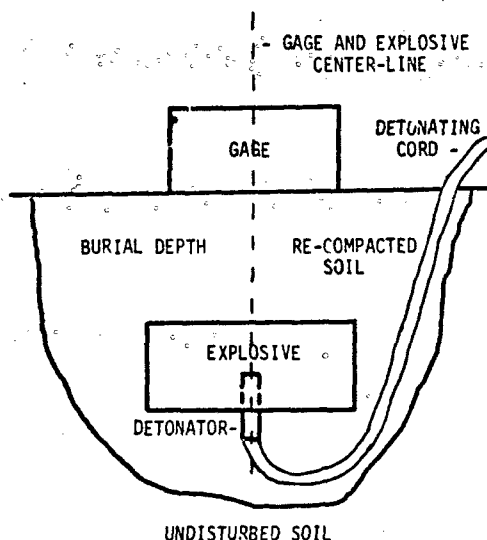


FIGURE 3. CHARGE AND GAGE PLACEMENT
SHOWING RE-COMPACTED AND UNDISTURBED
SOIL REGIONS

was used for the C-7 epoxy. The Gruneisen ratio was given by

$$\Gamma = \frac{\Gamma_0 \rho_0}{\rho} \quad (9)$$

Both materials were considered to be hydrodynamic, possessing no tensile strength. The shear modulus, G , was given in both cases by

$$G = \frac{3(1 - 2\nu)}{2(1 + \nu)} K \quad (10)$$

where ν = Poisson's ratio

$$K = \text{bulk modulus} = \rho c^2$$

Values of the input constants are given in Table 3.

The soil density and sound speed were varied according to the corresponding values shown in Table 2.

The major difficulty in computing explosively generated pressures is getting the explosive to reach its maximum or Chapman-Jouget (C-J) pressure. The grid of Figure 5 utilizes .06 cm x .05 cm computational zones inside the explosive and yielded a maximum pressure of 210 Kbar for the explosive, where the C-J pressure is 250 Kbar.

If the explosive had computationally reached its C-J pressure, the C-7 epoxy pressure would be expected to be slightly higher. The actual pressures computed, however, are compared with the experiment in Figure 6. A typical calculated pressure-time history is given in Figure 7.

Agreement between the calculations and experiment is quite good, particularly at the .85 inch and 5.10 inch burial depths. In the 5.10 inch case, the limits of the experimental values bound the calculated result. The difference at the 2.55 inch burial may be due in part to the variation in sound speed and density for the experiments as the pressure recorded increases with increasing soil density. The combination of $\rho_0 = 1.584 \text{ gr/cm}^3$, $c_0 = .0339 \text{ cm/\mu-sec}$ was used for the calculation. The soil equation of state does not consider soil voids or soil locking, so the calculated results could be expected to diverge from experiment at greater and greater burial depths. The calculated pressure for a C-7 target in contact with the charge surface ("zero" burial) provides a reasonable extrapolation of the data.

STRESS PREDICTION IN STEEL AND ALUMINUM

Realizing that C-7 epoxy and soda-lime glass are not targets of military interest, the data in Table 2 was used to predict the peak stresses that would be measured in steel and in aluminum targets under the same experimental conditions. The impedance match technique was first used as follows using the

TABLE 2. Peak Pressures and Test Conditions

TEST NUMBER	GAGE MATERIAL	EXPLOSIVE CONFIGURATION	BURIAL DEPTH (INCHES)	SOIL DENSITY (grams/cm ³)	SOIL SONIC SPEED (cm/μ-sec)	SOIL % MOISTURE	PEAK PRESSURE (Kbar)
2	C-7 epoxy	cylinder	0.85	1.568	0.0290	10.7	61.3
3	"	"	"	"	"	"	62.8
4	"	"	"	"	"	"	40.7
						AVERAGE	54.9
5	glass	cylinder	0.85	1.568*	0.0290*	10.7*	81.0
6	"	"	"	"	"	"	60.3
6a	"	"	"	1.584	0.0339	10.6	68.8
7	"	"	"	"	"	"	79.8
						AVERAGE	72.5

*Repeated from another test

TABLE 2. Peak Pressures and Test Conditions (Continued)

TEST NUMBER	GAGE MATERIAL	EXPLOSIVE CONFIGURATION	BURIAL DEPTH (INCHES)	SOIL DENSITY (grams/cm ³)	SOIL SONIC SPEED (cm/μ-sec)	SOIL % MOISTURE	PEAK PRESSURE (Kbar)
8	C-7 epoxy	sphere	0.85	1.568*	0.0290*	10.7*	63.6
9	"	"	"	"	"	"	44.5
10	"	"	"	"	"	"	33.3
						AVERAGE	47.1
11	glass	sphere	0.85	1.568*	0.0290*	10.7*	58.6
12	"	"	"	"	"	"	50.8
13	"	"	"	1.584*	0.0339*	10.6*	55.3
						AVERAGE	54.9
14	C-7 epoxy	cylinder	2.55	1.584*	0.0339*	10.6*	24.8
15	"	"	"	1.824*	0.0339*	15.7*	27.9
16	"	"	"	1.640	0.0381	11.8	26.5
						AVERAGE	26.4
17	glass	cylinder	2.55	1.824	0.0339*	15.7	36.3
18	"	"	"	"	"	"	36.7
19	"	"	"	1.640*	0.0381*	11.8*	40.7
						AVERAGE	37.9
20	C-7 epoxy	sphere	2.55	1.824*	0.0339*	15.7*	12.1
21	"	"	"	1.640*	0.0381*	11.8*	11.5
22	"	"	"	"	"	"	12.8
						AVERAGE	12.1
23	glass	sphere	2.55	1.640*	0.0381*	11.8*	13.3
24	"	"	"	"	"	"	26.7
25	"	"	"	"	"	"	13.4
						AVERAGE	17.8
26	C-7 epoxy	cylinder	5.10	1.832	0.0359	12.8	11.1
27	"	"	"	"	"	"	9.6
28	"	"	"	"	"	"	7.6
						AVERAGE	9.4
29	glass	cylinder	5.10	1.832*	0.0359*	12.8*	6.4
30	"	"	"	"	"	"	11.9
31	"	"	"	1.163	0.0359*	22.6	13.1
						AVERAGE	10.5
32	C-7 epoxy	sphere	5.10	1.163*	0.0359*	22.6*	9.9
33	"	"	"	"	"	"	6.7
34	"	"	"	"	"	"	3.0
						AVERAGE	6.5
35	glass	sphere	5.10	1.808	0.0305	12.6	---
36	"	"	"	"	"	"	1.6
37	"	"	"	"	"	"	7.2
						AVERAGE	7.2

*Repeated from another test

+Not measured, assumed value

equation for shock transmission:

$$P_T = \frac{2Z_2}{Z_1 + Z_2} P_I \quad (11)$$

(1) For each combination of burial depth and charge configuration, two simultaneous equations of the above form can be written, one for the C-7 target and one for the glass. In the first, P_T is experimentally measured

pressure and Z_2 is the impedance of the C-7. In the second, P_T is the pressure measured in the glass and Z_1 is the glass impedance. In

TABLE 3. Material Properties for TOODY-A Calculations

VARIABLE NAME	C-7 EPOXY	SOIL
ρ_0 , gr/cm ³	1.19	Variable
c_0 , cm/μ-sec	0.2563	Variable

TABLE 3: Material Properties
for TOODY-A Calculations (Continued)

VARIABLE NAME	C-7 EPOXY	SOIL
ν	0.3	0.45
ρ_0	0.79	1.0

both equations, the unknowns are Z_1 (the "effective" impedance of the soil) and P_I (the pressure in the soil adjacent to the target face).

(2) The simultaneous equations are solved, as shown below for the situation of a cylindrical charge with .85 inches burial.

$$\begin{aligned} \text{C-7: } 54.9 &= \frac{2(.3127)}{Z_1 + .3127} P_I \\ 54.9Z_1 + 17.167 &= .6254 P_I \\ P_I &= 87.784 Z_1 + 27.450 \end{aligned}$$

$$\begin{aligned} \text{Glass: } 72.5 &= \frac{2(1.4616)}{Z_1 + 1.4616} P_I \\ 72.5 Z_1 + 105.996 &= 2.9232 P_I \\ 72.5 Z_1 + 105.996 &= 256.61 Z_1 + 80.242 \\ Z_1 &= .1399 \\ P_I &= 39.73 \text{ Kbar} \end{aligned}$$

(3) Equation (12) is used again with the values of P_I and Z_1 being those calculated above, with Z_2 being now the impedance of steel or aluminum, P_T being the unknown.

These calculations were carried out for all test conditions and the results are presented in Figure 8.

A further check on these predicted stresses was made using the pressure-particle velocity curves of Figure 2. Using this method (Figure 9) the stresses measured in the epoxy and glass targets are located on the respective curves (here, the pressures for the cylindrical charge with .85 inch burial). Since both points were produced by measuring the stress transmitted from the same reflected wave for the soil, they are linearly connected and the resulting line is extended until it intersects the pressure-particle velocity curves for the aluminum and steel. These intersection points then represent the pressures that would be measured in these materials. This procedure was used on all data conditions, and the results are compared with those from the impedance match calculation in Table 4.

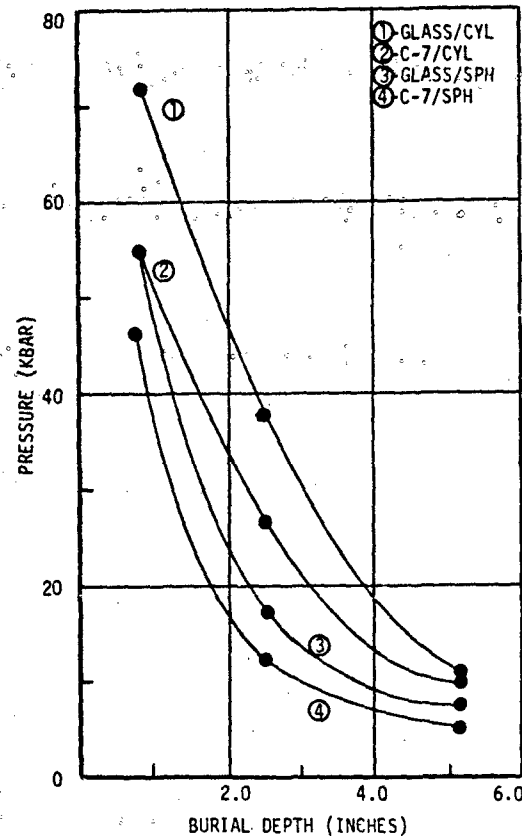


FIGURE 4. PEAK PRESSURES AS A FUNCTION OF BURIAL DEPTH FOR 1.5 LB PENTOLITE CHARGES (GAGE MAT'L/CHARGE CONFIG)

COMPARISON WITH PREVIOUS WORK

The cylindrical charge with .85 inch soil cover corresponds to a scaled distance of $Z = .117 \text{ ft/lb}^{1/3}$ for a target on the soil surface. Reference 1 reports pressures in steel for scaled distances of from .3 to 1.0 $\text{ft/lb}^{1/3}$. The graphically calculated pressure in steel at $Z = .117 \text{ ft/lb}^{1/3}$ shows good agreement with this previous work (Figure 10).

CONCLUSION

This program has furnished data on pressures generated at the ground surface by shallow buried explosive charges, and these pressures have been extrapolated to target materials of

military interest. The response of the C-7 epoxy gages have been simulated using the T00DY hydrodynamic computer code, and the predicted pressures in steel targets have been compared favorably with previous work.

REFERENCES

1. Wenzel, A. B. and Esparza, E. D., Measurement of Pressures and Impulses at Close Distances from Explosive Charges Buried and in Air, AD 903534L, 21 August 1973.
2. Morris, B. L., Evaluation of Non-Expendable Mine Clearing Roller Wheels Under Blast Attack, US Army Mobility Equipment Research and Development Center, TR-2005, April 1971.
3. Keough, D. D., Procedure for Fabrication and Operation of Manganin Shock Pressure Gages, Air Force Weapons Laboratory, AFWL-TR-68-57, August 1968.
4. Keough, D. D., Pressure Transducer for Measuring Shock Wave Profiles. Phase IX: Additional Gage Development, Final Report DASA 1414-1, November 1964.
5. Keough, D. D., Development of a High-Sensitivity Piezoresistive Shock Transducer for the Low Kilobar Range, DASA 2508, March 1970.
6. McQueen, R. G. and Marsh, M. P., Equation of State for Nineteen Metallic Elements from Shock-Wave Measurements to Two Megabars, Journal of Applied Physics, Vol. 31, Number 7, July 1960.
7. Rice, M. H., McQueen, R. G., and Walsh, J. M., Compression of Solids by Strong Shock Waves, Solid State Physics-Advances in Research and Applications, Vol. 6.
8. Lee, E. L., Hornig, H. C., and Kurz, J. W., Adiabatic Expansion of High Explosive Detonation Products, UCRL-50422, 2 May 1968.

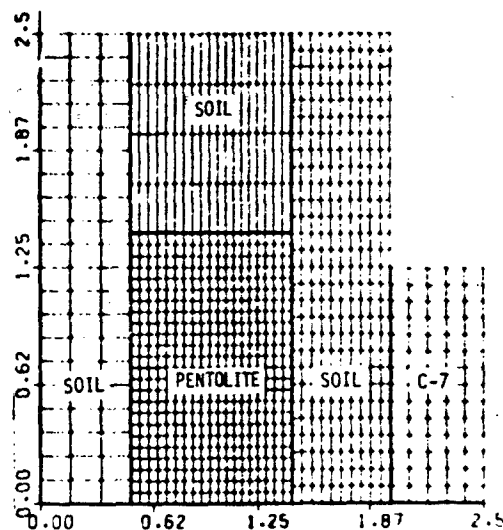


FIGURE 5. COMPUTATIONAL GRID FOR 1.5 LB PENTOLITE CYLINDER WITH 0.85 INCH SOIL COVER AND C-7 EPOXY TARGET, 1/4 SCALE (ALL DIMENSIONS IN CENTIMETERS)

TABLE 4. Comparison of Impedance Match and Graphical Estimates of Pressure in Steel and Aluminum Targets*

EXPLOSIVE CONFIGURATION	BURIAL DEPTH (INCHES)	PREDICTED STEEL PRESSURE (Kbar)		PREDICTED ALUMINUM PRESSURE (Kbar)	
		IMPEDANCE MATCH	GRAPHICAL	IMPEDANCE MATCH	GRAPHICAL
cylinder	0.85	77	81	74	74
sphere	0.85	57	58	55	56
cylinder	2.55	41	43	39	39
sphere	2.55	20	20	18	18
cylinder	5.10	11	11	11	11
sphere	5.10	7	7	7	7

*1.5 lb Pentolite charges.

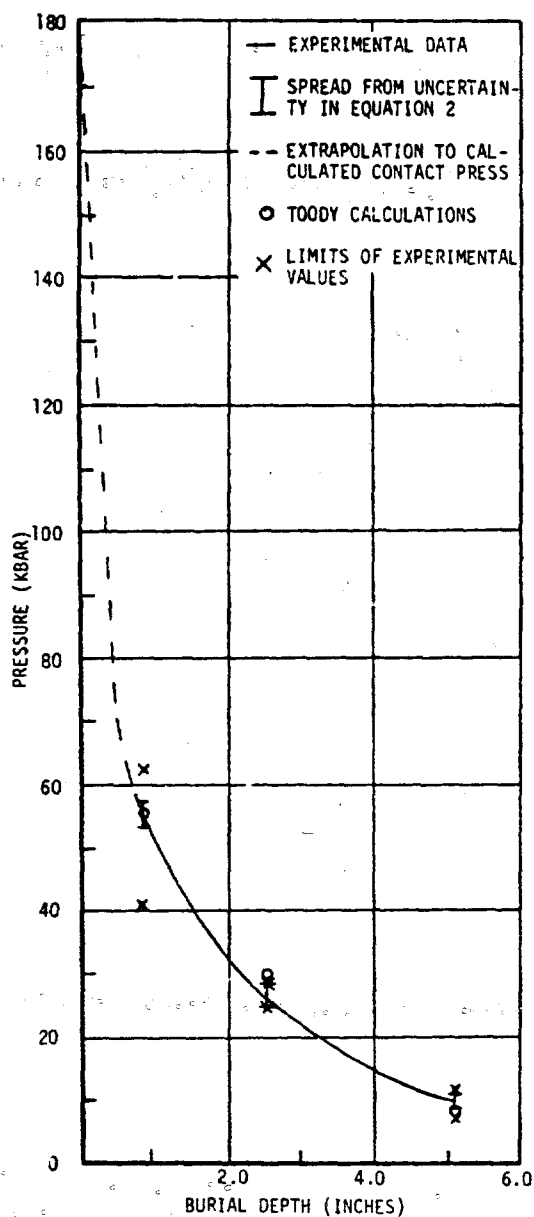


FIGURE 6. COMPARISON OF EXPERIMENTAL AND CALCULATED PEAK PRESSURES FOR CYLINDRICAL PENTOLITE CHARGES (1.5 LB), C-7 EPOXY TARGET

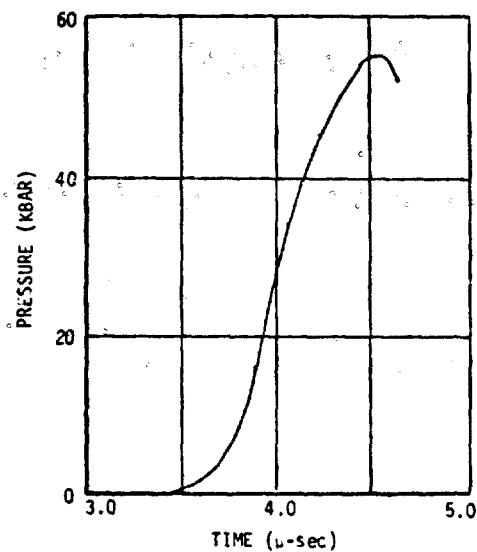


FIGURE 7. CALCULATED PRESSURE-TIME HISTORY FOR 0.85 INCH BURIAL (C-7 TARGET)

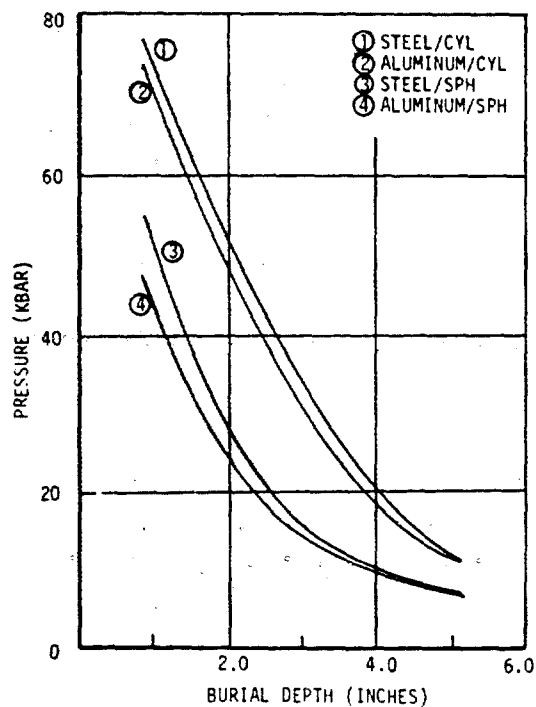


FIGURE 8. PREDICTED PRESSURES IN STEEL AND ALUMINUM TARGETS, IMPEDANCE MATCH CALCULATIONS

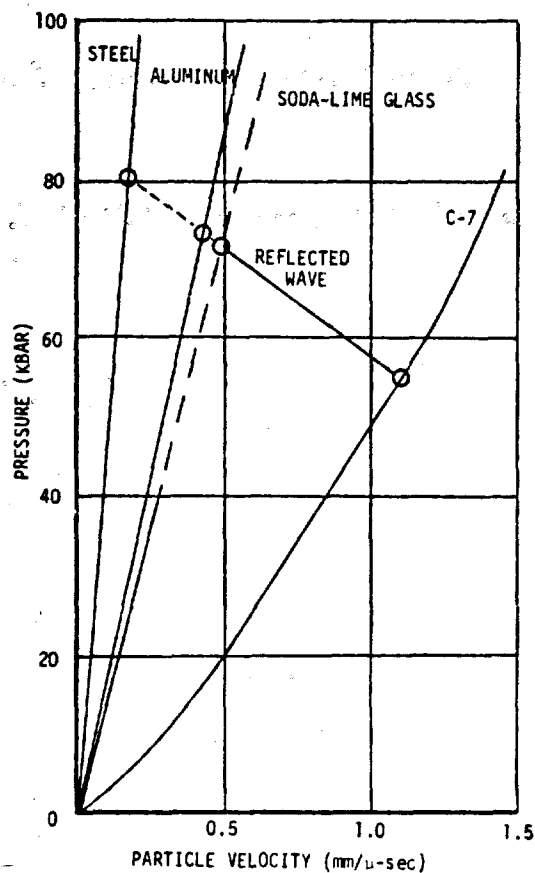


FIGURE 9. PRESSURE VS PARTICLE VELOCITY CURVES AND A TYPICAL SOLUTION TO DETERMINE MAXIMUM PRESSURE IN OTHER MATERIALS

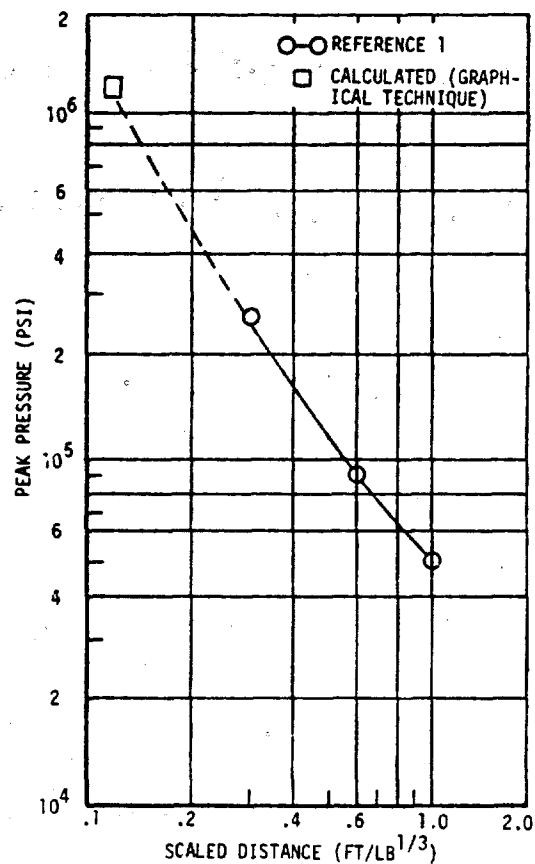


FIGURE 10. COMPARISON OF PREDICTED PRESSURE IN STEEL WITH PREVIOUS DATA

DISCUSSION

Mr. McKee (IIT Research Institute): Your analysis was two dimensional and yet it matched your experimental results correctly, does this imply that there is no three dimensional effect?

Mr. Morris: My entire set up was axisymmetric; I only did the calculations for the cylindrical gage, and with the combination of cylindrical targets and a cylindrical gage it worked out that if you were further from the center of the charge you might probably encounter three dimensional differences, but I don't believe that it would make that much difference at this very close distance.

Mr. Crawford (Los Alamos Scientific Lab): Have you attempted to sandwich your manganin gage between steel?

Mr. Morris: No I haven't, a contractor is currently doing this as part of another project.

Mr. McWhirter: When he sandwiches it in steel what does he use to keep it from shorting out?

Mr. Morris: You can use small layers of epoxy or anything that is very thin that will electrically isolate the gage from the conducting material, which would be the steel. All you really need is electrical insulation, and other work has shown that the pressures are not changed that much by doing it.